THE EFFECT OF ROCK PROPERTIES ON FRACTURE CONDUCTIVITY IN THE EAGLE FORD

A Thesis

by

ASHLEY FAYE KNORR

Submitted to the Office of Graduate and Professional Studies of
Texas A&M University
in partial fulfillment of the requirements for the degree of

MASTER OF SCIENCE

Chair of Committee,	A. Daniel Hill
Committee Members,	Ding Zhu
	Judith Chester
Head of Department,	A. Daniel Hill

May 2016

Major Subject: Petroleum Engineering

ABSTRACT

Unconventional reservoirs have become increasingly possible and economical due to the advances of hydraulic fracturing, a stimulation technique that creates highly conductive fractures that serve as pathways for hydrocarbons from the reservoir to the wellbore. This technique's success is determined by the rock's capability to fracture and the ability to sustain fracture conductivity. Several parameters, including formation properties, proppant type, and proppant concentration, affect the efficiency of fracture conductivity and should be taken into account for an optimal treatment.

The purpose of this study was to investigate the relationship between unpropped and propped fracture conductivity and the rock properties of outcrop samples from each of the facies of the Eagle Ford formation. Multiple samples were collected from each zone and mechanical properties were tested in both the z-direction and x-direction of the bedding planes. Compressive triaxial tests were performed on core samples of the outcrops in order to determine the elastic rock properties of Young's Modulus and Poisson's Ratio. Additionally, Brinell hardness tests were completed to determine the resistance of plastic deformation of the outcrop samples. Lastly, mineral composition was obtained by X-Ray Diffraction analysis.

The results of this study were compared to fracture conductivity data performed on the Eagle Ford formation. Within facies B1, the oil producing zone, the effect of anisotropy was present and revealed that the parallel (x-direction) samples had higher conductivity and higher Young's Modulus than samples perpendicular (z-direction) to the bedding planes. Throughout all the facies, unpropped conductivity was

predominantly influenced by the surface roughness. The propped fractures are more affected by proppant characteristics for fracture conductivity. At monolayer proppant concentration, proppant embedment is the main cause of conductivity loss due to permanent deformation. Fracture conductivity is influenced by several rock mechanical properties. Slower decline rates for propped conductivity were associated with higher surface roughness. Furthermore, the proppant pack characteristics dominate over the rock's mechanical properties when multilayer proppant concentration is applied.

DEDICATION

To my mother, who taught me to fight for what's important to me no matter how hard it may seem, to my father who believed in my education and perseverance, and to my husband who motivated me to pursue my dreams.

ACKNOWLEDGEMENTS

I would like to thank my advisors Dr. Ding Zhu and Dr. Daniel Hill for their guidance and support through the development of this research. I would also like to thank Dr. Judith Chester for being a member of my graduate committee.

I would like to thank Omar Enriquez Tenorio, Dante Guerra, Jesse Guerra, and Mark McGinley for their help and fruitful discussions regarding our research. I would also like to give a special thank you to Paola Perez Pena for sharing her knowledge and experiences with the triaxial testing equipment. I greatly appreciate the laboratory technicians at W.D. Von Gonten Laboratories for their help in the experimental work and troubleshooting. I would also like to thank RPSEA for their financial support through this research project.

Lastly, I would like to thank all of my friends, especially Rachael Cash, Emmanuel Belostrino, and Aaron Mendonsa, for providing support and fun distractions during the past two years.

NOMENCLATURE

A	Area (mm^2, in^2)
D	Indenter diameter (mm)
d_{avg}	Average diameter of indentation (mm)
E	Young's Modulus (psi, Mpa)
F	Force (kN, lbf, kgf)
HBW	Brinell hardness number (kgf/mm^2)
$k_f w_f$	Fracture Conductivity (md-ft)
$\left(k_f w_f\right)_0$	Fracture Conductivity at a closure stress of 0 psi (md-ft)
l	Initial length (in, mm)
l'	New length as a result of force (in, mm)
$LVDT$	Linear Variable Differential Transformers
Δl	Change in length (in, mm)
υ	Poisson's ratio
σ	Stress (psi, Mpa)
$\sigma_1, \sigma_2, \sigma_3$	Principal stresses (psi, Mpa)
σ_C	Fracture closure stress (psi, Mpa)
σ_D	Differential stress (psi, Mpa)
$\sigma_{x,}\sigma_{y,}\sigma_z$	Stress in the x-, y-, or z- direction (psi, MPa)
ε	Strain (-)
ε_a	Axial strain (-)

ε_l	Lateral strain (-)
ε_r	Radial strain (-)
$\varepsilon_{x,}\varepsilon_{y,}\varepsilon_z$	Strain in the x-, y-, or z- direction (-)
r	Radius (in, mm)
Δr	Change in radius (in, mm)
λ	Conductivity decline rate (psi^{-1})

TABLE OF CONTENTS

Page

ABSTRACT ii

DEDICATION iv

ACKNOWLEDGEMENTS v

NOMENCLATURE vi

TABLE OF CONTENTS viii

LIST OF FIGURES xi

LIST OF TABLES xvi

1 INTRODUCTION 1

1.1 Background 1
1.2 Eagle Ford Overview 4
1.3 Literature Review 8
1.3.1 Fracture Conductivity 8
1.3.2 Rock Mechanics 12
1.4 Problem Description 18
1.5 Research Objectives and Methodology 19

2 LABORATORY APPARATUS AND EXPERIMENTAL PROCEDURE 21

2.1 Description of Laboratory Apparatus 21
2.2 Experimental Procedure 31
2.2.1 Sample Collection 31
2.2.2 Sample Preparation 33
2.2.3 Replacement Linear Variable Differential Transformers Procedure 37
2.2.4 Refilling the Hydraulic Oil Reservoir Procedure 41
2.2.5 Rock Mechanical Properties Measurements 42
2.2.6 Elasticity 49
2.2.7 Hardness 54
2.2.8 Anisotropy 55
2.2.9 Surface Roughness 56
2.3 X-Ray Diffraction Analysis 57

2.3.1 Sample Preparation 58
2.3.2 X-Ray Diffraction Analysis 59

3 EXPERIMENTAL RESULTS AND DISCUSSION 61

3.1 Facies A Results 63
3.1.1 Facies A Rock Mechanics 64
3.1.2 Facies A Mineralogical Composition 68
3.1.3 Facies A Surface Roughness 69
3.1.4 Facies A Fracture Conductivity 70
3.2 Facies B1 Results 71
3.2.1 Facies B1 Rock Mechanics 72
3.2.2 Facies B1 Mineralogical Composition 76
3.2.3 Facies B1 Surface Roughness 77
3.2.4 Facies B1 Fracture Conductivity 79
3.3 Facies B2 Results 80
3.3.1 Facies B2 Rock Mechanics 80
3.3.2 Facies B2 Mineralogical Composition 85
3.4 Facies B3 Results 86
3.4.1 Facies B3 Rock Mechanics 87
3.4.2 Facies B3 Mineralogical Composition 89
3.5 Facies C Results 91
3.5.1 Facies C Rock Mechanics 91
3.5.2 Facies C Mineralogical Composition 95
3.5.3 Facies C Surface Roughness 96
3.5.4 Facies C Fracture Conductivity 98
3.6 Facies D Results 99
3.6.1 Facies D Rock Mechanics 99
3.6.2 Facies D Mineralogical Composition 104
3.6.3 Facies D Surface Roughness 106
3.6.4 Facies D Fracture Conductivity 107
3.7 Facies E Results 108
3.7.1 Facies E Rock Mechanics 108
3.7.2 Facies E Mineralogical Composition 113
3.7.3 Facies E Surface Roughness 114
3.7.4 Facies E Fracture Conductivity 116
3.8 Analysis of Rock Properties 117
3.9 Effect of Rock of Properties on Fracture Conductivity 124
3.10 Effect of Rock Properties on Unpropped Fracture Conductivity Loss 131
3.11 Effect of Rock Properties on Propped Fracture Conductivity Loss 138
3.11.1 100 Mesh Proppant 138
3.11.2 30/50 Mesh Proppant 145
3.12 Anisotropy of Mechanical Properties 151

4 CONCLUSIONS AND RECOMMENDATIONS 154

4.1 Conclusions 154
4.2 Recommendations 156

REFERENCES 158

APPENDIX A 166

LIST OF FIGURES

Page

Figure 1: Location of the Eagle Ford shale and the oil and gas windows of the formation (EIA, 2014) 5

Figure 2: Eagle Ford formation stratigraphy from outcrop locations (Gardner et al., 2013) 7

Figure 3: Embedment curve for 20-40 mesh bauxite proppant coverage on shale (Volk et al., 1981) 9

Figure 4: Long-term test results of proppant measured permeability over initial permeability (Cobb and Farrell, 1986) 10

Figure 5: Layered shale model schematic for both perpendicular (a) and parallel (b) to the bedding plane (Sone and Zoback, 2013) 15

Figure 6: Proppant embedment versus closure stress with increasing clay content (Alramahi et al., 2012) 16

Figure 7: Schematic of the RTX-1500 triaxial equipment (Perez Pena, 2015) 23

Figure 8: The triaxial cell 24

Figure 9: LVDTs connections at base of triaxial cell 25

Figure 10: Secured triaxial cell with axial load piston contact 26

Figure 11: Hydraulic oil cell pressure cabinet 27

Figure 12: Rock sample with LVDTs in place and secured in the triaxial base 28

Figure 13: Ferromagnetic cores used in triaxial testing 29

Figure 14: Platens and axial LVDTs 29

Figure 15: Radial LVDT and chain 30

Figure 16: Map of outcrop locations (Gardner et al., 2013) 32

Figure 17: Research group at Lozier Canyon 33

Figure 18: Wire configuration of LVDT to connector pins 38

Figure 19: LVDTs secured in a calibration device 39

Figure 20: Valves labeled for hydraulic oil cell pressure cabinet 42

Figure 21: Example of order to tighten each nut on the triaxial equipment 44

Figure 22: GCTS PLT-100 Brinell hardness apparatus 48

Figure 23: System of stresses in a triaxial compression test (Paterson and Wong, 2005) 52

Figure 24: Brinell hardness test (Mueller and Amro, 2015) 55

Figure 25: Transversely isotropic body in the X-Y bedding plane (Wong et al., 2008) 56

Figure 26: Laser profilometer used to calculate surface roughness (McGinley, 2015) 57

Figure 27: Agate mortar and pestle set used to crush Eagle Ford samples 58

Figure 28: Sieve apparatus used 59

Figure 29: Triaxial core sample orientations. 62

Figure 30: Sample naming methodology 62

Figure 31: Axial stress-strain curve for sample E-A-X-1 65

Figure 32: Radial stress-strain curve for sample E-A-X-1 65

Figure 33: Axial stress-strain curve for sample E-A-Z-1 66

Figure 34: Radial stress-strain curve for sample E-A-Z-1 66

Figure 35: Facies A mineralogy composition 69

Figure 36: Fracture surface of facies A parallel conductivity sample (Tenorio, 2016) 70

Figure 37: Summary of average conductivity behavior for facies A samples 71

Figure 38: Axial stress-strain curve for sample E-B-1-X-2 73

Figure 39: Radial stress-strain curve for sample E-B-1-X-2 73

Figure 40: Axial stress-strain curve for sample E-B-1-Z-3 74
Figure 41: Radial stress-strain curve for sample E-B-1-Z-3 74
Figure 42: Facies B1 mineralogy composition 77
Figure 43: Fracture surface of facies B1 perpendicular conductivity sample (Tenorio, 2016) 78
Figure 44: Summary of average conductivity behavior for facies B1 samples 80
Figure 45: Axial stress-strain curve for sample E-B-2-X-1 81
Figure 46: Radial stress-strain curve for sample E-B-2-X-1 82
Figure 47: Axial stress-strain curve for sample E-B-2-Z-1 82
Figure 48: Radial stress-strain curve for sample E-B-2-Z-1 83
Figure 49: Facies B2 mineralogy composition 86
Figure 50: Axial stress-strain curve for sample E-B-3-X-1 87
Figure 51: Radial stress-strain curve for sample E-B-3-X-1 88
Figure 52: Facies B3 mineralogy composition 90
Figure 53: Axial stress-strain curve for sample E-C-X-1 92
Figure 54: Radial stress-strain curve for sample E-C-X-1 92
Figure 55: Axial stress-strain curve for sample E-C-Z-1 93
Figure 56: Radial stress-strain curve for sample E-C-Z-1 93
Figure 57: Facies C mineralogy composition 96
Figure 58: Fracture surface of facies C parallel conductivity sample (Tenorio, 2016) 97
Figure 59: Summary of average conductivity behavior for facies C samples 99
Figure 60: Axial stress-strain curve for sample E-D-X-2 100
Figure 61: Radial stress-strain curve for sample E-D-X-2 101
Figure 62: Axial stress-strain curve for sample E-D-Z-1 101

Figure 63: Radial stress-strain curve for sample E-D-Z-1 102

Figure 64: Facies D mineralogy composition 105

Figure 65: Fracture surface of facies D parallel conductivity sample (Tenorio, 2016) 106

Figure 66: Summary of average conductivity behavior for facies D samples 108

Figure 67: Axial stress-strain curve for sample E-E-X-1 109

Figure 68: Radial stress-strain curve for sample E-E-X-1 110

Figure 69: Axial stress-strain curve for sample E-E-Z-1 110

Figure 70: Radial stress-strain curve for sample E-E-Z-1 111

Figure 71: Facies E mineralogy composition 114

Figure 72: Fracture surface of facies E parallel conductivity sample (Tenorio, 2016) 115

Figure 73: Summary of average conductivity behavior for facies E samples 117

Figure 74: Comparison of Young's modulus and Poisson's ratio across the Eagle Ford facies 119

Figure 75: Comparison of Brinell hardness number across the Eagle Ford facies 121

Figure 76: Average mineral composition 123

Figure 77: Comparison of unpropped conductivity for facies A, B1, and C 125

Figure 78: Comparison of unpropped conductivity for facies D and E 127

Figure 79: Average unpropped conductivity of each facies 129

Figure 80: Average unpropped conductivity with the exponential fit for facies A, B1, and C 132

Figure 81: Fracture surface of facies A parallel conductivity sample (Tenorio, 2016) 135

Figure 82: Average unpropped conductivity with the exponential fit for facies D and E 136

Figure 83: Average 0.1lb_m/ft^2 100 mesh propped conductivity with the exponential fit for facies A, B1, and C 139

Figure 84: Average 0.1lb_m/ft^2 100 mesh propped conductivity with the exponential fit for facies D and E 143

Figure 85: Average 0.1lb_m/ft^2 30/50 mesh propped conductivity with the exponential fit for facies A, B1, and C 145

Figure 86: Average 0.1lb_m/ft^2 30/50 mesh propped conductivity with the exponential fit for facies D and E 149

LIST OF TABLES

Page

Table 1: Summary of facies A mechanical properties....67

Table 2: Summary of facies A average surface roughness....70

Table 3: Facies A fracture conductivity experiments design....71

Table 4: Summary of facies B1 mechanical properties....75

Table 5: Summary of facies B1 average surface roughness....78

Table 6: Facies B1 fracture conductivity experiments design....79

Table 7: Summary of facies B2 mechanical properties....84

Table 8: Summary of facies B3 mechanical properties....89

Table 9: Summary of facies C mechanical properties....94

Table 10: Summary of facies C average surface roughness....97

Table 11: Facies C fracture conductivity experiments design....98

Table 12: Summary of facies D mechanical properties....103

Table 13: Summary of facies D average surface roughness....106

Table 14: Facies D fracture conductivity experiments design....107

Table 15: Summary of facies E mechanical properties....112

Table 16: Summary of facies E average surface roughness....115

Table 17: Facies E fracture conductivity experiments design....116

Table 18: Summary of mechanical properties....118

Table 19: Summary of unpropped surface roughness for facies A, B1, and C....127

Table 20: Summary of unpropped surface roughness for facies D and E....129

Table 21: Summary of unpropped surface roughness of each facies....131

Table 22: Unpropped decline rate constants for facies A-X, B1-X, B1-Z and C-X 132

Table 23: Unpropped decline rate constants and surface roughness for facies A-X, B1-X, and C-X overview 135

Table 24: Unpropped decline rate constants for facies D and E 136

Table 25: Unpropped decline rate constants and surface roughness for facies D and E overview 138

Table 26: 0.1lb_m/ft^2 100 mesh propped decline rate constants for facies A, B1, and C 139

Table 27: Summary of 0.1lb_m/ft^2 100 mesh propped surface roughness for facies A, B1, and C 141

Table 28: 0.1lb_m/ft^2 100 mesh propped decline rate constants and surface roughness for facies A-X, B1-X, and C-X overview 142

Table 29: 0.1lb_m/ft^2 100 mesh propped decline rate constants for facies D and E 143

Table 30: Summary of 0.1lb_m/ft^2 100 mesh propped surface roughness for facies D and E 145

Table 31: 0.1lb_m/ft^2 30/50 mesh propped decline rate constants for facies A, B1, and C 146

Table 32: Summary of 0.1lb_m/ft^2 30/50 mesh propped surface roughness for facies A, B1, and C 147

Table 33: 0.1lb_m/ft^2 30/50 mesh propped decline rate constants and surface roughness for facies A-X, B1-X, and C-X overview 149

Table 34: 0.1lb_m/ft^2 30/50 mesh propped decline rate constants for facies D and E 150

Table 35: Summary of 0.1lb_m/ft^2 30/50 mesh propped surface roughness for facies D and E 151

Table 36: Summary of anisotropy values 152

1 INTRODUCTION

1.1 Background

Hydrocarbon production from unconventional reservoirs has transformed the oil and gas industry in the United States. Unconventional reservoirs, typically shale formations, have low or ultra-low permeability. Due to this low permeability, unconventional reservoirs are difficult to produce from without any stimulation. For many decades, hydraulic fracturing has been used as the most common and effective method of stimulation techniques.

Hydraulic fracturing creates highly conductive fractures that serve as pathways for hydrocarbons from the reservoir to the wellbore. At high pressure, fracturing fluid composed of proppant, water, and chemicals is pumped downhole to the wellbore. Once the pressure exceeds the fracture initiation pressure, the fluid begins to break the rock and the fracture forms and propagates perpendicular to the direction of the minimum stress. After pumping has ceased, the pressure falls below the fracture pressure and the fracture generated closes. Proppant is used to sustain the fracture and keep the channel open. While there are several types of proppant used, most commonly used in industry are man-made ceramic and sand grain proppant. Ceramic proppant has high strength and high thermal resistance, which is ideal for high pressure reservoirs (Treviranus, 2013). Sand has low strength and is irregularly shaped, but is much cheaper and more widely used in industry. The propped fractures bypass formation damage and allow hydrocarbons to flow towards the wellbore for production (Economides et al., 2012).

The success of hydraulic fracturing is determined by its ability to sustain fracture conductivity, a measure of the fluid flow capability through the fractures.

Productivity of a well increases as a result of improved fracture conductivity, the product of fracture permeability and fracture width (Economides et al., 2012). There are several factors that affect successful and sustained fracture conductivity. Proppant type, proppant concentration, rock mechanical properties, and closure stress are some of the parameters that have been described and studied in literature. More specifically, surface roughness, hardness, and elastic properties are several rock mechanical properties that have been studied in connection to fracture conductivity. Surface roughness is an important factor in which a high surface roughness results in a smaller fracture width (Zoorabadi et al., 2015). This adversely affects unpropped fracture conductivity translating to lower fracture conductivity values. Proppant is widely used to sustain the fracture width created in hydraulic fracturing. However, proppant embedment is a common phenomenon that has an adverse effect on the rock's surface and fracture conductivity. Most shale formations are soft and ductile, this often leads to proppant embedment and decrease in fracture conductivity (Mueller and Amro, 2015). While propped fracture conductivity has improved overall conductivity, proppant type, proppant concentration, proppant durability, and closure stress are considerable factors that affect this improved conductivity (Chapman and Palisch, 2014). The rock mechanical properties have a substantial impact on fracture conductivity as well as the behavior of proppant used to sustain the fracture. The study of the relationship between the rock mechanical properties and fracture conductivity is meaningful because a better

understanding can improve productivity and reduce costs of operation. This is especially important considering the cost of hydraulic fracturing treatment per well is routinely millions of dollars.

The first commercial hydraulic fracturing treatment was performed in the Barnett Shale. Initially, conventional crosslinking fluid for fracture treatment was used. By 1997, Mitchell Energy transitioned into using slick water treatments with high concentration of proppant, but it was difficult to keep proppant placement (Matthews et al., 2010). As a result, smaller mesh proppant was used which allowed for higher concentrations that could transport further into the fracture (Matthews et al., 2010). This treatment allowed for higher production rates and decrease in costs. The success of the Barnett Shale influenced the development of other shale formations, including the Eagle Ford. In the Eagle Ford, similar Barnett slick water treatments were attempted, but the results differed greatly. While the Barnett is predominately gas-bearing siltstone reservoir with high brittleness, the Eagle Ford formation is both gas and oil producing clay rich limestone reservoir with more ductile properties (Stegent et al., 2010). Proppant embedment is highly probable due to the clay properties in the Eagle Ford. Consequently, the low concentration of small mesh proppant used in the Barnett slick water treatments was not effective enough to overcome proppant embedment and ensure the fracture stays open at high closure stress. To achieve higher conductivity, high concentration of larger mesh proppant with hybrid fluid systems was necessary to prevent proppant embedment in the Eagle Ford (Stegent et al., 2010). The Eagle Ford's hydraulic fracturing treatment successes and failures demonstrate that the relationship

between the rock's mechanical properties and fracture conductivity is incredibly valuable to ensure that a successful, cost-effective treatment option is chosen in the field.

1.2 Eagle Ford Overview

The Eagle Ford is a gas and oil producing play that lies in southwest Texas. The play was discovered due to the organic content testing of a core sample from an old 1950's dry well. Development of this soft, carbonate rich formation started in late 2008 and is now considered the second most developed unconventional formation. As of February 2016, oil and gas production of the Eagle Ford was reported at an estimated 1,200 thousand Barrels of oil per Day (bbl/day) and 6.6 Billion Cubic feet per Day (ft^3/day) of natural gas (EIA, 2016). The formation varies in depth from 4,000 feet to 12,000 feet that rests between the Austin Chalk and Buda Lime. It stretches 50 miles wide and 400 miles long and ranges in thickness depths of 120 to 350 feet (Gong et al., 2013).

Figure 1 shows the Eagle Ford location and the oil and gas windows of the formation. The Eagle Ford play is an Upper Cretaceous (Cenomanian to Coniacian) formation that is prolific in hydrocarbon resources (Donovan et al., 2012). While it is often referred to as a "shale", the Eagle Ford formation actually consists of organic-rich calcareous-mudrock. (EIA, 2014).

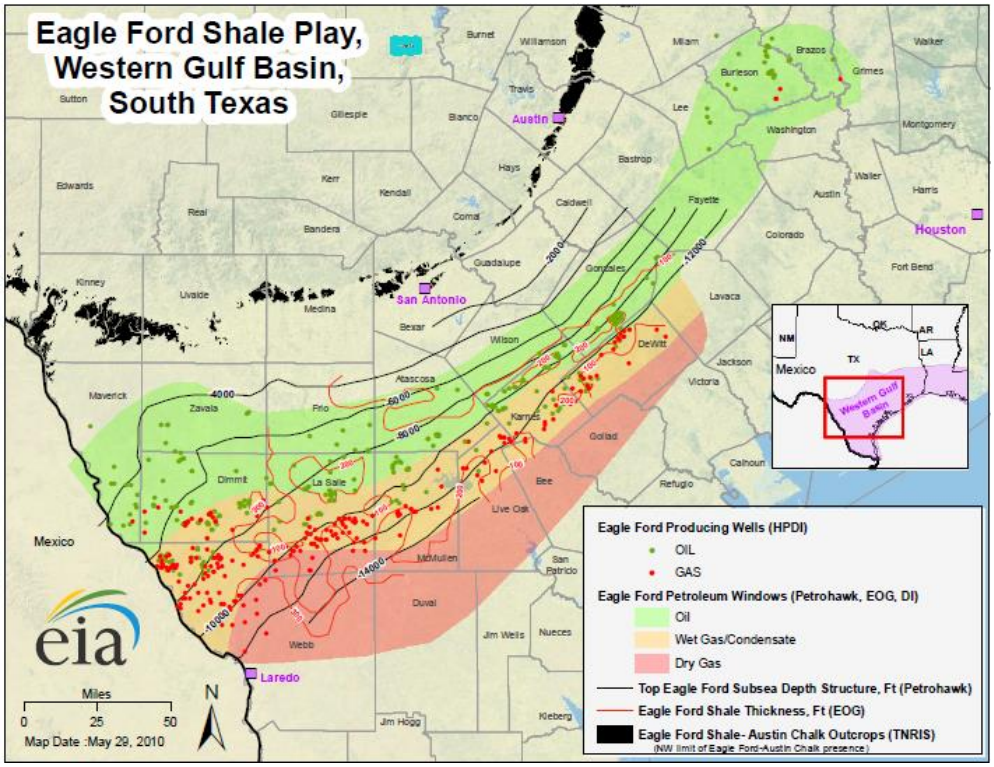

Figure 1: Location of the Eagle Ford shale and the oil and gas windows of the formation (EIA, 2014)

Five distinct vertical lithostratigraphic units comprise the Eagle Ford formation and are known as facies A through E. Heterogeneity throughout the facies and within each facies is distinctly present. Facies A is the deepest in the formation and consists of light grey interbedded grainstones and mudstone with an increasing TOC content (Donovan et al., 2012). Facies B is lies on top of facies A and has distinct variability, which resulted in sub-facies within the unit. This facies is rich in organic calcareous mudstone (Gardner et al., 2013). Sub-facies B1 and B2 have the highest TOC content found in the Eagle Ford formation due to an anoxic water environment providing favorable conditions. As a result, industry has focused on this lower section of facies B,

both B1 and B2, for production. Sub-facies B3, also known as the middle facies B, differs from the lower sub-facies due to present of thick bentonite beds causing a lower TOC content reading (Donovan et al., 2012). Overlying B3 are sub-facies B4 and B5, also known as Upper facies B, these units are dominated by black organic rich mudstones with thick bentonite beds with a slight increase in TOC content (Donovan et al., 2012). Facies C is third in the sequence and is located in the middle of the formation. Although facies B lithology is similar to C, this facies has more burrows indicative of an oxygenated environment. Facies C is characterized as having the lowest TOC, but the highest carbonate content (Donovan et al., 2012). The fourth unit in the Eagle Ford is facies D. This unit consists of massive packstone containing pebble-sized clasts of tan mudstones (Donovan et al., 2012). The upper most layer of the Eagle Ford is facies E, which consists of yellow ochre, thin-bedded limestone (Donovan et al., 2012). Facies A, B, and C are interpreted as one depositional sequence and facies D and E are a separate depositional sequence. In fact, facies D and E are considered as a sequence that is continued up into the Austin Chalk. Figure 2 displays the stratigraphy of the Eagle Ford facies at outcrop locations.

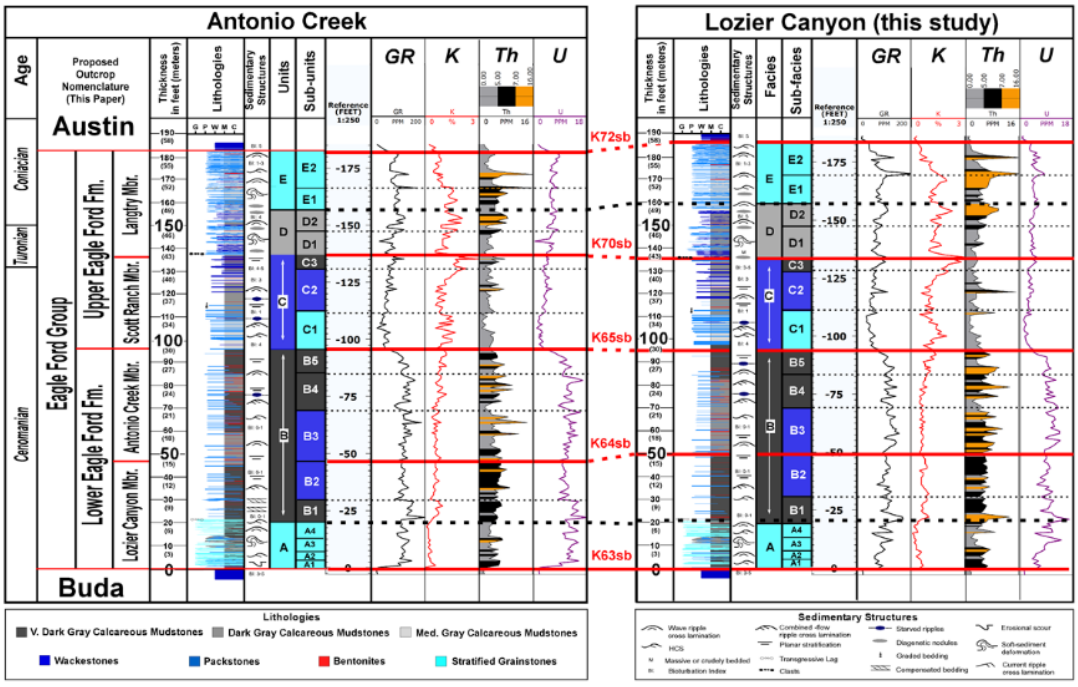

Figure 2: Eagle Ford formation stratigraphy from outcrop locations (Gardner et al., 2013)

Hydraulic fracturing treatments in the Eagle Ford differ depending on liquid or gas production. While the average lateral length is 4,500 feet and number of stages range from 10-20, the amount of proppant and fluid used varies. In the gas producing region, roughly 6,000 Million Gallons (Mgal) of slick water are used per treatment. However, the liquid rich area of the Eagle Ford requires less fluid. Often a hybrid mixture (both slick water and crosslinked) is needed for this area of the reservoir (Fan et al., 2011). Due to liquid producing region requiring higher fracture conductivity, the proppant concentration is nearly doubled with a lower pump rate used. Typically, larger mesh proppant, such as 100 Mesh, is used in the Eagle Ford.

1.3 Literature Review

1.3.1 Fracture Conductivity

The purpose of hydraulic fracturing is to create highly conductive pathways in low permeability formations. In order to increase well productivity, the fracture network created needs to withstand closure stress to sustain fracture conductivity. Large quantities of proppant are pumped downhole into these pathways in order to maintain the fracture width created. After hydraulic fracture stimulation is completed, sudden loss of fracture conductivity is often attributed to proppant embedment. In soft rock shales, proppant embedment is a prevalent occurrence. Embedment occurs at the interface area where the proppant pack and formation face meet due to the overburden load (Weaver et al., 2006). Proppant embedment can severely damage the rock, decrease fracture width, and adversely affect fracture conductivity (Wen et al., 2006). Yet, embedment is not the only factor that affects fracture conductivity. Formation properties, mineral composition, closure stress, surface roughness, proppant type, concentration, and characteristics, as well as fluid type are some components that affect the productivity of fracture conductivity and should be taken into account for an optimal treatment (Morales et al., 2011).

Fracture conductivity has been a research topic of interest for the oil and gas industry for several decades. Volk et al. (1981) investigated several factors affecting fracture closure, including proppant embedment, closure pressure, proppant characteristics and concentration, formation hardness and surface roughness on shale cores. While they concluded that the shale fracture closure rate was directly related to

the proppant contact area and surface roughness, the low mechanical strength and water sensitivity of shale significantly influences proppant embedment. As a result of proppant embedment, the fracture closure rate significantly increases and is even greater with partial monolayer proppant, i.e. 50%, as shown in Figure 3.

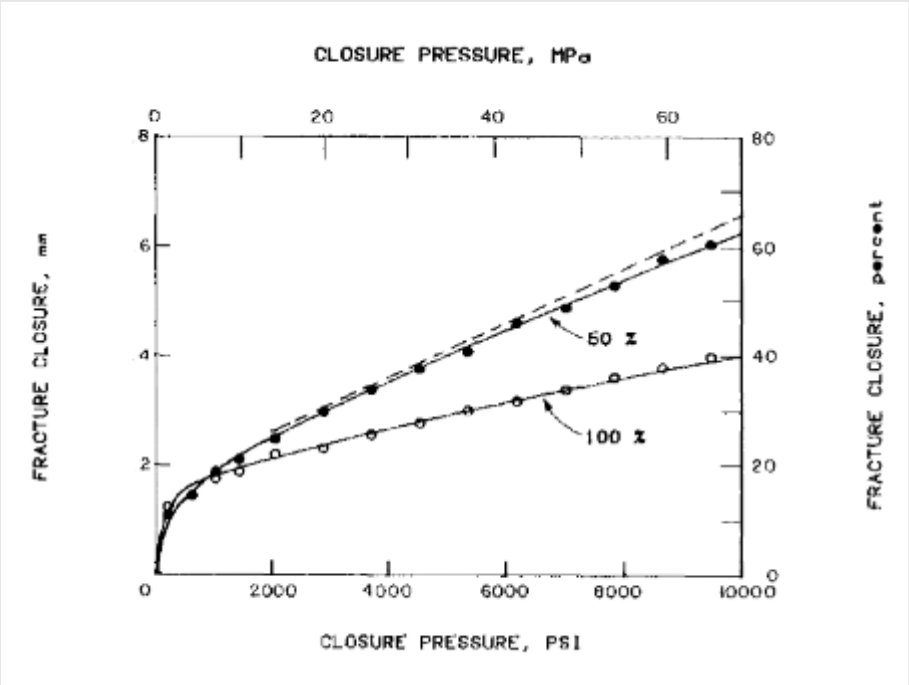

Figure 3: Embedment curve for 20-40 mesh bauxite proppant coverage on shale (Volk et al., 1981)

Proppant selection is a crucial expenditure in the hydraulic fracturing stimulation design. Selecting the wrong proppant for a treatment can negatively impact the well's productivity, resulting in poor fracture conductivity. Cobb and Farrell (1986) evaluated long-term proppant behavior between two steel plates using 2% KCl at 10,000 psi for man-made proppant and 5,000 psi for sand at 200°F. For both sets, they found a rapid

decline in proppant permeability and conductivity during the first month, possibly due to failure and consolidation of the proppant pack, followed by a slight decline during the remaining of the test. Figure 4 displays the long term results of the tested proppant's permeability ratio. During long-term production, proppant failure is important to prevent as long as possible. Proppant failure can induce fines migration, which plug the fracture permeability. Having a knowledgeable understanding of the mechanical properties and closure stresses of the formation are important when selecting a type of proppant. The interaction between the proppant and these factors could affect the fracture conductivity significantly.

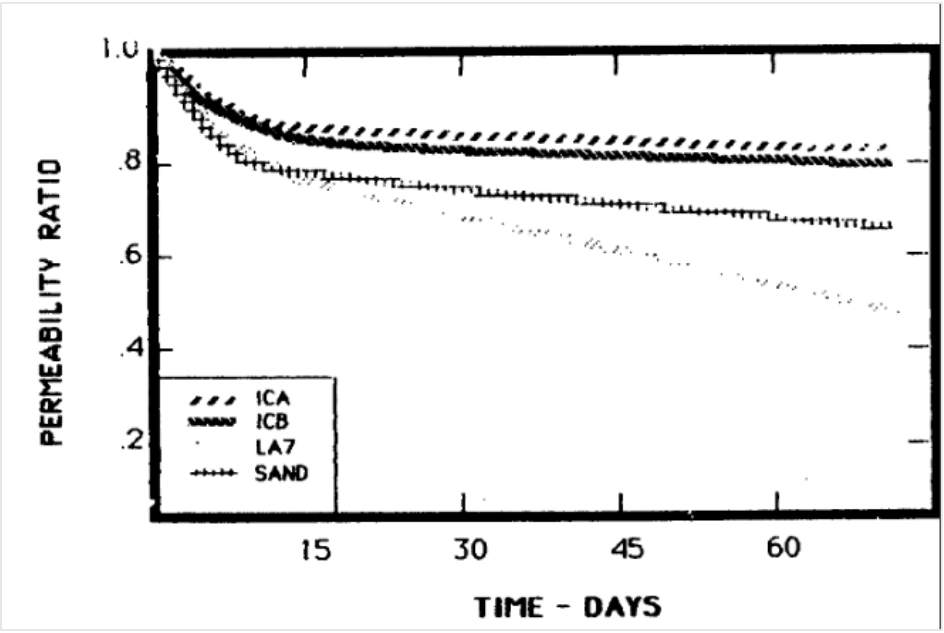

Figure 4: Long-term test results of proppant measured permeability over initial permeability (Cobb and Farrell, 1986)

Retaining fracture width is a key challenge in hydraulic fracturing. Although proppant is frequently used to prop the fracture open, the effect of fracturing fluid can severely impair the proppant permeability and ultimately conductivity. Hawkins (1988) conducted conductivity experiments on Ohio sandstone samples with 2 fracturing fluid mixtures, 2% KCl and uncrosslinked hydroxypropyl guar, with 20/40 mesh and 20/25 northern white sand. He concluded that when using sand proppant with aqueous-based fracturing fluids, the use of crosslinking and polymer concentrations should be minimal to maximize proppant permeability and the larger mesh proppant should be used at maximum concentration. Selection in type of fracturing fluid is a key decision in the design of hydraulic fracturing treatment and often a costly one. Water-based fracturing fluid, known as slick water, has been increasingly used in the field with low proppant concentrations, often referred to as a "waterfrac treatment," to stimulate low permeability reservoirs at a cost-effective manner. Fredd et al. (2000) performed waterfrac treatments experiments on East Texas Cotton Valley sandstone formation with 20/40 bauxite and Jordan sand at 0, 0.1, and 1 lb_m/ft^2. They concluded that the success of waterfrac treatments is greatly dependent on the formation properties, i.e. the degree of fracture displacement, magnitude of surface asperities and rock mechanical properties, which could be diminished by use of high strength proppant at high concentrations. When using low concentrations of proppant, the rock mechanical properties and surface asperities dominated fracture conductivity. Low viscosity slick water ideally allows the proppant to stay in suspension while transporting until the fracture closes. Preferably, the proppant, even at low concentrations, would settle across the base of the fracture.

However, often in low viscosity fluids, proppant settles out quicker creating multiple layers of proppant rather than an even distribution. As a result, the proppant is not able to transport deep into the formation. Despite the poor proppant distribution with slick water treatment, high pumping rates can induce more complex fractures increasing productivity (Kostenuk and Browne, 2010). Additionally, the costs associated with slick water treatments are considerably lower than with alternative fracturing fluids.

1.3.2 Rock Mechanics

A hydraulic fracturing treatment design using slick water cannot be simply duplicated and applied to each shale formation. The rock properties and characteristics of shale formations are distinctly different and a successful treatment in one play may result in disastrous results in another shale formation. In fact, large variability in lithology has been found between shale plays and even within a single shale formation as well (Passey et al., 2010). The rock mechanical properties of a shale formation play a significant role in the hydraulic fracturing treatment. Britt and Smith (2009) emphasized the importance of geomechanics and the state of stress of a shale play for a successful hydraulic fracturing stimulation. Additionally, Rickman et al. (2008) stressed that although the Barnett shale was the stimulus of hydraulic fracturing, each shale formation is distinct and unique. They highlighted that the mechanical rock properties, such as brittleness and mineralogy, are fundamental in completion designs. Brittle shales, i.e. the Barnett and Fayetteville shales, have natural fractures which react well to hydraulic fracturing and would have high Young's moduli and low Poisson's ratio. However, shales that are more ductile want to restore any fractures formed. Mineralogy, which can

be highly variable within a formation, also impacts the brittleness of a shale. The amount of quartz in a shale is directly related to the brittleness of a shale, in which higher amounts of quartz present lead to higher brittleness (Rickman et al., 2008).

The selection of fracturing fluid is a crucial factor in fracturing stimulation design; yet, the fluid used can have a detrimental impact on the formation and its rock mechanical properties. Several studies have been performed on shale formation sensitivity to fracturing fluids used. Das and Achalpurkar (2013) tested the Brinell hardness of three shale core samples from the same formation at both dry conditions and at 200°F with 3% KCl for 48 hours. They found that shale sample with the highest clay content had the highest softening effect resulting in a lower Brinell hardness value. Furthermore, the fracturing fluid compromised the sample's rock fabric resulting in a higher plasticity of the shale sample. Proppant embedment became more prevalent when fracturing fluid increased the plasticity of the fracture face. Holt et al. (2011) also concluded that fracturing fluids can lead to increase in plasticity of the shale. Additionally, they established that brittleness is sensitive to anisotropy.

Anisotropy is prevalent in shale plays due to orientation of clay particles, kerogen inclusions, microcracks, and layering (Sayers, 2013; Hornby et al., 1993). Shale anisotropy strongly influence the mechanical properties of shale. Historically, the Young's Moduli for shale plays measured parallel to the bedding plane are greater than when measured perpendicular to the bedding plane. Sone and Zoback (2013) offer an explanation as to why anisotropy heavily plays a role in the elastic behavior of shales. They examined the static and dynamic elastic properties for one inch diameter and two

inch in length cylindrical samples from Barnett, Eagle Ford, Haynesville, and Fort St. John shale plays in both perpendicular and parallel orientations to the bedding plane. The elastic properties of these rocks had high variability between the shale formations and within the play itself. Yet, a strong correlation to the rock fabric and the mineral composition, specifically the amount of clay and organic content, were observed with the elastic properties. The Young's modulus was ascertained to have an indirect relationship with the amount of clay and kerogen volume present. Furthermore, the static Poisson's ratio did not reveal any correlation with the sample's composition. However, both Poisson's ratio and Young's modulus indicated a strong relationship with anisotropy. In both cases, the parallel orientation samples had higher values when compared to the perpendicular orientation. Sone and Zoback (2013) proposed that the anisotropic behavior observed was due to the composite of a shale rock, which is comprised of two types of layers, "soft" and "stiff", seen in Figure 5. Clay and kerogen contents compose the "soft" layer and quartz, feldspars, and carbonates compose the "stiff" layer. These minerals influence the mechanical properties resulting in mechanical isotropic layers.

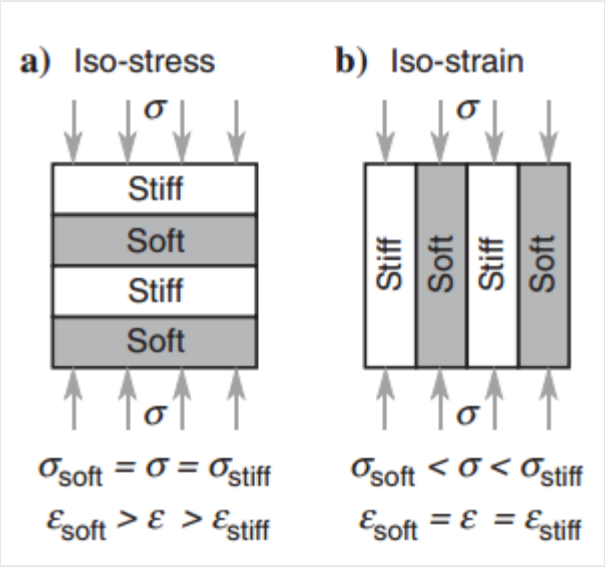

Figure 5: Layered shale model schematic for both perpendicular (a) and parallel (b) to the bedding plane (Sone and Zoback, 2013)

Li et al. (2015) also agreed with the shale fabric layers model presented by Sone and Zoback (2013). They propose that the shale formation on a larger scale is composed of a "stiff" matrix with "soft" layers throughout. Furthermore, Fjaer and Nes (2013) triaxial tested 1.5 inch by 3 inch core plugs from Mancos shale at various inclinations from parallel and perpendicular orientation. They found that the parallel direction had the highest Young's modulus with a decreasing trend in Young's moduli values as the orientation approached perpendicular orientation.

Understanding mechanical properties of a shale formation is an important component for an optimized hydraulic fracturing design treatment. The interaction between the rock and proppant is an important understanding that can adversely affect fracture conductivity and the well's productivity. Alramahi et al. (2012) performed

experiments on samples from different shale formations to test embedment of high strength proppant bauxite with increasing loads and while submerged in 3%KCl for 24 hours. They concluded that samples with low stiffness, usually with high clay content, resulted in the highest embedment, shown in Figure 6. Furthermore, proppant embedment has an indirect relationship with Young's Modulus. Loss in fracture conductivity and high proppant embedment were observed to be associated with high clay content or low static Young's modulus.

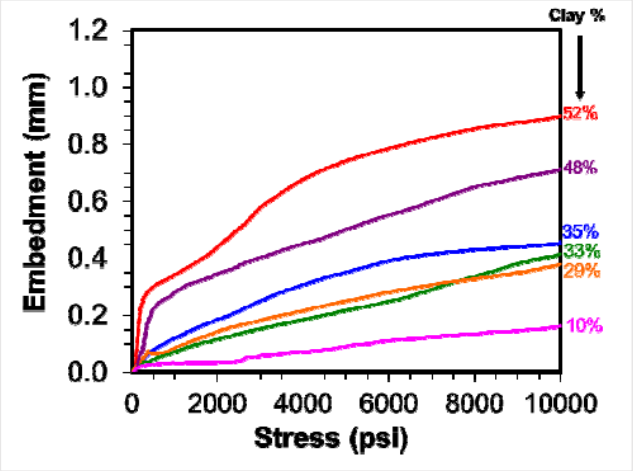

Figure 6: Proppant embedment versus closure stress with increasing clay content (Alramahi et al., 2012)

Several experimental fracture conductivity studies have been performed on different shale formations. Zhang et al. (2013) measured the conductivity of natural and induced fractures that either had shear displacement or were aligned from Barnett shale outcrops. Conductivity experiments were run for both unpropped and propped fractures with various proppant sizes and concentrations. They found that the unpropped fracture

conductivity had a direct relationship with brittleness. Loss in unpropped conductivity was due to the plastic mechanical compaction of the shale matrix layers and plastic deformation at the fracture surface. Additionally, larger surface asperities on the fracture surface resulted in higher unpropped fracture conductivity. Fracture conductivity is less dependent on the rock's mechanical properties as proppant concentration use increases. Experimental studies on fracture conductivity for Fayetteville and Eagle Ford shale were performed by Briggs (2014) and Guzek (2014), respectively. Their findings also concluded that the use of higher proppant concentration resulted in the rock mechanical properties becoming less important, similar to Zhang et al. (2013). Additionally, Jansen et al. (2015) investigated the relationship between fracture conductivity and rock properties of shale formations. They determined that unpropped fracture conductivity was dependent on the fracture surface topography. Additionally, propped fracture conductivity was dependent on the proppant type, concentration, and strength. However, the conductivity decline for monolayer proppant placement was determined to be related to Young's modulus. Higher values of Young's modulus resulted in slower decline of fracture conductivity. This was particularly true for Young's moduli less than 2MPsi. McGinley (2015) conducted experimental fracture conductivity research on the Marcellus shale formation in both vertically and horizontally orientated to the bedding planes. Vertical samples reported higher fracture conductivity results than horizontal samples. Furthermore, the propped fracture conductivity was not dependent on surface roughness or fracture orientation, but rather the anisotropic rock mechanical properties. Perez Pena (2015) studied the rock mechanical properties relationship to fracture

conductivity of Marcellus shale outcrops. She found that anisotropy effect was present for the Marcellus samples. Furthermore, higher Young's modulus values correlated to slower fracture conductivity decline. The loss of conductivity with monolayer proppant concentration was due to proppant embedment on the fracture surface. Perez Pena (2015) agreed with Jansen et al. (2015) in that the rock's mechanical properties are less influential in fracture conductivity when multilayer proppant concentration is used.

1.4 Problem Description

Onshore shale formations are now capable of producing significantly and economically regardless of the low permeability characteristics due to hydraulic fracturing. However, an optimal hydraulic fracturing treatment (equaling the highest and most sustainable production figures) requires a comprehensive understanding of the rock properties of the formation. In order to reach maximum fracture propagation, brittle zones of the hydrocarbon producing zones are targeted. These brittle zones are characterized as high Young's modulus and low Poisson's Ratio, which suggests that fractures are likely to form.

The successfulness of a hydraulic fracturing treatment is indicated by fracture conductivity. In order to maintain the fractures width, proppant must be placed within these fractures. The placement of proppant, proppant type, and proppant concentration are parameters that can be varied to maximize fracture conductivity. However, surface roughness, closure stress, and rock properties are other important parameters that effect fracture conductivity. Yet, the effects of these parameters on fracture conductivity varies within each shale formation. This study focuses on the relationship between rock

mechanical properties and mineralogy with unpropped and propped fracture conductivity of the Eagle Ford Shale outcrops. Furthermore, the orientation of the rock mechanical properties is also taken into account.

1.5 Research Objectives and Methodology

The purpose of this research is to study the relationship between fracture conductivity of the Eagle Ford Shale outcrops and its corresponding rock mechanical properties. Additionally, the effect the orientation of the rock samples has on this relationship is examined. Young's Modulus, Poisson's Ratio, and Brinell hardness, as well as mineral composition and surface roughness were the factors of interest in this study. Each parameter is investigated and compared to fracture conductivity, both unpropped and propped. Any correlation found could have a profound impact on optimization of hydraulic fracturing in industry.

1. Develop a standardized experimental procedure for outcrop samples to test for rock mechanical properties by using ASTM D4543 – 08 (2008) and ASTM D7012 – 14 (2014) industry standards for Triaxial compression testing.
2. Measure Young's Modulus and Poisson's Ratio for the Eagle Ford shale outcrops using the triaxial compression equipment in both perpendicular (z-direction) and parallel (x-direction) to the bedding planes. Each core plug in the x-direction has a corresponding fracture conductivity sample.
3. Develop a standardized experimental procedure for outcrop samples to test for Brinell hardness by using ASTM E10-14 (2015) industry standard for Brinell hardness testing.

4. Measure Brinell hardness for the Eagle Ford shale outcrops using the point load apparatus in both perpendicular (z-direction) and parallel (x-direction) to the bedding planes. Each core plug is used for triaxial compression testing afterwards.
5. Determine the mineral composition using X-Ray Diffraction (XRD) and measure surface roughness of the fracture conductivity samples.
6. Analyze the rock mechanical properties effect on the orientation of the bedding planes.
7. Analyze the effect on fracture conductivity on each property measured and conclude if each relationship is meaningful. Determine the dominating factor for fracture conductivity based on the Eagle Ford Shale outcrops.

2 LABORATORY APPARATUS AND EXPERIMENTAL PROCEDURE

This section describes the experimental procedures and laboratory equipment used to prepare samples and measure rock mechanical properties of the samples. All aspects of procedures were kept constant throughout experiments performed in order to ensure measurements could be compared.

2.1 Description of Laboratory Apparatus

The standards developed by the American Society for Testing and Materials International for measuring compressive strength and elastic moduli of intact rock specimens, known as ASTM D7012-14, were followed. This standard describes the experimental equipment required as well as the experimental procedures needed to test the elastic moduli of rock samples.

The GCTS RTX-1500 Triaxial Rock Testing System was used to measure Young's modulus and Poisson's ratio of rock samples. This system is specifically designed to control confining pressure and pore pressure while measuring the stress-strain properties of the rock sample. The RTX-1500 is able to measure properties of a rock sample up to 2 inches in diameter and 4 inches in length. A force capability of 1500 kN by the axial load piston is could be applied to the rock specimen. Confining pressure and pore pressure have limits up to 20,000 psi with this system. However, for the objectives of this research, the pressure limits and axial load limit were never reached. In fact, low confining pressure was used during experiments and the pore pressure capability was never used.

The GCTS RTX-1500 meets the specifications and requirements set by the International Society of Rock Mechanics (ISRM) to measure triaxial compression tests for rock specimens. Furthermore, the benefit of the GCTS RTX-1500 is that the deformation instrumentation is located internally as well as directly in contact with the rock specimen. The internal instrumentation uses two Linear Variable Differential Transformers (LVDTs) to measure the axial and one LVDT to measure radial deformation. These LVDTs have a sensitivity to read deformation measurements up 0.001 millimeters.

The GCTS RTX-1500 system encompasses the following components:

- GCTS hydraulic load frame with 1500 kN loading capability
- GCTS High Pressure Triaxial cell with a 20,000 psi capacity
- Seal piston/platen system to apply axial load
- Two 140 MPa servo-controller pressure intensifier system cabinets
- Internal deformation instrumentation (3 LVDTs)
- GCTS hydraulic power supply
- Data acquisition system (SCON-2000 Digital System Controller)
- Data acquisition software GCTS CATS

The GCTS RTX-1500 system and its components are represented in the schematic shown in Figure 7.

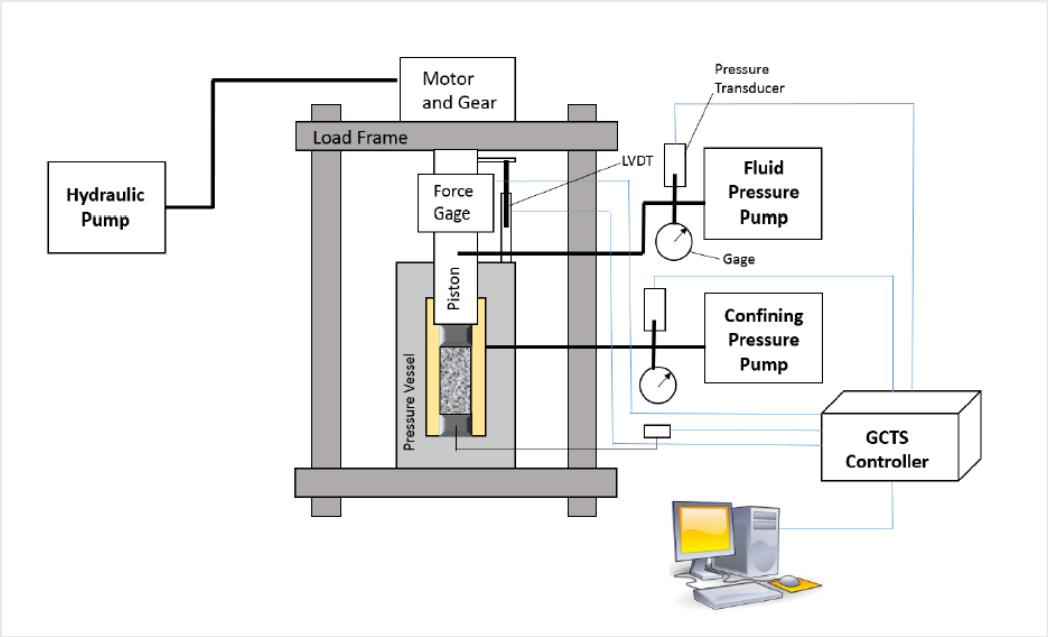

Figure 7: Schematic of the RTX-1500 triaxial equipment (Perez Pena, 2015)

The main component of the RTX-1500 system is the triaxial cell. This essential component is controlled by the hydraulic load frame and allows the testing of high pressures and axial loads (Figure 8).

Figure 8: The triaxial cell

At the base of the triaxial cell, there is small cylindrical component that allows the rock specimen to be screwed into place. Eight LVDTs connections circle the cylindrical component at the base of the cell. Figure 9 displays the three LVDT connections used in this research.

Figure 9: LVDTs connections at base of triaxial cell

The cell is fabricated with steel and is capable of producing a high pressure seal up to 20,000 psi between the base and the cell's wall. For operation, the seal must be secured for safety reasons. Once the base and cell have made contact, the nuts of the eight steel rods must be tightened. Serious leaks will occur is the nuts are not tight enough during operation. The top of the cell has a hole in the middle to allow the load piston to contact the rock specimen. This hole is sealed and no leaks will occur during test runs. The load piston is flat on the top to allow better contact with the axial load piston and a concave bottom for better contact with the convex surface of the top upper metal support. Figure 10 shows the triaxial cell secured and in contact with the axial load piston.

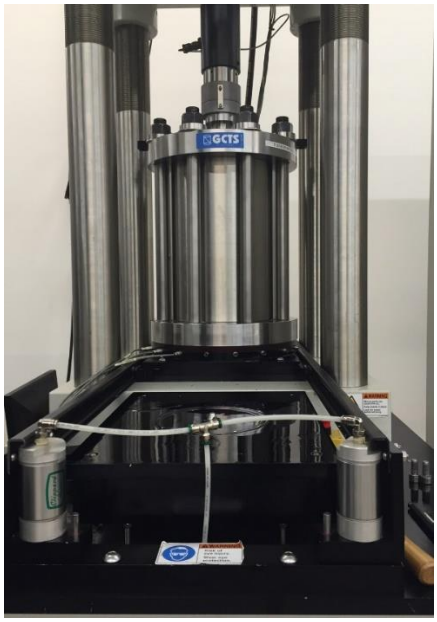

Figure 10: Secured triaxial cell with axial load piston contact

A cell pressure cabinet stores hydraulic oil that is used to apply the confining stress (Figure 11). The hydraulic oil reservoir of this cabinet has enough capacity to fill the empty triaxial cell. Compressed air at approximately 80 psi is used to push the oil to fill the triaxial cell or to drain it. An oil level indicator is fastened to the cabinet that displays when the oil level in the triaxial cell is full or emptied. Two valves isolate the reservoir from the cell once it is filled to apply cell pressure. The system is pressurized by the servo-controller cell pressure intensifier, which is capable of maintaining up to 20,000 psi cell pressure. A pressure transducer measures the cell pressure with a deviation +/- 0.1 MPa. Ensuring that the correct valves are opened and closed during operation is important. Excess pressure can damage equipment or operation of the systems.

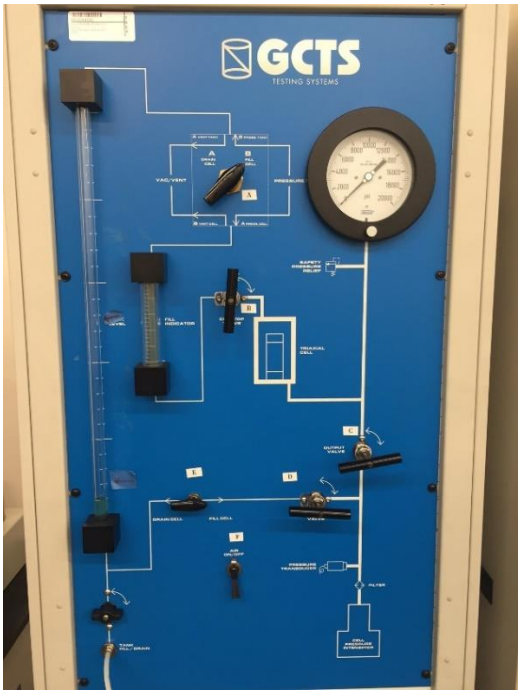

Figure 11: Hydraulic oil cell pressure cabinet

The internal deformation components for triaxial testing are sensitive sensors that are used in direct contact with rock specimens. Special care must be observed when assembling them to the sample. The rock sample is placed between two metal supports. The base of the bottom support is threaded and is able to screw into the base of the triaxial cell. While the top metal support has a convex top for better contact with the load piston. These metal supports are equipped to hold one inch diameter specimens. Each support has an O-ring for sealing purposes to ensure the rock specimen does not contact the hydraulic oil as well as a groove to secure the LVDT platens. Additionally, a thin polyolefin heat-shrink wrap is applied to the rock specimen and secured over the O-rings on the supports. This wrap isolates the rock sample from contacting the pressurized

hydraulic oil. Figure 12 shows a rock sample with LVDTs in place and secured in the triaxial base ready for a triaxial run.

Figure 12: Rock sample with LVDTs in place and secured in the triaxial base

There are three LVDTs used in the triaxial compression test. Each LVDT has a ferromagnetic core placed within it (Figure 13). The ferromagnetic core is positioned to avoid touching the internal walls of the LVDT. When deformation of a sample begins, the displacement of the ferromagnetic core is detected. The LVDTs used have a resolution of 0.001 mm.

Figure 13: Ferromagnetic cores used in triaxial testing

Two LVDTs are used for axial deformation readings during a triaxial test. These two sensors are secured in an aluminum platen (Figure 14).

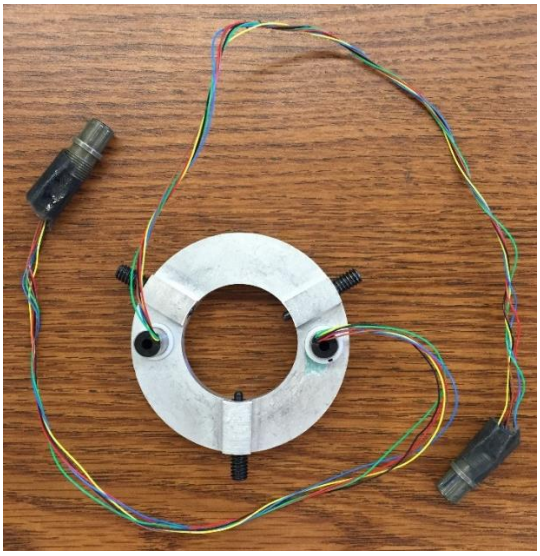

Figure 14: Platens and axial LVDTs

The ferromagnetic cores are fastened to the upper platen's two screws. Both platens are positioned to the metal supports by means of three lateral spring plungers. Extra care should be placed in when positioning the platens. Not only does the platens need to be firmly secured to the metal supports, but also the LVDTs must align with the screws in the top platen. Additionally, both platens must be completely parallel to each other. An error in reading axial deformation could result if proper installation is not followed. The third LVDT is used to measure radial deformations and is secured in a circumferential chain gauge which is wrapped around the circumference of the sample (Figure 15). Metal springs are used to hold the chain link in tension allowing the sample to deform radially without destroying the LVDT or the chain. The data acquisition GCTS CATS processes the signals of the LVDTs.

Figure 15: Radial LVDT and chain

Diligence must be observed when running experimental runs on a sample. A sample could unexpectedly fail and failure to notice this could result in damage to the LVDTs, platen, lateral spring plungers, or the ferromagnetic cores. Furthermore, it is crucial to take into consideration the maximum pressure the system is able to operate at.

2.2 Experimental Procedure

Three steps encompassed the experimental procedures for this research. These steps included: sample collection, sample preparation, and rock mechanical properties measurements. Procedures were kept constant throughout experiments performed in order to ensure measurements could be compared.

2.2.1 Sample Collection

Outcrop samples were collected at an area called Lozier Canyon and Antonio Creek in southwest Texas. A map of the outcrop locations is shown in Figure 16.

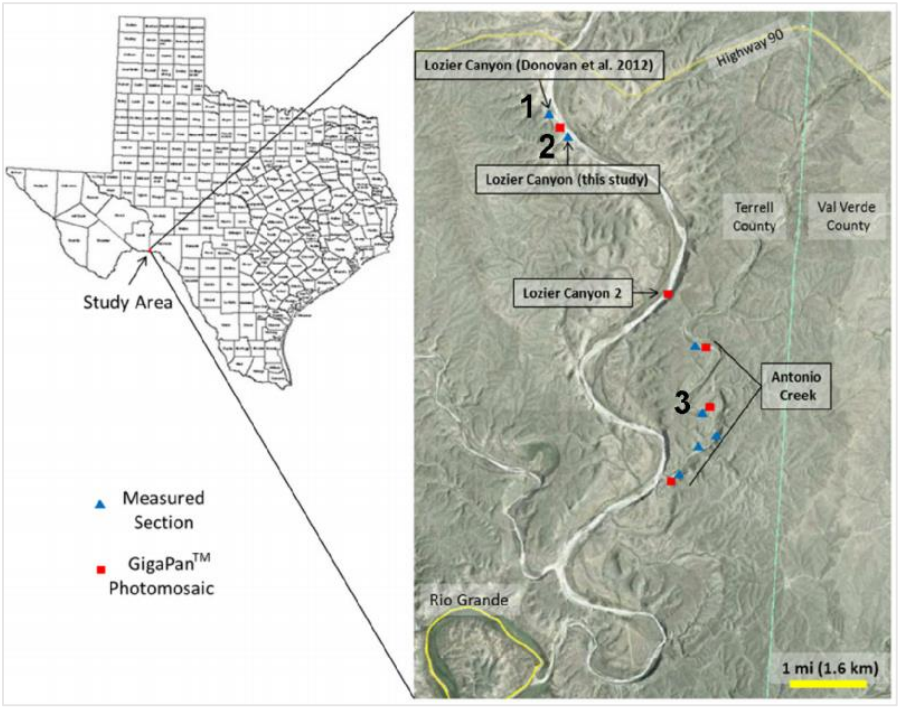

Figure 16: Map of outcrop locations (Gardner et al., 2013)

Large rock samples were collected from the sites that could be cut for both conductivity and rock mechanics core plugs. Rocks were excavated several feet into the rock formation to avoid samples that were weathered and exposed to the elements, as seen in the background of Figure 17.

Figure 17: Research group at Lozier Canyon

2.2.2 Sample Preparation

Cylindrical core plugs were cut from the outcrop samples for triaxial testing. Dimensions of the plugs were cut to two inch in length and one inch in diameter due to the triaxial metal supports are equipped to hold one inch diameter rock specimens. Samples were cut to reflect two orientations: z-direction (perpendicular) and x-direction (parallel) to the bedding planes. This is to account for the anisotropy found in shale formations. For each set of x-direction core plugs corresponding conductivity samples were cut to ensure that mechanical properties measured could be correlated. However, due to the limited dimensions of the rock outcrops collected, only corresponding z-direction conductivity samples were cut for the lower B facies outcrops.

ASTM International Standard Practices for Preparing Rock Core as Cylindrical Test Specimens and Verifying Conformance to Dimensional and Shape Tolerances, known as ASTM D4543-08, were followed for cutting rock samples for mechanical testing. This standard ensures that every core was cut within the tolerances to safeguard against associated errors with sample dimensions. The ASTM D4543-08 standard outlines the tolerances for the core samples as follows (2008):

- Minimum diameter of 1-7/8 inches, or 47 mm, and a length-to-diameter ratio (L/D) of 2.0 to 2.5
- The cylindrical surfaces of the rock specimen should be generally smooth and free of jerky irregularities, with all the elements straight to within 0.02 inches, or 0.508 mm over the full length of the rock specimen.
- The ends shall be cut parallel to each other and at right angles to the longitudinal axis. The end surfaces shall be surface ground or lapped flat to a tolerance not to exceed 0.001 inch.
- The ends should not depart from perpendicularity to the axis of the specimen by more than 0.25 degrees.

While these standards were attempted to be met with each core plug cut, it was not always possible to meet these standards. Outcrop samples were fragile and only a limited amount of rock sample was available, which made it difficult to always meet these strict standards.

After core plugs were cut to required dimensions, the samples were ready for triaxial compression testing. Prior to placing the rock specimen in the triaxial cell, several steps are required to prepare the sample. The full procedure is listed below:

1. Measure the height and diameter of the rock sample. Ensure that several readings of the middle diameter are taken obtain an accurate diameter value.
2. Ensure that both metal supports have their corresponding O-rings attached.
3. Place the core plug in the middle of the bottom metal support.
4. Measure and cut a piece of polyolefin heat-shrink tubing. Place tubing around the rock sample. Confirm the tubing is long enough to cover the O-rings on the metal supports.
5. Heat the shrink wrap from the bottom upwards and without any creases. Take care to ensure sample stays flat and centered on the metal support. Stop once heat shrink is tight around base of sample, but still loose at the top.
6. Let sample cool for a few minutes.
7. Place the bottom platen that holds the LVDTs around the sample, follow by the top platen. Confirm that platens are correctly positioned (LVDT wires pointing down to the bottom of the base metal support).
8. Place the top metal base on the top of the rock specimen. Ensure that the sample is centered and flat. Continue to heat the remaining shrink wrap until sample is completely restricted by the heat wrap.
9. Allow the rock sample to cool for a few minutes.

10. Mount the top LVDT platen to the top metal support with the three lateral spring plungers. Manually tighten the screws while keeping platen centered as much as possible.
11. Place the circumferential chain gauge around the rock specimen in the center. Use the springs to secure the ends to keep the chain gauge in place. The chain gauge should be snug around sample.
12. Mount the bottom LVDT platen to the bottom metal support with the three lateral spring plungers. Manually tighten the screws while keeping platen centered as much as possible. LVDTs should be aligned with the screws on the top platen.
13. Thread the ferromagnetic cores into the brass screws for all three LVDTs.
14. Make final adjustments for LVDT assembly:
    - Confirm that the ferromagnetic core is inside all the way within the LVDT; if not, readings will be incorrect.
    - Confirm that the ferromagnetic core is not touching the inside walls of the LVDT and that it can move freely.
    - Confirm the LVDT platen are firmly secure and not able to move to prevent shifting during testing. This will give inaccurate results during testing.
15. Screw assembly into the base of the triaxial cell until it is firmly secure.
16. Connect the LVDT wires to the corresponding ports.
17. Reset the LVDTs readings on the GCTS CATS software.

18. Adjust the initial position of the LVDT cores using the top brass screws. Make sure that LVDTs can reach a sufficient range of measurement without contacting the top metal support. Set the starting value of the axial deformation LVDTs to -1.8 mm and the radial deformation LVDT to +0.5 mm.

After the completion of these steps, the core sample is ready for triaxial testing.

2.2.3 Replacement Linear Variable Differential Transformers Procedure

Due to the sensitive nature of the Linear Variable Differential Transformers (LVDT), a LVDT may break from wear and tear or from unexpected failure of a sample. The following procedure should be followed for preparing a new LVDT:

1. Obtain a replacement LVDT (LVDT CD 375-100) and a new amphenol industrial connector.
2. Ensure each wire of LVDT is capable of a voltage of 10 volts.
3. Loosely braid wires and solder wires to corresponding pins on the connector. Use caution due to the sensitivity of the wires.
4. Figure 18 Figure 18 shows the correct configuration of wires to the connector pins on an amphenol industrial connector.

Pin A	+ Excitation = Brown wire
Pin D	- Excitation = Yellow wire
Pin B	+ Signal = Red wire
Pin C	- Signal = Black wire
Blue and Green wires are soldered together and not on a pin. These wires should not touch other wires that are soldered.	

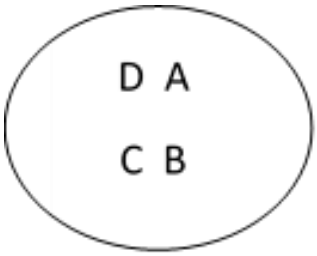

Figure 18: Wire configuration of LVDT to connector pins

5. Once soldering is completed, tape painters tape around the top of the connector to just below the connector's raised middle section.
6. Ensure that the tape is firm around the middle section to the top of the connector. Roughly a quarter inch of tape should be above the connector.
7. Apply epoxy into area of soldered wires within the tape until the soldered wires are covered.
8. Allow epoxy to cure for several hours. Ensure that the blue and green wires are not touching the base pins while curing.
9. After epoxy has cured, remove the blue tape.

The new LVDT is now ready to be calibrated. The following procedure should be followed for calibrating a new LVDT:

1. Install the new LVDT on the calibration device. Ensure the platen are parallel and properly secured (Figure 19).

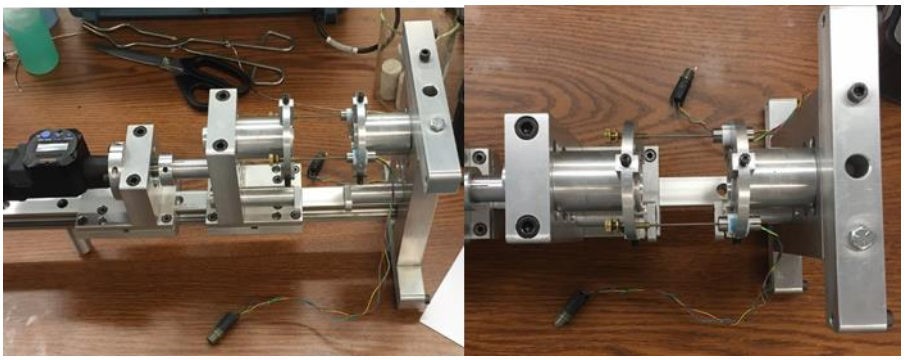

Figure 19: LVDTs secured in a calibration device

2. Attach the connector to its corresponding base plug on the base of the triaxial cell.
3. On the GCTS CATS Software, go to system, click inputs, and proceed to click analog.
4. Select the type of sensor you are calibrating (i.e. axial deformation 1).
5. Click edit and then calibrate
6. A screen will come up with suggestion of 11 points. Click ok.
7. A new screen will appear with a graph, 11 points, and board voltage. Select 3rd degree. Keep the values of the 11 points as indicated by the program.
8. Ensure the LVDTs plugs are connected to the designated plugs on the GCTS plugs.
9. Maneuver the calibrator device so that 0 voltage appears on the board voltage indicator on the screen.
10. Once 0 voltage has been set, re-zero calibration tool.
11. Ensure the calibration tool is in mm as the GCTS CATS software reads mm.

12. Alter the calibration reader to the first indicated value of the 11 points given in the software. For example, the first point would read -2.5 mm. Set the calibration tool to -2.5 mm. Once the calibrator reads -2.5 mm, click read. The voltage value of the mm reading will be recorded.
13. Repeat this step for all 11 points.
14. Once 11 steps are completed, click export.
15. Click spreadsheet and save.

After calibrating a new LVDT, the calibration needs to be confirmed that it was accurately performed. The following procedure ensures this:

1. On the GCTS CATS software, check the max error value to ensure it is within an acceptable value (i.e. a range of ± 0.113 mm is considered acceptable).
2. After the error check, select a value on the LVDT within the -2.5 mm to +2.5 mm range.
3. Compare the calibrator value with the digital viewer screen on the GCTS CATS software. If the values are similar within a couple mm or exact, the calibration is considered good.
4. Close out the calibration screen and the analog screen by clicking ok.

The LVDTs are calibrated and ready for use in triaxial compression testing. Also, the ferromagnetic core and the brass screw used during the LVDT calibration must always be used with its corresponding LVDT during experimental testing.

2.2.4 Refilling the Hydraulic Oil Reservoir Procedure

After completing many triaxial tests, the hydraulic oil reservoir begins to deplete. The reservoir must maintain a certain level in order for the triaxial cell to completely fill. The following procedure should be followed for refilling the hydraulic oil reservoir:

1. Turn valve A in drain cell position.
2. Open the cell top valve (B).
3. Close the output valve (C).
4. Close the recharge/dump valve (D).
5. Turn valve E to “fill cell.”
6. Hook up tubing to tank fill/drain nozzle.
7. Place Tubing in oil supply source.
8. Turn on air supply (F).
9. Wait a few seconds, turn tank fill/drain black valve to open, shown in Figure 20 circled.
10. Fill oil reservoir.

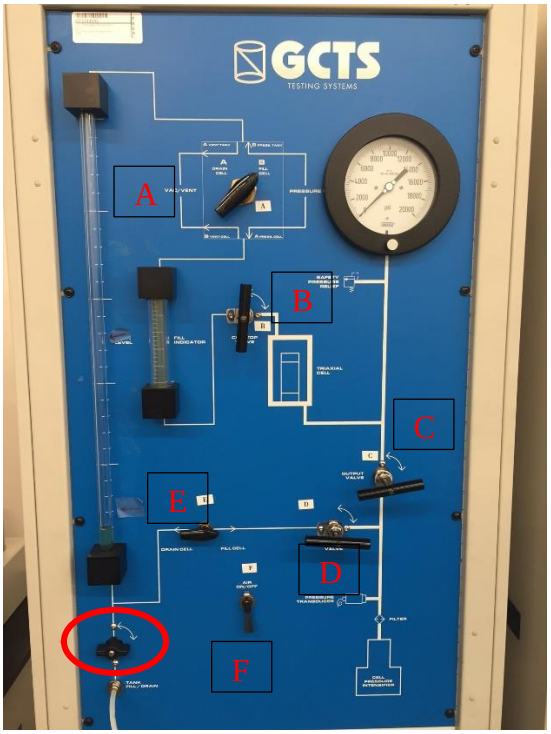

Figure 20: Valves labeled for hydraulic oil cell pressure cabinet

Once oil reservoir is full:

1. Turn tank fill/drain black valve to close.
2. Turn off air supply (F).

2.2.5 Rock Mechanical Properties Measurements

2.2.5.1 Triaxial Test

One of the objectives of this research was to obtain the Young's modulus and Poisson's ratio of the Eagle Ford formation throughout all facies. ASTM International developed a standard for test methods for measuring compressive strength and elastic

moduli of intact rock specimens, known as ASTM D7012-14, to measure mechanical properties.

However, due to the quality of the outcrop samples obtained, minor deviations from the standard were made. The procedure created was for testing two inch in length and one inch in diameter core plugs and consistency was kept to ensure data was comparable. Additionally, core samples were tested at 2 MPa confining stress. This was to ensure the sample remains intact in case of failure. The Young's modulus and Poisson's ratio measurements are altered due to this minor confining stress applied. Adding any confining stress will result in an increased value of Young's modulus and a decreased value of Poisson's ratio. For this research though, the addition of a low confining stress would result in minimal difference in values obtained.

Each sample had three cases of applied stress at three different rates. The first trial was run at 4 MPa/min until 10 MPa was reached. The second trial was run at 3 MPa/min until 20 MPa was reached. The third trial was run at 2 MPa/min until desired peak stress is reached. The unloading rate of each load trial was 2Mpa/minute until a 1MPa contact pressure was reached. The cores were loaded and unloaded several times and at different rates in order to remove any non-elasticity and imperfections typically present in sedimentary rocks with void spaces. The peak stress value ranged from 6000 psi to 8000 psi depending on the sample.

A detailed procedure for measuring the elastic rock properties of core plugs after samples were prepared is described below:

1. Turn on the hydraulic pump (Low P) to drive the servos.

2. Lower the triaxial cell using the cell lift controller. Ensure that no LVDT wires or objects are caught as the cell is lowered.
3. Unscrew the cell lift from the triaxial cell and raise the cell lift to its original position.
4. Place the eight cell rod nuts on each rod. Tighten each nut in a star formation and ensure that each nut is fully tighten to avoid dangerous high pressure leaks. Figure 21 shows an example of the order to tighten the nuts.

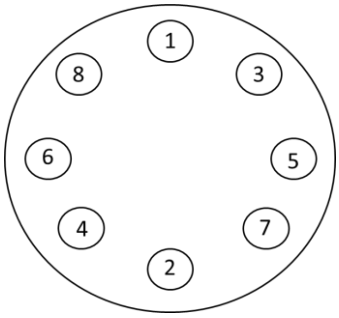

Figure 21: Example of order to tighten each nut on the triaxial equipment

5. Lift the triaxial assembly using the roller lift and push it back until the piston aligns with axial load piston.
6. Switch off the roller lift and deactivate the lift assembly from the user interface.
7. Using the controller, lower the axial load piston slowly until contact is made with the cell piston.
8. Apply 1 MPa contact deviator stress with the axial load piston. The sample is now under load.

9. On the triaxial pressure intensifier cabinet, turn valves A and E to Fill Cell. Open valves B, C, and D.
10. Fill the triaxial cell with hydraulic oil from the triaxial pressure intensifier cabinet by turning on the air switch (F).
11. Once the fill indicator is full on the triaxial pressure intensifier cabinet, turn off the air switch (F) and isolate the triaxial cell by closing valves B and D.
12. Using the cell pressure controller on the software, apply a constant confining stress of 2 MPa. Allow the system to reach equilibrium.
13. Create a new Project in the GCTS software and from there create a new specimen. Enter the diameter and length of the sample being tested for proper strain calculations.
14. Set the LVDT deformation sensors to zero.
15. Reset any graphs displayed.
16. Execute the triaxial test program.
    a. Increase the differential stress at a rate of 4 MPa/min until 10 MPa is reached. (Loading Process)
    b. Ramp down the differential stress at 2 MPa/min until 1 MPa is reached (Unloading Process)
    c. Pause the experiment for a minute
    d. Decrease the differential stress at a rate of 3 MPa/min until 20 MPa is reached. (Loading Process)

e. Ramp down the differential stress at 2 MPa/min until 1 MPa is reached (Unloading Process)
f. Pause the experiment for a minute
g. Decrease the differential stress at a rate of 2 MPa/min until desired peak stress is reached. (Loading Process)
h. Ramp down the differential stress at 2 MPa/min until 1 MPa is reached, (Unloading Process)

17. Stop the triaxial test program.
18. Lower the cell confining pressure to 0.1 Mpa.
19. Open valves B and D and turn on the air switch (F) to begin draining to from the cell to the reservoir. This process takes about 20 minutes. The fill indicator will empty once cell is completely emptied.
20. Turn off the air switch and allow cell to reach atmospheric pressure.
21. Lower the differential stress to 0.5 MPa.
22. Slowly raise the axial load piston making sure there is no residual air pressure still present. The piston will raise if residual air pressure still present.
23. Once axial load piston no longer is in contact with the piston, continue to raise the axial load piston until it is completely up in its original position.
24. Turn on the lift assembly on the software and turn on the roller lift to raise the triaxial cell.
25. Bring the triaxial cell forward and turn off the roller lift.
26. Unscrew the eight cell rod nuts in a similar order (Figure 21).

27. Lower the cell lift and secure the screws to attach the lift to the triaxial cell.
28. Turn on the vacuum air.
29. Slowly raise the triaxial cell with the lift.
30. Unplug the LVDTs and unscrew the bottom metal support from the equipment.
31. Inspect the sample to ensure that no oil infiltrated the sample and that LDVT ring holders are still secure and tight. Results may be altered if oil penetrated the sample. The sample must be dried to be retested if this occurs.
32. Remove the instrumentation carefully from the sample.
    a. First, remove the ferromagnetic cores.
    b. Remove the circumferential chain gauge and its springs.
    c. Cut the sample jacket and remove the upper metal support.
    d. Remove the LVDT ring holders.
    e. Remove sample from bottom metal support.
33. Export experimental data to an excel file using the GCTS software.
34. Analyze the data.

2.2.5.2 Brinell Hardness

Another objective of this research was to obtain the Brinell hardness values of the Eagle Ford formation throughout all facies. The GCTS PLT-100 apparatus was used to perform Brinell hardness experiments (Figure 22). ASTM International developed a standard to test Brinell hardness of metallic materials, known as ASTM E10-14. Although this standard was specifically for metallic materials, the standard was applied to the rock samples tested. As a result, some deviations from the standard were made.

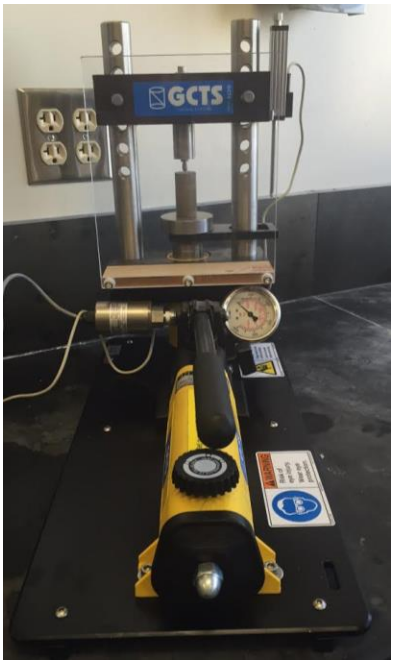

Figure 22: GCTS PLT-100 Brinell hardness apparatus

A 1/8 inch (3.175 mm) tungsten ball indenter was used to apply the force on the surface of the core plug samples. Since a ball indenter of this diameter was not listed in the standard, the two force-diameter ratios of 10 and 5 for a ball indenter with a diameter of 2.5 mm was used as a standard. Consequently, a force of 0.5 kN and 1 kN were applied to each sample three times, respectively. The indentation diameters measured were across and down due to the oval nature of the indentations. An average of all six indentations created was taken to give the average Brinell hardness number for each facies.

A detailed procedure for measuring the Brinell hardness of the core plugs is described below:

1. Place core plug under the indenter. Ensure that the indentation is not too close to the edge.
2. Zero the force reading on the apparatus.
3. Use the piston to bring the sample to contact the indenter.
4. Once contact is made, execute the Brinell hardness procedure
    - Use the piston to apply a load of 0.5 kN
    - Let the set applied force dwell for 10-15 seconds.
    - Record the actual maximum force reached.
    - Release the piston and allow sample to separate from the indenter.
    - Repeat indentation procedure for two more indentations at 0.5 kN.
    - Once 0.5 kN force indentations are completed, repeat procedure three additional times at a force of 1 kN.
5. Measure the indentation diameters across and down and record values.
6. Analyze data collected.

2.2.6 Elasticity

Elasticity is defined as a material's ability to endure and recover from deformations produced by forces. As a force is applied to an object, the material experiences deformation. However, if the deformation is elastic, the object returns to its original shape and dimensions once the force is no longer applied. The concepts of strain and stress are integral in the theory of elasticity. The force applied to a solid over a cross-sectional area is known as stress. While the geometry of a solid is an independent

factor, the stress required to deform an object is highly dependent on the material composition of a solid. As explained, stress is defined as:

$$\sigma = \frac{F}{A} \tag{2.1}$$

where F is the force applied; A is the cross sectional area; and σ is the stress component.

The relative deformation of an object due to the force applied is known as the concept of strain. More specifically, strain is defined as the change in length due to deformation per unit length. Strain is expressed as:

$$\varepsilon = \frac{l - l'}{l} = -\frac{\Delta l}{l} \tag{2.2}$$

where l is the initial length; l' is the new length; Δl is the change in length of the object from the force; and ε is the strain.

Hooke's law implies a linear relationship of elasticity between the applied stressed and strains of an object and is defined in equation 2.3.

$$\sigma = E\varepsilon \tag{2.3}$$

where σ is the stress component; ε is the strain; and E is the elastic moduli.

However, equation 2.3 displays Hooke's law in the simplest form. Since samples are three-dimensional, Hooke's law can be applied to describe linear behavior to 3 dimensions as well. This relationship is described as:

$$\varepsilon_x = \frac{1}{E}\Big(\sigma_x - \upsilon\big(\sigma_y + \sigma_z\big)\Big) \tag{2.4}$$

$$\varepsilon_y = \frac{1}{E}\Big(\sigma_y - \upsilon(\sigma_x + \sigma_z)\Big) \tag{2.5}$$

$$\varepsilon_z = \frac{1}{E}(\sigma_z - \upsilon\big(\sigma_x + \sigma_y\big)) \tag{2.6}$$

where E is the elastic moduli that measures the stiffness of an object, or its impedance to compression; σ is the stress component within a 3D space; ε is the strain component within a 3D space; and υ is the Poisson's ratio. The subscripts describe orientation to the axis, either x, y or z.

As a consequence of the applied stress, the sample also expands laterally. This lateral expansion relative to the reduction in length is expressed as Poisson's ratio. As an elastic parameter, it measures the lateral elongation compared to the axial deformation. Poisson's ratio is described as:

$$\upsilon = -\frac{\varepsilon_{lateral}}{\varepsilon_{axial}} \tag{2.7}$$

ε_{axial} is the axial deformation and $\varepsilon_{lateral}$ is the lateral deformation. Due to the cylindrical shape of the core plugs used, the lateral expansion is actually correlated to the change in diameter. As a result, the radial deformation is denoted as:

$$\varepsilon_{lateral} = \varepsilon_{radial} = \frac{\Delta r}{r} \tag{2.8}$$

where ε_{radial} is the radial deformation; r is the radius; and Δr is the change in radius of the object from the force.

The Poisson's ratio, in relation to cylindrical samples, is therefore expressed as:

$$\upsilon = -\frac{\varepsilon_{radial}}{\varepsilon_{axial}} \tag{2.9}$$

The study of measuring Young's modulus and Poisson's ratio involves experimental work on rock samples under stress conditions. The most universal process to measure these elastic properties is by means of triaxial compression. A confining pressure and uniaxial stress are applied to reach a triaxial state of stress. The stress state in a triaxial compression test on a cylindrical sample is shown in Figure 23 below.

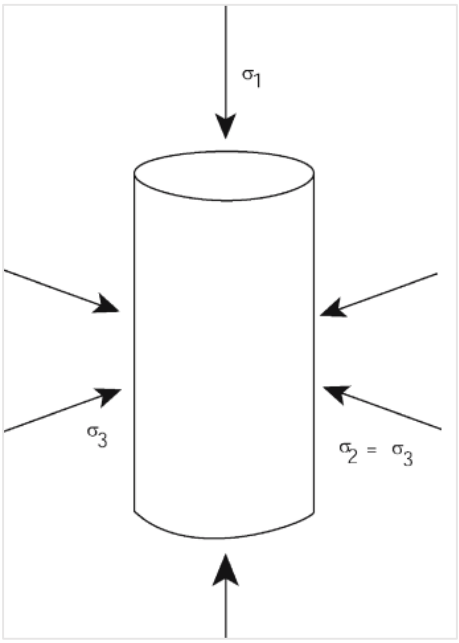

Figure 23: System of stresses in a triaxial compression test (Paterson and Wong, 2005)

There are three types of stresses commonly labelled as the greatest, intermediate, and least principal stresses, which are σ_1, σ_2, and σ_3, respectively, and are displayed on

Figure 23. Typically for a triaxial test, the σ_2 and σ_3 stresses equal to each other and are applied as a confining pressure at both the top and bottom of the sample as well as radially. The confining pressure also applies a force to the loading piston within a triaxial test to a sample. While the confining pressure is typically held constant within a test, increasing the fixed confining pressure will affect Young's modulus and Poisson's ratio values of a sample. This is especially applicable in measuring Poisson's ratio as the higher confining pressure could prevent the sample from expanding. In a triaxial test, the amount of axial stress that deviates from the confining pressure is referred to as differential stress. This term reflects the difference between the greatest and least principal stresses, shown in equation 2.10. The plotted graphs presented in this study uses differential stress values.

$$\sigma_d = \sigma_1 - \sigma_3 \tag{2.10}$$

where σ_d is the differential stress; σ_1 is the greatest principal stress; and σ_3 is the least principal stress.

A triaxial test produces two types of plots needed to calculate the Young's modulus and Poisson's Ratio values. The slope of the linear section of the differential stress plotted against the axial strain generates the Young's modulus value of a sample, often expressed as E. Linear least-squares curve fit is applied to this linear section of the curve. Similarly, Poisson's ratio can be ascertained from plotting the differential stress against the radial strain. By using the linear least-squares curve fit on the straight section of this curve, the slope of the radial curve is determined. The negative slope of the axial

curve over the slope of the radial curve yields the Poisson's Ratio of the sample, shown in equation 2.11.

$$\upsilon = -\frac{slope\ of\ axial\ curve}{slope\ of\ radial\ curve} = -\frac{E}{slope\ of\ lateral\ curve} \tag{2.11}$$

2.2.7 Hardness

While the elastic behavior of a rock is important, the analysis of how the rock behaves plastically has added value as well. Plastic behavior of the surface of the rock plays an important role in the loss of fracture conductivity. This study analyzes the indentation of rock samples by means of Brinell hardness.

The conductive pathways created by hydraulic fracturing serve as conduits for hydrocarbon production. In order to maintain the fracture width, large quantities of proppant are pumped downhole. However, the effects of proppant can have adverse effects on the surface of the fracture. Proppant penetrates the fracture surface leaving a permanent indent. This phenomenon is called proppant embedment and it leads to a decline in fracture conductivity. Embedment is an indication of the plastic deformation behavior and the ductility on the fracture surface. The ductility of the rock is indicates the degree of plastic deformation without fracturing (Mueller and Amro, 2015).

Quantifying the surface hardness of the rock is a reliable method to determine the effects of proppant embedment. The hardness determines the resistance of the rock's surface against an applied load and it is a good indicator of proppant embedment at the surface of soft, clay-rich shale formations. Brinell hardness method applies a force with a small tungsten ball into the rock's surface, seen in Figure 24.

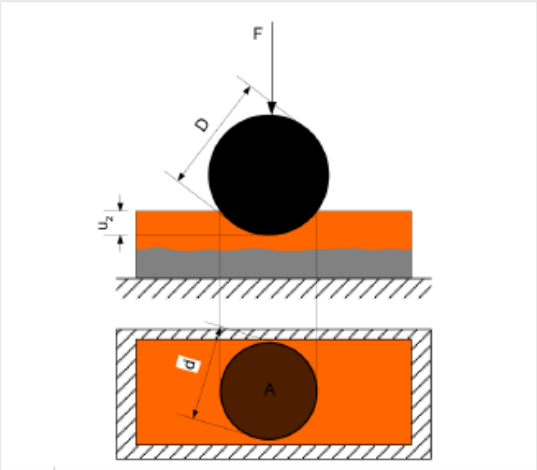

Figure 24: Brinell hardness test (Mueller and Amro, 2015)

Calculating the Brinell hardness number (HBW) [kgf/mm^2] is expressed as:

$$HBW = \frac{2F_{kgf}}{\pi D\left(D - \sqrt{D^2 - d_{avg}^2}\right)} \tag{2.12}$$

$$d_{avg} = \frac{d_1 + d_2}{2} \tag{2.13}$$

F is the applied force in kgf, D is the diameter of the ball in mm, and d_{avg} is the measured mean diameter of the indentation in mm, d_1 is the first diameter of indentation (mm), and d_2 is the second diameter of indentation (mm).

2.2.8 Anisotropy

Anisotropy in shale is present and the elastic properties are strongly affected by it. However for simplification reasons, anisotropy is often ignored when evaluating the elastic rock properties. This can lead to sizable errors in calculating these properties. Additionally, shales formations commonly have beddings or laminations that are composed of clay particles typically orientated in the parallel direction to the horizontal

plane. The direction along a bedding plane will always have the same elastic properties. However, the vertical, or z-direction, will have varied elastic properties from layer to layer. This is commonly referred to as transverse isotropy. Figure 25 displays transverse isotropic bedding planes. Anisotropy is prevalent in shale plays due to orientation of clay particles, kerogen inclusions, microcracks, and layering (Sayers, 2013; Hornby et al., 1993).

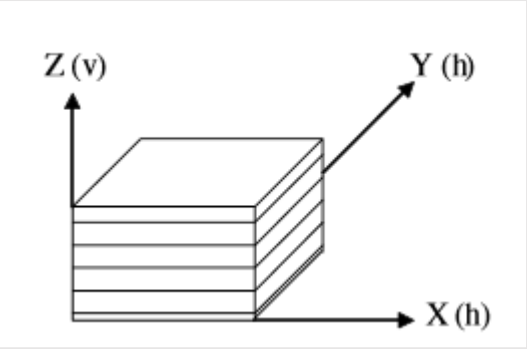

Figure 25: Transversely isotropic body in the X-Y bedding plane (Wong et al., 2008)

2.2.9 Surface Roughness

The surface roughness of the conductivity samples were assessed as a factor affecting the measured fracture conductivity and its decline rate. In order to determine the fracture surface roughness, a root-mean-square roughness calculation was applied (Enriquez Tenorio, 2016).

$$R_{RMS} = \sqrt{\frac{1}{n}\sum_{i=1}^{n} y_i^2} \tag{2.14}$$

$$y_i = |y - \bar{y}| \tag{2.15}$$

where R_{RMS} is the root-mean-square roughness, $\bar{y}$ is the arithmetic average, y is the specific point's height. Fractured conductivity samples displayed non-linearity characteristics, such as peaks and valleys. A laser profilometer was used to calculate the surface roughness, shown in Figure 26. Each sample was scanned with the laser profilometer with an accuracy of 0.000001 inches.

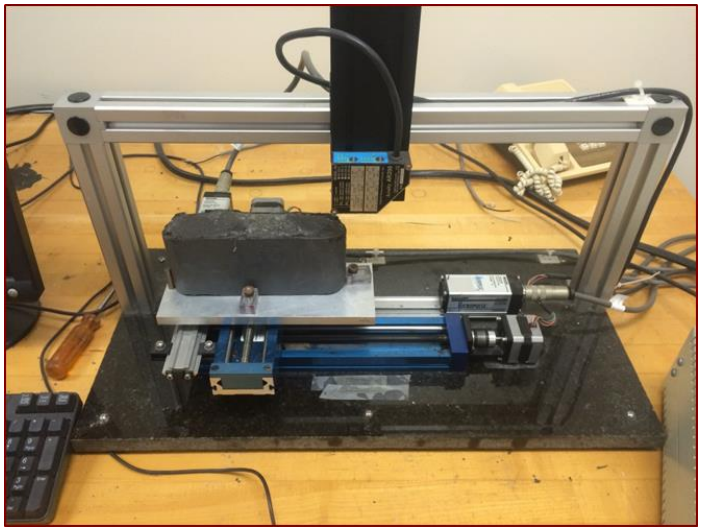

Figure 26: Laser profilometer used to calculate surface roughness (McGinley, 2015)

2.3 X-Ray Diffraction Analysis

Mineralogy composition of 10 Eagle Ford outcrop samples were obtained by XRD analysis. Each facies of the Eagle Ford was tested and analyzed. The sample

preparation, XRD experiment and analysis were executed at the Harold Vance Department of Petroleum Engineering.

2.3.1 Sample Preparation

Samples were crushed into powder substance using an agate mortar and pestle set (Figure 27). The homogenous fine powder was required to pass through 200 micrometers sieve (Figure 28). Several grams per sample were collected to run XRD analysis.

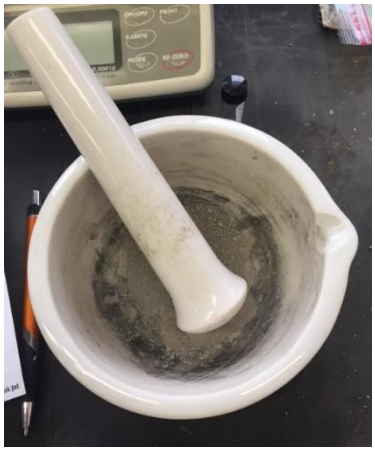

Figure 27: Agate mortar and pestle set used to crush Eagle Ford samples

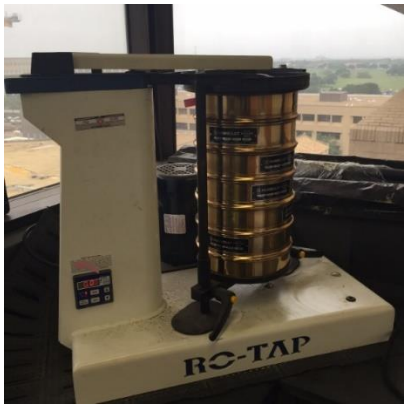

Figure 28: Sieve apparatus used

2.3.2 X-Ray Diffraction Analysis

X-ray diffraction (XRD) is an analytical method used to identify and quantify the mineralogy of crystalline and fine-grained materials in rocks. Each mineral and compound in a rock has a distinct identifying characteristic. An X-ray Diffraction apparatus consists of three components: an X-ray tube, sample holder, and an X-ray detector. The homogenous finely ground sample is placed in the sample holder. X-rays are produced in a cathode ray tube as a result of heating a filament. The electrons produced are accelerated toward the sample by applying voltage. Once inner electrons of the sample are displaced, the characteristic X-ray ranges are yielded. These X-ray ranges are compared to known identifying mineral characteristics to determine mineral composition.

There are several methods and software programs available for analyzing X-ray diffraction results. The software used in this study, Diffract Eva V.3, uses the method called the reference intensity ratio (RIR) method. This method analyzes a diffractogram

pattern of the mineral mixture and compares the sample pattern to known reference intensity ratios from a database of a pure phase mineral. With proper sample preparation, this technique of analysis has an accuracy of about $\pm 3 wt$ % (Hillier 1999). However in this experimental study, it is possible that a decrease in accuracy occurred due to sample preparation, mesh sized used, or human error. To quantify this error would be extremely difficult.

3 EXPERIMENTAL RESULTS AND DISCUSSION

Eagle Ford outcrop samples from each facies were collected and used to run triaxial compression tests, Brinell hardness tests, and X-ray diffraction analysis. Lozier Canyon and Antonio Creek were outcrop locations for these samples. Large rock samples were collected from the sites that could be cut for both conductivity and rock mechanics core plugs. They were excavated several feet into the rock face to avoid samples that were weathered and exposed to the elements. Triaxial cores were cut in both parallel (x-direction) and perpendicular (z-direction) to the bedding planes with the exception of facies B3. Figure 29 displays the sample orientation used in testing. Samples were labeled with a specific naming methodology, seen in Figure 30, to indicate orientation. The correlation between the rock mechanical properties and the measured fracture conductivity was studied.

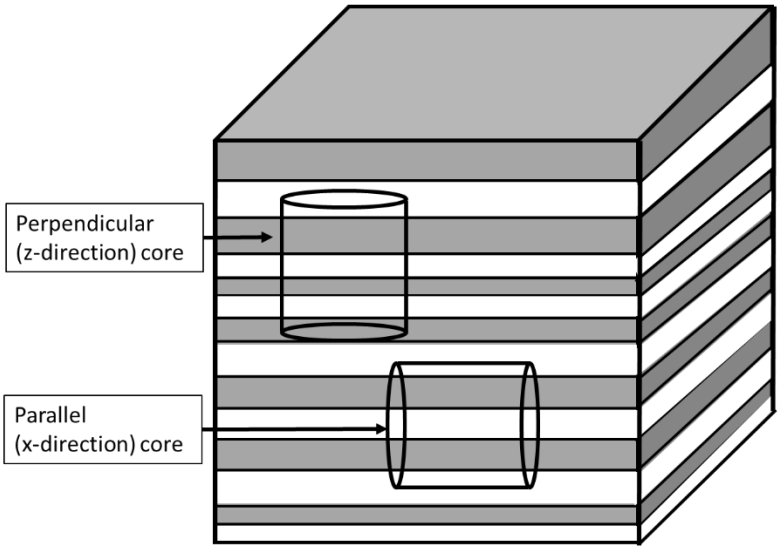

Figure 29: Triaxial core sample orientations

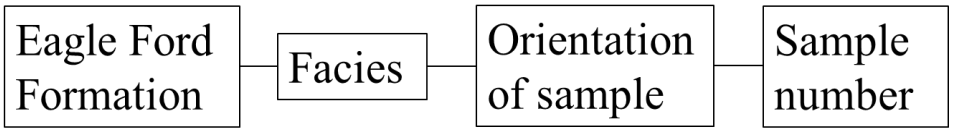

Figure 30: Sample naming methodology

The following experimental results sections present the elastic properties from triaxial compression testing. It should be noted that many of the axial stress-strain curves do not fit the linear trend at lower stresses. This could be due to several possibilities. The most influential reasoning of these findings would be at the lower stresses, the pore spaces and microcracks within the rock sample begin to close. This causes the sample to rearrange and deform, but it does not signify a permanent deformation of the core plug sample. Additionally, both the top and bottom of samples are required to be completely flat and level. While samples may had appeared to be flat, several samples were not

completely leveled. Sandpaper was used to sand down samples by hand to obtain a leveled surface, but some error may be associated with this method. However after the initial deviation, axial stress-strain curves become more linear. Moreover though, many samples tested in triaxial compression exhibited a non-linear deviation near 2000 psi. This is believed to be due to the experimental error associated with setup. More specifically, the platen are screwed in place and secured to the metal supports holding the rock sample. During the experiment, the metal supports may have shifted due to the force applied causing the platens to shift as well. As a result, the axial LVDT readings deviated before repositioning again to the expected linear readings. Additionally, the radial stress-strain curves have much more curvature than the linear axial stress-strain curves. Due to this curvature, the linear fit was much more subjective. Fit ranges were manually selected for both the axial and radial stress-strain curves and in most cases were consistently the same range.

In addition to the elastic properties being presented, the Brinell hardness numbers as well as the X-ray diffraction analysis of each facies is provided as well. All data given is analyzed as well. Furthermore, the surface roughness of conductivity samples are summarized. Lastly, the measured fracture conductivity results is presented. Analysis of the relationships between the rock characteristics and the fracture conductivity is evaluated.

3.1 Facies A Results

This section provides the rock mechanical properties measured, fracture conductivity results, and mineralogical composition of facies A.

3.1.1 Facies A Rock Mechanics

Four triaxial core plugs from facies A, three in X-direction and one in Z-direction, were cut and used in rock mechanical properties analysis. Each sample had three loading cycles applied. The third loading cycle used to evaluate the elastic properties and was only plotted. An example of an axial and radial stress-strain curve for a parallel orientation (x-direction) sample of facies A is displayed in Figure 31 and Figure 32, respectively. Additionally, an axial and radial stress-strain curve for a perpendicular orientation (z-direction) sample of facies A is shown in Figure 33 and Figure 34, respectively. The complete triaxial compression test results can be found in Appendix A.

Each of the samples underwent the same loading process. The samples were first loaded to 1450 psi, 10 MPa, followed by a second loading to 2900 psi, 20 Mpa. The third and last loading was increased to 4400 psi, 30 MPa. However, sample E-A-X-1 had a higher loading set point at 5800 psi, 40 MPa, but failed at a pressure of 5500 psi, 38 MPa, unexpectedly. Conductivity samples of this facies were tested up to 6000 psi.

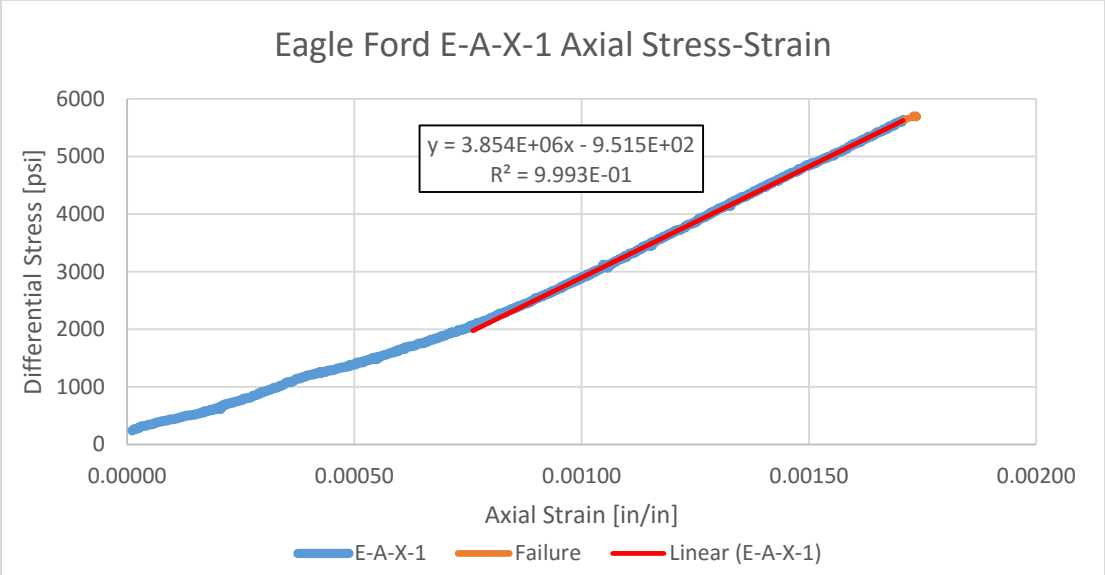

Figure 31: Axial stress-strain curve for sample E-A-X-1

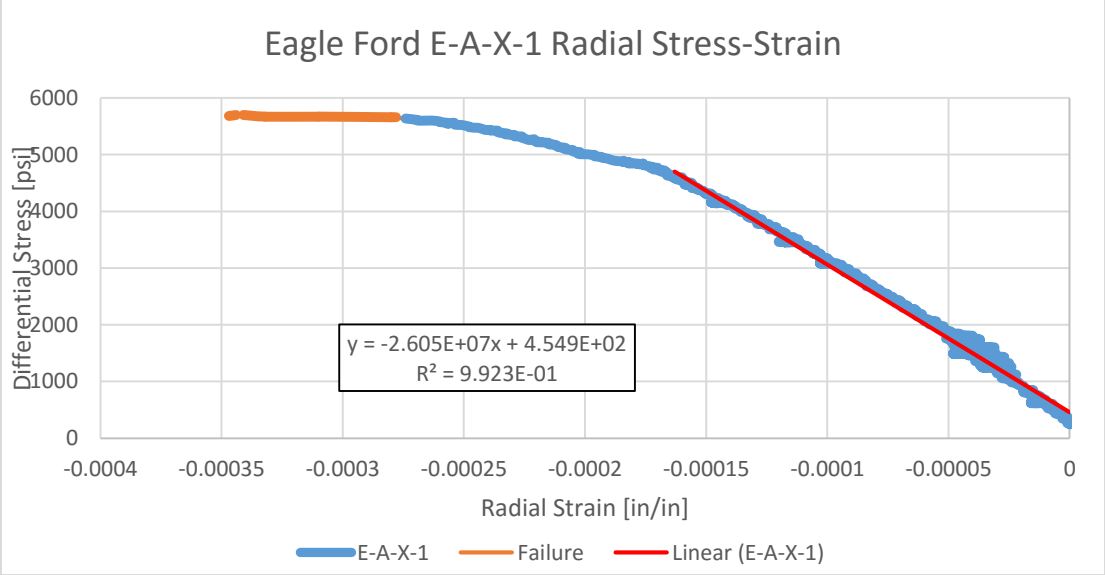

Figure 32: Radial stress-strain curve for sample E-A-X-1

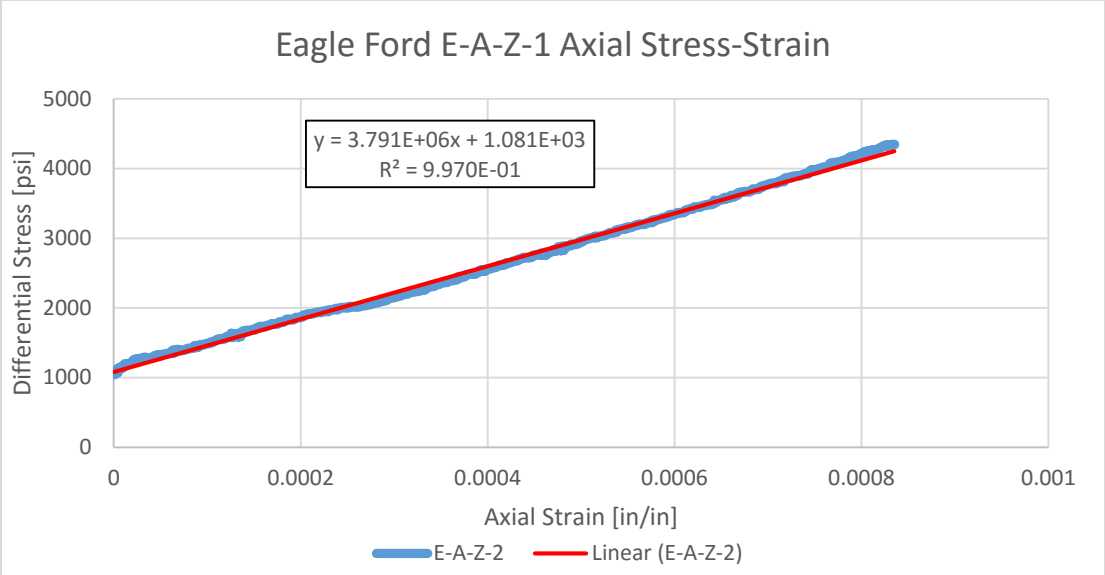

Figure 33: Axial stress-strain curve for sample E-A-Z-1

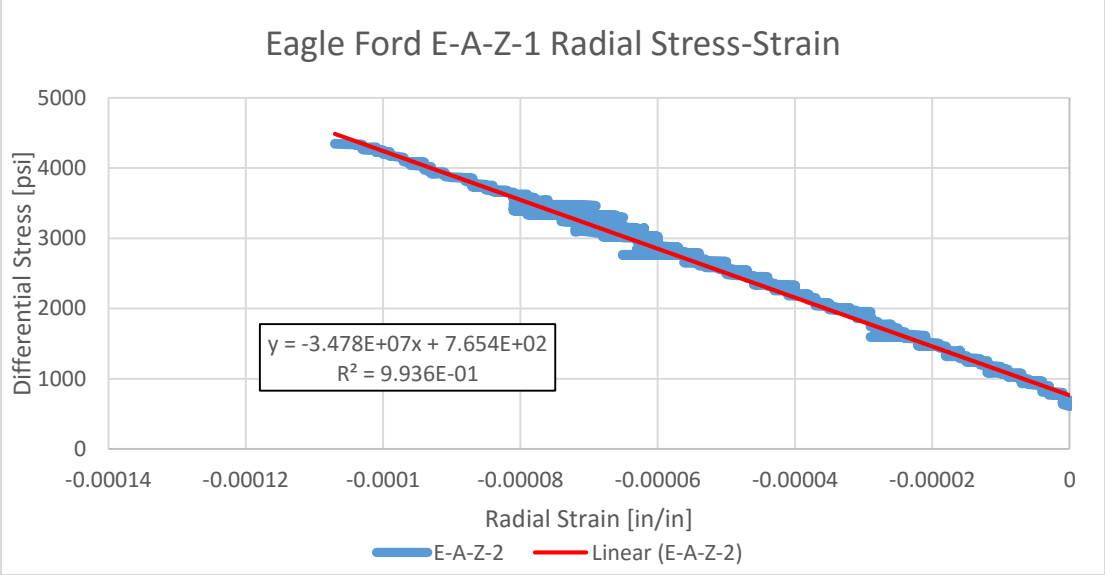

Figure 34: Radial stress-strain curve for sample E-A-Z-1

Additionally, Brinell hardness tests were performed on each of the triaxial core plugs prior to triaxial compression testing. Each sample was tested at a force of 0.5 kN

and 1.0 kN with three indentations each, respectively. All Brinell hardness numbers were averaged together for each sample. For this study, average Brinell hardness number for each bedding orientation is reported.

Results of the four triaxial core plugs (3 X-direction and 1 Z-direction) in Facies A tested are shown in Table 1:

Table 1: Summary of facies A mechanical properties

	E-A-X (Parallel)			E-A-Z (Perpendicular)		
Samples	Young's Modulus [psi]	Poisson's ratio [-]	Brinell Hardness Number [kgf/mm^2]	Young's Modulus [psi]	Poisson's ratio [-]	Brinell Hardness Number [kgf/mm^2]
Sample 1	3.85E+06	0.148	-	3.79E+06	0.109	-
Sample 2	3.11E+06	0.119	-	-	-	-
Sample 3	4.97E+06	0.165	-	-	-	-
Average	**3.98E+06**	**0.144**	**91.91**	**3.79E+06**	**0.109**	**105.64**
Standard Deviation	9.39E+05	2.29E-02	6.65	-	-	14.85
Percentage Standard Deviation	24%	16%	7%	-	-	14%

The difference in the elastic rock properties between the x-direction and z-direction samples is minimal. The average Young's modulus for the x-direction samples was 3.98 Mpsi, which is only slightly higher than the Young's modulus for the Z-direction, 3.79 Mpsi. This indicates that the parallel samples are only slighter stiffer than the perpendicular samples. It would seem that anisotropy does not play a major role in this facies with the ratio of parallel Young's modulus to the perpendicular value being

almost one to one. Additionally, the Poisson's ratio follows the same trend of the Young's modulus values. The parallel samples have a greater Poisson's ratio average than the perpendicular sample. The slight difference in the averages may be a result of the different layers of mineralogy present in the samples. Since the difference in the elastic properties is minimal, it would be difficult to conclude a significant effect on the conductivity values. Moreover, the perpendicular samples have a higher Brinell hardness number than the parallel samples. This trend does not follow the elastic trends found. A possible explanation is that the perpendicular sample's rock surface was tested on a "stiff" layer with hard minerals present such as quartz. However due to there being only one perpendicular sample, further testing of additional perpendicular samples would be needed in order to obtain a better representative average. The difference between the Brinell hardness values reported suggest that there could be a considerable effect on fracture conductivity. Overall the rock properties measurements obtained present a low variation between the two orientations.

3.1.2 Facies A Mineralogical Composition

The mineral composition of Facies A samples were determined using X-ray Diffraction (XRD) analysis. Diffrac.Eva V3 software was used for analysis. Two samples were chosen randomly to compare mineralogy. The results are presented in Figure 35.

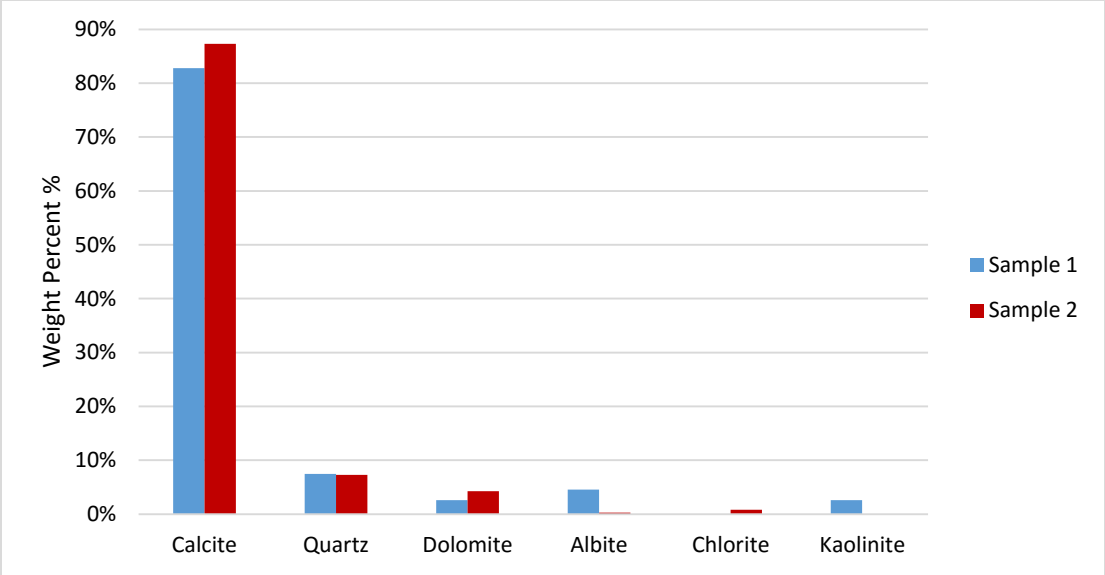

Figure 35: Facies A mineralogy composition

Overall, the two samples tested have similar mineralogical composition, with the exception of the types of clays present. Since the mineralogical composition of the two samples are nearly identical, this suggests that the mineralogy is the influencing factor for the similar measured rock mechanical properties. However, it is difficult to determine the extent of influence without further samples tested for mineralogical composition. The average composition of these samples was approximately 85% calcite, 7% quartz, 3.5% dolomite, 2.5% albite, 0.8% chlorite, and 2.6% kaolinite.

3.1.3 Facies A Surface Roughness

Surface roughness is a possible parameter that could affect fracture conductivity. Tenorio (2016) quantified the surface roughness of each sample of facies A tested for fracture conductivity using a laser profilometer to scan the surface. The Root Mean Square (RMS) error method was used to calculate the deviation of the measurement

from the best fit plane. Figure 36 shows a parallel (x-direction) fractured conductivity sample. Visually, the sample seems relatively flat at the fractured surface and the bedding planes are visible. A complete summary of surface roughness of samples is displayed in Table 2 (Tenorio, 2016).

Table 2: Summary of facies A average surface roughness

	Average RMS Error [in]
Unpropped Average	0.223
30/50 Mesh Average	0.230
100 Mesh Average	0.243

Figure 36: Fracture surface of facies A parallel conductivity sample (Tenorio, 2016)

3.1.4 Facies A Fracture Conductivity

Fracture conductivity tests were performed on the x-direction of facies A samples. Table 3 displays the fracture conductivity experiments design for facies A (Tenorio, 2016).

Table 3: Facies A fracture conductivity experiments design

Proppant type	Proppant Mass	Areal Proppant Concentration	Number of tests
Unpropped	-	-	4
30/50 Mesh	3.4 g	$0.1 lb_m/ft^2$	1
100 Mesh	3.4 g	$0.1 lb_m/ft^2$	3

The samples were tested unpropped, at 0.10 lb/ft^2 areal concentration of both 30/50 mesh and 100 mesh white sand. A summary of the averaged fracture conductivity for facies A is displayed in Figure 37.

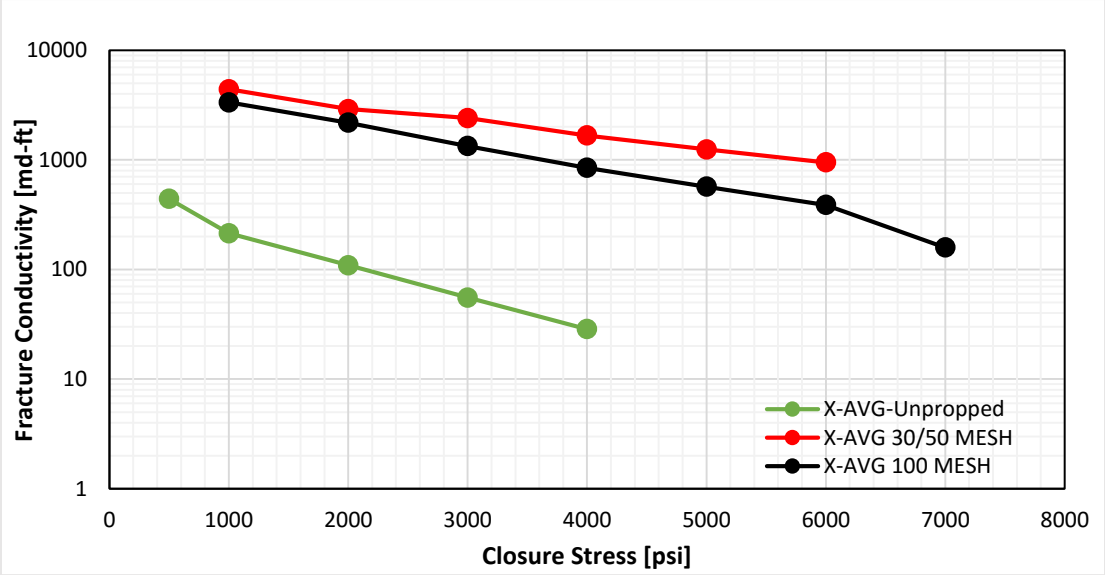

Figure 37: Summary of average conductivity behavior for facies A samples

3.2 Facies B1 Results

This section provides the rock mechanical properties measured, fracture conductivity results, and mineralogical composition of facies B1.

3.2.1 Facies B1 Rock Mechanics

Six triaxial core plugs from facies B1, three in X-direction and three in Z-direction, were cut and used in rock mechanical properties analysis. Each sample had three loading cycles applied. The third loading cycle used to evaluate the elastic properties and was only plotted. An example of an axial and radial stress-strain curve for a parallel orientation (x-direction) sample of facies B1 is displayed in Figure 38 and Figure 39, respectively. Additionally, an axial and radial stress-strain curve for a perpendicular orientation (z-direction) sample of facies B1 is shown in Figure 40 and Figure 41, respectively. The complete triaxial compression test results can be found in Appendix A.

Each of the samples underwent the same loading process. The samples were first loaded to 1450 psi, 10 MPa, followed by a second loading to 2900 psi, 20 Mpa. The third and last loading was increased to 7250 psi, 50 MPa. Conductivity samples of this facies were tested up to 6000 psi.

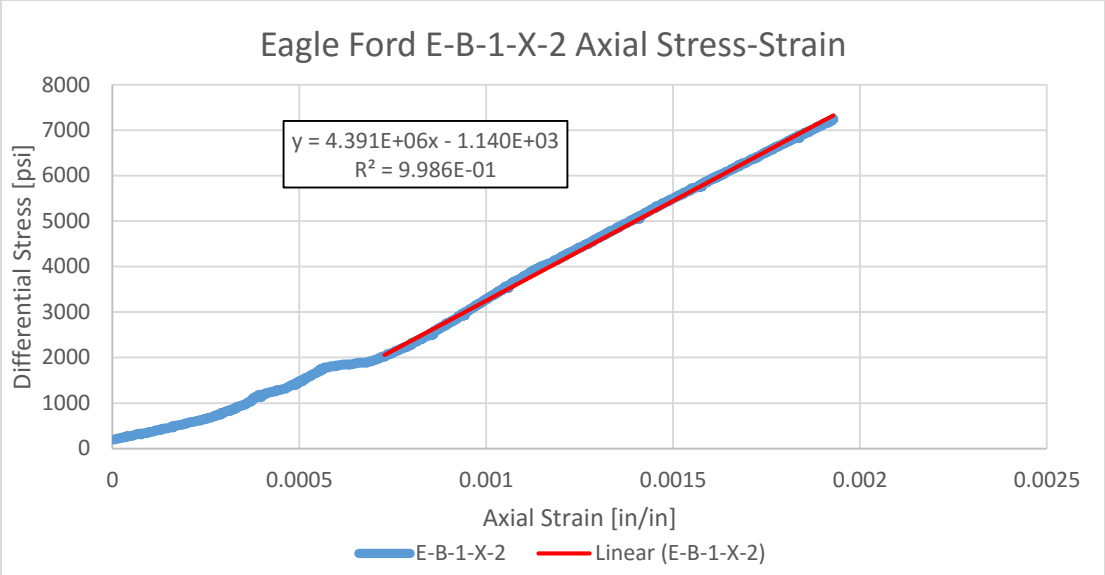

Figure 38: Axial stress-strain curve for sample E-B-1-X-2

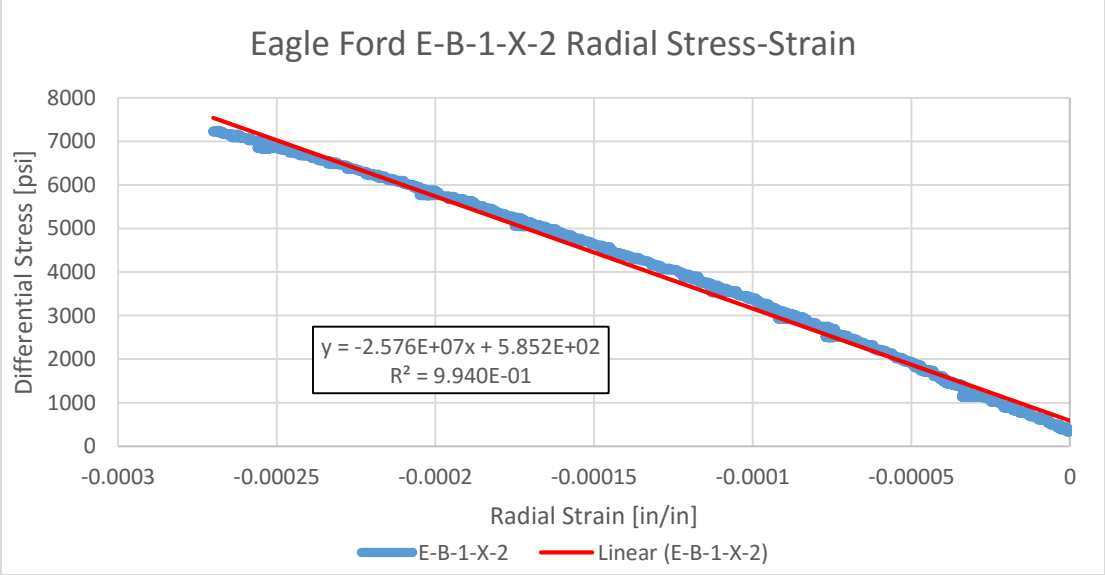

Figure 39: Radial stress-strain curve for sample E-B-1-X-2

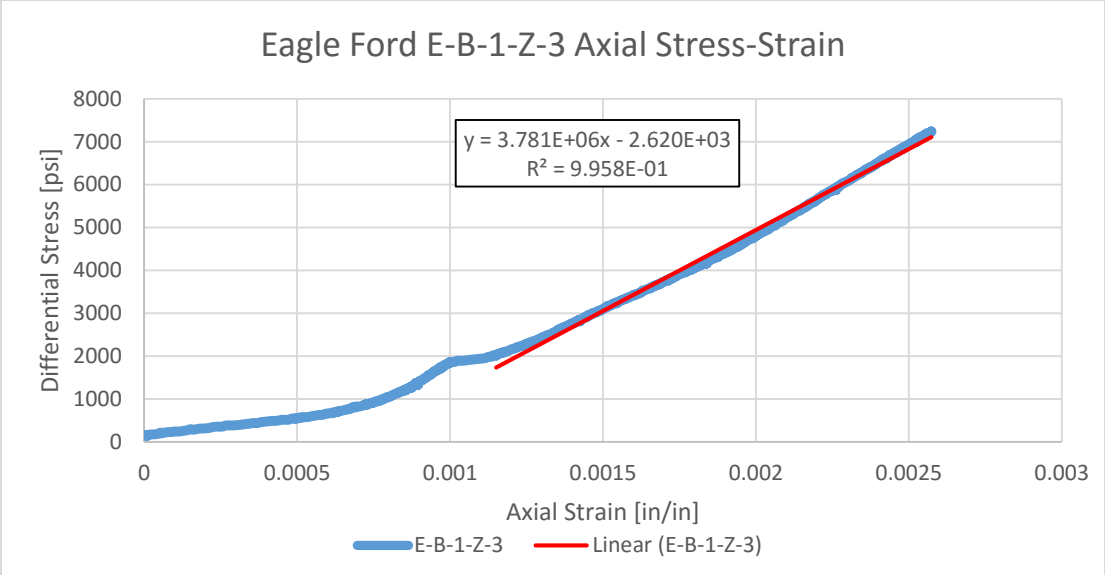

Figure 40: Axial stress-strain curve for sample E-B-1-Z-3

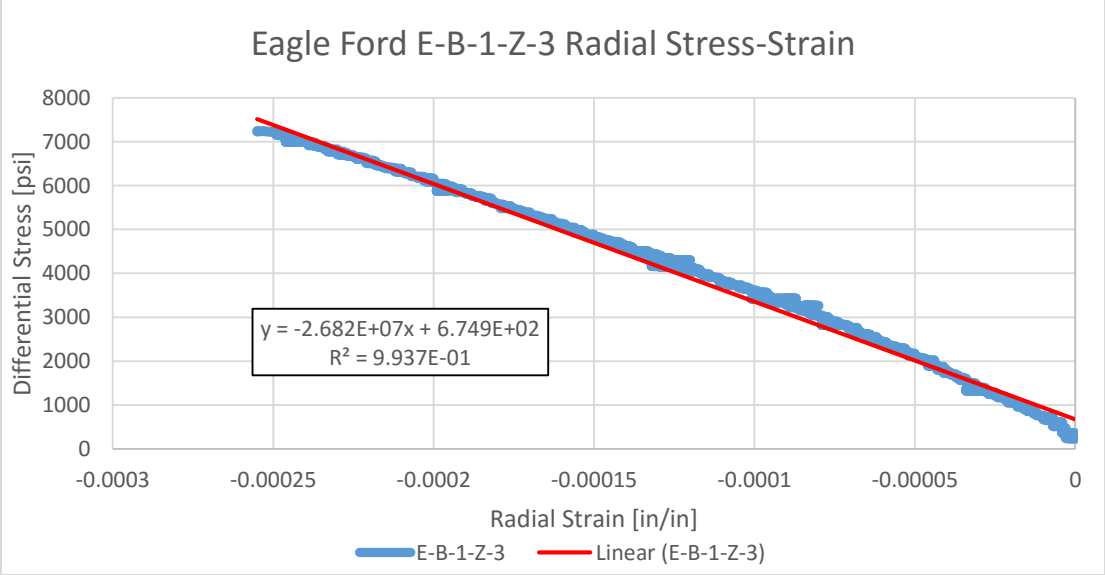

Figure 41: Radial stress-strain curve for sample E-B-1-Z-3

Additionally, Brinell hardness tests were performed on each of the triaxial core plugs prior to triaxial compression testing. Each sample was tested at a force of 0.5 kN

and 1.0 kN with three indentations each, respectively. All Brinell hardness numbers were averaged together for each sample. For this study, average Brinell hardness number for each bedding orientation is reported.

Results of the four triaxial core plugs (3 X-direction and 3 Z-direction) in Facies B1 tested are shown in Table 4:

Table 4: Summary of facies B1 mechanical properties

	E-B-1-X (Parallel)			E-B-1-Z (Perpendicular)		
Samples	Young's Modulus [psi]	Poisson's ratio [-]	Brinell Hardness Number [kgf/mm^2]	Young's Modulus [psi]	Poisson's ratio [-]	Brinell Hardness Number [kgf/mm^2]
Sample 1	4.15E+06	0.178	-	3.53E+06	0.146	-
Sample 2	4.39E+06	0.170	-	3.27E+06	0.139	-
Sample 3	4.15E+06	0.168	-	3.78E+06	0.141	-
Average	**4.23E+06**	**0.172**	**101.81**	**3.53E+06**	**0.142**	**90.90**
Standard Deviation	1.39E+05	4.95E-03	1.40	2.57E+05	3.75E-03	3.82
Percentage Standard Deviation	3%	3%	1%	7%	3%	4%

The difference in the elastic rock properties between the x-direction and z-direction samples is comparably different. The average Young's modulus for the x-direction samples was 4.23 Mpsi, which was higher than the Young's modulus for the Z-direction, 3.53 Mpsi. This indicates that the parallel samples are stiffer than the perpendicular samples. In fact, the ratio of parallel to perpendicular samples is larger than seen in Facies A. It would seem that anisotropy does play a possible role in this

facies. The large difference in Young's modulus further suggests that it could have an effect on fracture conductivity. Additionally, the Poisson's ratio follow the same trend of the Young's modulus values. The parallel samples have a greater Poisson's ratio average than the perpendicular sample. The difference in the averages may be a result of the different layers of mineralogy present in the samples. However, it is difficult to assess the effect Poisson's ratio has on fracture conductivity due to the minimal difference between orientations. Moreover, the parallel samples have a higher Brinell hardness number than the perpendicular samples. This follows the elastic trends found for this facies. Furthermore, the standard deviation reported for Brinell hardness numbers is minimal suggesting that the samples were reasonably homogeneous in mineral composition on the rock surface of the samples tested. The difference between the Brinell hardness number values reported suggest that there could be a possible effect on fracture conductivity. Overall the rock properties measurements obtained present a sizeable disparity between the two orientations.

3.2.2 Facies B1 Mineralogical Composition

The mineral composition of Facies B1 samples were determined using X-ray Diffraction (XRD) analysis. Diffrac.Eva V3 software was used for analysis. Two samples were chosen randomly, one perpendicular and one parallel, to compare mineralogy. The results are presented in Figure 42.

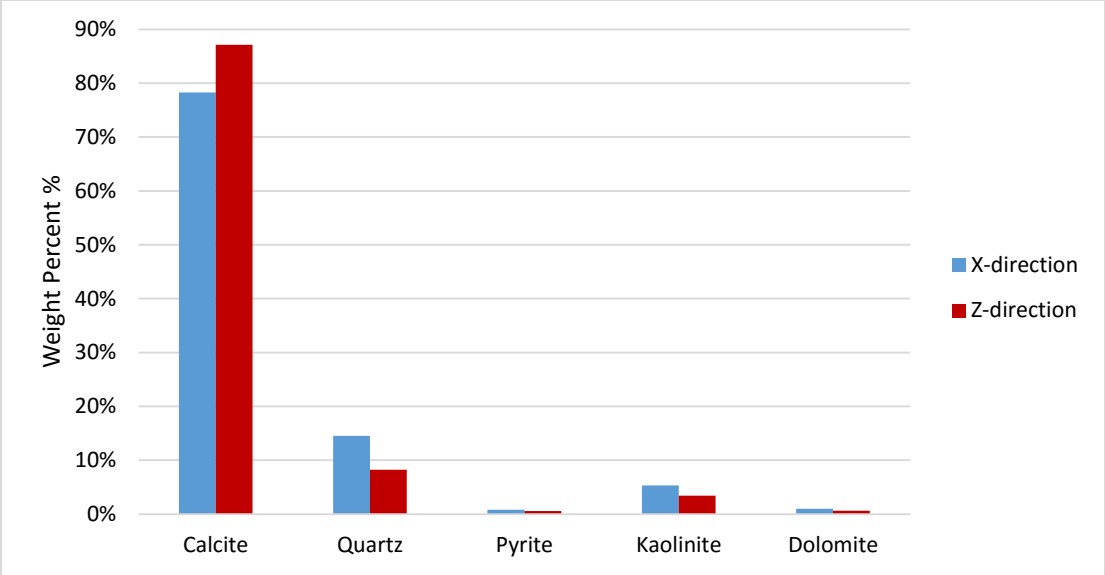

Figure 42: Facies B1 mineralogy composition

Overall, the two samples tested have relatively similar mineralogical composition. The z-direction sample has higher calcite present, but lower amount of quartz compared to the x-direction sample tested. The differences in the elastic rock properties measured could be accounted for by the mineral compositions reported. The x-direction sample has a larger amount of quartz, a hard mineral, which suggests why the parallel samples have a higher Young's modulus. However, it is difficult to determine the extent of influence without further samples tested for mineralogical composition. The average composition of these samples was approximately 83% calcite, 11% quartz, 0.7% pyrite, 0.8% dolomite, and 4% kaolinite.

3.2.3 Facies B1 Surface Roughness

Surface roughness is a possible parameter that could affect fracture conductivity. Tenorio (2016) quantified the surface roughness of each sample of facies B1 tested for

fracture conductivity using a laser profilometer to scan the surface. The Root Mean Square (RMS) error method was used to calculate the deviation of the measurement from the best fit plane. Figure 43 shows a perpendicular (z-direction) fractured conductivity sample. Visually, the sample has some ridges on the fractured surface. A complete summary of surface roughness of samples is displayed in Table 5 (Tenorio, 2016).

Table 5: Summary of facies B1 average surface roughness

	Average RMS Error [in]
E-BL-Z Unpropped	0.167
E-BL-Z 30/50 Mesh	0.200
E-BL-Z 100 Mesh	0.180
E-BL-X Unpropped	0.230
E-BL-X-30/50 Mesh	0.212
E-BL-X-100 Mesh	0.197

Figure 43: Fracture surface of facies B1 perpendicular conductivity sample (Tenorio, 2016)

3.2.4 Facies B1 Fracture Conductivity

Fracture conductivity tests were performed on both the x-direction and z-direction of facies B1 samples. Table 6 displays the fracture conductivity experiments design for facies B1 (Tenorio, 2016).

Table 6: Facies B1 fracture conductivity experiments design

Proppant type	Orientation	Proppant Mass	Areal Proppant Concentration	Number of tests
Unpropped	Z-direction	-	-	3
30/50 Mesh	Z-direction	3.4 g	$0.1 lb_m/ft^2$	1
100 Mesh	Z-direction	3.4 g	$0.1 lb_m/ft^2$	3
Unpropped	X-direction	-	-	4
30/50 Mesh	X-direction	3.4 g	$0.1 lb_m/ft^2$	4
100 Mesh	X-direction	3.4 g	$0.1 lb_m/ft^2$	7

Fracture conductivity tests were performed on both the x-direction and z-direction of facies B1, also known as B-Lower, samples. The samples were tested unpropped, at 0.10 lb/ft^2 areal concentration of both 30/50 mesh and 100 mesh white sand. A summary of the averaged fracture conductivity is displayed in Figure 44.

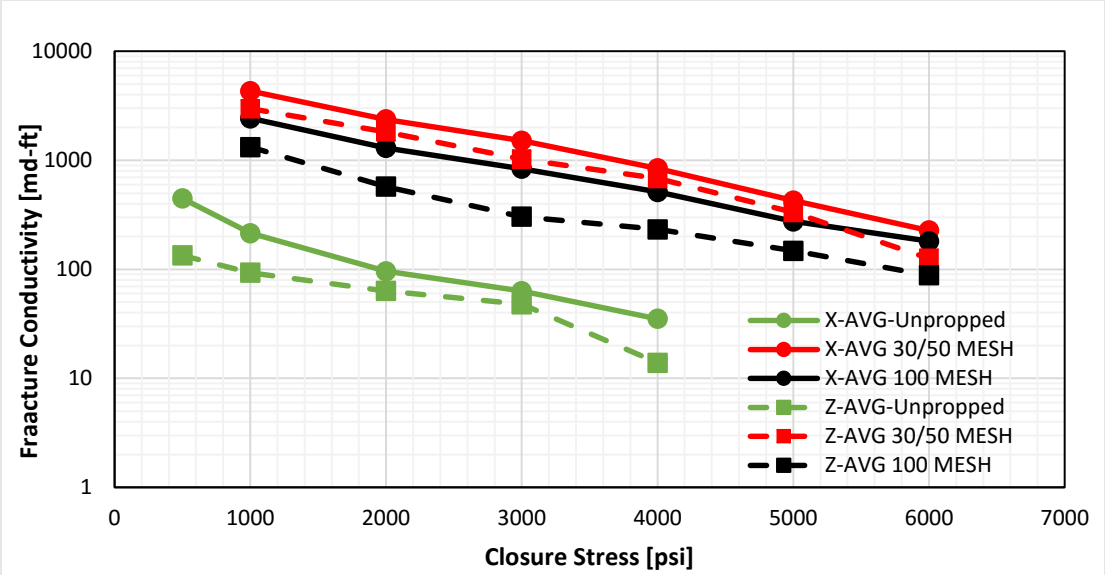

Figure 44: Summary of average conductivity behavior for facies B1 samples

3.3 Facies B2 Results

This section provides the rock mechanical properties measured and mineralogical composition of facies B2.

3.3.1 Facies B2 Rock Mechanics

Five triaxial core plugs from facies B2, two in X-direction and three in Z-direction, were cut and used in rock mechanical properties analysis. Each sample had three loading cycles applied. The third loading cycle used to evaluate the elastic properties and was only plotted. An example of an axial and radial stress-strain curve for a parallel orientation (x-direction) sample of facies B2 is displayed in Figure 45 and Figure 46, respectively. Additionally, an axial and radial stress-strain curve for a perpendicular orientation (z-direction) sample of facies B2 is shown in Figure 47 and

Figure 48, respectively. The complete triaxial compression test results can be found in Appendix A.

Each of the samples underwent the same loading process. The samples were first loaded to 1450 psi, 10 MPa, followed by a second loading to 2900 psi, 20 Mpa. The third and last loading was increased to a range of 4400psi to 7250 psi, 30-50 MPa, depending on the sample. Conductivity samples were not tested for this B sub-facies.

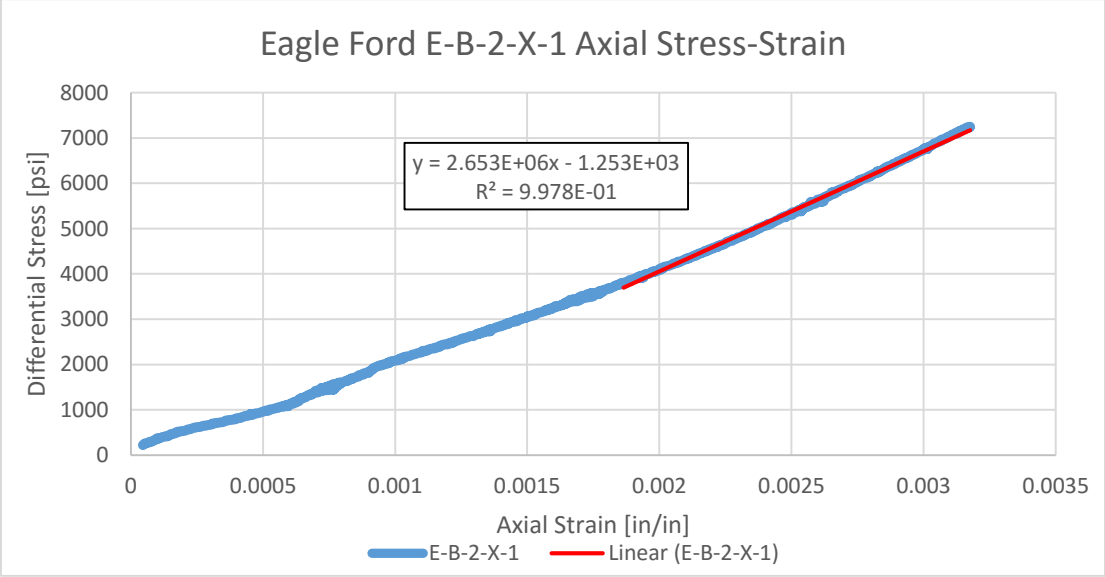

Figure 45: Axial stress-strain curve for sample E-B-2-X-1

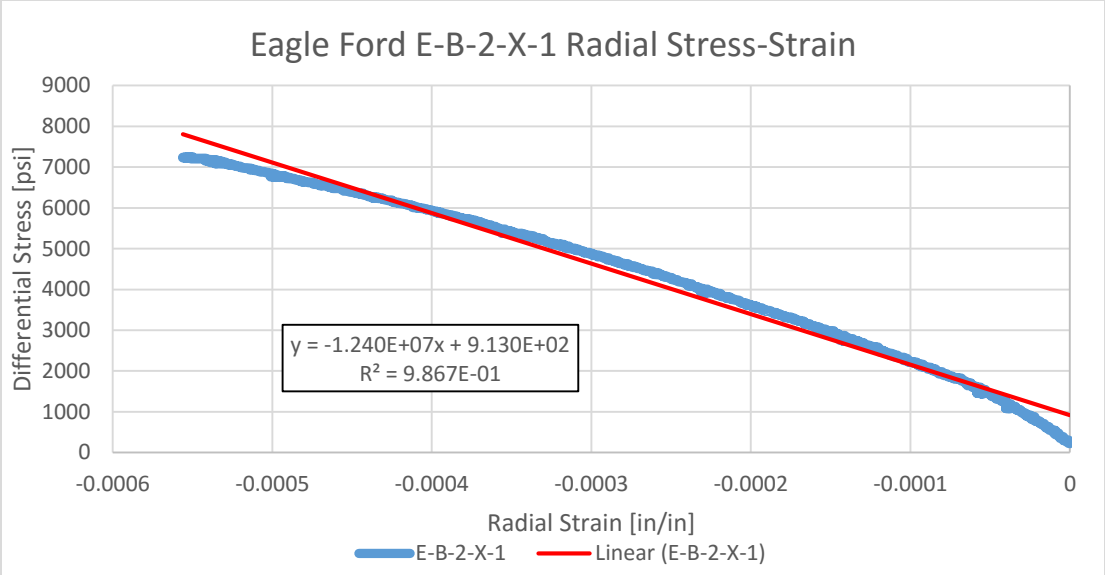

Figure 46: Radial stress-strain curve for sample E-B-2-X-1

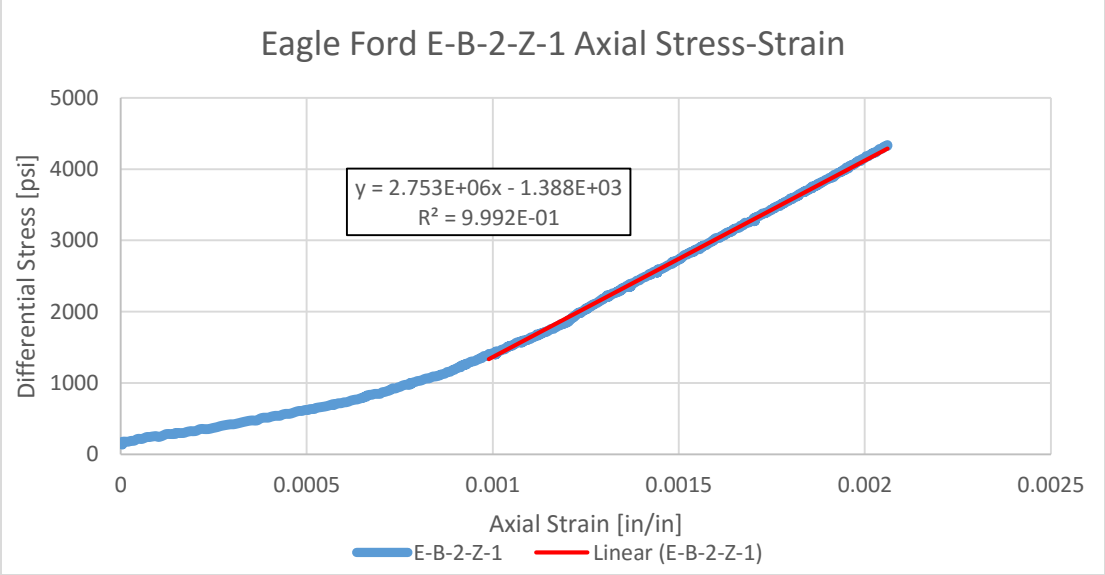

Figure 47: Axial stress-strain curve for sample E-B-2-Z-1

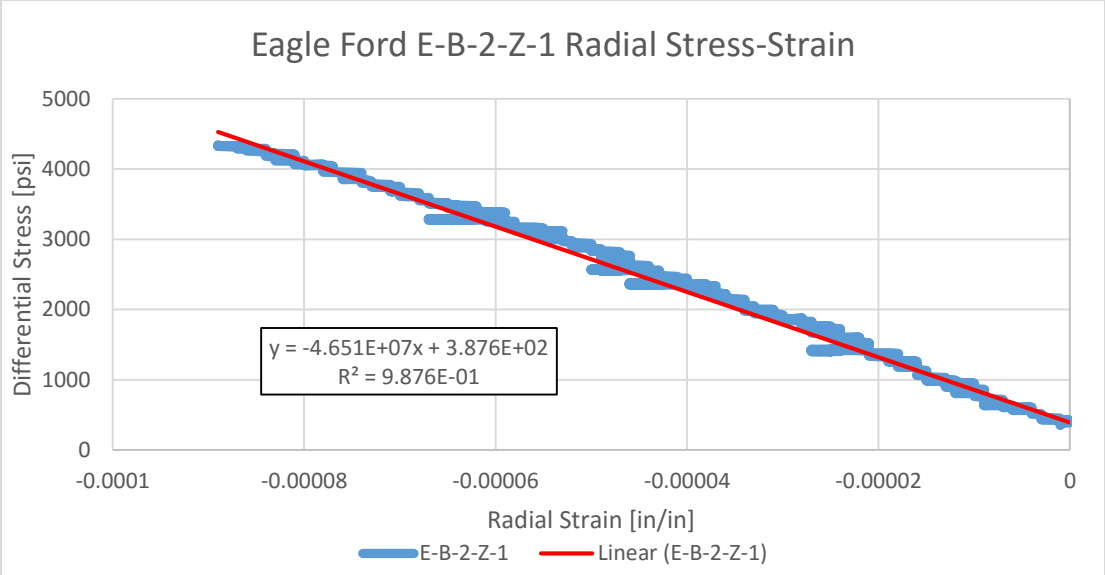

Figure 48: Radial stress-strain curve for sample E-B-2-Z-1

Additionally, Brinell hardness tests were performed on each of the triaxial core plugs prior to triaxial compression testing. Each sample was tested at a force of 0.5 kN and 1.0 kN with three indentations each, respectively. All Brinell hardness numbers were averaged together for each sample. For this study, average Brinell hardness number for each bedding orientation is reported.

Table 7 shows the results of the five triaxial core plugs (2 X-direction and 3 Z-direction) tested in Facies B2:

Table 7: Summary of facies B2 mechanical properties

	E-B-2-X (Parallel)			E-B-2-Z (Perpendicular)		
Samples	Young's Modulus [psi]	Poisson's ratio [-]	Brinell Hardness Number [kgf/mm^2]	Young's Modulus [psi]	Poisson's ratio [-]	Brinell Hardness Number [kgf/mm^2]
Sample 1	2.65E+06	0.214	-	2.75E+06	0.059	-
Sample 2	4.92E+06	0.133	-	4.18E+06	0.199	-
Sample 3	-	-	-	3.57E+06	0.156	-
Average	**3.80E+06**	**0.174**	**124.49**	**3.51E+06**	**0.138**	**101.32**
Standard Deviation	1.6E+06	5.71E-02	7.28	7.18E+05	7.18E-02	16.37
Percentage Standard Deviation	42%	33%	6%	20%	52%	16%

The difference in the elastic rock properties between the x-direction and z-direction samples is slightly different. The average Young's modulus for the x-direction samples was 3.80 Mpsi, which was higher than the Young's modulus for the Z-direction, 3.51 Mpsi. This indicates that the parallel samples are stiffer than the perpendicular samples. This is similar to the trend found in facies B1. In fact, facies B1 reported a higher Young's modulus value for parallel samples, 4.23 Mpsi, compared to facies B2, 3.80 Mpsi. Furthermore, the ratio of Young's modulus for parallel to perpendicular samples is smaller than seen in facies B1. It would seem that anisotropy may play a role in this facies, but not as significantly as facies B1. Additionally, the Poisson's ratio follow the same trend of the Young's modulus values. The parallel samples have a greater Poisson's ratio average than the perpendicular sample. The difference in the averages may be a result of the different layers of mineralogy present in the samples.

Moreover, the parallel samples have a higher Brinell hardness number than the perpendicular samples. This follows the elastic trends found for this facies. This facies has a higher hardness number reported in comparison to facies B1. This could be due to the mineral composition of this facies. This is further explored in section 3.3.2 below. Additionally, the large deviation within the Brinell hardness number value reported for z-direction indicates the large variability within the mineral composition between the rock samples and the surface tested of each sample. While the elastic properties measured reported have a small variation, the Brinell hardness numbers difference suggests a significant difference between the two orientations.

3.3.2 Facies B2 Mineralogical Composition

The mineral composition of Facies B2 samples were determined using X-ray Diffraction (XRD) analysis. Diffrac.Eva V3 software was used for analysis. Two samples were chosen randomly to compare mineralogy. The results are presented in Figure 49.

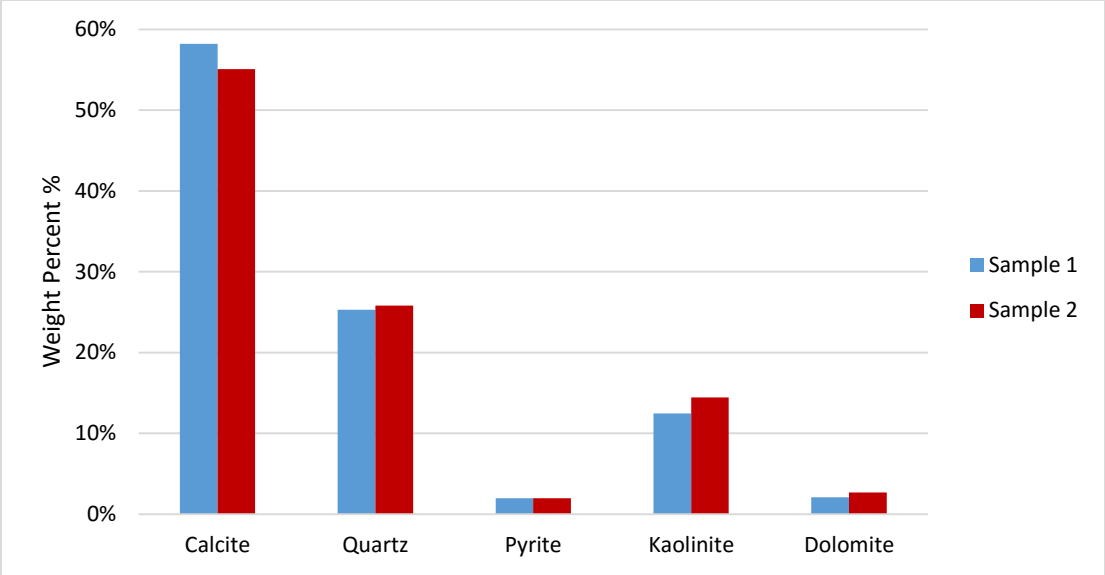

Figure 49: Facies B2 mineralogy composition

Overall, the two samples tested have comparatively similar mineralogical composition. These samples have reportedly higher quartz content and much lower calcite composition than compared to facies B1 samples. This could possibly explain the much higher Brinell hardness number reported as quartz is relatively harder than calcite. However, it is difficult to determine the extent of influence on elastic properties without further samples tested for mineralogical composition. The average composition of these samples was approximately 57% calcite, 25% quartz, 2% pyrite, 2.4% dolomite, and 13.5% kaolinite.

3.4 Facies B3 Results

This section provides the rock mechanical properties measured of facies B3.

3.4.1 Facies B3 Rock Mechanics

Two triaxial core plugs from facies B3, both in X-direction, were cut and used in rock mechanical properties analysis. Each sample had three loading cycles applied. The third loading cycle used to evaluate the elastic properties and was only plotted. An example of an axial and radial stress-strain curve for a parallel orientation (x-direction) sample of facies B3 is displayed in Figure 50 and Figure 51, respectively. The complete triaxial compression test results can be found in Appendix A.

Each of the samples underwent the same loading process. The samples were first loaded to 1450 psi, 10 MPa, followed by a second loading to 2900 psi, 20 Mpa. The third and last loading was increased to 6000 psi, 40 MPa. Conductivity samples were not tested for this B sub-facies.

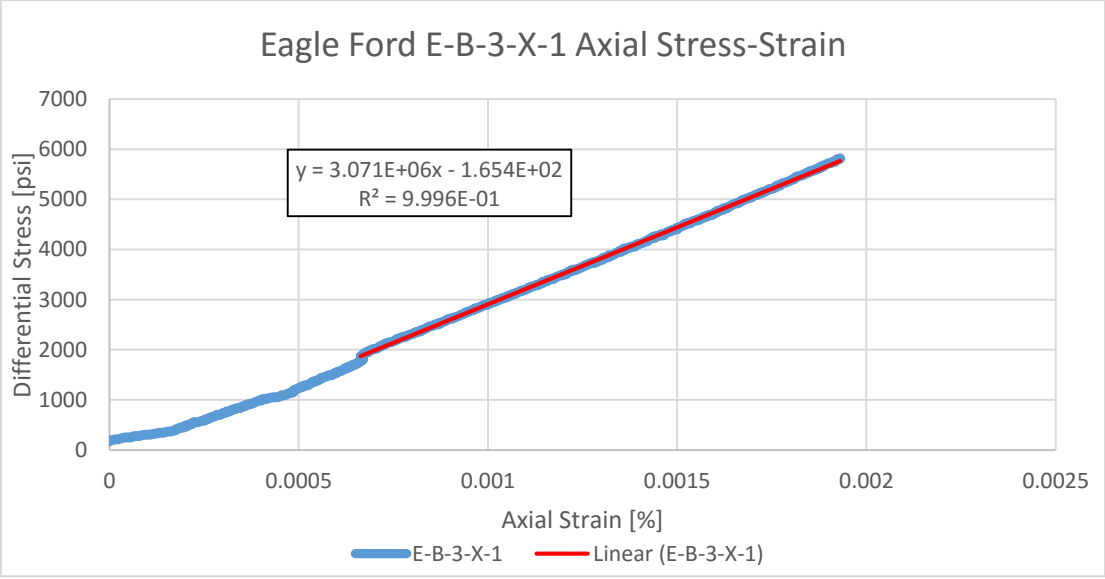

Figure 50: Axial stress-strain curve for sample E-B-3-X-1

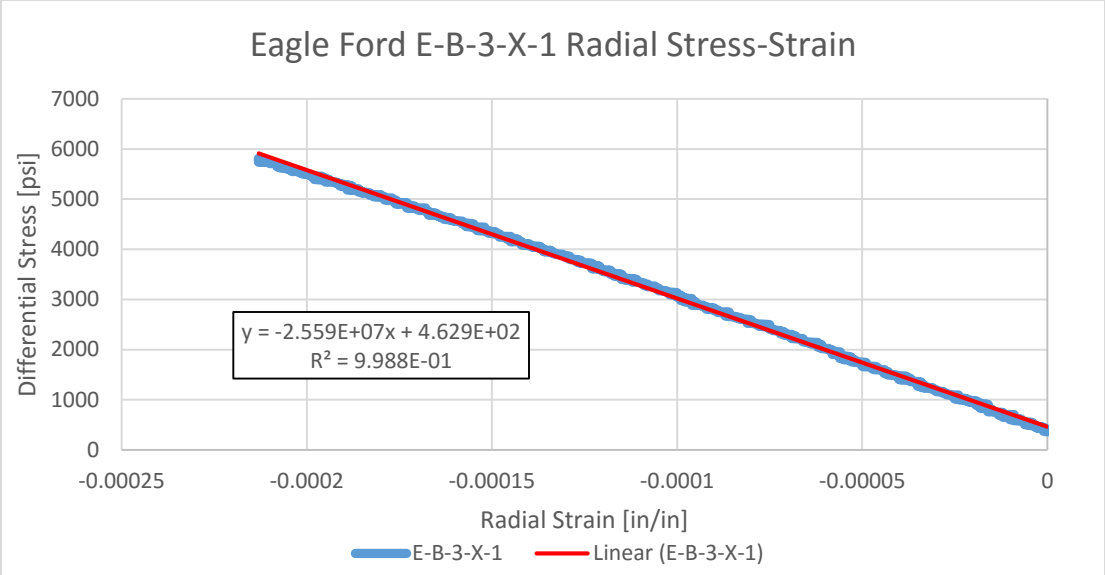

Figure 51: Radial stress-strain curve for sample E-B-3-X-1

Additionally, Brinell hardness tests were performed on each of the triaxial core plugs prior to triaxial compression testing. Each sample was tested at a force of 0.5 kN and 1.0 kN with three indentations each, respectively. All Brinell hardness numbers were averaged together for each sample. For this study, average Brinell hardness number for each bedding orientation is reported.

Results of the two triaxial core plugs (2 X-direction) in Facies B3 tested are shown in Table 8:

Table 8: Summary of facies B3 mechanical properties

	E-B-3-X (Parallel)		
Samples	Young's Modulus [psi]	Poisson's ratio [-]	Brinell Hardness Number [kgf/mm^2]
Sample 1	3.07E+06	0.120	-
Sample 2	2.63E+06	0.117	-
Sample 3	-	-	-
Average	**2.85E+06**	**0.119**	**90.08**
Standard Deviation	1.62E+06	1.90E-03	7.64
Percentage Standard Deviation	4%	2%	8%

The average Young's modulus for the x-direction samples, 2.85 Mpsi, which was much lower than both the x-direction Young's moduli for facies B1 and B2, 4.23 Mpsi and 3.80 Mpsi respectively. These samples were much softer than its counterparts in facies B1 and B2. Additionally, the Poisson's ratio is reportedly lower in value compared to B1 and B2, but not significantly. Moreover, the parallel B3 samples have a lower Brinell hardness number, 90.08 kgf/mm^2, than both parallel samples from B1 and B2. This could be due to the mineral composition of this facies. The variability of the Brinell hardness number reported expresses a possible mineral composition variability within samples and the sample surfaces themselves.

3.4.2 Facies B3 Mineralogical Composition

The mineral composition of Facies B2 samples were determined using X-ray Diffraction (XRD) analysis. Diffrac.Eva V3 software was used for analysis. Two

samples were chosen randomly to compare mineralogy. The results are presented in Figure 52.

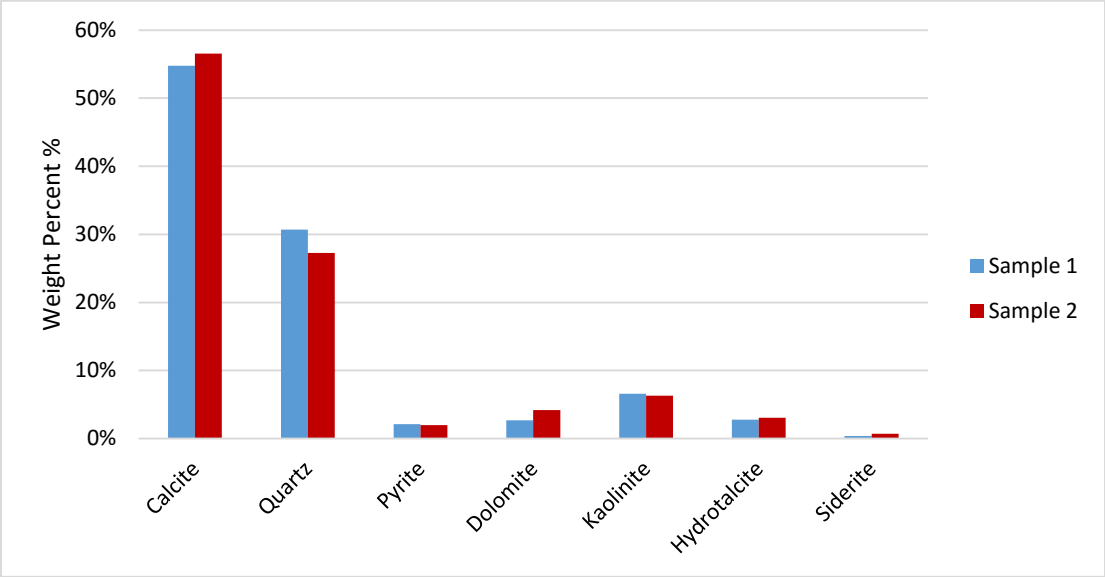

Figure 52: Facies B3 mineralogy composition

Overall, the two samples tested have comparatively similar mineralogical composition. These samples have the highest quartz content and the lowest calcite amount across all facies. Yet, this sub-facies had the lowest Young's modulus reported. Another mineral may be affecting the Young's modulus. Both samples have fairly high content of kaolinite and hydrotalcite compared to other facies, which are relatively soft when compared to quartz and calcite. It is possible that both of these minerals are dominating the elastic properties. However, it is difficult to determine the extent of influence on elastic properties. Furthermore, the Brinell hardness is one of the lowest values reported. Considering the amount of quartz present, the Brinell hardness would be

expected to be higher. It is possible that the surface tested was dominated by the softer minerals resulting in lower value compared to facies B1 and B2. The average composition of these samples was approximately 56% calcite, 29% quartz, 2% pyrite, 3.4% dolomite, 6.5% kaolinite, 3% hydrotalcite, and 0.5% siderite.

3.5 Facies C Results

This section provides the rock mechanical properties measured, fracture conductivity results, and mineralogical composition of facies C.

3.5.1 Facies C Rock Mechanics

Six triaxial core plugs from facies C, three in X-direction and three in Z-direction, were cut and used in rock mechanical properties analysis. Each sample had three loading cycles applied. The third loading cycle used to evaluate the elastic properties and was only plotted. An example of an axial and radial stress-strain curve for a parallel orientation (x-direction) sample of facies C is displayed in Figure 53 and Figure 54, respectively. Additionally, an axial and radial stress-strain curve for a perpendicular orientation (z-direction) sample of facies C is shown in Figure 55 and Figure 56, respectively. The complete triaxial compression test results can be found in Appendix A.

Each of the samples underwent the same loading process. The samples were first loaded to 1450 psi, 10 MPa, followed by a second loading to 2900 psi, 20 Mpa. The third and last loading was increased to 4400 psi, 30 MPa. Conductivity samples of this facies were tested up to 6000 psi.

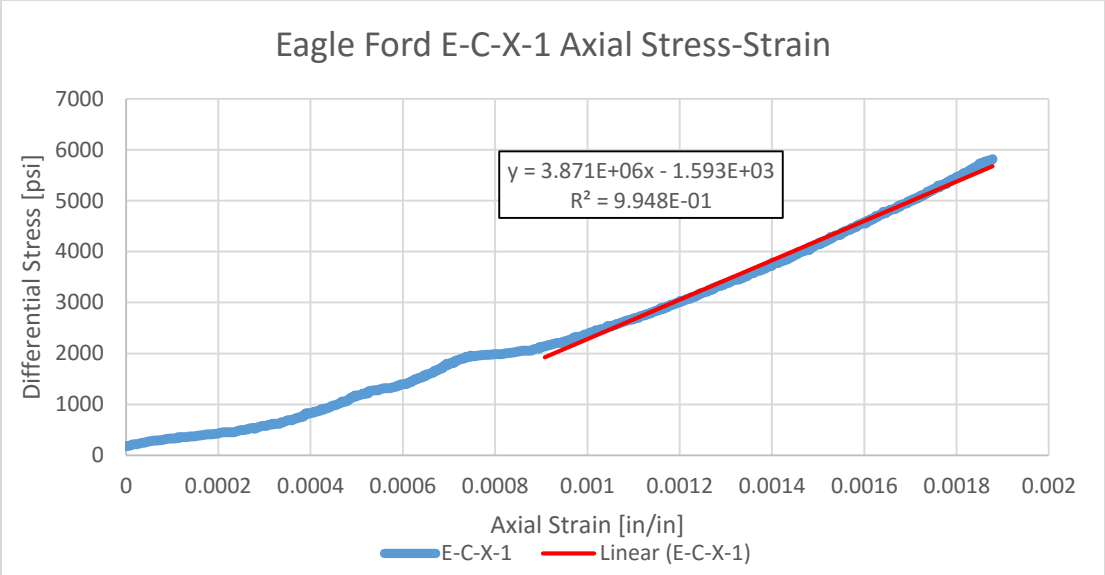

Figure 53: Axial stress-strain curve for sample E-C-X-1

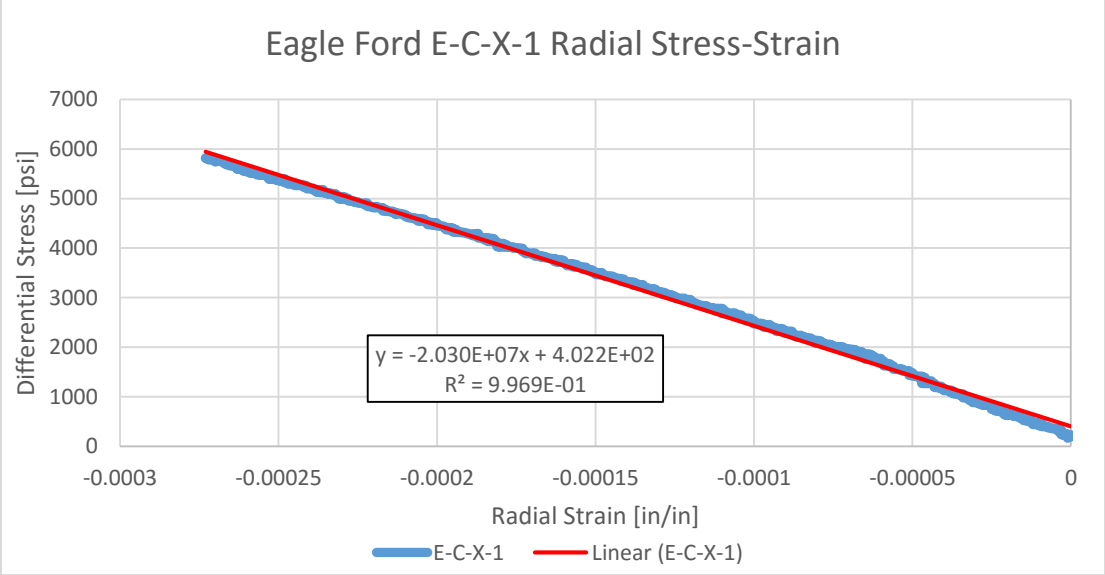

Figure 54: Radial stress-strain curve for sample E-C-X-1

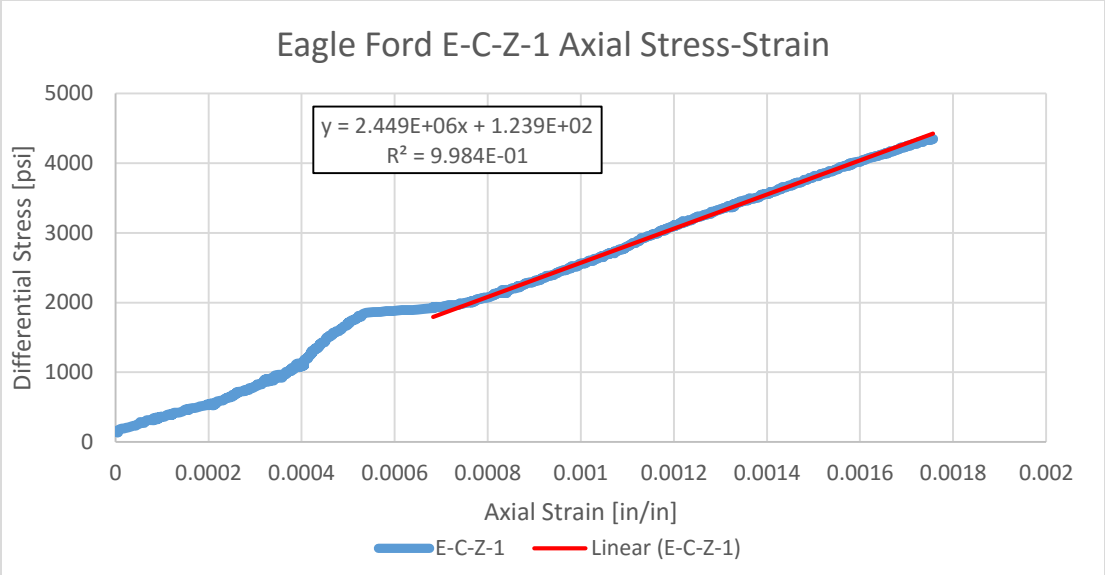

Figure 55: Axial stress-strain curve for sample E-C-Z-1

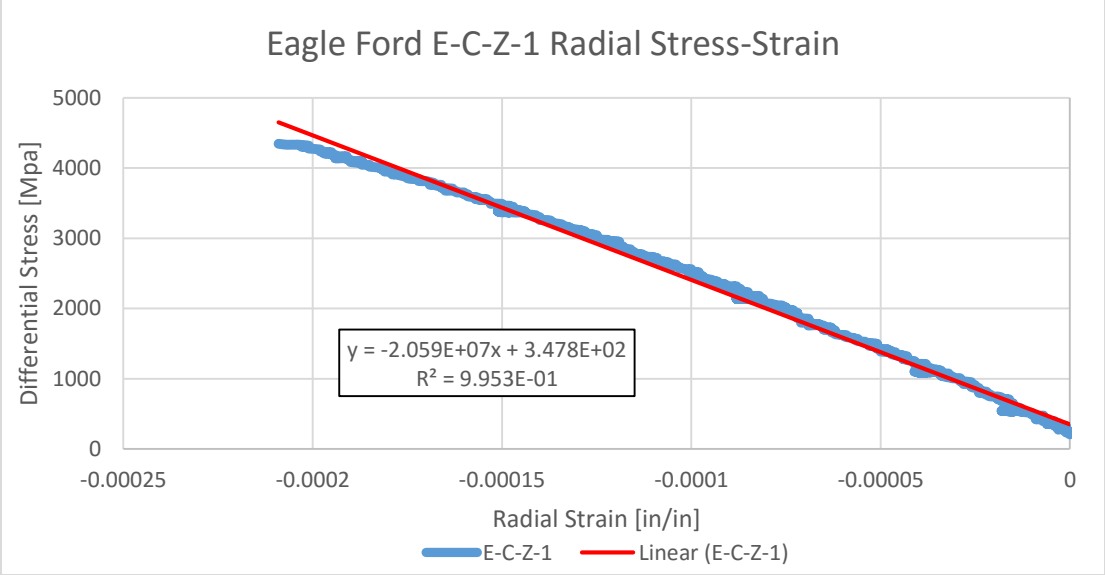

Figure 56: Radial stress-strain curve for sample E-C-Z-1

Additionally, Brinell hardness tests were performed on each of the triaxial core plugs prior to triaxial compression testing. Each sample was tested at a force of 0.5 kN

and 1.0 kN with three indentations each, respectively. All Brinell hardness numbers were averaged together for each sample. For this study, average Brinell hardness number for each bedding orientation is reported.

Results of the six triaxial core plugs (3 X-direction and 3 Z-direction) in Facies C tested are shown in Table 9:

Table 9: Summary of facies C mechanical properties

	E-C-X (Parallel)			E-C-Z (Perpendicular)		
Samples	Young's Modulus [psi]	Poisson's ratio [-]	Brinell Hardness Number [kgf/mm^2]	Young's Modulus [psi]	Poisson's ratio [-]	Brinell Hardness Number [kgf/mm^2]
Sample 1	3.87E+06	0.191	-	2.50E+06	0.119	-
Sample 2	3.60E+06	0.153	-	2.09E+06	0.103	-
Sample 3	3.88E+06	0.192	-	3.99E+06	0.159	-
Average	**3.78E+06**	**0.178**	**81.87**	**2.84E+06**	**0.127**	**68.31**
Standard Deviation	1.62E+05	2.22E-02	2.41	1.01E+06	2.93E-02	5.39
Percentage Standard Deviation	4%	12%	3%	35%	23%	8%

The difference in the elastic rock properties between the x-direction and z-direction samples is comparably different. The average Young's modulus for the x-direction samples was 3.78 Mpsi, which was much higher than the Young's modulus for the Z-direction, 2.84 Mpsi, indicating that the parallel samples are stiffer. In fact, the ratio of parallel to perpendicular samples is largest throughout the facies. Anisotropy does play a role in the mechanical properties within zone C. Furthermore, the Young's

modulus reported is the lowest values amongst all the facies characterized. The large difference in Young's modulus further suggests that it could have an effect on fracture conductivity. Additionally, the Poisson's ratio follow the same trend of the Young's modulus values. The parallel samples are slightly greater for Poisson's ratio average than the perpendicular sample. However, it is difficult to assess the effect Poisson's ratio has on fracture conductivity due to the minimal difference between orientations. Moreover, the parallel samples have a higher Brinell hardness number than the perpendicular samples. This follows the elastic trends found for this facies. In fact, the Brinell hardness values reported are the lowest reported throughout the zones. Furthermore, the standard deviation reported for Brinell hardness is nominal suggesting that the samples were reasonably homogeneous in mineral composition on the rock surface of the samples tested. The difference between the parallel and perpendicular Brinell hardness values reported suggest that there could be a possible effect on fracture conductivity. Overall the rock properties measurements obtained present a considerable difference between the two orientations.

3.5.2 Facies C Mineralogical Composition

The mineral composition of Facies C samples were determined using X-ray Diffraction (XRD) analysis. Diffrac.Eva V3 software was used for analysis. Two samples, 1 x-direction and 1 z-direction, were chosen randomly to compare mineralogy. The results are presented in Figure 57.

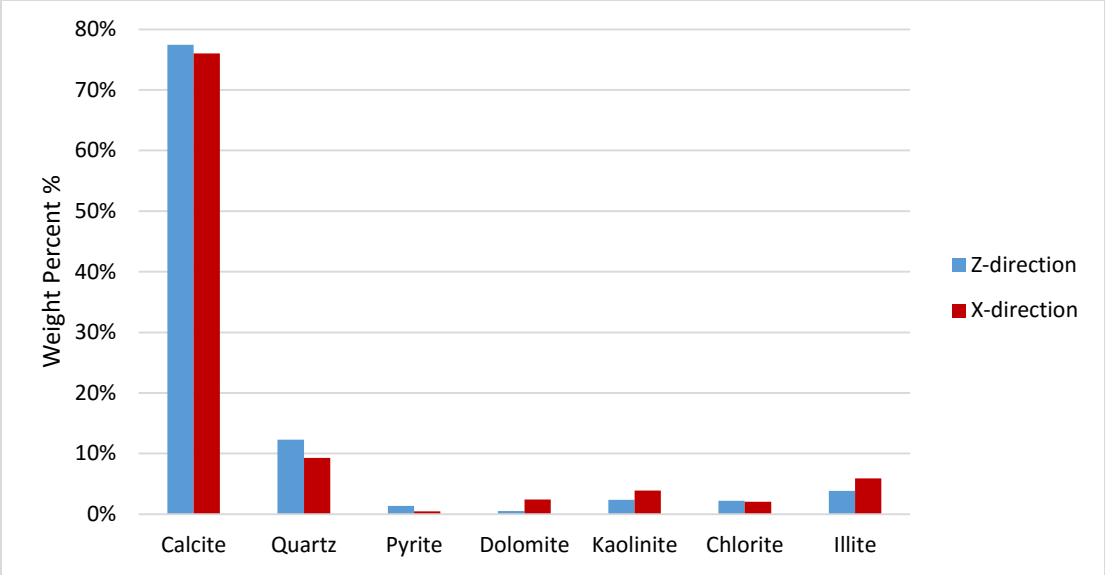

Figure 57: Facies C mineralogy composition

Overall, the two samples tested have reasonably similar mineralogical composition. This facies has less calcite content compared to A and B1, but not as low compared to facies B2. Additionally, the quartz content detected is similar to facies B1 samples. This facies had the three types of clay detected: Kaolinite, Chlorite, and Illite. The average composition of these samples was approximately 77% calcite, 11% quartz, 0.9% pyrite, 1.5% dolomite, 2% kaolinite, 3% chlorite, and 5% illite. The overall clay content present in these two samples results in nearly 10%. Due to clay being a soft mineral, this could be the influencing factor of both the elastic properties and the Brinell hardness number values reported for this facies.

3.5.3 Facies C Surface Roughness

Surface roughness is a possible parameter that could affect fracture conductivity. Tenorio (2016) quantified the surface roughness of each sample of facies C tested for

fracture conductivity using a laser profilometer to scan the surface. The Root Mean Square (RMS) error method was used to calculate the deviation of the measurement from the best fit plane. Figure 58 shows a Parallel (x-direction) fractured conductivity sample. Visually, the sample has several deep ridges on the fractured surface. A complete summary of surface roughness of samples is displayed in Table 10 (Tenorio, 2016).

Table 10: Summary of facies C average surface roughness

	Average RMS Error [in]
E-C-X Unpropped	0.165
E-C-X-30/50 Mesh	0.175
E-C-X-100 Mesh	0.175

Figure 58: Fracture surface of facies C parallel conductivity sample (Tenorio, 2016)

3.5.4 Facies C Fracture Conductivity

Fracture conductivity tests were performed on the x-direction of facies C samples. Table 11 displays the fracture conductivity experiments design for facies C (Tenorio, 2016).

Table 11: Facies C fracture conductivity experiments design

Proppant type	Orientation	Proppant Mass	Areal Proppant Concentration	Number of tests
Unpropped	X-direction	-	-	2
30/50 Mesh	X-direction	3.4 g	$0.1 lb_m/ft^2$	3
100 Mesh	X-direction	3.4 g	$0.1 lb_m/ft^2$	5

Fracture conductivity tests were performed only on the x-direction of facies C samples. The samples were tested unpropped, at 0.10 lb/ft^2 areal concentration of both 30/50 mesh and 100 mesh white sand. A summary of the averaged fracture conductivity is displayed in Figure 59.

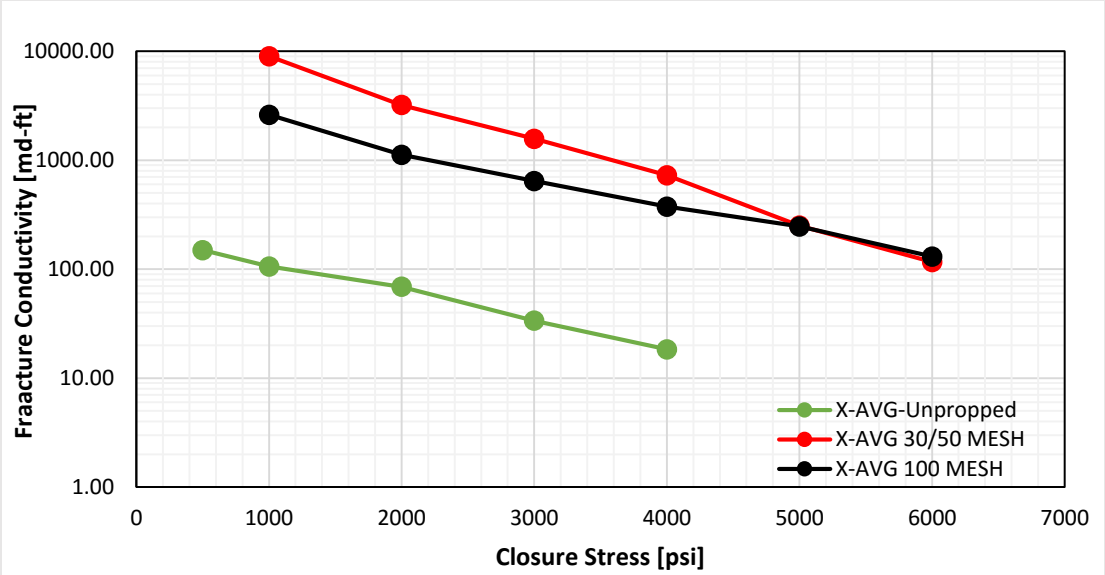

Figure 59: Summary of average conductivity behavior for facies C samples

3.6 Facies D Results

This section provides the rock mechanical properties measured, fracture conductivity results, and mineralogical composition of facies D.

3.6.1 Facies D Rock Mechanics

Five triaxial core plugs from facies D, two in X-direction and three in Z-direction, were cut and used in rock mechanical properties analysis. Each sample had three loading cycles applied. The third loading cycle used to evaluate the elastic properties and was only plotted. An example of an axial and radial stress-strain curve for a parallel orientation (x-direction) sample of facies D is displayed in Figure 60 and Figure 61, respectively. Additionally, an axial and radial stress-strain curve for a perpendicular orientation (z-direction) sample of facies D is shown in Figure 62 and

Figure 63, respectively. The complete triaxial compression test results can be found in Appendix A.

Each of the samples underwent the same loading process. The samples were first loaded to 1450 psi, 10 MPa, followed by a second loading to 2900 psi, 20 Mpa. The third and last loading was increased up to 5000 psi, 35 MPa. Conductivity samples of this facies were tested up to 6000 psi.

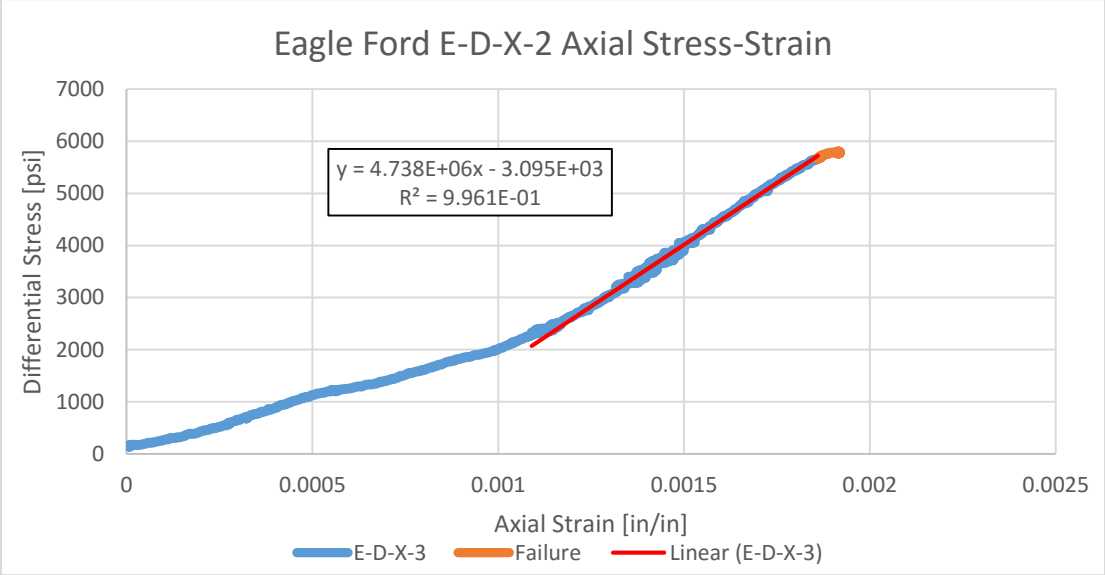

Figure 60: Axial stress-strain curve for sample E-D-X-2

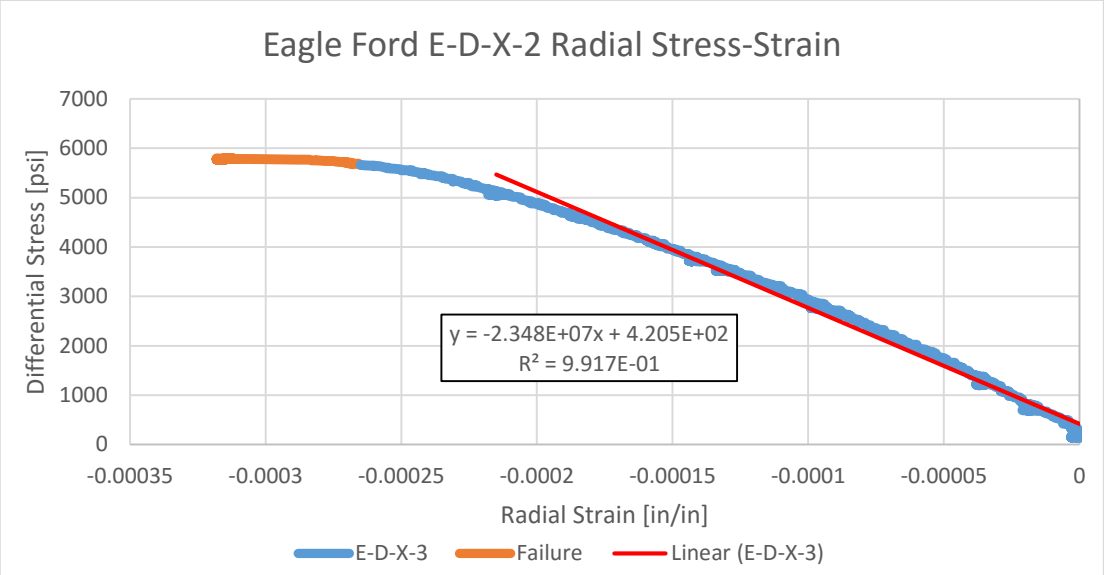

Figure 61: Radial stress-strain curve for sample E-D-X-2

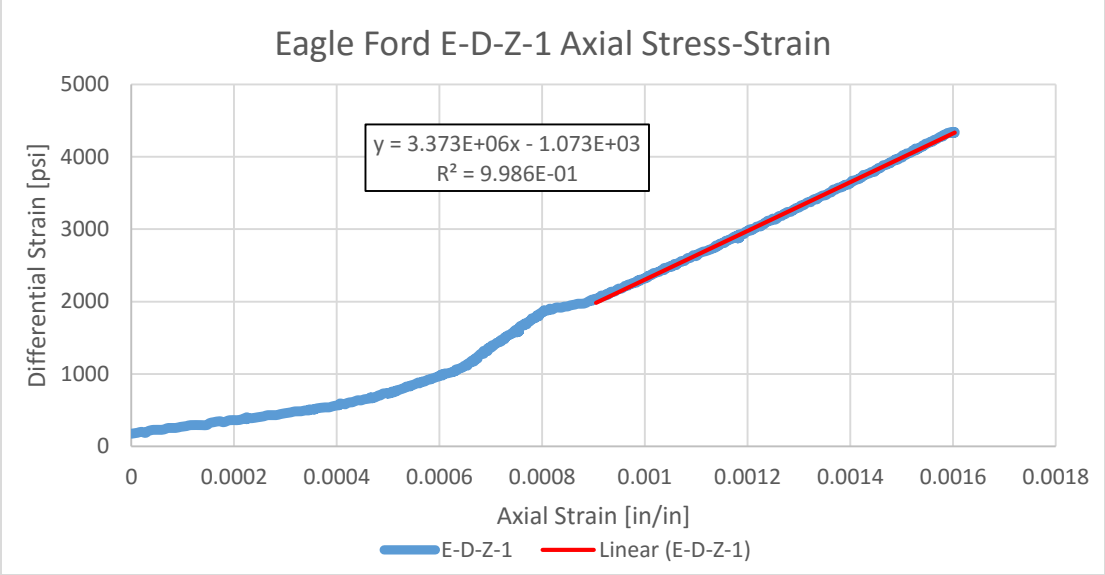

Figure 62: Axial stress-strain curve for sample E-D-Z-1

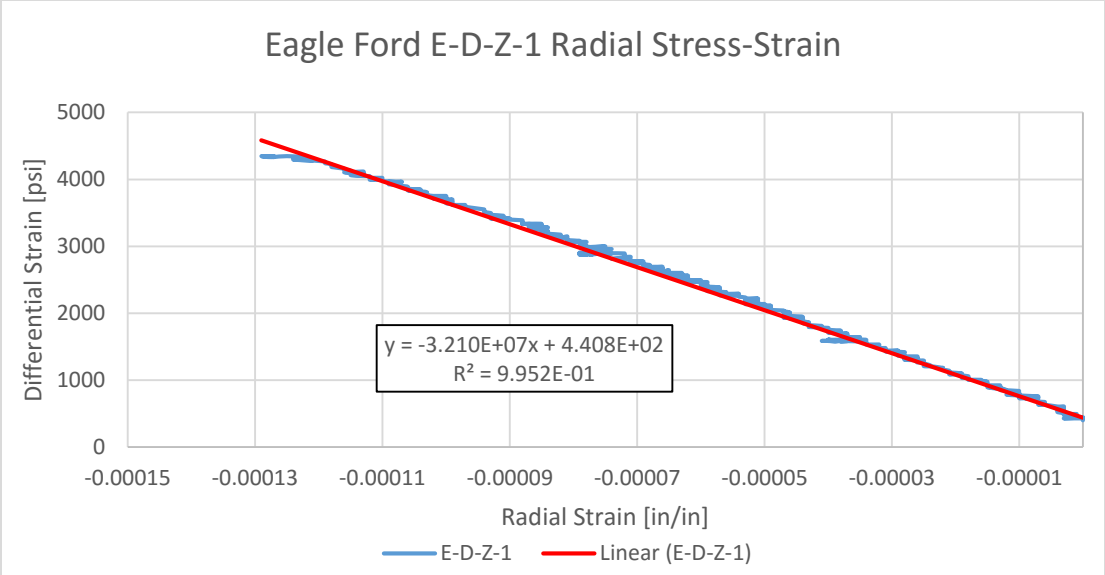

Figure 63: Radial stress-strain curve for sample E-D-Z-1

Additionally, Brinell hardness tests were performed on each of the triaxial core plugs prior to triaxial compression testing. Each sample was tested at a force of 0.5 kN and 1.0 kN with three indentations each, respectively. All Brinell hardness numbers were averaged together for each sample. For this study, average Brinell hardness number for each bedding orientation is reported.

Table 12 displays the results of the five triaxial core plugs (2 X-direction and 3 Z-direction) tested in Facies D.

Table 12: Summary of facies D mechanical properties

	E-D-X (Parallel)			E-D-Z (Perpendicular)		
Samples	Young's Modulus [psi]	Poisson's ratio [-]	Brinell Hardness Number [kgf/mm^2]	Young's Modulus [psi]	Poisson's ratio [-]	Brinell Hardness Number [kgf/mm^2]
Sample 1	4.90E+06	0.165	-	3.37E+06	0.105	-
Sample 2	4.74E+06	0.202	-	4.39E+06	0.123	-
Sample 3	-	-	-	3.63E+06	0.119	-
Average	**4.82E+06**	**0.184**	**91.66**	**3.80E+06**	**0.116**	**92.26**
Standard Deviation	1.15E+05	2.58E-02	14.46	5.26E+05	9.54E-03	4.94
Percentage Standard Deviation	2%	14%	16%	14%	8%	5%

The difference in the elastic rock properties between the x-direction and z-direction samples is distinct. The average Young's modulus for the x-direction samples was 4.82 Mpsi, which was higher than the Young's modulus for the Z-direction, 3.80 Mpsi. Again, this indicates that the parallel samples are stiffer than the perpendicular samples. In fact, the ratio of parallel to perpendicular samples was one of the highest amongst the facies. Anisotropy appears to play a role within zone D measured mechanical properties. The large difference in Young's modulus further suggests that it could have an effect on fracture conductivity. Moreover, the Poisson's ratio follow the same trend of the Young's modulus values. The parallel samples have a greater Poisson's ratio average than the perpendicular sample. The difference in the averages may be a result of the different layers of mineralogy present in the samples. However, it is difficult to weigh the effect Poisson's ratio has on fracture conductivity due to the

minimal difference between orientations. Additionally, the perpendicular samples have a slightly higher average of Brinell hardness number. In fact, the difference in Brinell hardness number is only 0.6. Anisotropy may not play a role in the Brinell hardness number reported for facies D due to this minor difference. However, the standard deviation of the parallel samples, 16%, is quite large indicating that within the x-direction samples suggesting a large heterogeneity in composition on the surface tested. The small difference between the Brinell hardness number values makes it difficult to attribute any effect it has on fracture conductivity. Overall, the Young's modulus measurements obtained present a considerable difference between the two orientations. However, the Poisson's ratio and Brinell hardness numbers obtained have minimal differences between the two types of orientations.

3.6.2 Facies D Mineralogical Composition

The mineral composition of a Facies D sample was determined using X-ray Diffraction (XRD) analysis. Diffrac.Eva V3 software was used for analysis. One sample was chosen randomly to compare mineralogy. The results are presented in Figure 64.

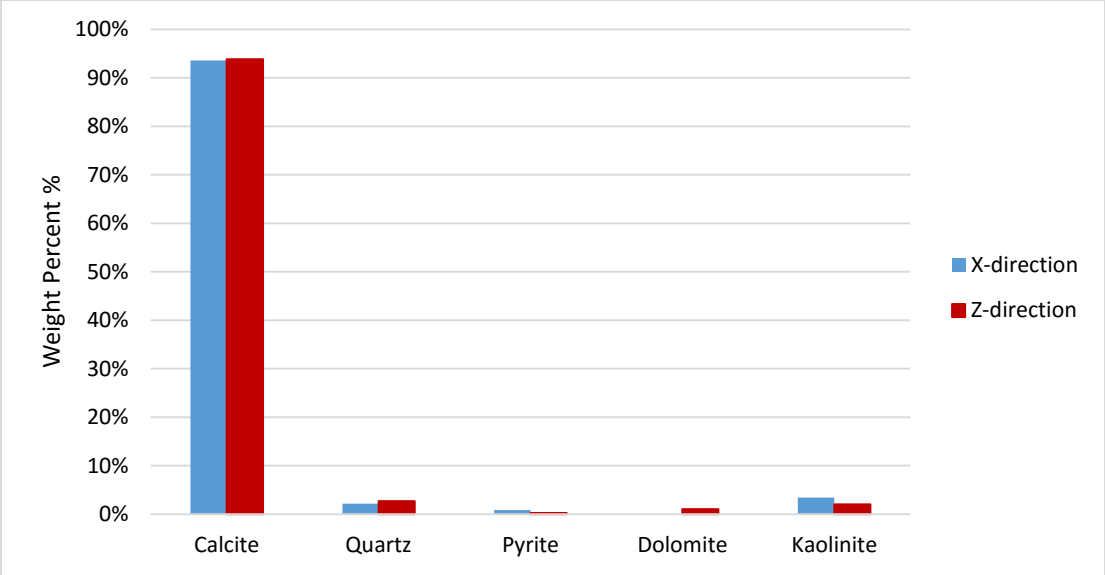

Figure 64: Facies D mineralogy composition

This facies has the highest calcite content and the lowest amount of quartz detected compared to all the facies tested. Compositionally, the facies D was very similar to facies E mineralogical composition. The mineralogical composition of this sample is approximately 94% calcite, 2% quartz, 0.5% pyrite, 1% dolomite, and 3% kaolinite. The lack of any other mineral being more than 5% content signifies that calcite is the dominant factor in this mineralogical composition possibly dominating the rock mechanical properties seen for this facies. Possibly, another factor could be influencing these rock properties though. However, the Brinell hardness number values reported are almost identical regardless of the orientation. This could be due to the high dominant calcite content present in both samples regardless of orientation suggesting a lack of anisotropy.

3.6.3 Facies D Surface Roughness

Surface roughness is a possible parameter that could affect fracture conductivity. Tenorio (2016) quantified the surface roughness of each sample of facies D tested for fracture conductivity using a laser profilometer to scan the surface. The Root Mean Square (RMS) error method was used to calculate the deviation of the measurement from the best fit plane. Figure 65 shows a parallel (x-direction) fractured conductivity sample. On inspection, the fracture face is relatively smooth with the rough ridges near the end. A complete summary of surface roughness of samples is displayed in Table 13 (Tenorio, 2016).

Table 13: Summary of facies D average surface roughness

	Average RMS Error [in]
E-D-X Unpropped	0.260
E-D-X-30/50 Mesh	0.285
E-D-X-100 Mesh	0.270

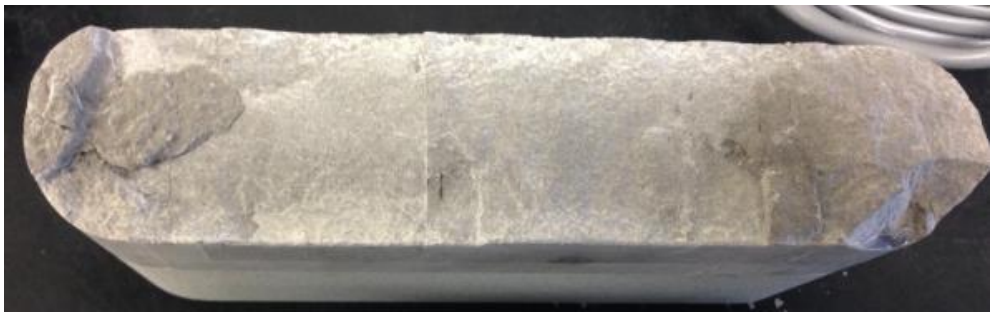

Figure 65: Fracture surface of facies D parallel conductivity sample (Tenorio, 2016)

3.6.4 Facies D Fracture Conductivity

Fracture conductivity tests were performed on the x-direction of facies D samples. Table 14 displays the fracture conductivity experiments design for facies D (Tenorio, 2016).

Table 14: Facies D fracture conductivity experiments design

Proppant type	Orientation	Proppant Mass	Areal Proppant Concentration	Number of tests
Unpropped	X-direction	-	-	3
30/50 Mesh	X-direction	3.4 g	$0.1 lb_m/ft^2$	2
100 Mesh	X-direction	3.4 g	$0.1 lb_m/ft^2$	4

Fracture conductivity tests were performed only on the x- direction of facies D samples. The samples were tested unpropped, at 0.10 lb/ft^2 areal concentration of both 30/50 mesh and 100 mesh white sand. A summary of the averaged fracture conductivity is displayed in Figure 66.

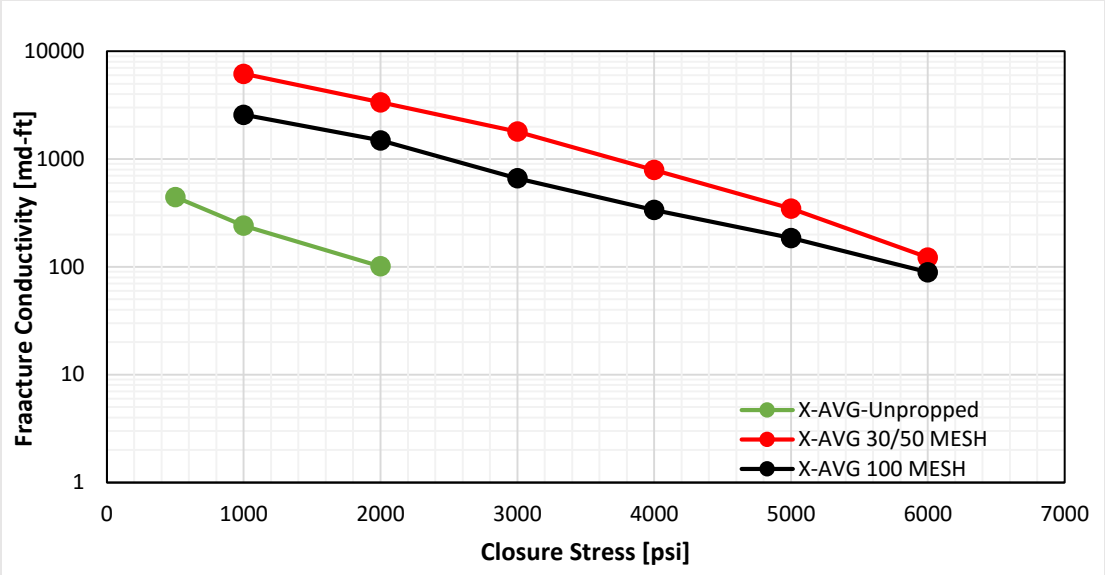

Figure 66: Summary of average conductivity behavior for facies D samples

3.7 Facies E Results

This section provides the rock mechanical properties measured, fracture conductivity results, and mineralogical composition of facies E.

3.7.1 Facies E Rock Mechanics

Four triaxial core plugs from facies E, two in X-direction and two in Z-direction, were cut and used in rock mechanical properties analysis. Each sample had three loading cycles applied. The third loading cycle used to evaluate the elastic properties and was only plotted. An example of an axial and radial stress-strain curve for a parallel orientation (x-direction) sample of facies E is displayed in Figure 67 and Figure 68, respectively. Additionally, an axial and radial stress-strain curve for a perpendicular orientation (z-direction) sample of facies E is shown in Figure 69 and Figure 70, respectively. The complete triaxial compression test results can be found in Appendix A.

Each of the samples underwent the same loading process. The samples were first loaded to 1450 psi, 10 MPa, followed by a second loading to 2900 psi, 20 Mpa. The third and last loading was increased up to 5800 psi, 40 MPa. Conductivity samples of this facies were tested up to 6000 psi.

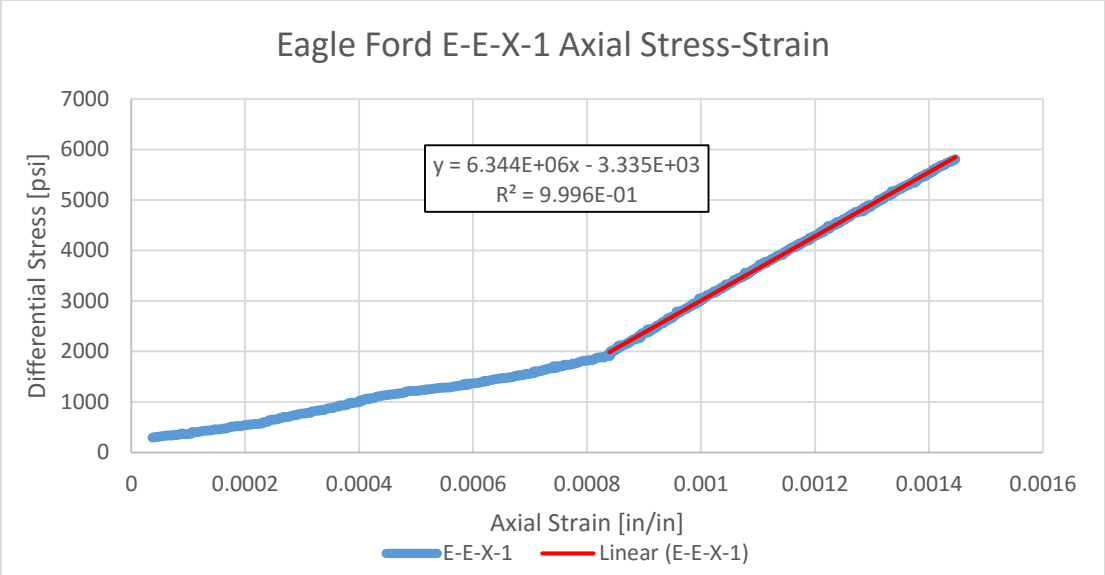

Figure 67: Axial stress-strain curve for sample E-E-X-1

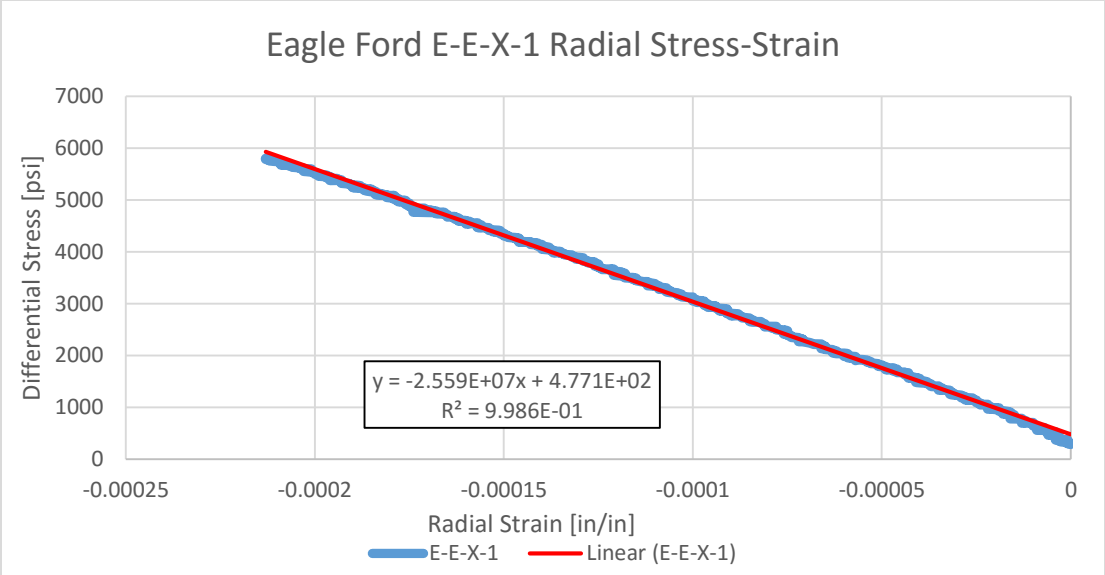

Figure 68: Radial stress-strain curve for sample E-E-X-1

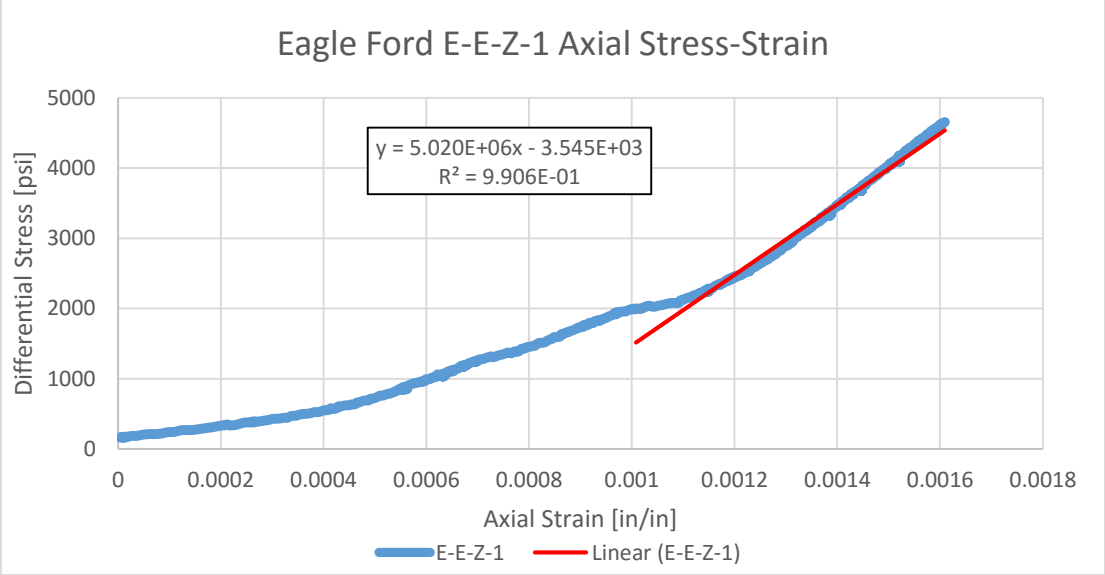

Figure 69: Axial stress-strain curve for sample E-E-Z-1

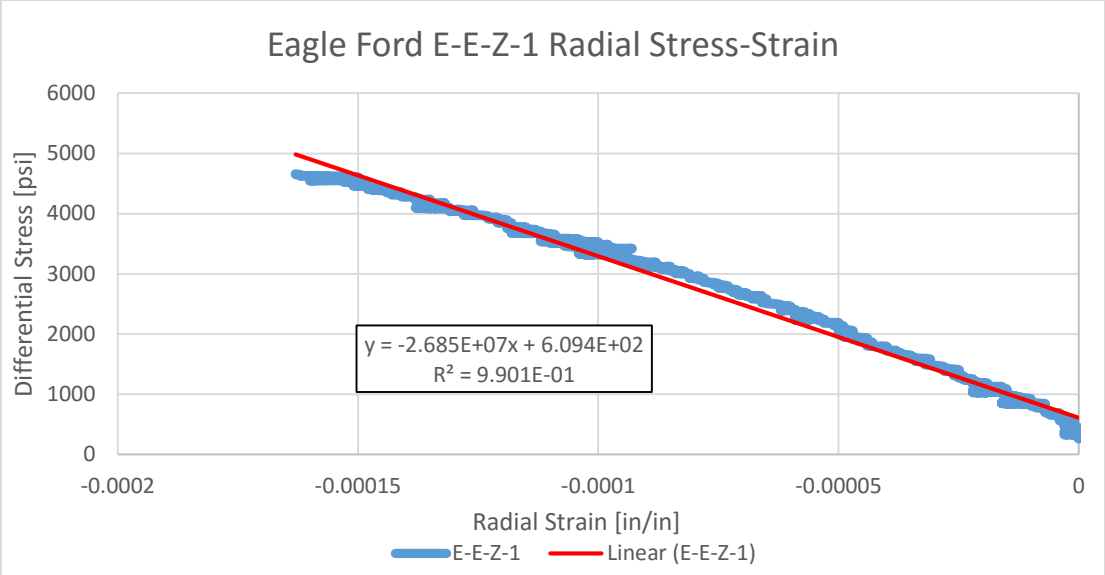

Figure 70: Radial stress-strain curve for sample E-E-Z-1

Additionally, Brinell hardness tests were performed on each of the triaxial core plugs prior to triaxial compression testing. Each sample was tested at a force of 0.5 kN and 1.0 kN with three indentations each, respectively. All Brinell hardness numbers were averaged together for each sample. For this study, average Brinell hardness number for each bedding orientation is reported. Results of the four triaxial core plugs (2 X-direction and 2 Z-direction) in Facies E tested are shown in Table 15:

Table 15: Summary of facies E mechanical properties

	E-E-X (Parallel)			E-E-Z (Perpendicular)		
Samples	Young's Modulus [psi]	Poisson's ratio [-]	Brinell Hardness Number [kgf/mm^2]	Young's Modulus [psi]	Poisson's ratio [-]	Brinell Hardness Number [kgf/mm^2]
Sample 1	6.34E+06	0.248	-	5.02E+06	0.187	-
Sample 2	4.85E+06	0.170	-	4.51E+06	0.150	-
Sample 3	-	-	-	-	-	-
Average	**5.60E+06**	**0.209**	**90.85**	**4.76E+06**	**0.168**	**57.30**
Standard Deviation	1.05E+06	5.54E-02	0.17	3.61E+05	2.61E-02	26.35
Percentage Standard Deviation	19%	27%	0%	8%	15%	46%

The difference in the elastic rock properties between the x-direction and z-direction samples is distinctly different. The average Young's modulus for the x-direction samples was 5.60 Mpsi, which was higher than the Young's modulus for the Z-direction, 4.76 Mpsi. This indicates that the parallel samples are stiffer than the perpendicular samples. The ratio of parallel to perpendicular samples indicated anisotropy plays a possible role within zone E. Furthermore, the clear difference in Young's modulus suggests that it is a factor in fracture conductivity. The Poisson's ratio follow the same trend of the Young's modulus values. The parallel samples have a greater Poisson's ratio average than the perpendicular sample. The difference in the averages may be a result of the different layers of mineralogy present in the samples. However, the difference in Poisson's ratio based on the orientation is slightly larger than other facies, but it is difficult to accredit this parameter to have any effect on fracture

conductivity. Furthermore, the elastic properties of facies E are the highest compared to the entire formation tested. The parallel samples have a higher average of Brinell hardness number following the same trend as the elastic properties. The Brinell hardness number average reported for perpendicular samples had the lowest value amongst the facies tested. However, the standard deviation of the parallel samples is significantly large, 46%, indicating that within the samples tested there was large heterogeneity within the samples and the rock surface tested. Anisotropy is present in the Brinell hardness values presented with a large ratio between the parallel and perpendicular samples. Additionally, the Brinell hardness values had the largest difference between orientations. Overall the rock properties measurements obtained present a sizable difference between the two orientations.

3.7.2 Facies E Mineralogical Composition

The mineral composition of a facies E sample was determined using X-ray Diffraction (XRD) analysis. Diffrac.Eva V3 software was used for analysis. One sample was chosen randomly to compare mineralogy. The results are presented in Figure 71.

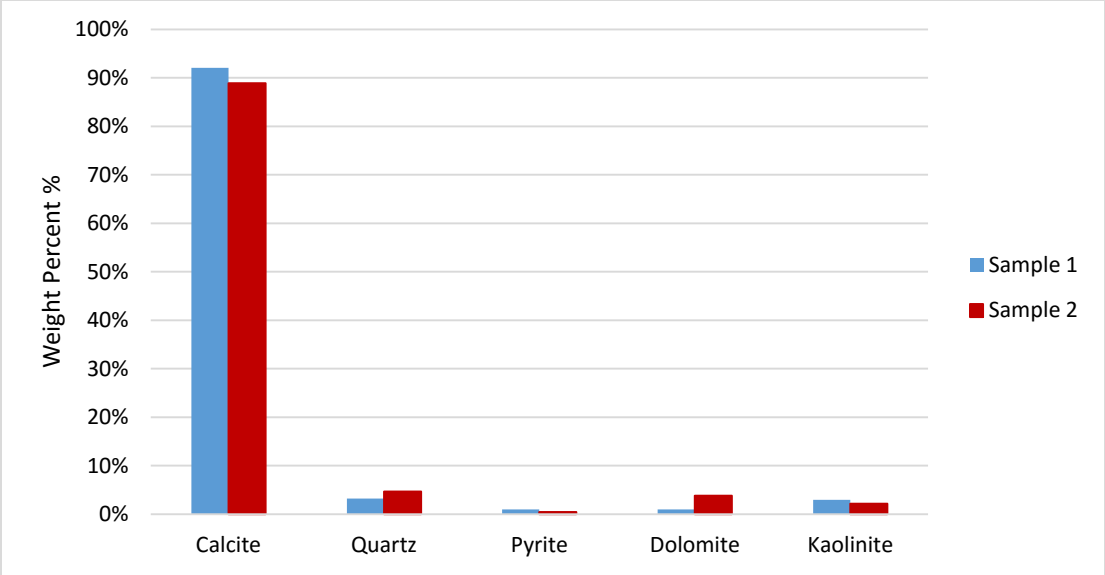

Figure 71: Facies E mineralogy composition

The mineral composition of this facies is very similar to the composition of facies D. A high calcite content and low quartz content was detected. The average composition of these samples was approximately 90% calcite, 4% quartz, 0.7% pyrite, 2.4% dolomite and 2.5% kaolinite. This facies has slightly more quartz, a hard mineral, compared to facies D. This could possibly explain why the young's modulus values are higher than facies D. The z-direction Brinell hardness value was reportedly much lower than the x-direction Brinell hardness regardless of the high dominant calcite content seen in this facies. However, the z-direction value had a large deviation suggesting that the surface tested lacked mineral homogeneity.

3.7.3 Facies E Surface Roughness

Surface roughness is a possible parameter that could affect fracture conductivity. Tenorio (2016) quantified the surface roughness of each sample of facies E tested for

fracture conductivity using a laser profilometer to scan the surface. The Root Mean Square (RMS) error method was used to calculate the deviation of the measurement from the best fit plane. Figure 72 shows a parallel (x-direction) fractured conductivity sample. The sample pictured shows a relative roughness across the entire sample surface, but also the bedding planes are visible. A complete summary of surface roughness of samples is displayed in Table 16 (Tenorio, 2016).

Table 16: Summary of facies E average surface roughness

	Average RMS Error [in]
E-D-X Unpropped	0.190
E-D-X-30/50 Mesh	0.203
E-D-X-100 Mesh	0.203

Figure 72: Fracture surface of facies E parallel conductivity sample (Tenorio, 2016)

3.7.4 Facies E Fracture Conductivity

Fracture conductivity tests were performed on the x-direction of facies E samples. Table 17 displays the fracture conductivity experiments design for facies E (Tenorio, 2016).

Table 17: Facies E fracture conductivity experiments design

Proppant type	Orientation	Proppant Mass	Areal Proppant Concentration	Number of tests
Unpropped	X-direction	-	-	3
30/50 Mesh	X-direction	3.4 g	$0.1 lb_m/ft^2$	2
100 Mesh	X-direction	3.4 g	$0.1 lb_m/ft^2$	4

Fracture conductivity tests were performed only on the x- direction of facies E samples. The samples were tested unpropped, at 0.10 lb/ft^2 areal concentration of both 30/50 mesh and 100 mesh white sand. A summary of the averaged fracture conductivity is displayed in Figure 73.

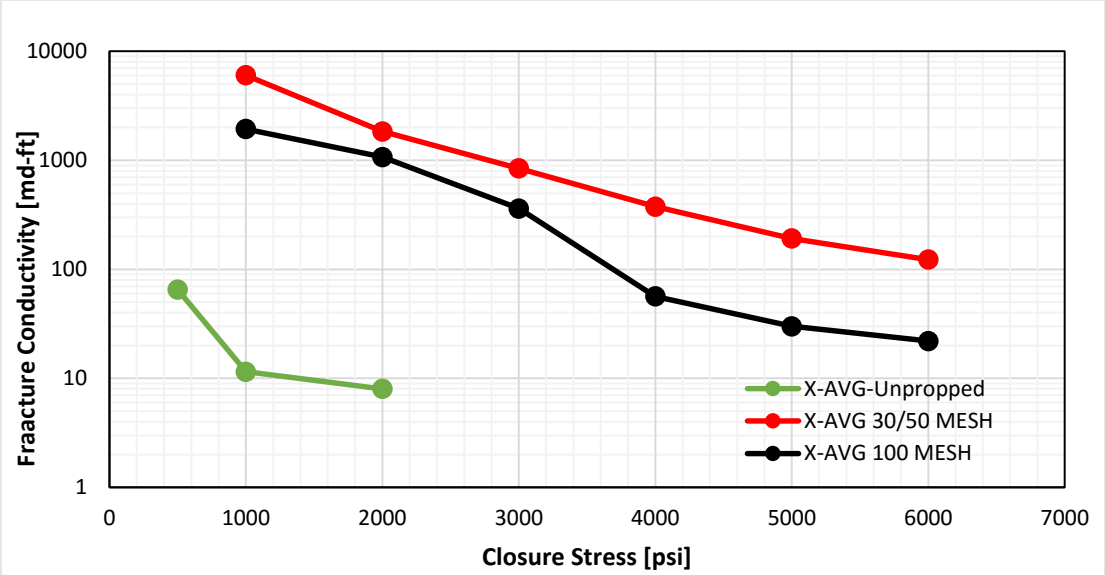

Figure 73: Summary of average conductivity behavior for facies E samples

3.8 Analysis of Rock Properties

In order to evaluate the effect of the measured rock properties on fracture conductivity, it is essential to assess the differences between the samples from each facies as well as the effects of sample orientation. Table 18 provides a compilation of the mechanical properties of each facies and orientation. Figure 74 displays a comparison of Young's modulus and Poisson's ratio across the Eagle Ford facies.

Table 18: Summary of mechanical properties

		X-direction (Parallel)			Z-direction (Perpendicular)		
		Young's Modulus [psi]	**Poisson's ratio [-]**	**Brinell Hardness Number [kgf/mm^2]**	**Young's Modulus [psi]**	**Poisson's ratio [-]**	**Brinell Hardness Number [kgf/mm^2]**
A	Avg.	3.98E+06	0.144	91.91	3.79E+06	0.109	105.64
	Stan. Dev.	9.39E+05	2.29E-02	6.65	-	-	14.85
	% Stan. Dev.	24%	16%	7%	-	-	14%
B 1	Avg.	4.23E+06	0.172	101.81	3.53E+06	0.142	90.90
	Stan. Dev.	1.39E+05	4.95E-03	1.40	2.57E+05	3.75E-03	3.82
	% Stan. Dev.	3%	3%	1%	7%	3%	4%
B 2	Avg.	3.80E+06	0.174	124.49	3.51E+06	0.138	101.32
	Stan. Dev.	1.6E+06	5.71E-02	7.28	7.18E+05	7.18E-02	16.37
	% Stan. Dev.	42%	33%	6%	20%	52%	16%
B 3	Avg.	2.85E+06	0.119	90.08	-	-	-
	Stan. Dev.	1.62E+06	1.90E-03	7.64	-	-	-
	% Stan. Dev.	4%	2%	8%	-	-	-
C	Avg.	3.78E+06	0.178	81.87	2.84E+06	0.127	68.31
	Stan. Dev.	1.62E+05	2.22E-02	2.41	1.01E+06	2.93E-02	5.39
	% Stan. Dev.	4%	12%	3%	35%	23%	8%
D	Avg.	4.82E+06	0.184	91.66	3.80E+06	0.116	92.26
	Stan. Dev.	1.15E+05	2.58E-02	14.46	5.26E+05	9.54E-03	4.94
	% Stan. Dev.	2%	14%	16%	14%	8%	5%

Table 18: Continued

		X-direction (Parallel)			Z-direction (Perpendicular)		
		Young's Modulus [psi]	Poisson's ratio [-]	Brinell Hardness Number [kgf/mm^2]	Young's Modulus [psi]	Poisson's ratio [-]	Brinell Hardness Number [kgf/mm^2]
E	Avg.	5.6E+06	0.209	90.85	4.76E+06	0.168	57.30
	Stan. Dev.	1.05E+06	5.54E-02	0.17	3.61E+05	2.61E-02	26.35
	% Stan. Dev.	19%	27%	0%	8%	15%	46%

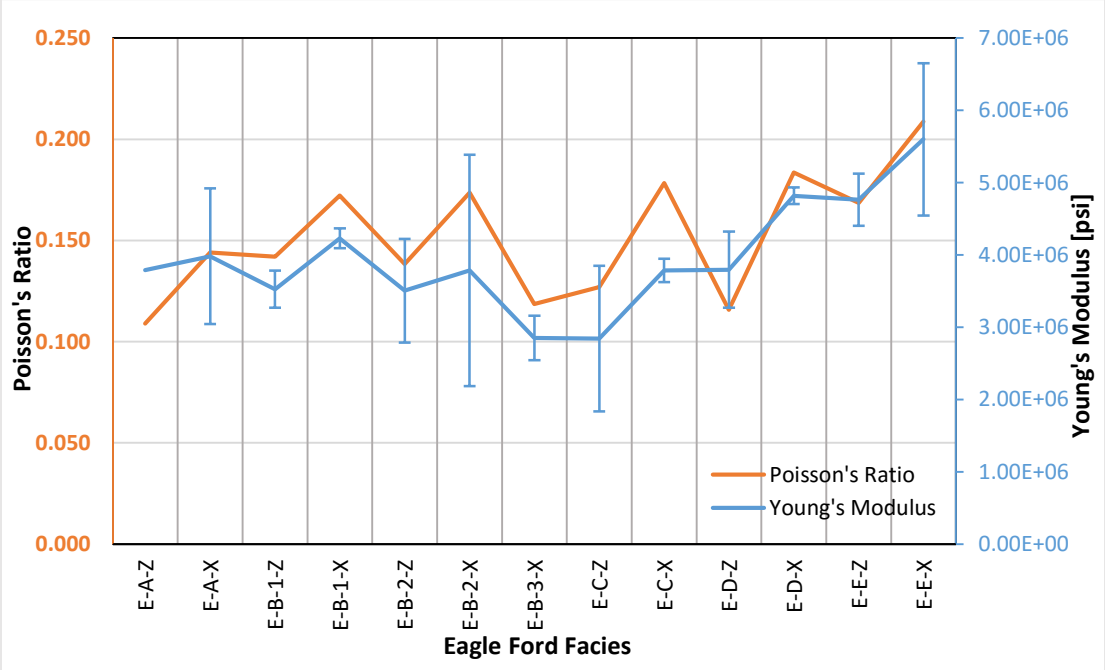

Figure 74: Comparison of Young's modulus and Poisson's ratio across the Eagle Ford facies

The Young's modulus values are noticeably different across the Eagle Ford facies. Facies A had the least effect on orientation with a ratio of parallel to

perpendicular Young's modulus of 1.05. Although Facies B1 is directly above facies A in the formation, the Young's modulus is considerably different. Facies B1 has a high parallel to perpendicular Young's modulus ratio, 1.20, which suggests the orientation strongly effects on the conductivity. Facies C had the lowest averages of Young's modulus for both orientations. In fact, facies C had the largest ratio of parallel to perpendicular for Young's modulus at 1.33 suggesting a strong dependence on the orientation of the samples. Facies D and facies E have the highest Young's moduli values of the measured facies. Geologically, both facies D and facies E are considered to be more similar to the Austin Chalk than the lower Eagle Ford formation. A possibility is the mineralogical composition of facies D and facies E is strongly affecting the elastic properties measured.

Figure 75 displays a comparison of Brinell hardness number across the Eagle Ford facies.

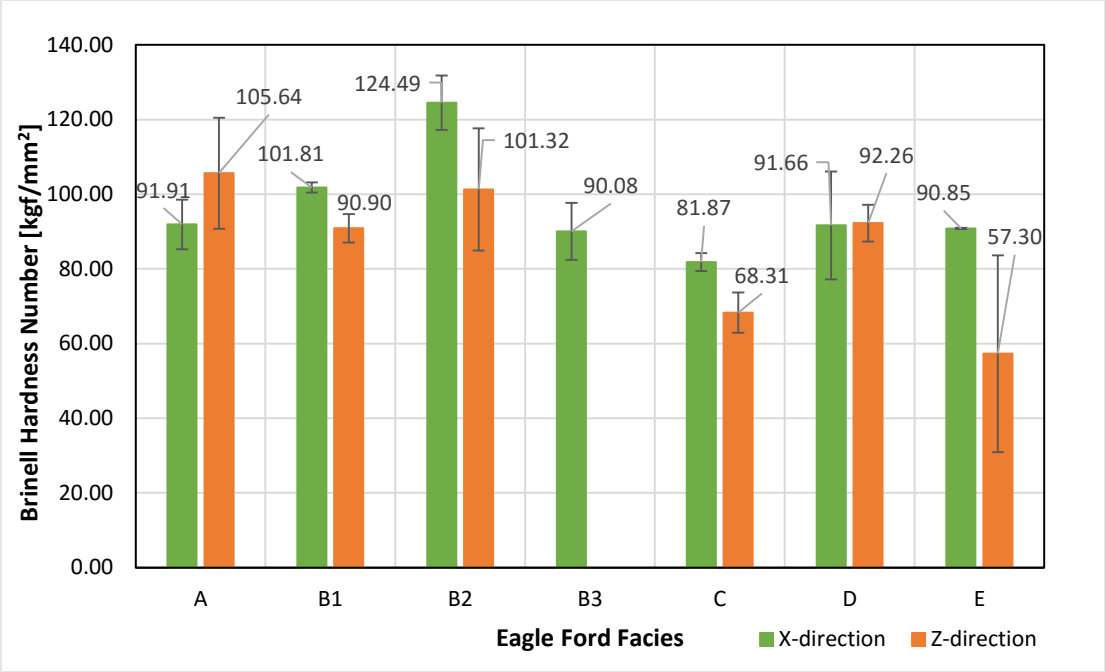

Figure 75: Comparison of Brinell hardness number across the Eagle Ford facies

Facies A and facies C are the only facies with a higher Brinell hardness number for the perpendicular orientation. A possible explanation is that the perpendicular sample's rock surface was tested on a "stiff" layer with hard minerals present such as quartz. The lower Eagle Ford facies A through B3 have the highest Brinell hardness number range. Even though facies B1 had a minimal difference between the two orientations, but there could be a possible effect on fracture conductivity. Furthermore, the standard deviation reported for facies B1 is marginal suggesting that the samples were reasonably homogeneous in mineral composition on the rock surface of the samples tested. Facies C reported are the lowest Brinell hardness number throughout the zones suggesting the mineral composition is a factor. Additionally, the low Brinell hardness values of facies C could be a factor in the measured conductivity results. The

perpendicular samples of Facies D had a slightly higher average of Brinell hardness number than facies E. In fact, the difference in Brinell hardness is only 0.6. However, the standard deviation of the parallel samples is quite large indicating that within the x-direction samples suggesting a large heterogeneity in composition on the surface tested. The small difference between the Brinell hardness values makes it difficult to attribute any effect it has on fracture conductivity. Lastly, Facies E had the largest ratio of parallel to perpendicular Brinell hardness number suggesting the orientation of a sample is dominating factor. However, the standard deviation of the parallel samples is significantly large signifying that there was heterogeneity of mineralogical composition within the surface tested. This large deviation between the two orientations within facies E implies an influence in fracture conductivity.

Figure 76 presents the average mineral composition across the Eagle Ford facies.

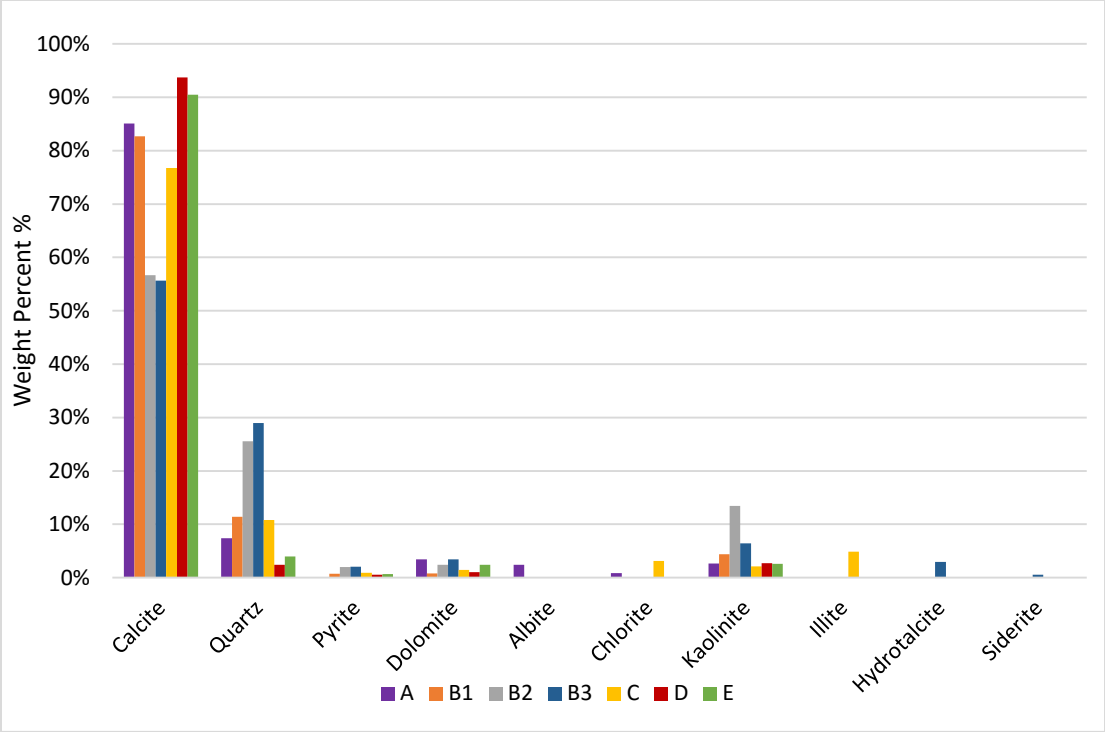

Figure 76: Average mineral composition

A large variation of mineralogical composition across the Eagle Ford facies can be observed. With the exception of facies B2 and B3, calcite content was significantly high in all facies. Facies B1 had more quartz present suggesting that the quartz content is contributing to higher Young's modulus and Brinell hardness values compared to facies A. Furthermore, facies B3 had the largest quartz composition, 29%. Yet, when compared to similar facies A, B1 and B2, facies B2 had higher Young's modulus values suggesting that another mineral is influencing the elastic properties and Brinell hardness of facies B3. Furthermore, the Brinell hardness numbers stated for facies B2 was the largest when compared to the other facies suggesting that the quartz was a dominating mineral in Brinell hardness testing. Facies C had less calcite content compared to facies A and

facies B1, but not as low as facies B2 and B3. Additionally, the quartz content detected is similar to facies B1 samples. Facies C had the three types of clay: kaolinite, chlorite, and illite, detected with an overall clay content of 10%. Due to clay being a soft mineral, this could be the influencing factor of both the low Young's modulus and the Brinell hardness number values described for this facies. Facies D had the highest calcite content, 94%, and the lowest amount of quartz, 2%, detected compared to all the facies tested. The mineralogical composition of facies D was the most similar to facies E. Both facies D and facies E had the highest Young's modulus values and the highest calcite amount present suggesting that the calcite content is the dominating factor. The Brinell hardness numbers are relatively low for facies D and E when compared to facies B2 implying the quartz content contributes to the Brinell hardness numbers. Lastly, Facies E has slightly more quartz, a hard mineral, compared to facies D. This could possibly explain why the young's modulus values are higher than facies D. However, it should be noted that the mineral compositions obtained may have some source of error due to sample preparation, mesh sized used, or even human error.

3.9 Effect of Rock of Properties on Fracture Conductivity

Fracture conductivity experiments were performed on each facies, with the exception of B2 and B3. Each facies was tested for unpropped conductivity, conductivity with $0.1 lb_m/ft^2$ 30/50 Mesh white sand, and with $0.1 lb_m/ft^2$ 100 Mesh white sand. In order to fully explore the relationship between the rock properties and fracture conductivity, experimental parameters were keep constant. This section only explores the relationship between unpropped fracture conductivity and the rock's properties. A

better correlation can be determined as proppant is not influencing the fracture conductivity. The analysis of unpropped conductivity was first evaluated with facies A through facies C separate from facies D and facies E. This is due to both facies D and facies E behaving very similarly mechanically and its mineralogical composition. As well as, both facies D and E are considered as a separate sequence in the Eagle Ford formation, compared to facies A, B, and C, that is continued up into the Austin Chalk (Donovan et al., 2012). Figure 77 shows a comparison of facies A, facies B1, and facies C.

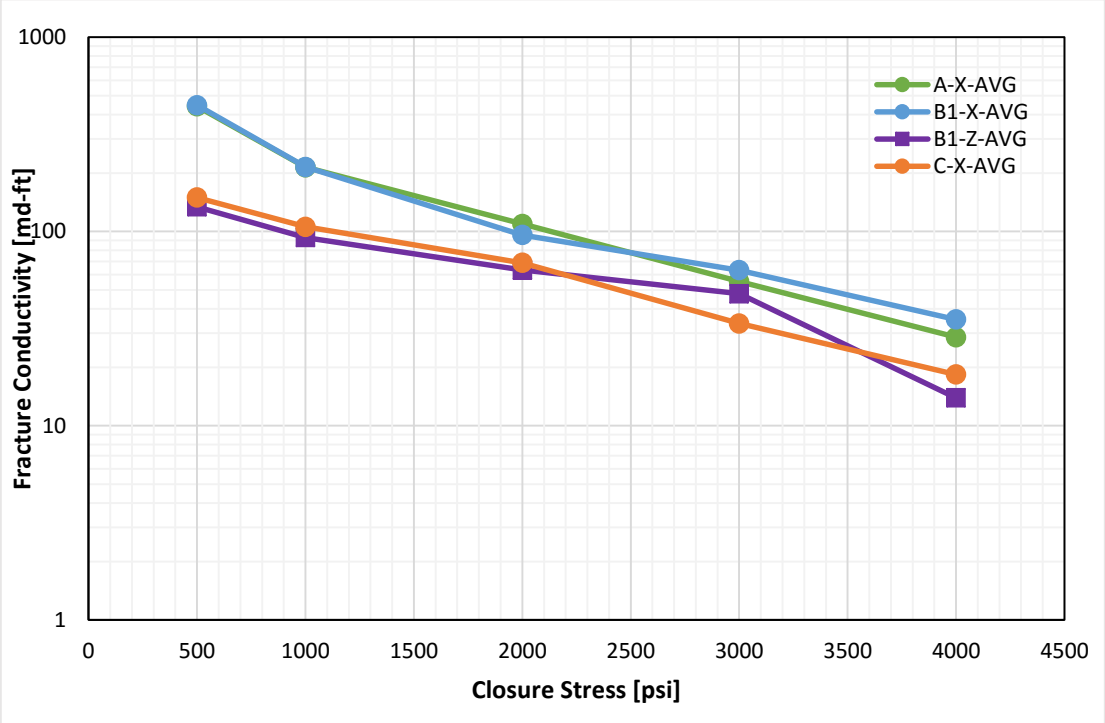

Figure 77: Comparison of unpropped conductivity for facies A, B1, and C

Both facies A and B1-X have the highest fracture conductivity. Interestingly, the x-direction (parallel) also has higher conductivity than the z-direction (perpendicular) orientation in facies B1. The rock properties can explain the unpropped fracture conductivity behavior seen above. Both facies A and facies B1-X have higher Young's modulus compared to facies B1-Z and C. A higher Young's modulus can maintain a wider fracture width for fluid to flow through. Although facies B1-X has a higher Poisson's ratio than B1-Z, the range of Poisson's ratios for facies A through facies C is too tight to determine if this could be a contributing factor of the conductivity behavior. Additionally, facies B1-X has a higher Brinell hardness number compared to its counterpart facies B1-Z. A higher Brinell hardness number translates into a harder rock surface with greater resistance to deformation at an applied load. Although facies C follows the curve of facies B1-Z, it seems to have a steeper decline. The Young's modulus for Facies C was only slightly higher than facies B1-Z. It would appear that another mechanical property was contributing to this unpropped conductivity. In fact, facies C had the lowest Brinell hardness number, meaning the lowest resistance to deformation as stress was applied. As the load increases, the surface deformation may lead to fines migrations reducing the fracture conductivity. Additionally, Table 19 displays the summarized surface roughness of unpropped conductivity. Both facies A and facies B1-Z have higher average RMS error meaning that a rougher fracture surface may have contributed to higher unpropped conductivity compared to facies B1-Z and facies C. It is clear that the rock's properties of facies A, B1, and C play a role in

unpropped fracture conductivity. However, it is not possible to determine the main driver in the influence of unpropped conductivity for these facies.

Table 19: Summary of unpropped surface roughness for facies A, B1, and C

	Average RMS Error [in]
Unpropped A-X Average	0.223
Unpropped B1-X Average	0.230
Unpropped B1-Z Average	0.167
Unpropped C-X Average	0.165

The analysis of unpropped conductivity of facies D and facies E was first completed separately from facies A through facies C. Figure 78 shows a comparison of facies D and E.

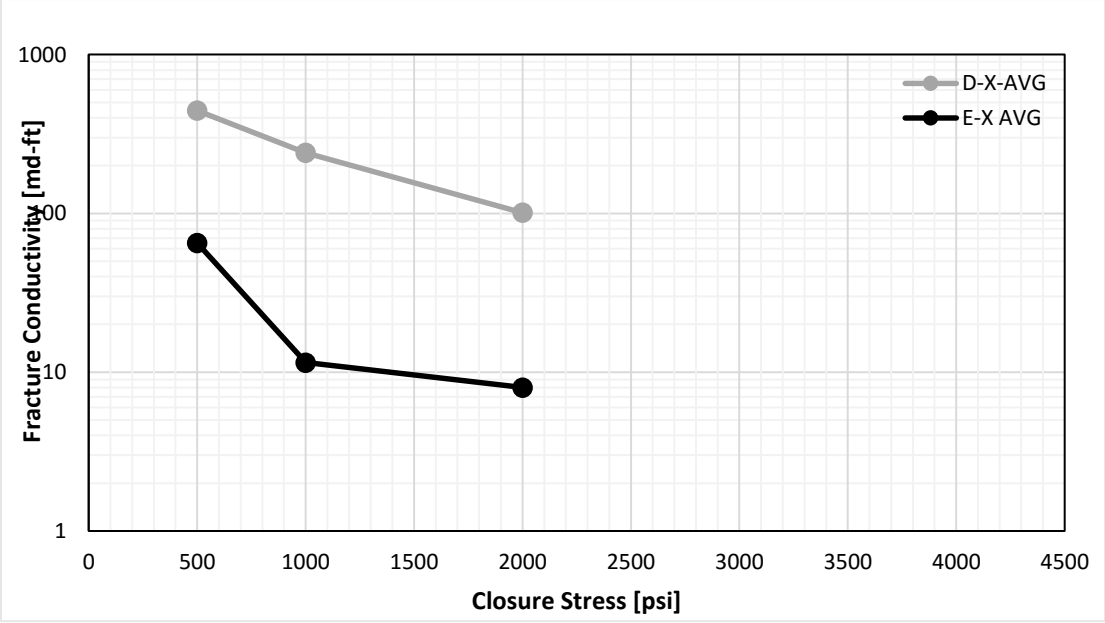

Figure 78: Comparison of unpropped conductivity for facies D and E

As seen in Figure 78, facies D has higher conductivity than facies E. In fact, unpropped fracture conductivity of facies E is an order of magnitude less. The rock properties of these two facies may explain this behavior. Interestingly, facies E reported a higher Young's modulus than facies D. Typically, a higher Young's modulus would produce higher fracture conductivity. Consequently, the Young's modulus must not be contributing to these fracture conductivities or at least another rock property is dominating over it. Additionally, the Poisson's ratio of facies E is higher than facies D. A higher Poisson's ratio may produce microcracks within a rock sample as stress increases. Yet, facies E still has lower unpropped fracture conductivity. As a result, Poisson's ratio seems to not be contributing to these fracture conductivities. Moreover, the Brinell hardness numbers reported for both facies are nearly identical with facies D only marginally higher. As a result, the two facies have comparable resistance in surface deformation. Due to this negligible difference, it is difficult to clearly attribute the higher unpropped conductivity of Facies D to its Brinell hardness number.

Table 20 displays the summarized surface roughness of unpropped conductivity. Analysis of the surface roughness of facies D and E reveals that the fracture surface of facies D has a higher surface roughness. It appears that this surface roughness of facies D is contributing to a higher unpropped fracture conductivity. However, it is not possible to completely establish that the surface roughness is the only dominating force in these fracture conductivities of these two facies.

Table 20: Summary of unpropped surface roughness for facies D and E

	Average RMS Error [in]
Unpropped D-X Average	0.260
Unpropped E-X Average	0.190

Figure 79 shows the average unpropped fracture conductivity for all facies.

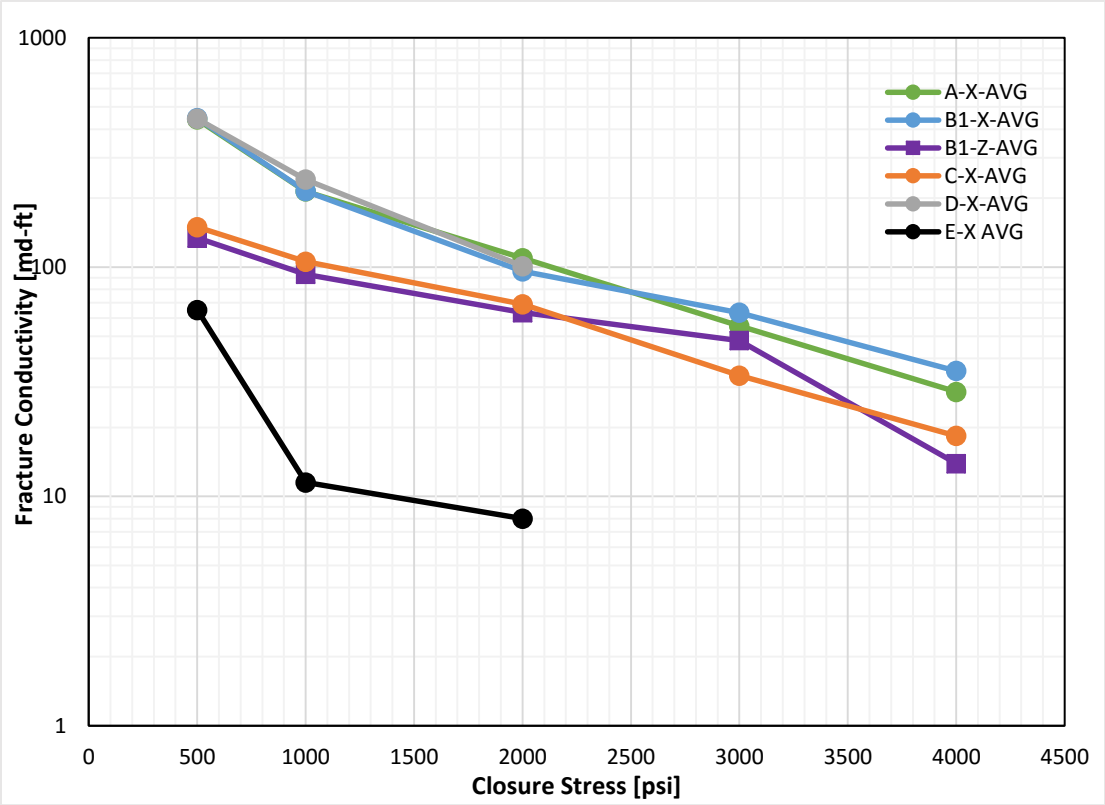

Figure 79: Average unpropped conductivity of each facies

There are three distinct groups seen within the unpropped conductivities of all the facies. Facies D, facies A, and facies B1-X have the highest unpropped conductivity

and could be categorized as group 1. Facies B1-Z and facies C are the second set of unpropped conductivities grouped together. The data points at 500 psi for both facies B1-Z and facies C start at 150 md-ft, roughly three times less than the first group. The last group, facies E, has the lowest conductivity and is one order of magnitude lower than group one. When analyzing the unpropped fracture conductivities across all the facies, the convention of a higher Young's modulus translating into a higher fracture conductivity does not apply. Facies E has the highest Young's modulus, but the lowest fracture conductivity. Young's modulus cannot be a determining factor in the unpropped fracture conductivities when analyzing across all facies. Moreover, the range of Poisson's ratios between the zones is too tight to determine if this could be a contributing factor of the conductivity behavior. The Brinell hardness numbers reported for each facies is also narrow in range to conclude that it is a dominating factor in the unpropped fracture conductivities. The last assessed parameter is surface roughness of the fracture surface. Table 21 shows a comprehensive overview of the average surface roughness of each facies. Interestingly, the three facies with the highest unpropped conductivity have the highest surface roughness. While, facies C, facies B1-Z, and facies E had the lowest average surface roughness. The surface roughness appears to be parameter affecting the fracture conductivity. However the average surface roughness of facies E is not the lowest, yet facies E has the lowest unpropped conductivity. Another controlling factor must be contributing to the low conductivity of facies E. Ultimately, the analysis of unpropped fracture conductivity across all facies did not produce a main

influencer of the rock's properties highlighted in this study. It is possible that another factor not featured in this work is affecting the conductivity.

Table 21: Summary of unpropped surface roughness of each facies

	Average RMS Error [in]
Unpropped A-X Average	0.223
Unpropped B1-X Average	0.230
Unpropped B1-Z Average	0.167
Unpropped C-X Average	0.165
Unpropped D-X Average	0.260
Unpropped E-X Average	0.190

3.10 Effect of Rock Properties on Unpropped Fracture Conductivity Loss

An increase in closure stress relates to a loss in fracture conductivity. In the previous section 3.9, the relationship between the mechanical properties and unpropped fracture conductivity was investigated. The effect of closure stress in each facies and its relationship with the mechanical properties is examined in this section. Jansen (2014) proposed the following correlation to illustrate how conductivity behaves at different closure stresses:

$$k_f w_f \cong \left(k_f w_f\right)_0 e^{-\lambda \sigma_c} \tag{3.1}$$

$\left(k_f w_f\right)_0$ is the initial conductivity value at a closure stress of 0 psi, λ is the conductivity decline rate constant, and σ_c is the closure stress (psi). Figure 80 shows the average unpropped fracture conductivity of facies A, B1, and C.

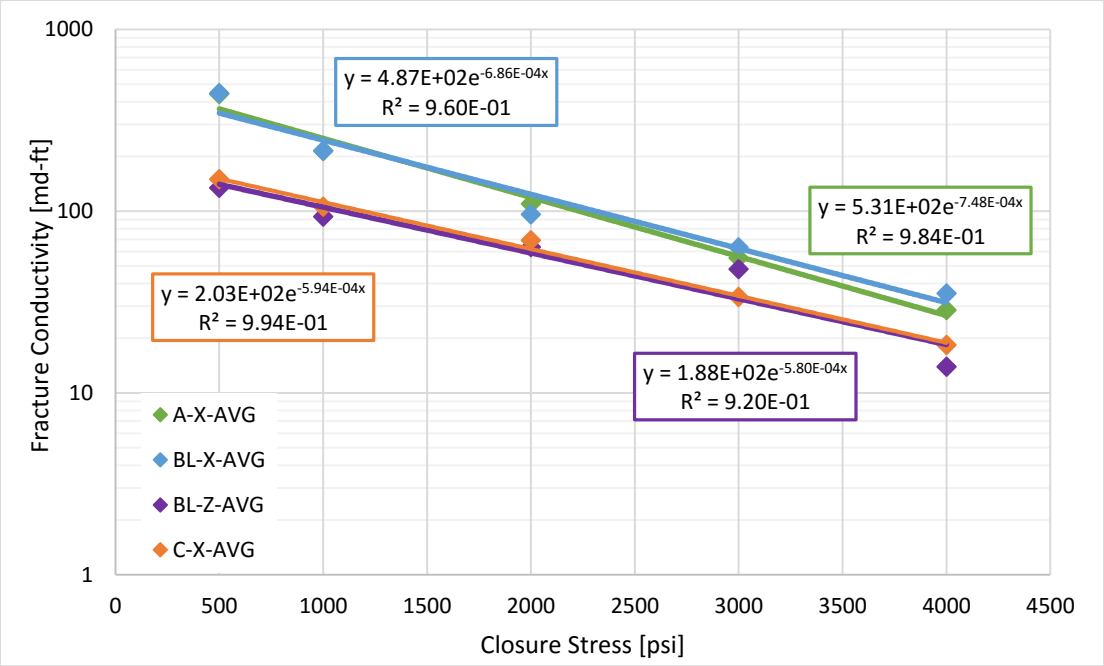

Figure 80: Average unpropped conductivity with the exponential fit for facies A, B1, and C

The exponential trend lines for facies A, B1, and C fit well with the unpropped fracture conductivity curves. Table 22 displays the unpropped decline rate constants for facies A, B1, and C for X orientation.

Table 22: Unpropped decline rate constants for facies A-X, B1-X, B1-Z and C-X

Sample	Unpropped Decline Rate Constant [1/psi]
Facies A-X	7.48×10^{-4}
Facies B1-X	6.86×10^{-4}
Facies B1-Z	5.80×10^{-4}
Facies C-X	5.94×10^{-4}

The expectation is that a lower decline rate constant would correlate with a higher Young's modulus. However facies B1-Z has the lowest decline curve constant and the lowest Young's modulus. Furthermore, facies C has the second lowest decline rate constant and a lower Young's modulus compared to facies A and B1. Facies A and B1-X had the fastest decline rate constants and the highest Young's moduli. A possible explanation is that the range of Young's moduli, 0.70 Mpsi, with these facies is quite small making it difficult to distinctly correlate with the expectation. Furthermore with the close range in Young's moduli, the differences between the decline curve constants is quite small as well. Another factor, besides Young's modulus, must be the main influencer on the decline rate and fracture conductivity. A look at the Brinell hardness numbers with each facies does not offer much insight into the unpropped decline rate. Facies B1-X has the highest Brinell hardness number, but also one of the fastest decline rates. While facies C has the lowest Brinell hardness number, facies B1-Z has the slowest decline rate. It is not possible to see how much influence Brinell hardness has with the unpropped fracture conductivity decline rate, if any. Surface roughness may be affecting the decline rates of these facies instead. Both facies B1-Z and facies C have lower surface roughness compared to facies B1-X and A. This correlation implies that higher surface roughness adversely affects fracture conductivity as closure stress increases. Both facies A and B1-X had the fastest decline rate and the highest surface asperities. Facies B1-Z has the lowest rate of decline with a lower surface roughness, but not the lowest roughness. It is difficult to completely quantify the full influence of the surface roughness with facies B1-Z in the analysis. The orientation of the bedding plane

for the Z-direction would be expected to behave differently for fracture conductivity than in the X-direction. While the X-direction has the fluid flowing through several bedding planes, the Z-direction orientation theoretically has a single bedding plane that fluid flows through. The bedding plane of which the fracture is generated for Z-direction could be a soft or stiff layer within the shale. As a result, the conductivity results could be drastically different within Z-bedding plane orientation samples from the same facies due to the mechanical properties associated with the soft and stiff minerals. Furthermore, there were only a handful of samples measured for conductivity in the Z-direction and within only one facies. Further conductivity experiments would need to be run in all facies for the Z-direction to further validate any Z bedding plane orientation conclusions to be found.

After omitting B1-Z decline rates, a trend is seen with facies A-X, B1-X, and C with conductivity decline rates and surface roughness. Facies C has a lower surface roughness compared to facies B1-X and A-X. While facies A has the fastest decline with a high surface roughness, facies B1-X has the highest surface roughness. This correlation implies that higher surface roughness adversely affects fracture conductivity as closure stress increases. A possible reasoning that could explain this discrepancy is that surface roughness measurements are taken prior to the conductivity experiments performed. Facies A had distinct bedding planes seen within conductivity samples (Figure 81). These bedding planes seen within these samples created weak points while closure stress was applied. Fractured pieces from the surface were found after conductivity experiments concluded. It is possible that these fractured pieces contributed

to a faster decline than seen with facies B1-X creating pinch points. Additionally, the fractured surface after the experiment would have a higher surface roughness than initial values. The larger the surface asperities or higher the surface roughness contributes to a faster unpropped decline rate, seen in Table 23. It should also be mentioned that the number of unpropped fracture conductivity experiments performed for each facies was small. More fracture conductivity experiments would be needed for a better representation.

Figure 81: Fracture surface of facies A parallel conductivity sample (Tenorio, 2016)

Table 23: Unpropped decline rate constants and surface roughness for facies A-X, B1-X, and C-X overview

Sample	Unpropped Decline Rate Constant [1/psi]	Average RMS Error [in]
Facies A-X	7.48×10^{-4}	0.223
Facies B1-X	6.86×10^{-4}	0.230
Facies C-X	5.94×10^{-4}	0.165

Figure 82 show the average unpropped fracture conductivity of facies D and E.

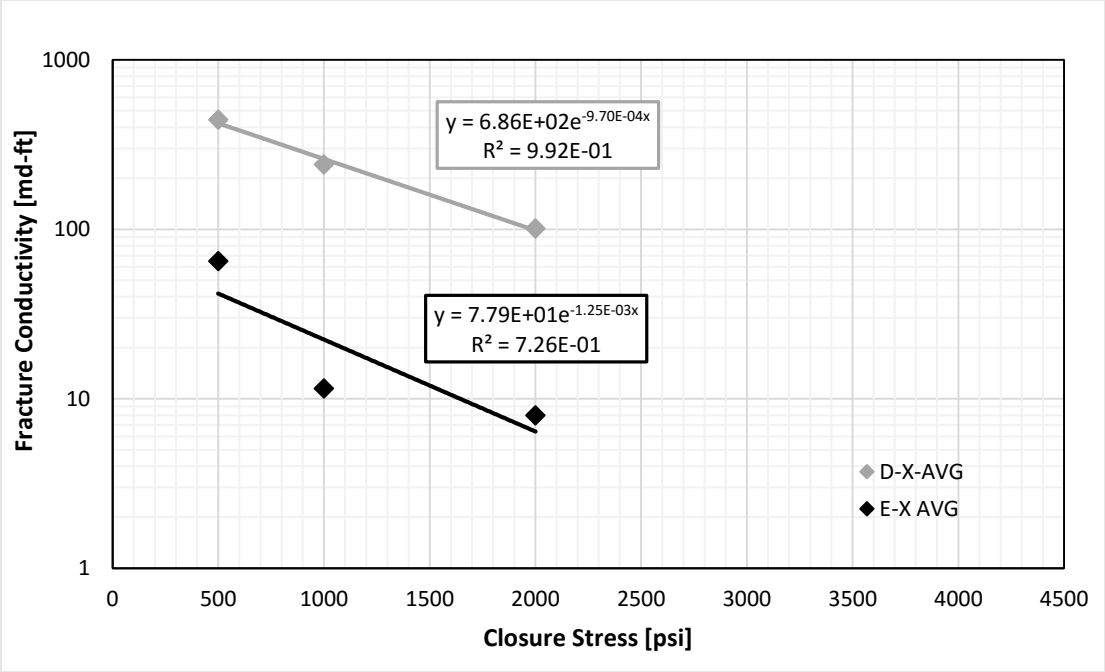

Figure 82: Average unpropped conductivity with the exponential fit for facies D and E

The exponential trend line for facies D fits well with the unpropped fracture conductivity curves, but facies E has a loose correlation for a trend line. Both facies have only three data points. To obtain a more accurate fit, more data points would be needed. Table 24 displays the unpropped decline rate constants for facies D and E.

Table 24: Unpropped decline rate constants for facies D and E

Sample	Unpropped Decline Rate Constant [1/psi]
Facies D-X	9.70×10^{-4}
Facies E-X	1.25×10^{-3}

Again, the expectation is that a lower decline rate constant would correlate with a higher Young's modulus. Facies D has the lower decline curve constant and the lower Young's modulus. While Facies E has the highest Young's modulus and the highest decline curve constant overall. These findings would suggest that another factor, besides Young's modulus, may be the main influencer on the decline rate and fracture conductivity. Surface roughness may be affecting the decline rates of these two facies instead. Possibly due to the difference in rock properties and a different depositional sequence of facies D and E compared to the other facies, a different correlation was found with surface roughness. Analysis of the surface roughness of facies D and E reveals that the fracture surface of facies D has a higher surface roughness. Yet, facies D has a slower decline rate compared to facies E implying that larger surface asperities decreases the rate of decline. This correlation regarding surface roughness is very loose though. The number of data points for the unpropped fracture conductivity minimal causing it to be difficult to have an accurate assessment of the unpropped decline constant and its driving factor. Table 25 displays an overview of decline rate with surface roughness for facies D and E. Moreover, the Brinell hardness numbers reported for both facies are nearly identical with facies D only marginally higher. As a result, the two facies have comparable resistance in surface deformation, but extremely different in decline rates. Due to this slight difference, it is difficult to clearly attribute the faster decline rate of facies E with Brinell hardness. Furthermore more experimental conductivity runs should be completed to acquire a larger data set, as only three samples from each facies was tested for unpropped.

Table 25: Unpropped decline rate constants and surface roughness for facies D and E overview

Sample	Unpropped Decline Rate Constant [1/psi]	Average RMS Error [in]
Facies D-X	$9.70x10^{-4}$	0.260
Facies E-X	$1.25x10^{-3}$	0.190

3.11 Effect of Rock Properties on Propped Fracture Conductivity Loss

The type of proppant type used, concentration used, and its characteristics, such as strength, are known factors that affect the propped fracture conductivity. Two types of proppant were used for experimental fracture conductivities measurements for all facies. Samples were first tested with $0.1lb_m/ft^2$ 100 Mesh white sand proppant and remaining quality samples were retested for fracture conductivity with $0.1lb_m/ft^2$ 30/50 Mesh white sand proppant. Proppant concentrations used were approximately monolayer on the fracture surface removing proppant pack effects of the conductivity. The largest factor in loss of fracture conductivity is proppant embedment as the closure stress increases. Proppant embedment causes a decrease in fracture width resulting in a loss in fracture conductivity.

3.11.1 100 Mesh Proppant

Figure 83 shows the average $0.1lb_m/ft^2$ 100 mesh propped conductivity with the exponential fit for facies A, B1, and C. It should be noted that the in order to obtain the best exponential fit the maximum closure stress was 5000 psi.

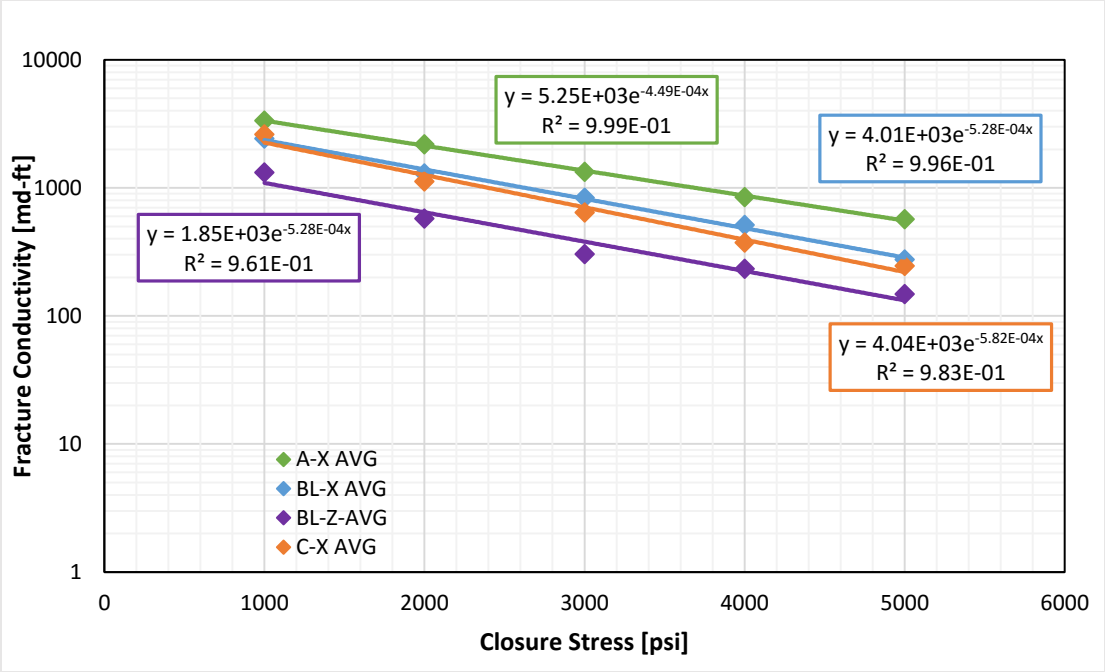

Figure 83: Average 0.1lb$_m$/ft^2 100 mesh propped conductivity with the exponential fit for facies A, B1, and C

The exponential trend lines for facies A, B1, and C fit extremely well for 100 mesh propped fracture conductivity curves. Table 26 displays the 100 mesh propped decline rate constants for facies A, B1, and C.

Table 26: 0.1lb$_m$/ft^2 100 mesh propped decline rate constants for facies A, B1, and C

Sample	0.1lb$_m$/ft^2 100 mesh propped Decline Rate Constant [1/psi]
Facies A-X	4.49×10^{-4}
Facies B1-X	5.28×10^{-4}
Facies B1-Z	5.28×10^{-4}
Facies C-X	5.82×10^{-4}

Again, the expectation is that a lower decline rate constant would correlate with a higher Young's modulus. Facies A has the slowest decline rate and one of the highest Young's modulus. However, facies B1 in both directions has the same rate of decline regardless of B1-X having the largest Young's modulus of the three facies examined here. The fastest decline rate is seen with facies C, yet this facies does not have the lowest Young's modulus. The Young's moduli range is quite tight between the facies though. This could be affecting from seeing a clear trend between Young's moduli and decline rate. Plus, another factor, besides Young's modulus, may be acting as a driving force on the decline rate. As mentioned previously, the largest factor contributing to loss of conductivity when proppant is used is proppant embedment. The best indication of how the rock surface interacts with proppant is the Brinell hardness number. Facies C has the lowest Brinell hardness number of these facies. A low hardness number indicates a softer rock surface. It would seem that facies C would be the most affected by proppant embedment possibly contributing to the fastest decline rate. Facies B1-X has a higher Brinell hardness compared to B1-Z, but not by much. Furthermore, facies A had a very similar hardness number to facies B1-Z. All three have hardness values above 90, suggesting that the embedment behaves very similarly on the surface of these three facies when above 90. Although facies A has the slowest decline rate, the difference in decline rates between A and B1 is $7.9x10^{-5}$, which is quite small. Additionally, the surface roughness must be examined as a possible factor affecting these decline rates. Table 27 shows the average surface roughness for 100 mesh proppant. Facies A has the highest surface roughness and the slowest decline rate. Yet both facies B1-Z and C have

the same average surface roughness, but facies C has the fastest decline. Based on these observations, the surface roughness may be playing a role in the decline rate.

Table 27: Summary of $0.1 lb_m/ft^2$ 100 mesh propped surface roughness for facies A, B1, and C

	Average RMS Error [in]
A-X Average	0.243
B1-X Average	0. 197
B1-Z Average	0.180
C-X Average	0.175

Again, it is difficult to completely quantify the full influence of the surface roughness with facies B1-Z in the analysis. The orientation of the bedding plane for the Z-direction would be expected to behave differently for fracture conductivity than in the X-direction. While the X-direction has the fluid flowing through several bedding planes, the Z-direction orientation theoretically has a single bedding plane that fluid flows through. The bedding plane of which the fracture is generated for Z-direction could be a soft or stiff layer within the shale. As a result, the conductivity results could be drastically different within Z-bedding plane orientation samples from the same facies due to the mechanical properties associated with the soft and stiff minerals. Furthermore, there were only a handful of samples measured for conductivity in the Z-direction and within only one facies. Further conductivity experiments would need to be run in all facies for the Z-direction to further validate any Z bedding plane orientation conclusions to be found.

After omitting B1-Z decline rates, a trend is seen with facies A-X, B1-X, and C with conductivity decline rates and surface roughness. Facies C has a lower surface roughness compared to facies B1-X and A-X and the fastest decline in conductivity. While facies A has the slowest decline with the highest surface roughness. Facies B1-X also follows this trend. This correlation implies that higher surface roughness associated with proppant has a slower rate of conductivity decline as closure stress increases, seen in Table 28.

Table 28: 0.1lb$_m$/ft^2 100 mesh propped decline rate constants and surface roughness for facies A-X, B1-X, and C-X overview

Sample	Unpropped Decline Rate Constant [1/psi]	Average RMS Error [in]
Facies A-X	$4.49x10^{-4}$	0.243
Facies B1-X	$5.28x10^{-4}$	0.197
Facies C-X	$5.82x10^{-4}$	0.175

Figure 84 shows the average 0.1lb$_m$/ft^2 100 mesh propped conductivity with the exponential fit for facies D and E. It should be noted that the in order to obtain the best exponential fit the maximum closure stress was 5000 psi, similar to facies A-C.

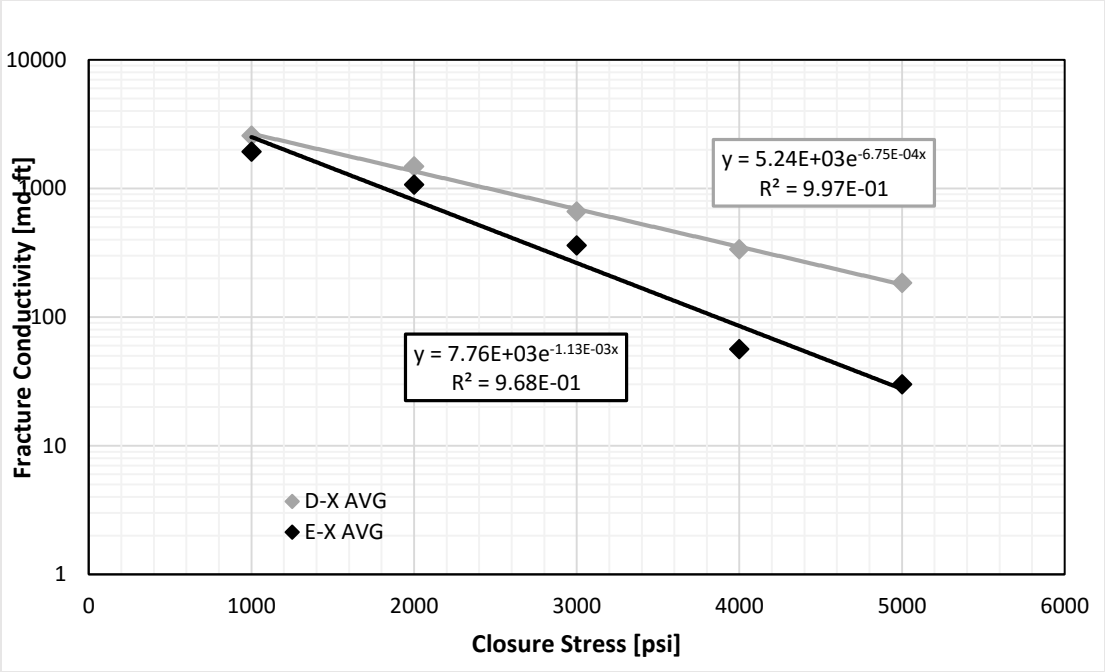

Figure 84: Average 0.1lb$_m$/ft^2 100 mesh propped conductivity with the exponential fit for facies D and E

The exponential trend lines for facies D and E fit very well for 100 mesh propped fracture conductivity curves. Table 29 displays the 100 mesh propped decline rate constants for facies D and E.

Table 29: 0.1lb$_m$/ft^2 100 mesh propped decline rate constants for facies D and E

Sample	0.1lb$_m$/ft^2 100 Mesh Decline Rate Constant [1/psi]
Facies D-X	9.70×10^{-4}
Facies E-X	1.25×10^{-3}

As stated earlier, typically a higher Young's modulus would produce a slower rate of decline. However, facies E has the highest Young's modulus amongst all facies tested and the fastest decline rate between facies D and E. Facies D has a slower decline rate and a lower Young's modulus. It is clear that another factor must be influencing the decline rate since facies D and E do not follow the conventional wisdom. Brinell hardness exhibits a good indication of how the rock behaves with proppant embedment. Facies D had a slightly higher Brinell hardness number than facies E. A higher Brinell number signifies that proppant embedment is less likely to transpire as the rock surface is harder leading to more resistance in deformation. Yet with a difference of less than one between the two facies, it is not possible to definitively define Brinell hardness as a leading factor in the decline rates. An analysis of the surface roughness of the two facies may lead to a possible driving factor of decline rate. Table 30 shows the average surface roughness for 100 mesh proppant. Facies D had a higher average surface roughness compared to facies E suggesting that the rougher surface leads to a slower decline. A similar trend was found in the 100 mesh proppant analysis of facies A-C. The surface roughness may be playing a role in the decline rate associated with proppant embedment, yet the exact amount of impact is not possible to calculate. Likewise to facies A, B1, and C, both facies D and E samples tested with 100 mesh were reused from unpropped fracture conductivity experiments. The end results may have been affected due to this.

Table 30: Summary of 0.1lb$_m$/ft^2 100 mesh propped surface roughness for facies D and E

	Average RMS Error [in]
D-X Average	0.270
E-X Average	0.203

3.11.2 30/50 Mesh Proppant

Figure 85 shows the average 0.1lb$_m$/ft^2 30/50 mesh propped conductivity with the exponential fit for facies A, B1, and C. It should be noted that the in order to obtain the best exponential fit the maximum closure stress was 5000 psi.

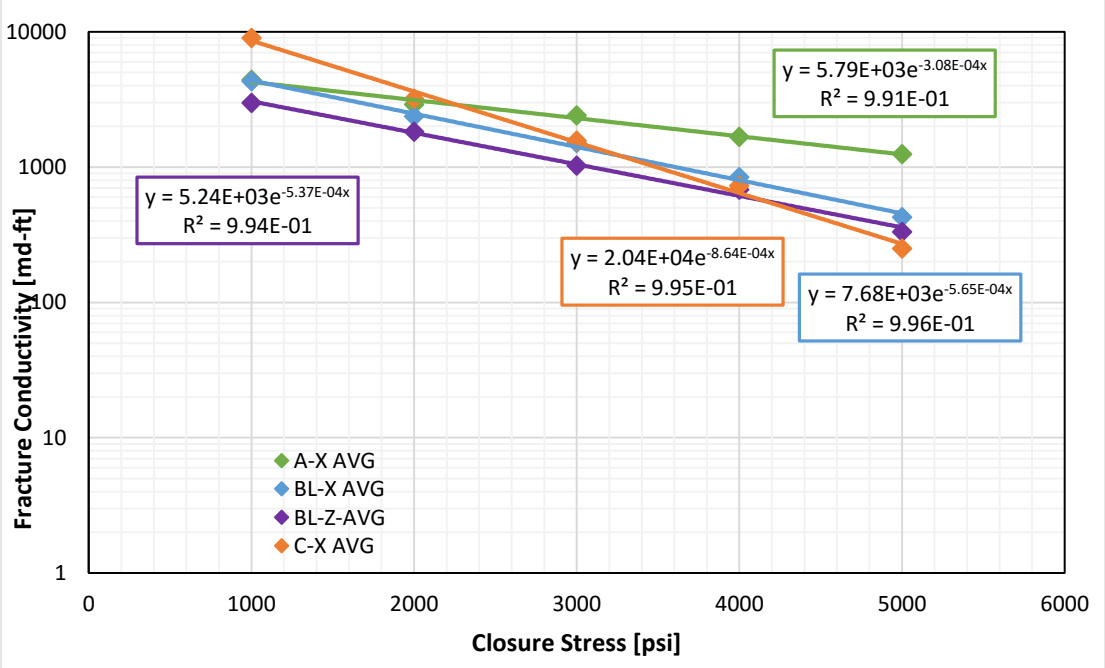

Figure 85: Average 0.1lb$_m$/ft^2 30/50 mesh propped conductivity with the exponential fit for facies A, B1, and C

The exponential trend lines for facies A, B1, and C fit really well for 30/50 mesh propped fracture conductivity curves. Table 31 displays the 30/50 mesh propped decline rate constants for facies A, B1, and C.

Table 31: 0.1lb$_m$/ft^2 30/50 mesh propped decline rate constants for facies A, B1, and C

Sample	Unpropped Decline Rate Constant [1/psi]
Facies A-X	3.08×10^{-4}
Facies B1-X	5.65×10^{-4}
Facies B1-Z	5.37×10^{-4}
Facies C-X	8.64×10^{-4}

Similarly to 100 mesh, facies A has the slowest decline rate and one of the highest Young's modulus. Again, facies C has the fastest decline compared to the other two facies. Typically, a lower decline rate constant would correlate with a higher Young's modulus. While facies A has one of the higher Young's modulus values, it does not have the highest value between the facies. Furthermore, facies C also has one of the lower Young's modulus, but not the absolute lowest value. When analyzing the decline rates between the two orientations of facies B1, the higher Young's modulus (B1-X) has a faster decline rate. Based on these observations, it appears Young's modulus is once again not the driving force for the decline rates for 30/50 mesh proppant. An evaluation of the Brinell hardness number should be taken into effect as well. Facies C has the lowest Brinell hardness number of these facies indicating a softer rock surface. It would

seem that facies C would be the most affected by proppant embedment possibly contributing to the fastest decline rate. Facies B1-X had a higher Brinell hardness compared to B1-Z, but not by much. Furthermore, facies A had a very similar hardness number to facies B1-Z, yet a much slower decline rate. With the exception of facies C, a clear trend of decline rate and Brinell hardness is established. Analyzing the surface roughness may be a possible factor affecting these decline rates. Table 32 shows the average surface roughness for 30/50 mesh proppant. Once again, facies A has the highest surface roughness and the slowest decline rate. Facies C has the lowest surface roughness and the fastest decline rate. A higher surface roughness suggests a slower decline rate. Yet, closer analysis of facies B1 has slightly different results. The rate of decline for B1-X is slightly higher than B1-Z by $2.7x10^{-5}$.

Table 32: Summary of $0.1lb_m/ft^2$ 30/50 mesh propped surface roughness for facies A, B1, and C

	Average RMS Error [in]
A-X Average	0.230
B1-X Average	0.212
B1-Z Average	0.200
C-X Average	0.175

Again, it is difficult to completely quantify the full influence of the surface roughness with facies B1-Z in the analysis. The orientation of the bedding plane for the Z-direction would be expected to behave differently for fracture conductivity than in the X-direction. While the X-direction has the fluid flowing through several bedding planes,

the Z-direction orientation theoretically has a single bedding plane that fluid flows through. The bedding plane of which the fracture is generated for Z-direction could be a soft or stiff layer within the shale. As a result, the conductivity results could be drastically different within Z-bedding plane orientation samples from the same facies due to the mechanical properties associated with the soft and stiff minerals. Furthermore, there were only a handful of samples measured for conductivity in the Z-direction and within only one facies. Further conductivity experiments would need to be run in all facies for the Z-direction to further validate any Z bedding plane orientation conclusions to be found.

After omitting B1-Z decline rates, a trend is seen with facies A-X, B1-X, and C with conductivity decline rates and surface roughness. Facies C has a lower surface roughness compared to facies B1-X and A-X and the fastest decline in conductivity. While facies A has the slowest decline with the highest surface roughness. Facies B1-X also follows this trend. This correlation implies that higher surface roughness associated with proppant has a slower rate of conductivity decline as closure stress increases, seen in Table 33. A similar conclusion was found for facies A-X, B1-X and C-X with 100 mesh proppant. Furthermore, it should be noted that conductivity experiments for 30/50 mesh were performed on samples that had already been tested for unpropped and 100 mesh proppant. As a result, some proppant embedment effects from 100 mesh testing. Additionally, less samples were available for testing with this type of proppant.

Table 33: 0.1lb$_m$/ft^2 30/50 mesh propped decline rate constants and surface roughness for facies A-X, B1-X, and C-X overview

Sample	0.1lb$_m$/ft^2 30/50 mesh propped Decline Rate Constant [1/psi]	Average RMS Error [in]
Facies A-X	$3.08x10^{-4}$	0.230
Facies B1-X	$5.65x10^{-4}$	0.212
Facies C-X	$8.64x10^{-4}$	0.175

Figure 86 shows the average 0.1lb$_m$/ft^2 30/50 mesh propped conductivity with the exponential fit for facies D and E. It should be noted that the in order to obtain the best exponential fit the maximum closure stress was 5000 psi, similar to facies A-C.

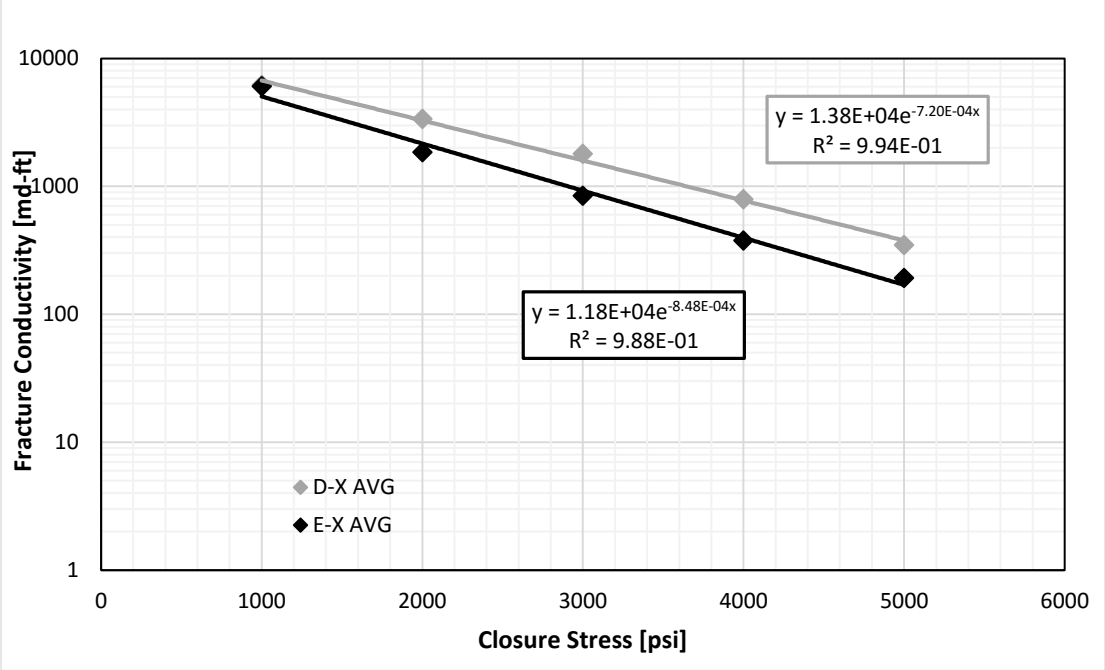

Figure 86: Average 0.1lb$_m$/ft^2 30/50 mesh propped conductivity with the exponential fit for facies D and E

The exponential trend lines for facies D and E fit actually well for 30/50 mesh propped fracture conductivity curves. Table 34 displays the 30/50 mesh propped decline rate constants for facies D and E.

Table 34: 0.1lb$_m$/ft^2 30/50 mesh propped decline rate constants for facies D and E

Sample	Unpropped Decline Rate Constant [1/psi]
Facies D-X	7.20×10^{-4}
Facies E-X	8.48×10^{-4}

Similarly to 100 mesh, facies D had the slower decline rate and a lower Young's modulus compared to facies E. The conventional understanding is that the higher Young's modulus would have a slower decline rate. Yet with 30/50 mesh proppant as well 100 mesh, facies D and E defy that logic. A clear notion that the Young's modulus for these two facies is not a dominating factor, if any factor, in the decline rates. An assessment of the Brinell hardness numbers may offer potential insight into the decline rates seen with facies D and E. Facies D had a slightly higher Brinell hardness number than facies E, by 0.81. A higher Brinell number signifies that proppant embedment is less likely to occur as the rock surface is harder leading to more resistance in deformation. Yet this minimal difference between the two facies does not allow Brinell hardness to be a definitive leading factor in the decline rates. A look into the surface roughness of the two facies with 30/50 mesh proppant could lead to a potential factor

into the decline rates observed. Table 35 shows the average surface roughness for 30/50 mesh proppant samples. Facies D had a higher average surface roughness compared to facies E once again suggesting that the rougher surface leads to a slower decline. A similar trend was found in the 100 mesh proppant analysis of facies D and E. The surface roughness may be playing a role in the decline rate associated with proppant embedment. Likewise to facies A, B1, and C, conductivity experiments for 30/50 mesh were performed on samples that had already been tested for unpropped and 100 mesh proppant. As a result, some proppant embedment effects from 100 mesh testing and a change in the fracture surface could have affected the conductivity results. Additionally, less samples were available for testing with this type of proppant.

Table 35: Summary of 0.1lb$_m$/ft^2 30/50 mesh propped surface roughness for facies D and E

	Average RMS Error [in]
D-X Average	0. 285
E-X Average	0. 203

3.12 Anisotropy of Mechanical Properties

Anisotropy of both the elastic properties and the Brinell hardness numbers can be observed in several facies (Table 36). Facies C had the one of the most pronounce anisotropy ratio between the parallel and perpendicular samples in both Young's modulus and Brinell hardness. Facies D showed the second highest Young's modulus-parallel to Young's modulus-perpendicular ratio, but the anisotropy was not present in

the Brinell hardness ratio. Both facies E and facies B1 had similar anisotropy ratios for Young's modulus, but facies E had the highest anisotropy ratio for Brinell hardness. While, facies A had minimal anisotropy between the two orientations for Young's modulus. Both facies A and D had a Brinell hardness ratio of perpendicular to parallel due to the z-direction having higher values.

Table 36: Summary of anisotropy values

Sample	Anisotropy- Average Young's Modulus $C' = \left(\frac{E_{max}}{E_{min}}\right)$	Anisotropy- Average Brinell Hardness $C' = \left(\frac{HBW_{max}}{HBW_{min}}\right)$
Facies A	1.05	1.15
Facies B1	1.20	1.12
Facies B2	1.08	1.23
Facies C	1.33	1.20
Facies D	1.27	1.01
Facies E	1.18	1.59

Anisotropy may explain the decline rates and conductivity values seen within this study. Facies E had the highest decline rates across all the facies and proppant types. Interestingly, facies E had the highest anisotropy ratio for Brinell hardness and a slightly high anisotropy ratio for Young's modulus. Furthermore, facies C had the highest Young's modulus anisotropy ratio and a high Brinell hardness ratio. The propped decline rates for facies C were consistently the fastest as well. While the anisotropy ratios provide insight into the decline rates observed, the range in both Young's modulus and

Brinell hardness ratios are relatively narrow. A conclusive trend of these ratios could not be attained.

4 CONCLUSIONS AND RECOMMENDATIONS

4.1 Conclusions

This study presented a comparison of the rock's properties and fracture conductivity results, both unpropped and propped, for Eagle Ford outcrops samples. Brinell hardness tests were first performed on the surface of one inch diameter core plugs to determine the Brinell hardness numbers of each facies. Triaxial compression tests were then performed to determine the elastic properties of Young's modulus and Poisson's ratio. X-ray Diffraction analysis was completed to determine the mineralogical composition. Additionally, a profilometer was used to quantify the surface roughness of the fracture conductivity samples. The experimental results of the rock's mechanical properties were combined with fracture conductivity results performed in a different study in order to formulate the following conclusions and observations:

1. The mechanical properties experimental results show a large range for both elastic properties and Brinell hardness numbers across all facies analyzed. All facies exhibited anisotropy with a ratio (parallel to perpendicular) for both Young's modulus and Brinell hardness number greater than 1 with the exception of facies A and facies D. Facies C had the highest anisotropic ratio (parallel to perpendicular) for Young's modulus and facies E had the highest anisotropic ratio (parallel to perpendicular) for Brinell hardness number.
2. Mineralogical composition played a key role in the mechanical properties observed in this study.

3. Conductivity behavior is controlled by a combination of rock mechanical properties and proppant properties.
4. In unpropped fracture conductivity, the magnitude of the fracture conductivity was dominated by the fracture surface roughness. A rougher surface allowed for a greater initial flow path for fluids. A greater Young's modulus did not always reduce the conductivity loss associated with unpropped conductivity. Also, a high Brinell hardness number did not always necessarily correlate with a slower decline rate.
5. For Propped conductivity, proppant embedment plays a major role in loss of conductivity.
    a. Facies A-X, B-X, and C-X
        i. Unpropped: High surface roughness lead to a faster rates of fracture conductivity decline.
        ii. 100 mesh: High surface roughness lead to a slower decline rates observed due to proppant embedment.
        iii. 30/50 mesh: High surface roughness lead to a slower decline rates observed due to proppant embedment.
    b. Facies D and E
        i. Unpropped: High surface roughness lead to slower rates of fracture conductivity decline.
        ii. 100 mesh: High surface roughness lead to a slower decline rates associated with proppant embedment. The elastic properties and

Brinell hardness did not show a clear trend relating to the decline rates.

iii. 30/50 mesh: High surface roughness lead to a slower decline rates associated with proppant embedment. The elastic properties and Brinell hardness did not show a clear trend relating to the decline rates.

4.2 Recommendations

The scope of this study can be further expanded into several directions, the following are recommendations:

1. The conclusions of this work is based on a handful of fracture conductivity experiments performed on each facies and in one orientation (x-direction). Further conductivity experimental work should be performed in both orientations.
2. Additionally, further studies of other shale formations should be tested in both unpropped and with the same type and amount of proppant to test the relationships found in this study.
3. Conductivity measurements with proppant fluid interaction should be performed to understand the relationship of the rock's properties and mineralogy and its conductivity.
4. Further mechanical testing should be performed in order to fully understand the rock's mechanical behavior and conductivity.

5. Similar mechanical properties testing and fracture conductivity studies should be completed on downhole shale cores from the Eagle Ford formation to obtain more complete analysis of the rock's properties and fracture conductivity.

REFERENCES

Alramahi, B., Sundberg, M.I. (2012). Proppant Embedment and Conductivity or Hydraulic Fractures in Shales. US Rock Mechanics / Geomechanics Symposium. Chicago, Illinois. 2012. Copyright 2012 ARMA, American Rock Mechanics Association.

ASTM Standard D4543-08. (2008). Standard Practices for Preparing Rock Core as Cylindrical Test Specimens and Verifying Conformance to Dimensional and Shape Tolerances. ASTM International. West Conshohocken, PA, 2008. DOI:10.1520/D4543-08. www.astm.org

ASTM Standard D7012-14. (2014). Standard Test Methods for Compressive Strength and Elastic Moduli of Intact Rock Core Specimens under Varying States of Stress and Temperatures. ASTM International. West Conshohocken, PA, 2014. DOI: 10.1520/D7012-14. www.astm.org

ASTM Standard E10-14. (2015). Standard Test Method for Brinell Hardness of Metallic Materials. ASTM International. West Conshohocken, PA, 2014. DOI: 10.1520/E0010-15A. www.astm.org

Briggs, K. (2014). The Influence of Vertical Location on Hydraulic Fracture Conductivity in the Fayetteville Shale. Master's Thesis: Texas A&M University Petroleum Engineering. Copyright 2014, Kathryn Elizabeth Briggs.

Britt, L.K., Smith, M.B. (2009). Horizontal Well Completion, Stimulation Optimization, And Rick Mitigation. 2009 SPE Eastern Regional Meeting. Charleston, West Virginia. Copyright 2009. Society of Petroleum Engineers.

Chapman, M., Palisch, T. (2014). Fracture Conductivity- Design considerations and benefits in unconventional reservoirs. Jour. of Petro. Sci. and Eng. 124: 407-415.

Cobb, S.L., Farrell, J.J. (1986). Evaluation of Long-Term Proppant Stability. International Meeting on Petroleum Engineering. Beijing, China. Copyright 1986. Society of Petroleum Engineers.

Das, P., Achalpurkar, M. (2013). Impact of Rock Mechanics and Formation Softening Analysis in Shale Fracturing Design. SPE Kuwait Oil and Gas Show and Conference. Mishref, Kuwait. Copyright 2013. Society of Petroleum Engineers.

Economides, M.J., Hill, D.A., Ehlig-Economides, C., Zhu, D. (2012). Petroleum Production Systems, Second Edition. Englewood Cliff, N.J. PTR Prentice Hall.

EIA. (2014, December). Updates to the EIA Eagle Ford Play Maps. Map retrieved January 2016 from https://www.eia.gov/maps/pdf/eagleford122914.pdf.

EIA. (2016, February). Drilling Productivity Report. Retrieved January 2016 from https://www.eia.gov/petroleum/drilling/#tabs-summary-2.

Enriquez Tenorio, O. (2016). A comprehensive study of the Eagle Ford shale fracture conductivity. Master's Thesis. Texas A&M University Petroleum Engineering. Copyright 2016, Omar Enriquez Tenorio.

Fan, L., Martin, R., Thompson, J., Atwood, K., Robinson, J., Lindsay, G. (2011). An Integrated Approach for Understanding Oil and Gas Reserves Potential in Eagle Ford Shale Formation. SPE Unconventional Resources Conference-Canada. Calgary, Alberta, Canada. Copyright 2011. Society of Petroleum Engineers.

Fjaer, E., Nes, O.-M. (2013). Strength Anistropy of Mancos Shale. 47th US Rock Mechanics/ Geomechanics Symposium. San Francisco, CA. Copyright 2015, American Rock Mechanics Association.

Fredd, C.N., McConnel, S.B., Boney, C.L., England, K.W. (2000). Experimental Study of Hydraulic Fracture Conductivity Demonstrates the Benefits of Using Proppants. SPE Rocky Mountain Regional/Low Permeability Resrevoirs Symposium. Denver, CO. Copyright 2000. Society of Petroleum Engineers.

Gardner, R., Pope, M. C., Wehner, M. P., Donovan, A. D. (2013). Comparative Stratigraphy of the Eagle Ford Group Strata in Lozier Canyon and Antonio Creek, Terrell County, Texas. GCAGS Journal 2(1): 42-52.

Gong, X., Tian, Y., McVay, D.A., Ayer, W.B., Lee, W.J. (2013). Assessment of Eagle Ford Shale Oil and Gas Resources. SPE Unconventional Resources Conference-Canada. Calgary, Alberta, Canada. Copyright 2013. Society of Petroleum Engineers.

Guzek, J. (2014). Fracture Conductivity of the Eagle Ford Shale. Master's Thesis. Texas A&M University Petroleum Engineering. Copyright 2014, James J. Guzek.

Hawkins, G.W. (1988). Laboratory Study of Proppant-Pack Permeability Reduction Caused by Fracturing Fluids Concentrated During Closure. 63rd Annual Technical Conference and Exhibition of the Society of Petroleum Engineers. Houston, TX. Copyright 1988, Society of Petroleum Engineers.

Hillier, S. (2000). Accurate quantitative analysis of clay and other minerals in sandstones by XRD: comparison of a Rietvald and a reference intensity ratio (RIR) and the importance of sample preparation. Clay Minerals 35: 291-302.

Holt, R.M., Fjaer,E., Nes, O.M. et al. (2011). A shaly look at Brittleness. Paper ARMA 11-366 presented at the 45th US Rock Mechanics/ Geomechanics Symposium, San Francisco, California, Usa 26-29 June.

Hornby, B.E., Schwartz, L.M., Hudson, J.A. (1993). Effective Medium Modeling of the Electrical and Elastic Properties of Anisotropic Porous Media. 1993 SEG Annual Meeting. Washington, D.C. Copyright 1993. Society of Exploration Geophysicists.

Jansen, T. (2014). The effect of rock properties on hydraulic fracture conductivity in the Eagle Ford and Fayetteville Shales. Master's Thesis. Texas A&M University Petroleum Engineering. Copyright 2014, Timothy A. Jansen.

Kostenuk, N., Browne, D.J. (2010). Improved Proppant Transport System for Slickwater Shale Fracturing. Canadian Unconventional Resources & International Petroleum Conference. Calgary, Alberta, Canada. Copyright 2010, Society of Petroleum Engineers.

Li, W., Jin, F., Salviato, M., Cusatis, G. (2015) Modeling of Failure Behavior of Anisotropic Shale Using Lattice Discrete Particle Model. 49th US Rock Mechanics/ Geomechanics Symposium. San Francisco, CA. Copyright 2015, American Rock Mechanics Association.

Matthews, H. L., Schein, G. W., Malone, M. (2007). Stimulation of Gas Shales: They're All the Same Right?. Paper SPE 106070. SPE Hydraulic Fracturing Technology Conference. College Station, TX, USA. Copyright 2007, Society of Petroleum Engineers.

McGinley, M. (2015). The effects of fracture orientation and anisotropy on hydraulic fracture conductivity in the Marcellus Shale. Master's Thesis. Texas A&M University Petroleum Engineering. Copyright 2015, Mark J. McGinley.

Morales, R.H., Suarez-Rivera, R., Edelman, E. (2011). Experimental Evaluation of Hydraulic Fracture Impairment in Shale Reservoirs. 45th US Rock Mechanics/Geomechanics Symposium. San Francisco, CA. Copyright 2011, American Rock Mechanics Association.

Mueller, M., Amro, M. (2015). Indentation Hardness for Improved Proppant Embedment Prediction in Shale Formations. SPE European Damage Conference and Exhibition. Budapest, Hungary. Copyright 2015, Society of Petroleum Engineers.

Passey, Q.R., Bohacs, K.M., Esch, W.L., Klimentidis, R., Sinha, S. (2010). From Oil-Prone Source Rock to Gas-Producing Shale Reservoir – Geologic and Petrophysical Characterization of Unconventional Shale-Gas Reservoirs. CPS/SPE International Oil & Gas Conference and Exhibition. Beijing, China. Copyright 2010, Society of Petroleum Engineers.

Paterson, M. S. and Wong, T. (2005). Experimental Rock Deformation – The Brittle Field, Second Edition. Springer-Verlag Berlin Heidelberg, The Netherlands, 2005. ISBN: 3-540-24023-3.

Perez Pena, P.A. (2015). The effect of rock properties on fracture conductivity in the Marcellus Shale. Master's Thesis. Texas A&M University Petroleum Engineering. Copyright 2015, Paola Alejandra Perez Pena.

Sayers, C. M. (2013). The effect of anisotropy on the Young's moduli and Poisson's ratios of shales. Geophysical Prospecting, 61: 416–426. DOI: 10.1111/j.1365-2478.2012.01130.x

Sone, H., and M. D. Zoback, (2013). Mechanical properties of shale gas reservoir rocks — Part 1: Static and dynamic elastic properties and anisotropy. Geophysics, 78(5):D381-D392. DOI: 10.1190/geo2013-0050.1.

Sone, H., and M. D. Zoback, (2013). Mechanical properties of shale gas reservoir rocks — Part 2: Ductile creep, brittle strength, and their relation to the elastic modulus. Geophysics, 78(5), D393-D402. DOI: 10.1190/geo2013-0050.1.

Stegent, N.A., Wagner, A.L., Mullen, J., Borstmayer, R.E., Engineering a Successful Fracture-Stimulation Treatment in the Eagle Ford Shale. SPE Tight Gas Completions Conference. San Antonio, TX. Copyright 2010, Society of Petroleum Engineers.

Treviranus, I. (2012, January). *Importance of Size and Shape for Proppants Quality*. Powerpoint presentation at the ASTM Subcommittee D18.26 on Hydraulic Fracturing, Jacksonville, FL.

Volk, L.J., Raible, C.J., Carroll, H.B. (1981). Embedment of high strength proppant into low-permeability reservoir rock. SPE/DOE Low Permeability Symposium. Denver, CO. Copyright 1981, Society of Petroleum Engineers.

Weaver, J.D., Nyuyen, P.D., van Batenburg, D. (2006). Sustaining Conductivity. SPE International Symposium and Exhibition on Formation Damage Control. Lafayette, LA. Copyright 2006, Society of Petroleum Engineers.

Wen, Q., Zhang, S., Wang, L., Liu, Y., Li, X. (2007). The effect of proppant embedment upon the long-term conductivity of fractures. Journal of Petroleum Science and Engineering 55(3-4): 221-227.

Wong, R.C.K., Schmitt, D.R., Collis, D., Gautam, R. (2008). Inherent transversely isotropic elastic parameters of over-consolidated shale measured by ultrasonic waves and their comparison with static and acoustic in situ log measurements. J. Geophys. Eng. 5: 103-117.

Zhang, Junjing, Kamenov, A., Zhu, D., Hill, A.D. (2013). Laboratory Measurement of Hydraulic Fracture Conductivities in the Barnett Shale. SPE Hydraulic 103 Fracturing Technology Conference, The Woodlands, Texas, 2013. Copyright 2013, Society of Petroleum Engineers.

Zoorabadi, M., Saydam, S., Timms, W., Hebblewhite, B. (2015). Non-linear flow behavior of rough fractures having standard JRC profiles. Int. J. of Rock Mech. and Min. Sci. 76: 192-199.

APPENDIX A

Eagle Ford Facies A

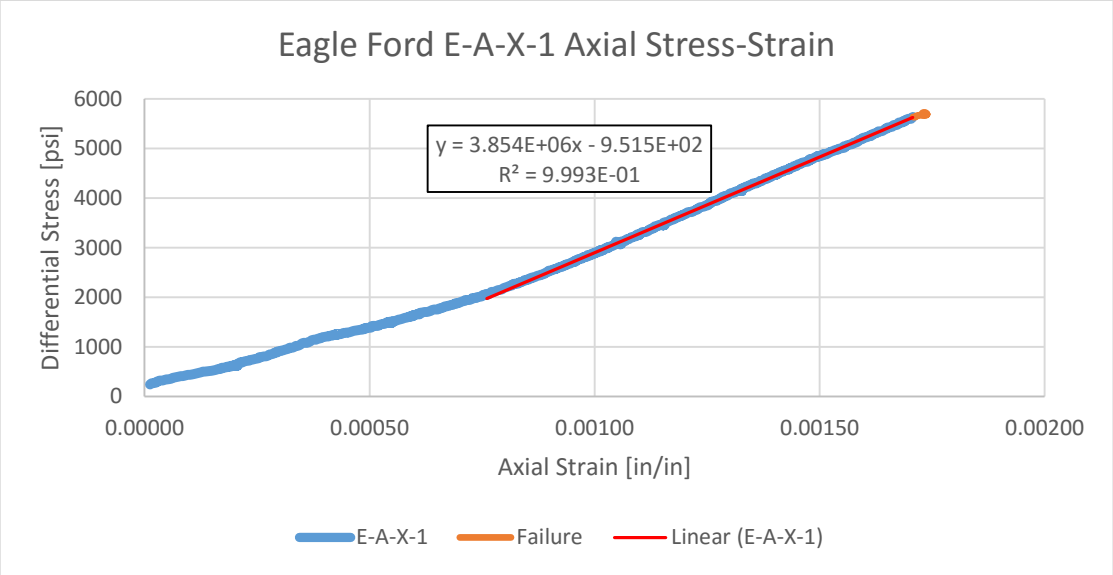

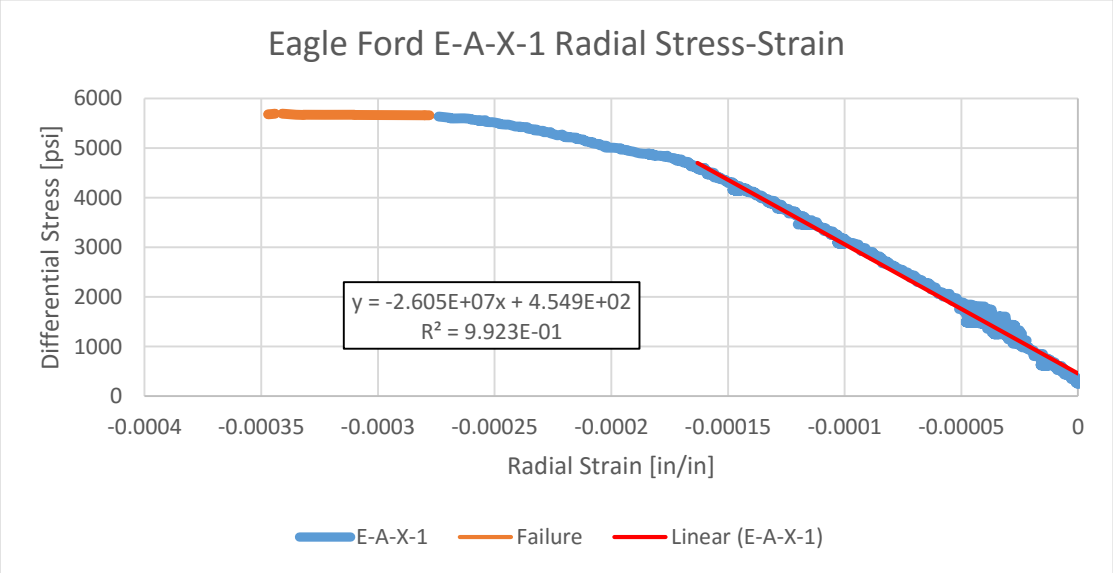

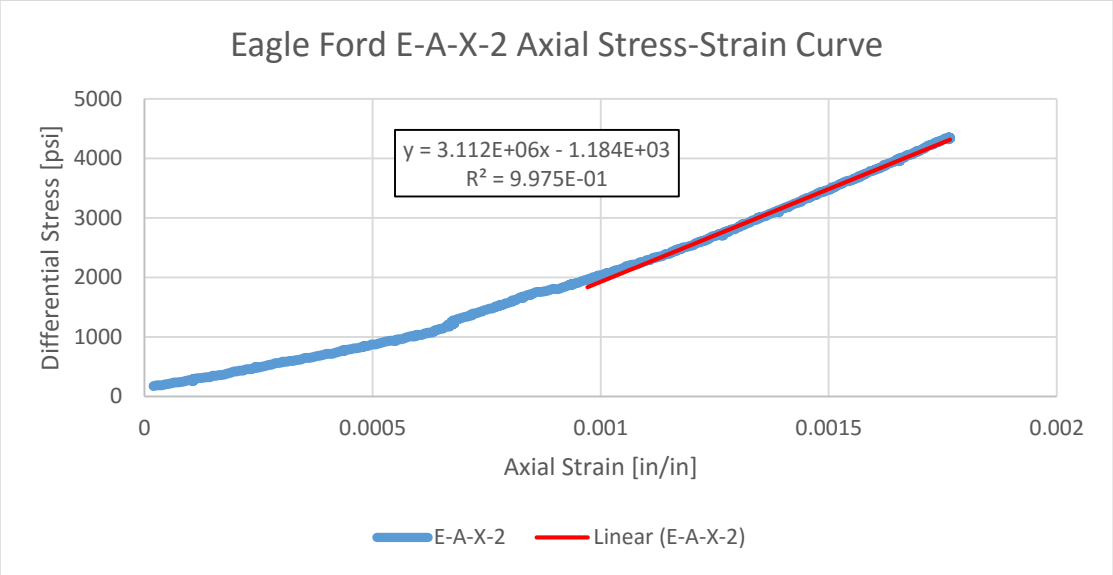
Eagle Ford E-A-X-2 Axial Stress-Strain Curve
y = 3.112E+06x - 1.184E+03
R² = 9.975E-01
Differential Stress [psi]
5000
4000
3000
2000
1000
0
0
0.0005
0.001
0.0015
0.002
Axial Strain [in/in]
E-A-X-2
Linear (E-A-X-2)

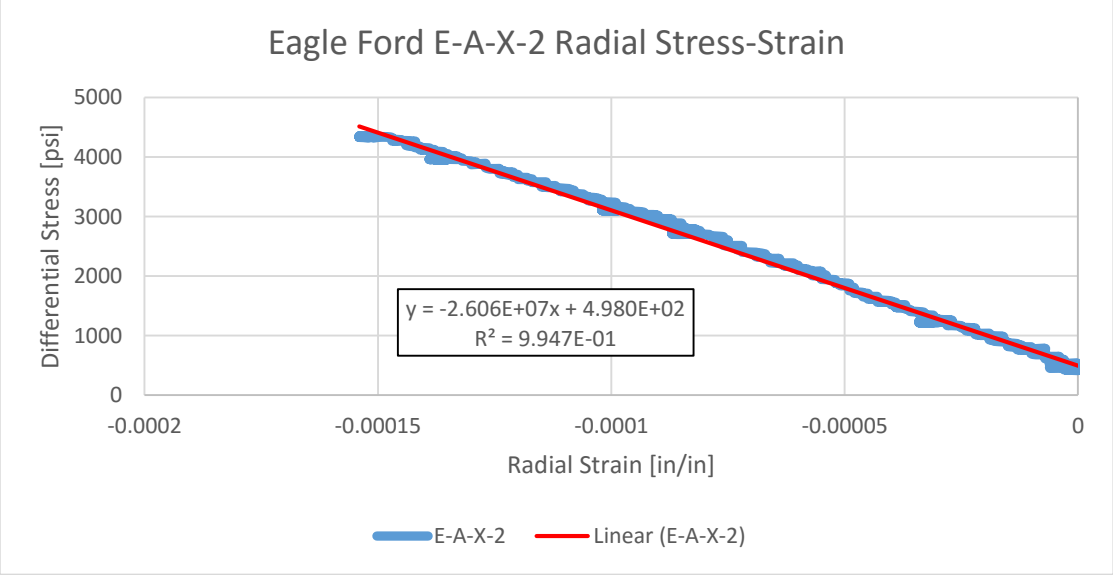
Eagle Ford E-A-X-2 Radial Stress-Strain
y = -2.606E+07x + 4.980E+02
R² = 9.947E-01
Differential Stress [psi]
5000
4000
3000
2000
1000
0
-0.0002
-0.00015
-0.0001
-0.00005
0
Radial Strain [in/in]
E-A-X-2
Linear (E-A-X-2)

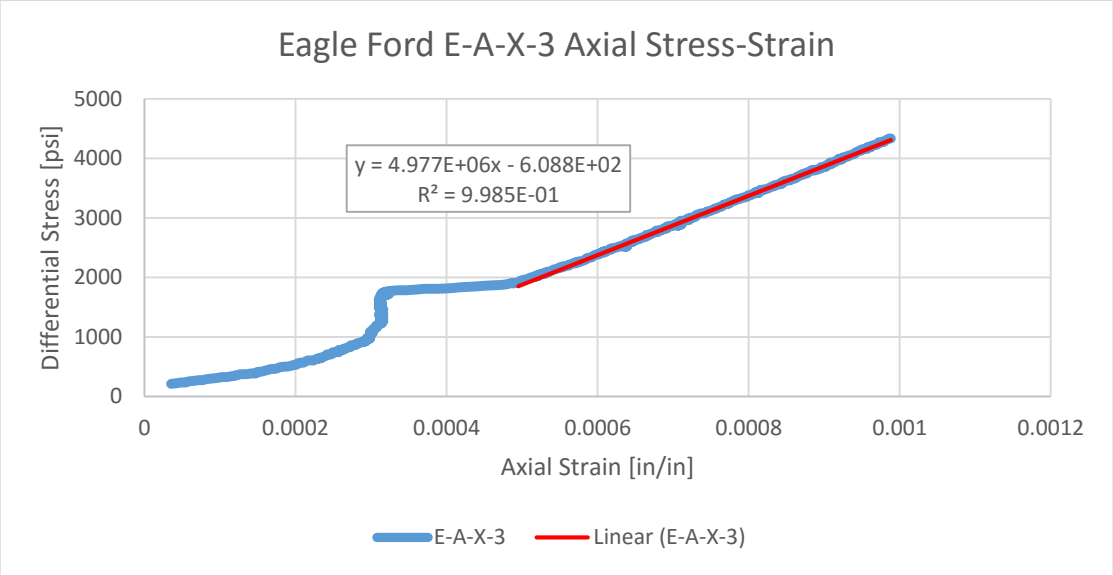
Eagle Ford E-A-X-3 Axial Stress-Strain
y = 4.977E+06x - 6.088E+02
R² = 9.985E-01
Differential Stress [psi]
5000
4000
3000
2000
1000
0
0
0.0002
0.0004
0.0006
0.0008
0.001
0.0012
Axial Strain [in/in]
E-A-X-3
Linear (E-A-X-3)

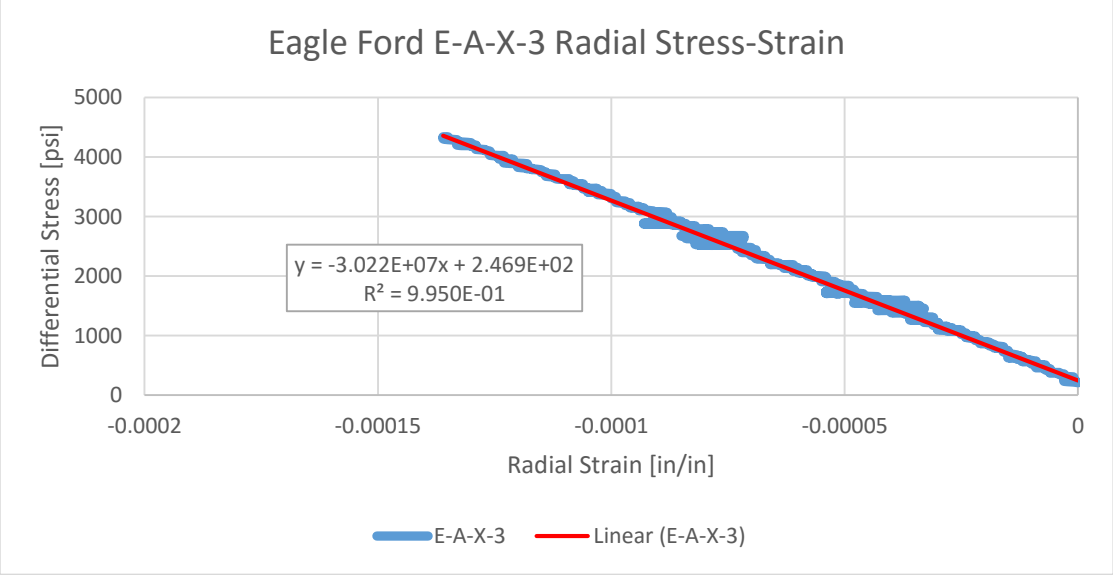
Eagle Ford E-A-X-3 Radial Stress-Strain
y = -3.022E+07x + 2.469E+02
R² = 9.950E-01
Differential Stress [psi]
5000
4000
3000
2000
1000
0
-0.0002
-0.00015
-0.0001
-0.00005
0
Radial Strain [in/in]
E-A-X-3
Linear (E-A-X-3)

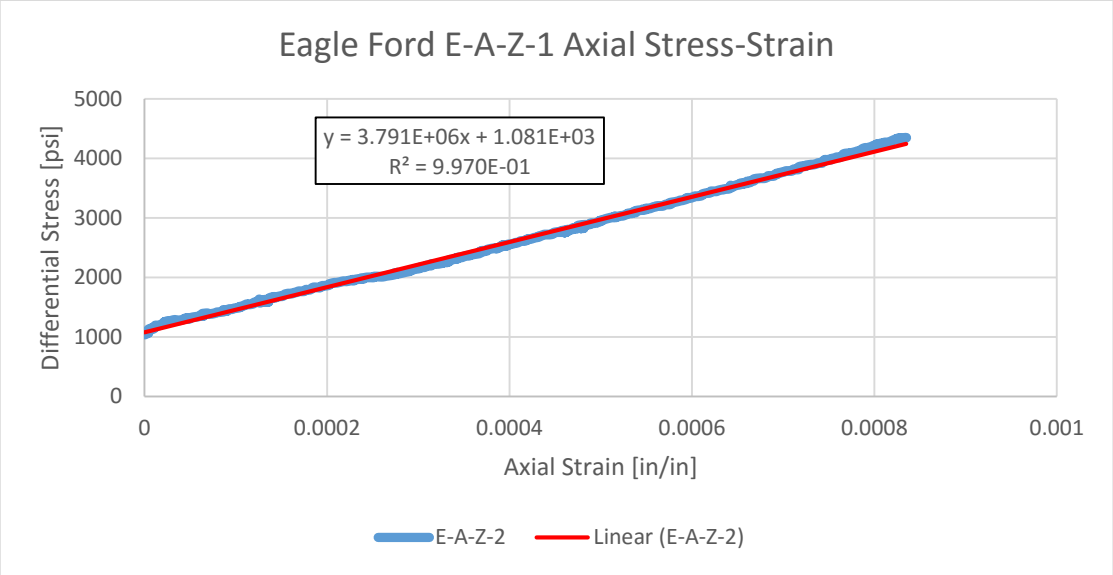
Eagle Ford E-A-Z-1 Axial Stress-Strain
y = 3.791E+06x + 1.081E+03
R² = 9.970E-01
Differential Stress [psi]
5000
4000
3000
2000
1000
0
0
0.0002
0.0004
0.0006
0.0008
0.001
Axial Strain [in/in]
E-A-Z-2
Linear (E-A-Z-2)

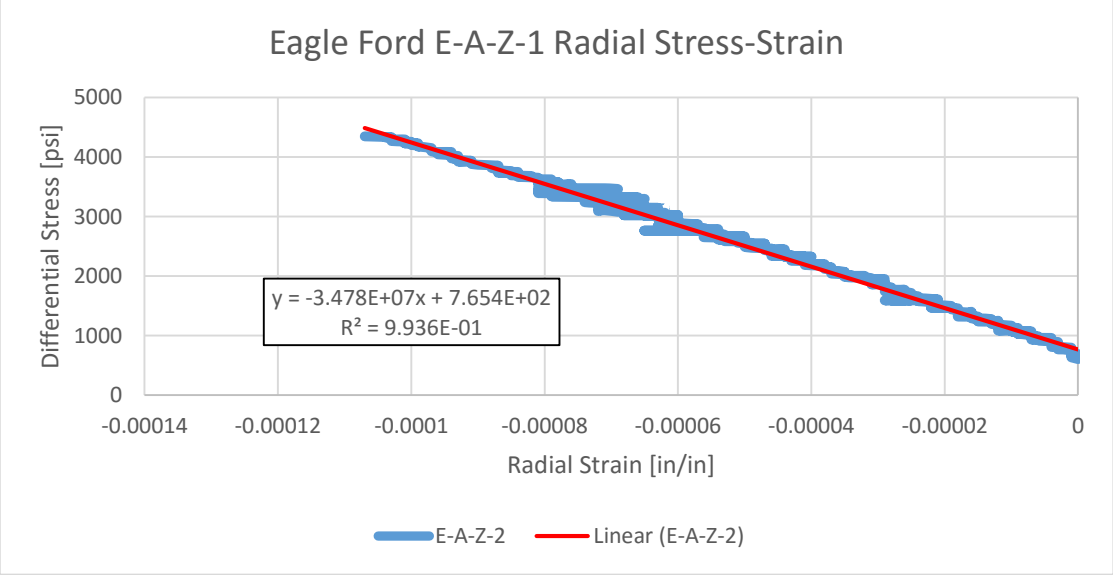
Eagle Ford E-A-Z-1 Radial Stress-Strain
y = -3.478E+07x + 7.654E+02
R² = 9.936E-01
Differential Stress [psi]
5000
4000
3000
2000
1000
0
-0.00014
-0.00012
-0.0001
-0.00008
-0.00006
-0.00004
-0.00002
0
Radial Strain [in/in]
E-A-Z-2
Linear (E-A-Z-2)

Eagle Ford Facies B1

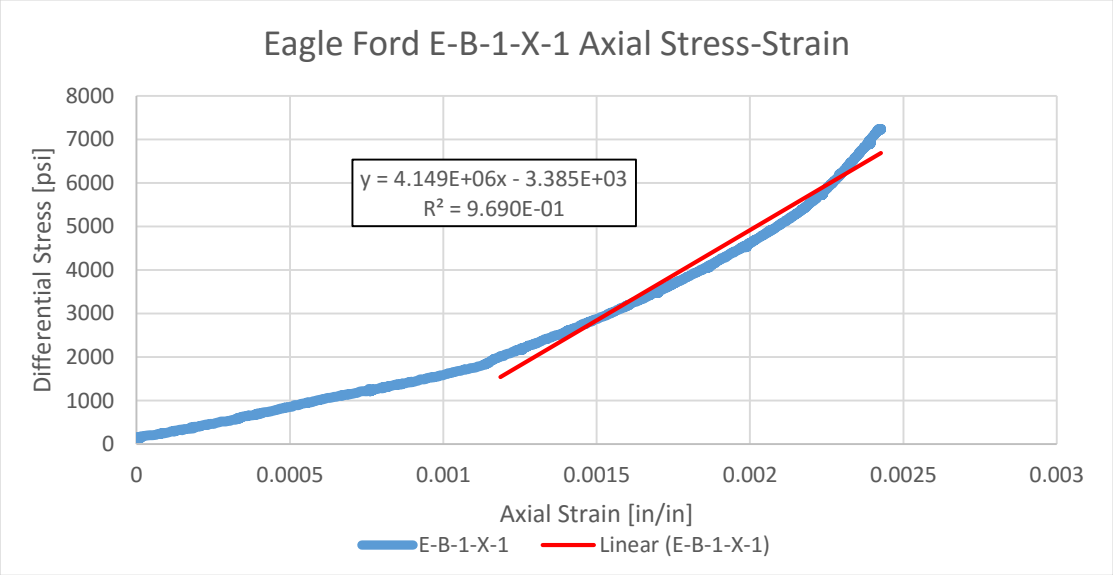

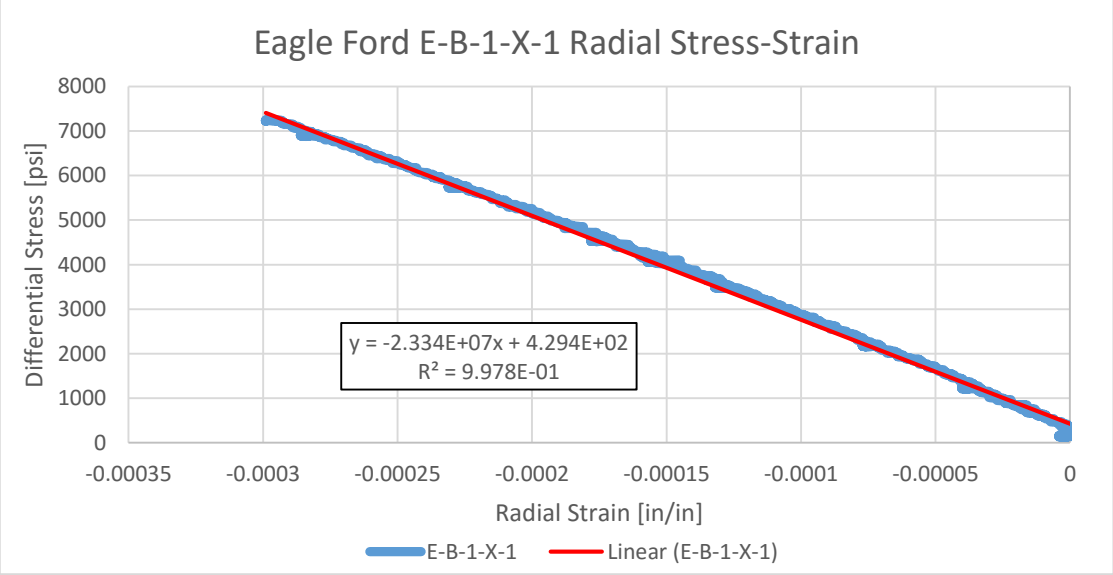

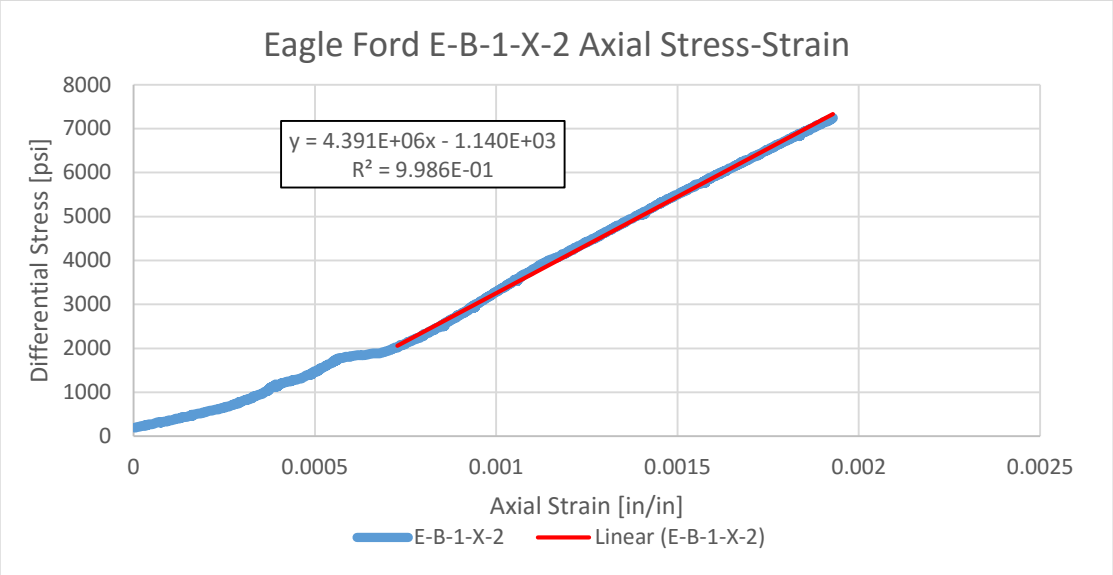
Eagle Ford E-B-1-X-2 Axial Stress-Strain
y = 4.391E+06x - 1.140E+03
R² = 9.986E-01
Differential Stress [psi]
8000
7000
6000
5000
4000
3000
2000
1000
0
0
0.0005
0.001
0.0015
0.002
0.0025
Axial Strain [in/in]
E-B-1-X-2
Linear (E-B-1-X-2)

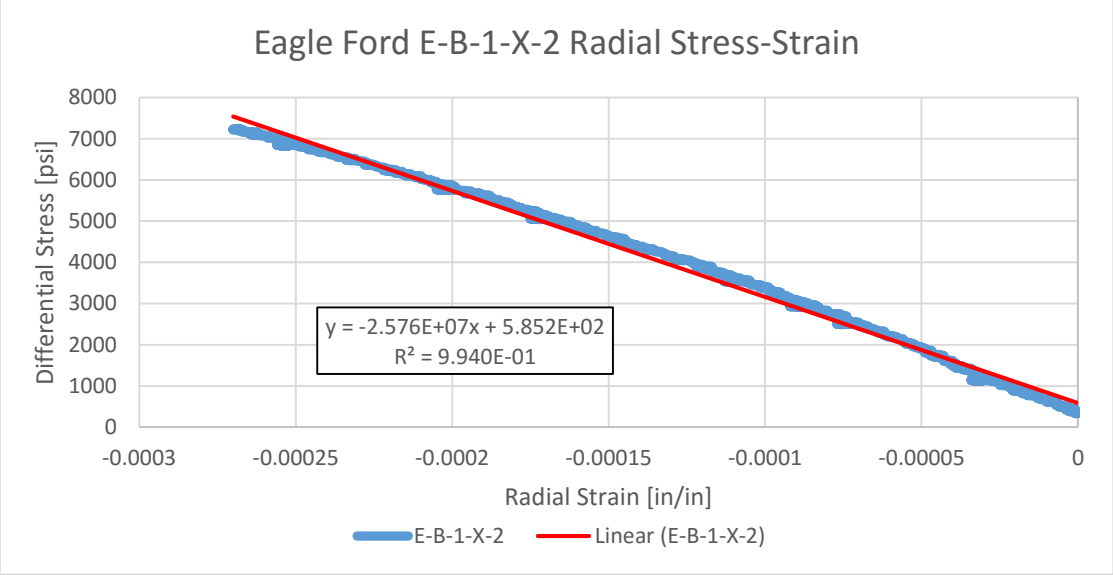
Eagle Ford E-B-1-X-2 Radial Stress-Strain
y = -2.576E+07x + 5.852E+02
R² = 9.940E-01
Differential Stress [psi]
8000
7000
6000
5000
4000
3000
2000
1000
0
-0.0003
-0.00025
-0.0002
-0.00015
-0.0001
-0.00005
0
Radial Strain [in/in]
E-B-1-X-2
Linear (E-B-1-X-2)

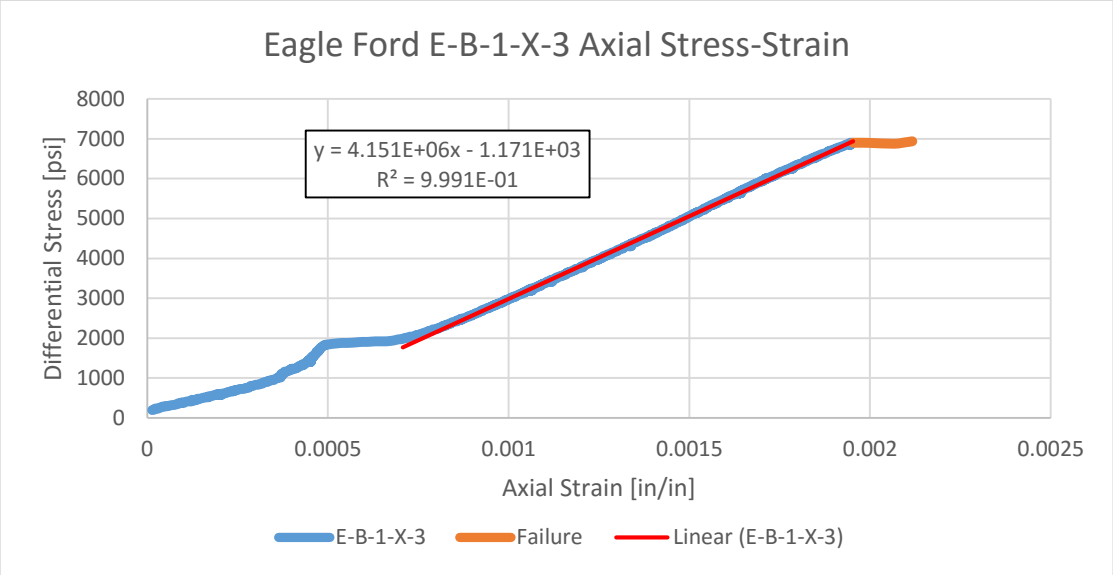
Eagle Ford E-B-1-X-3 Axial Stress-Strain
y = 4.151E+06x - 1.171E+03
R² = 9.991E-01
Differential Stress [psi]
8000
7000
6000
5000
4000
3000
2000
1000
0
0
0.0005
0.001
0.0015
0.002
0.0025
Axial Strain [in/in]
E-B-1-X-3
Failure
Linear (E-B-1-X-3)

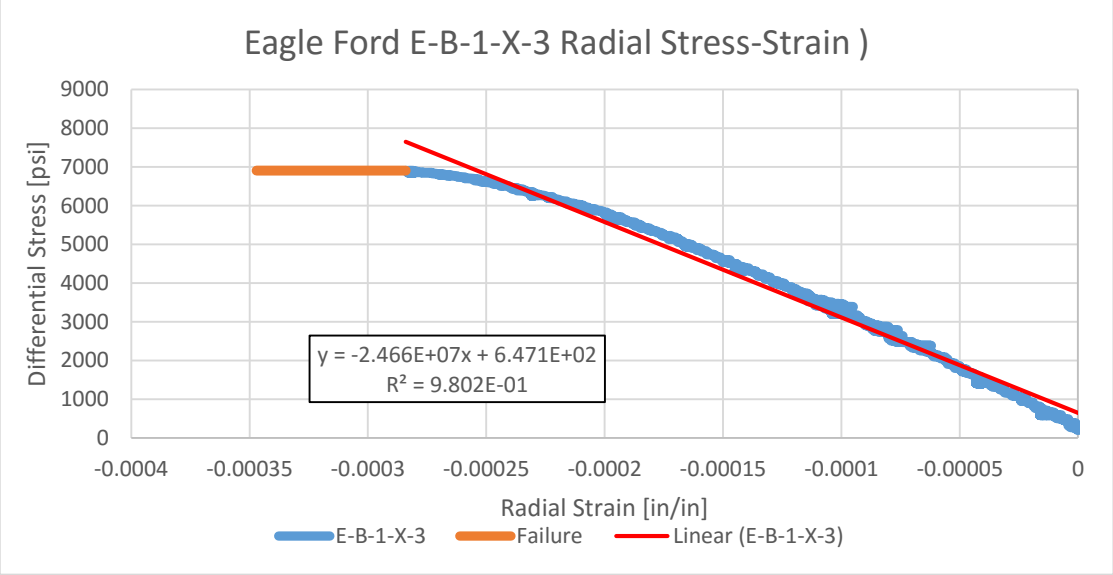
Eagle Ford E-B-1-X-3 Radial Stress-Strain)
y = -2.466E+07x + 6.471E+02
R² = 9.802E-01
Differential Stress [psi]
9000
8000
7000
6000
5000
4000
3000
2000
1000
0
-0.0004
-0.00035
-0.0003
-0.00025
-0.0002
-0.00015
-0.0001
-0.00005
0
Radial Strain [in/in]
E-B-1-X-3
Failure
Linear (E-B-1-X-3)

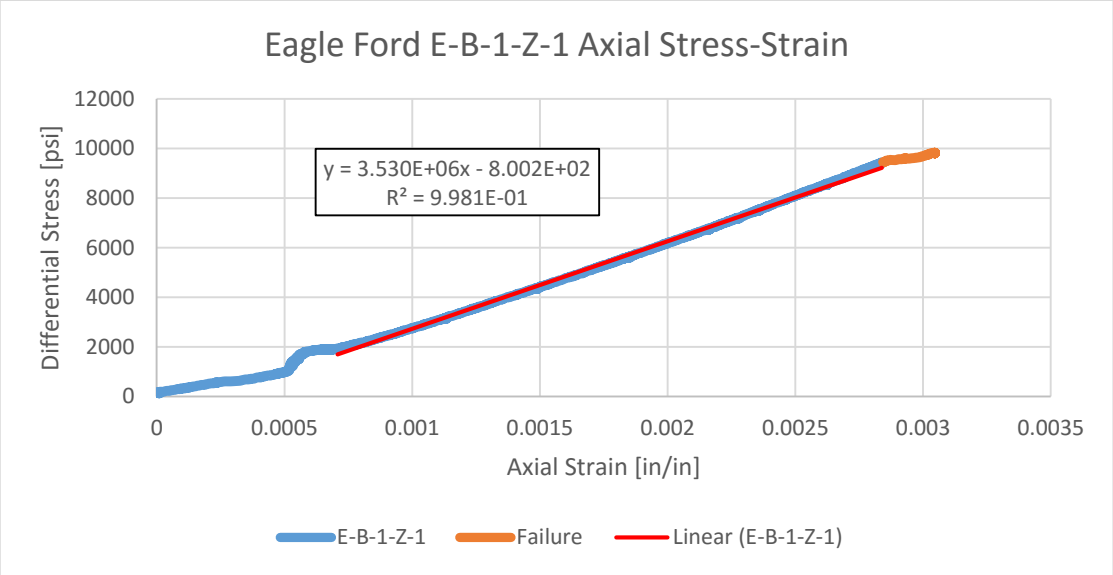
Eagle Ford E-B-1-Z-1 Axial Stress-Strain
Differential Stress [psi]
12000
10000
8000
6000
4000
2000
0
y = 3.530E+06x - 8.002E+02
R² = 9.981E-01
0
0.0005
0.001
0.0015
0.002
0.0025
0.003
0.0035
Axial Strain [in/in]
E-B-1-Z-1
Failure
Linear (E-B-1-Z-1)

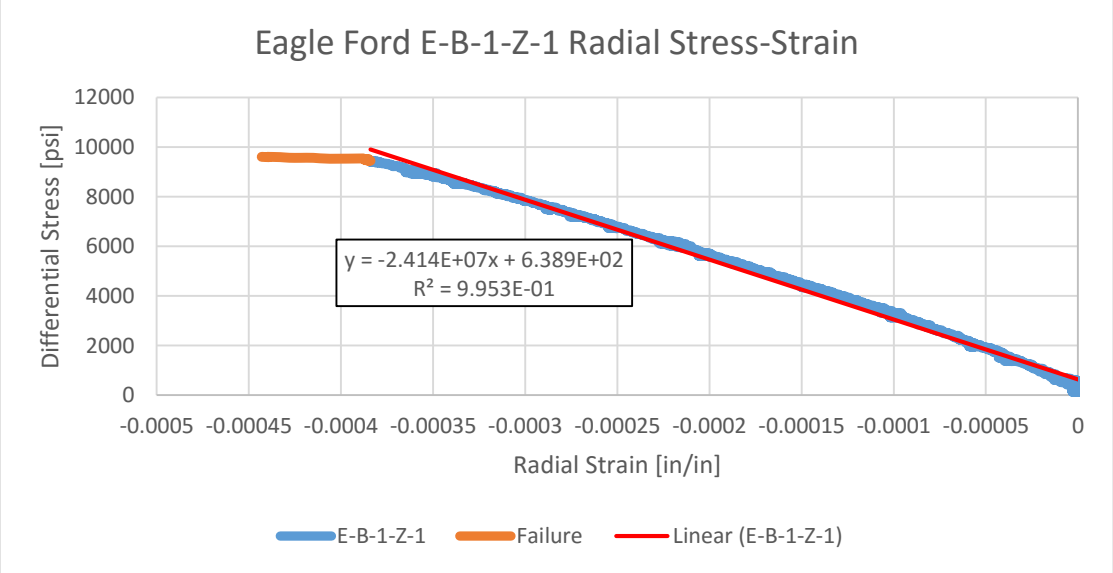
Eagle Ford E-B-1-Z-1 Radial Stress-Strain
Differential Stress [psi]
12000
10000
8000
6000
4000
2000
0
y = -2.414E+07x + 6.389E+02
R² = 9.953E-01
-0.0005
-0.00045
-0.0004
-0.00035
-0.0003
-0.00025
-0.0002
-0.00015
-0.0001
-0.00005
0
Radial Strain [in/in]
E-B-1-Z-1
Failure
Linear (E-B-1-Z-1)

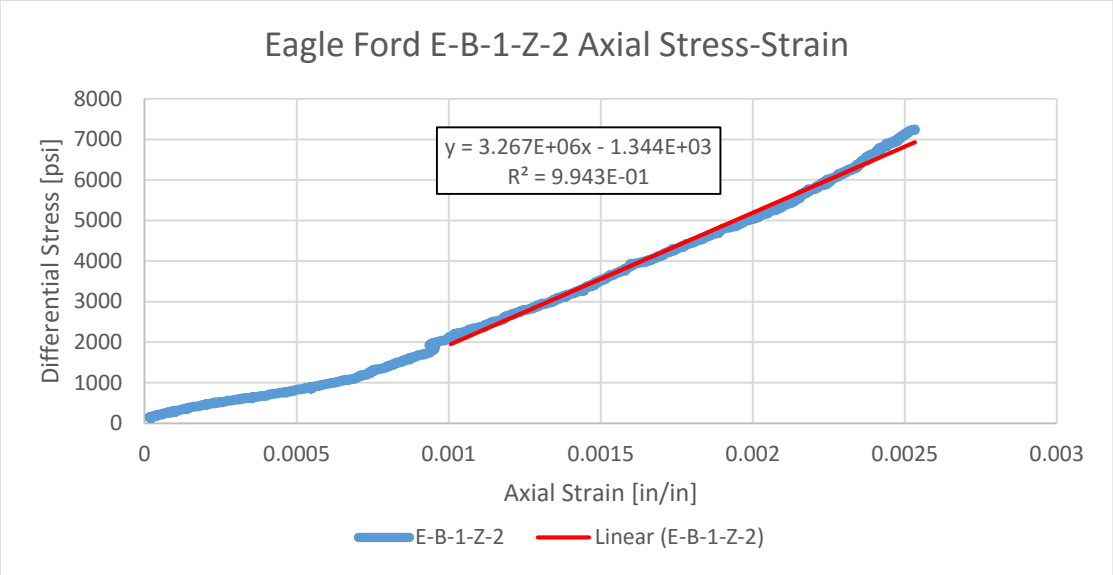
Eagle Ford E-B-1-Z-2 Axial Stress-Strain
y = 3.267E+06x - 1.344E+03
R² = 9.943E-01
Differential Stress [psi]
8000
7000
6000
5000
4000
3000
2000
1000
0
0
0.0005
0.001
0.0015
0.002
0.0025
0.003
Axial Strain [in/in]
E-B-1-Z-2
Linear (E-B-1-Z-2)

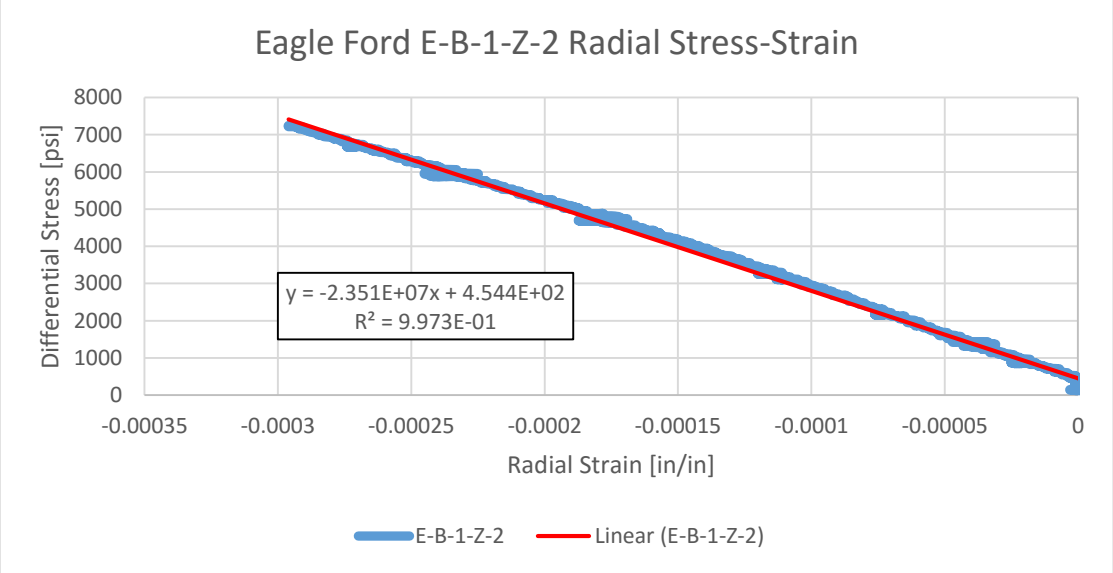
Eagle Ford E-B-1-Z-2 Radial Stress-Strain
y = -2.351E+07x + 4.544E+02
R² = 9.973E-01
Differential Stress [psi]
8000
7000
6000
5000
4000
3000
2000
1000
0
-0.00035
-0.0003
-0.00025
-0.0002
-0.00015
-0.0001
-0.00005
0
Radial Strain [in/in]
E-B-1-Z-2
Linear (E-B-1-Z-2)

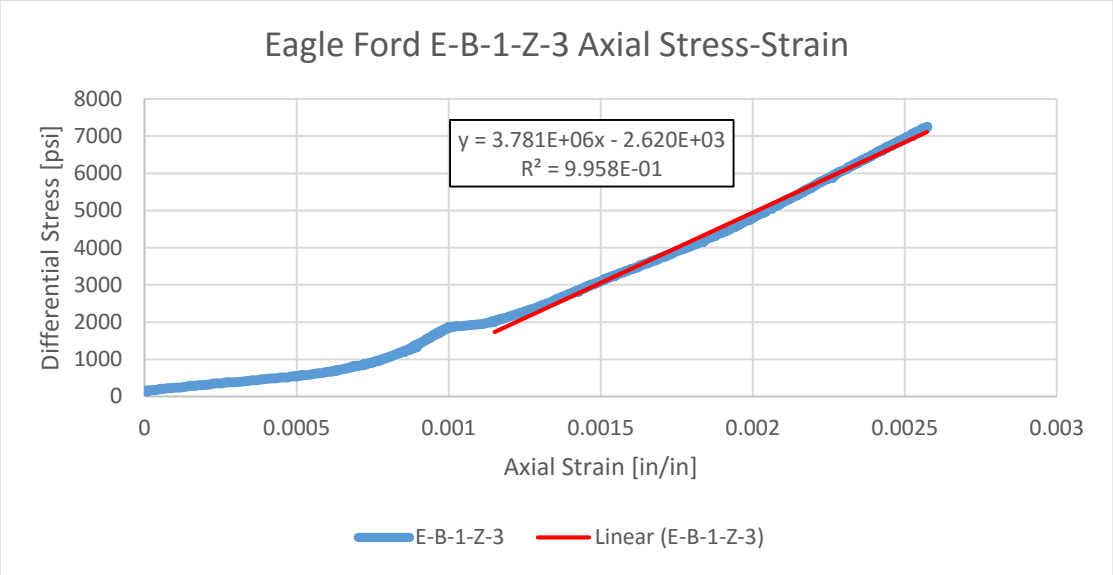
Eagle Ford E-B-1-Z-3 Axial Stress-Strain
y = 3.781E+06x - 2.620E+03
R² = 9.958E-01
Differential Stress [psi]
8000
7000
6000
5000
4000
3000
2000
1000
0
0
0.0005
0.001
0.0015
0.002
0.0025
0.003
Axial Strain [in/in]
E-B-1-Z-3
Linear (E-B-1-Z-3)

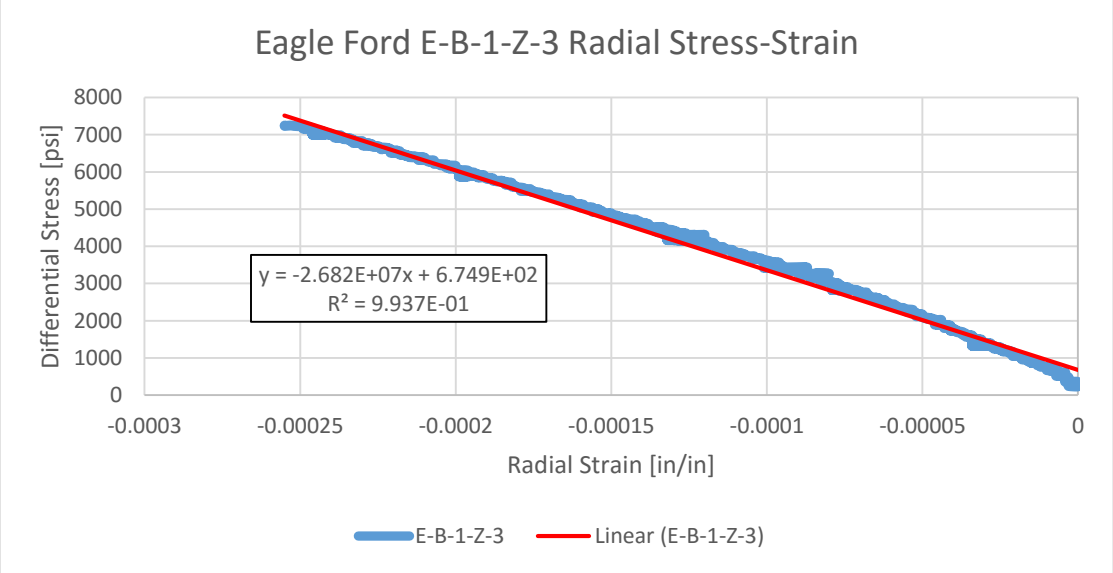
Eagle Ford E-B-1-Z-3 Radial Stress-Strain
y = -2.682E+07x + 6.749E+02
R² = 9.937E-01
Differential Stress [psi]
8000
7000
6000
5000
4000
3000
2000
1000
0
-0.0003
-0.00025
-0.0002
-0.00015
-0.0001
-0.00005
0
Radial Strain [in/in]
E-B-1-Z-3
Linear (E-B-1-Z-3)

Eagle Ford Facies B2

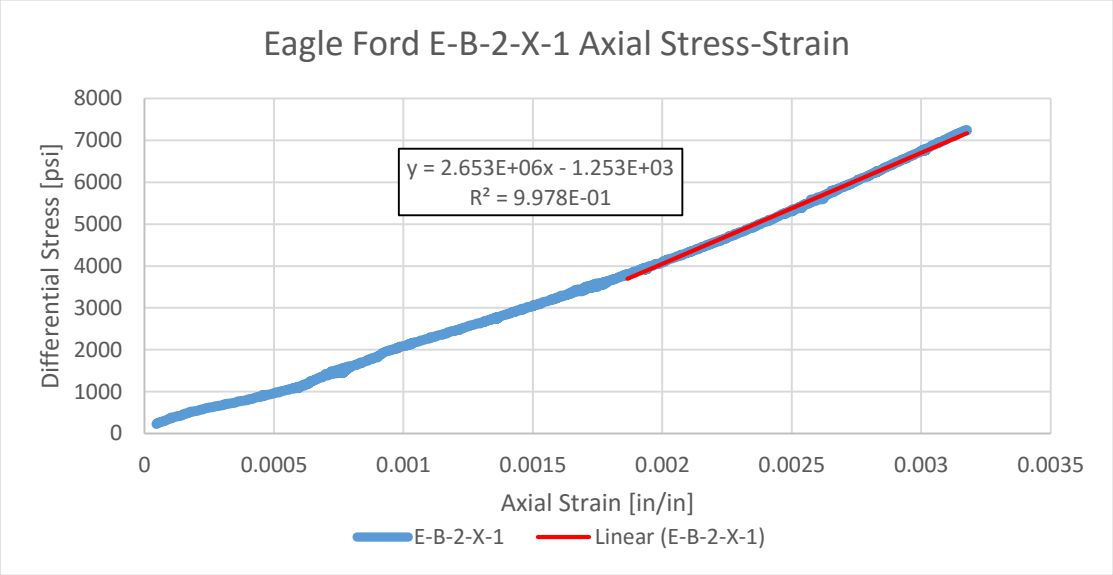

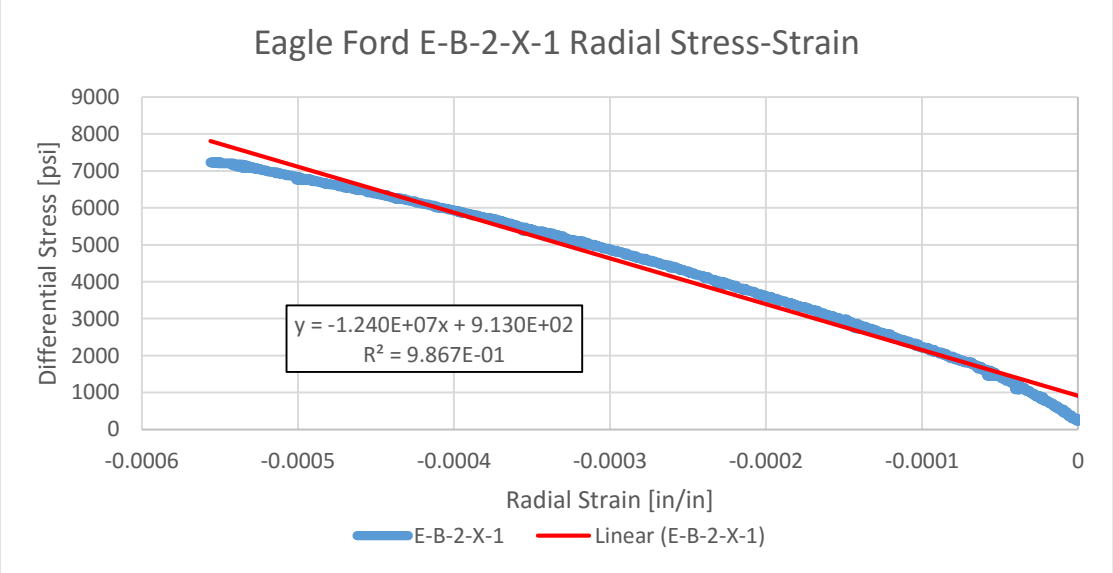

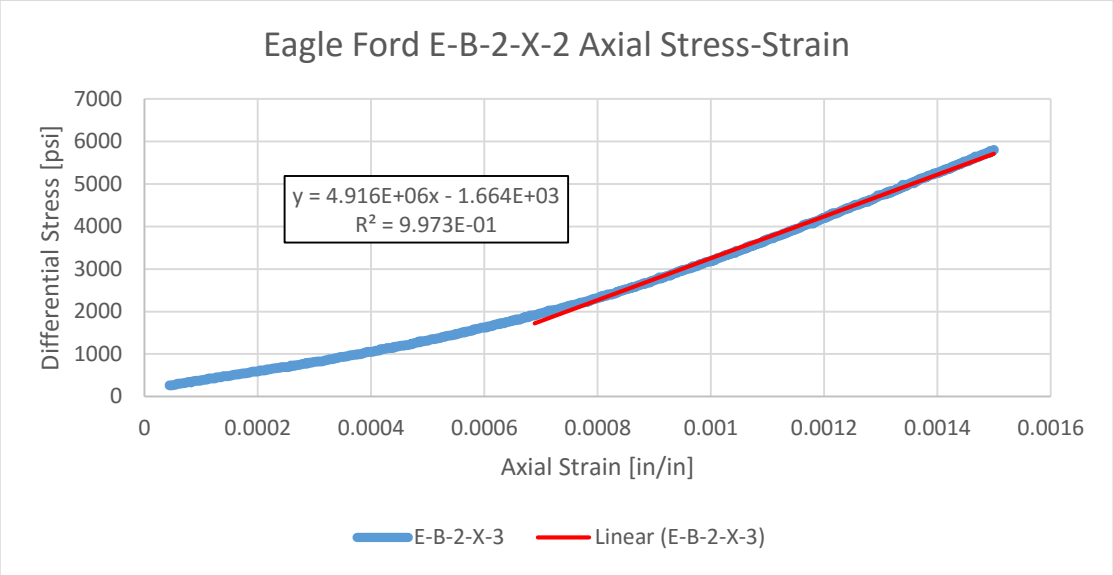
Eagle Ford E-B-2-X-2 Axial Stress-Strain
Differential Stress [psi]
7000
6000
5000
4000
3000
2000
1000
0
y = 4.916E+06x - 1.664E+03
R² = 9.973E-01
0
0.0002
0.0004
0.0006
0.0008
0.001
0.0012
0.0014
0.0016
Axial Strain [in/in]
E-B-2-X-3
Linear (E-B-2-X-3)

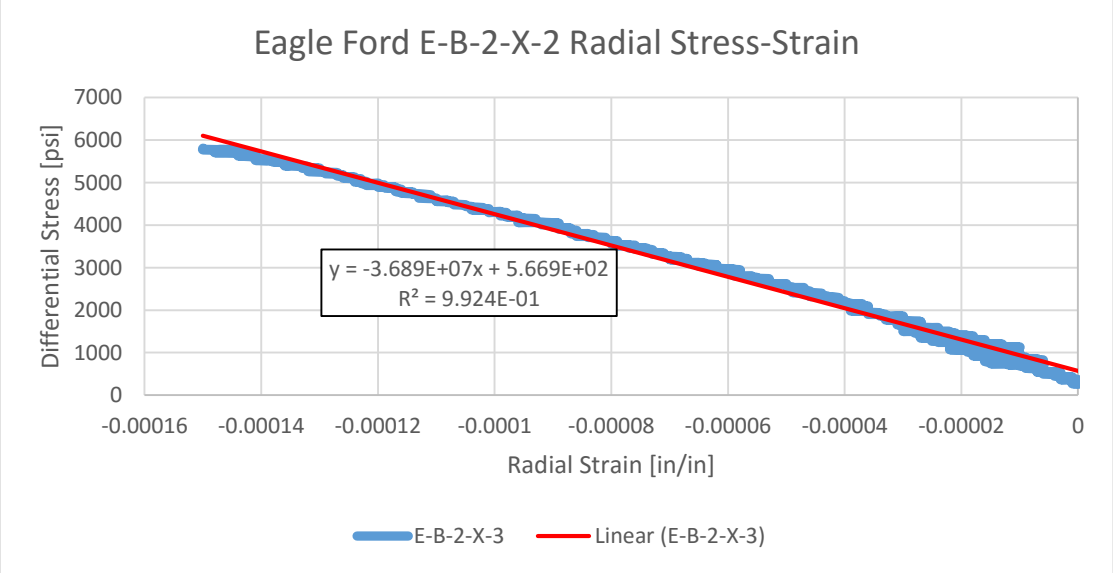
Eagle Ford E-B-2-X-2 Radial Stress-Strain
Differential Stress [psi]
7000
6000
5000
4000
3000
2000
1000
0
y = -3.689E+07x + 5.669E+02
R² = 9.924E-01
-0.00016
-0.00014
-0.00012
-0.0001
-0.00008
-0.00006
-0.00004
-0.00002
0
Radial Strain [in/in]
E-B-2-X-3
Linear (E-B-2-X-3)

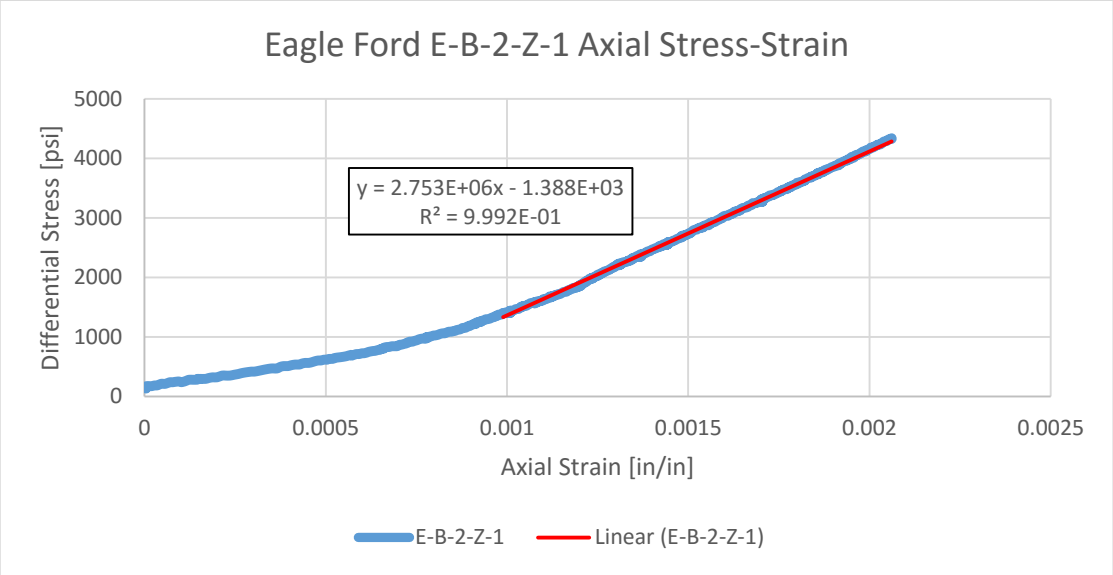
Eagle Ford E-B-2-Z-1 Axial Stress-Strain
Differential Stress [psi]
5000
4000
3000
2000
1000
0
y = 2.753E+06x - 1.388E+03
R² = 9.992E-01
0
0.0005
0.001
0.0015
0.002
0.0025
Axial Strain [in/in]
E-B-2-Z-1
Linear (E-B-2-Z-1)

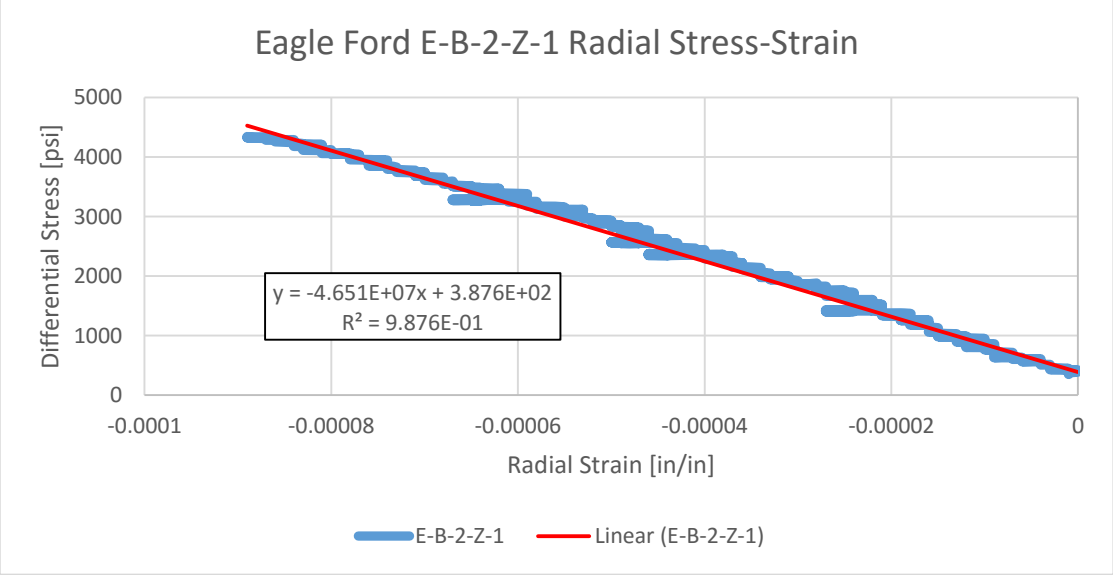
Eagle Ford E-B-2-Z-1 Radial Stress-Strain
Differential Stress [psi]
5000
4000
3000
2000
1000
0
y = -4.651E+07x + 3.876E+02
R² = 9.876E-01
-0.0001
-0.00008
-0.00006
-0.00004
-0.00002
0
Radial Strain [in/in]
E-B-2-Z-1
Linear (E-B-2-Z-1)

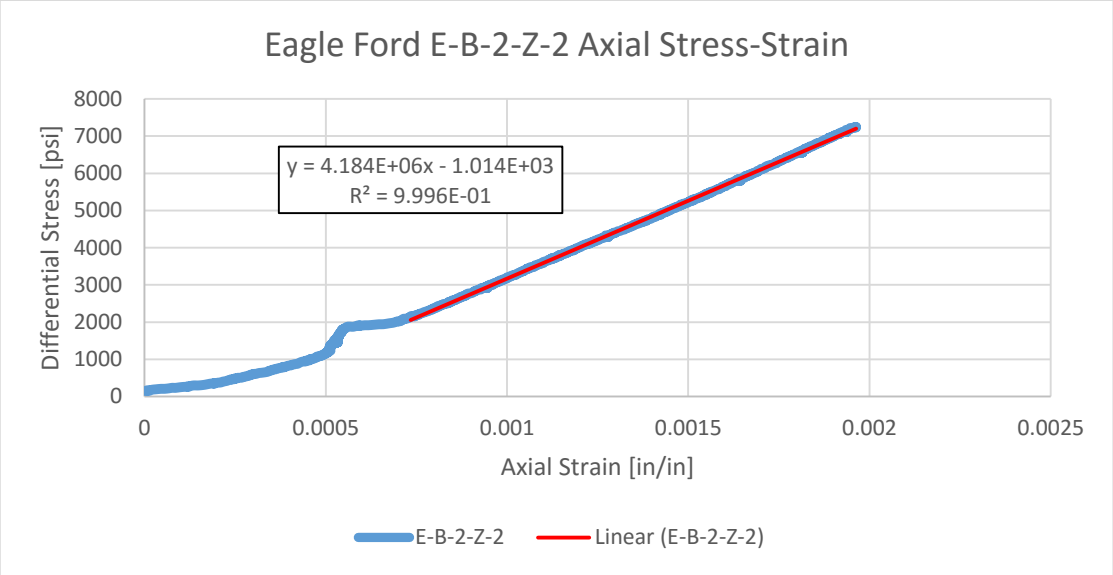
Eagle Ford E-B-2-Z-2 Axial Stress-Strain
Differential Stress [psi]
8000
7000
6000
5000
4000
3000
2000
1000
0
y = 4.184E+06x - 1.014E+03
R² = 9.996E-01
0
0.0005
0.001
0.0015
0.002
0.0025
Axial Strain [in/in]
E-B-2-Z-2
Linear (E-B-2-Z-2)

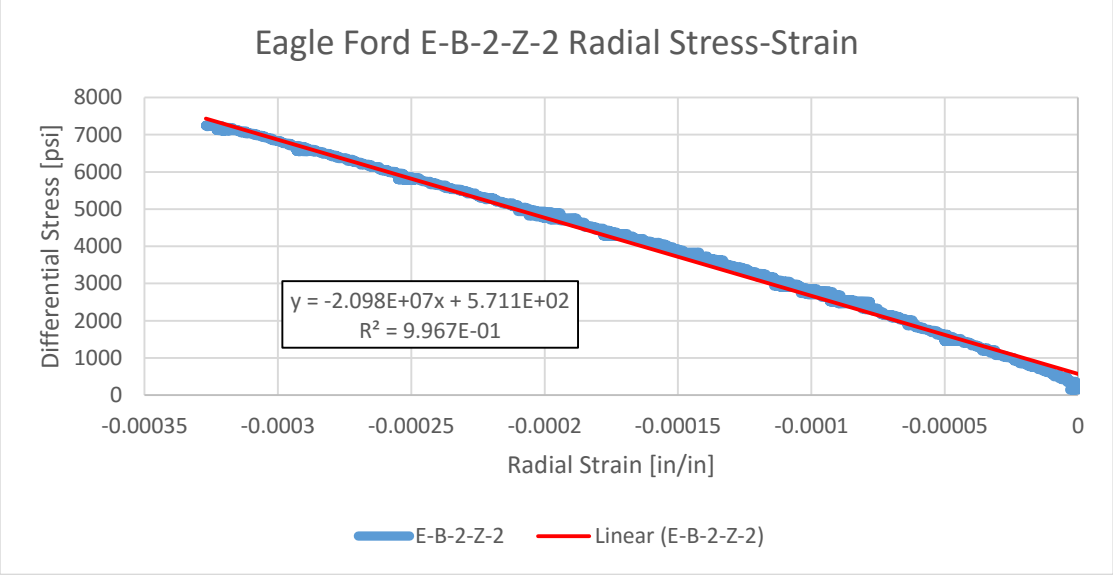
Eagle Ford E-B-2-Z-2 Radial Stress-Strain
Differential Stress [psi]
8000
7000
6000
5000
4000
3000
2000
1000
0
y = -2.098E+07x + 5.711E+02
R² = 9.967E-01
-0.00035
-0.0003
-0.00025
-0.0002
-0.00015
-0.0001
-0.00005
0
Radial Strain [in/in]
E-B-2-Z-2
Linear (E-B-2-Z-2)

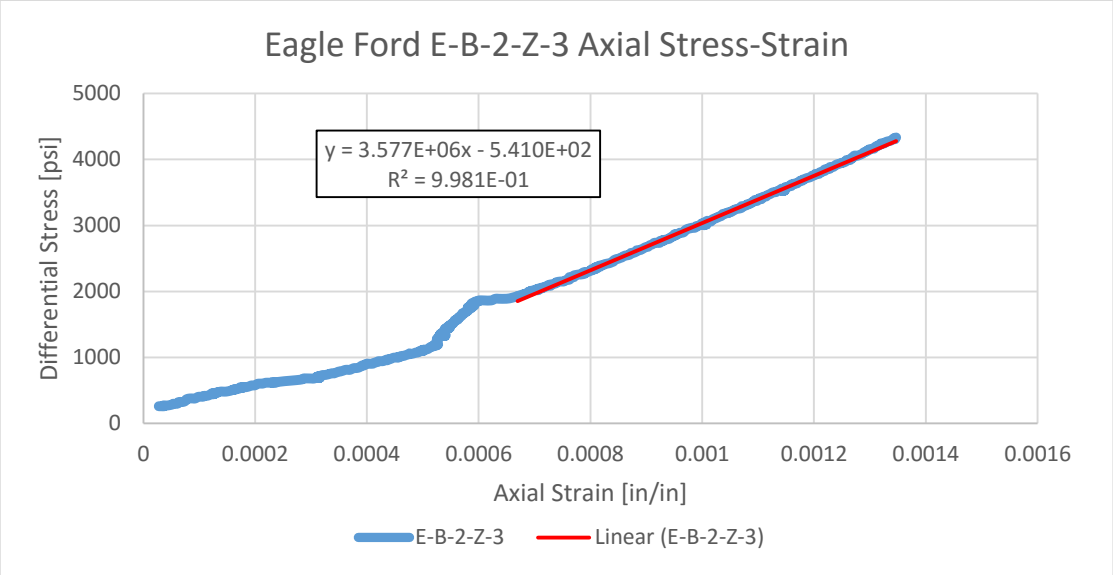
Eagle Ford E-B-2-Z-3 Axial Stress-Strain
y = 3.577E+06x - 5.410E+02
R² = 9.981E-01
Differential Stress [psi]
5000
4000
3000
2000
1000
0
0
0.0002
0.0004
0.0006
0.0008
0.001
0.0012
0.0014
0.0016
Axial Strain [in/in]
E-B-2-Z-3
Linear (E-B-2-Z-3)

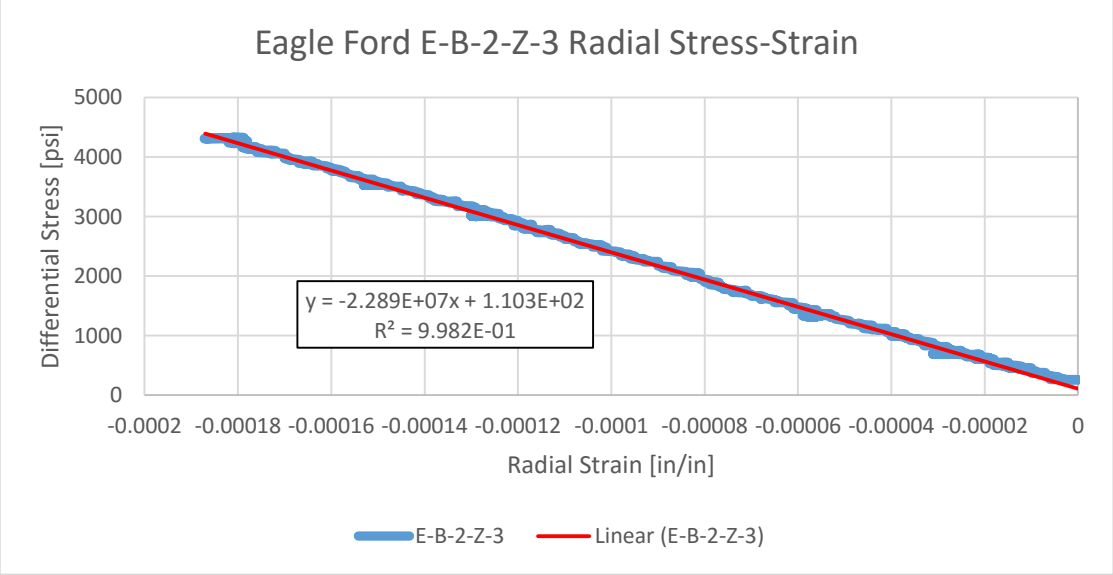
Eagle Ford E-B-2-Z-3 Radial Stress-Strain
y = -2.289E+07x + 1.103E+02
R² = 9.982E-01
Differential Stress [psi]
5000
4000
3000
2000
1000
0
-0.0002
-0.00018
-0.00016
-0.00014
-0.00012
-0.0001
-0.00008
-0.00006
-0.00004
-0.00002
0
Radial Strain [in/in]
E-B-2-Z-3
Linear (E-B-2-Z-3)

Eagle Ford Facie B3

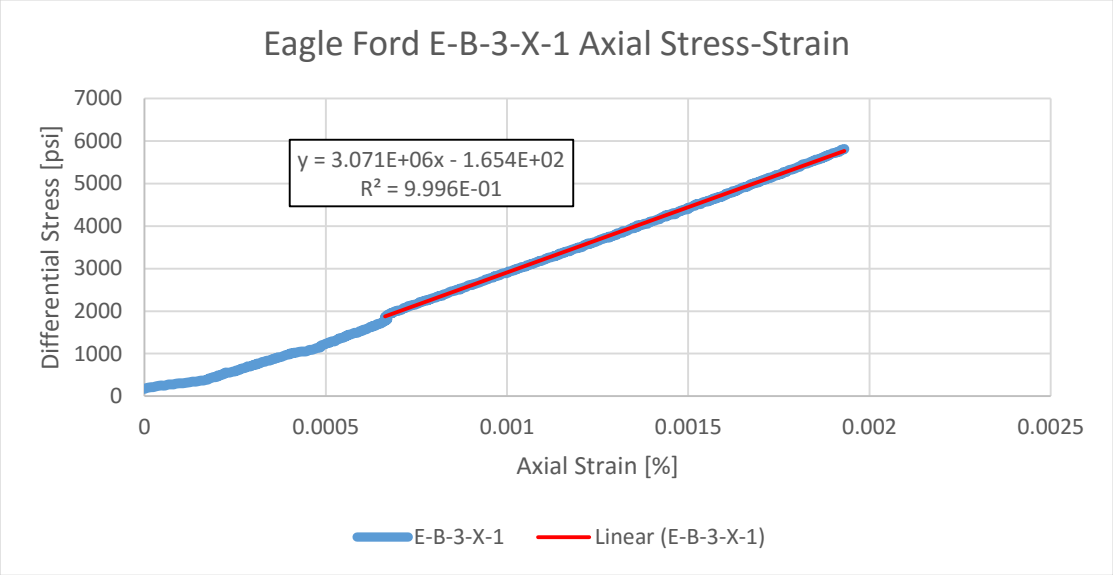

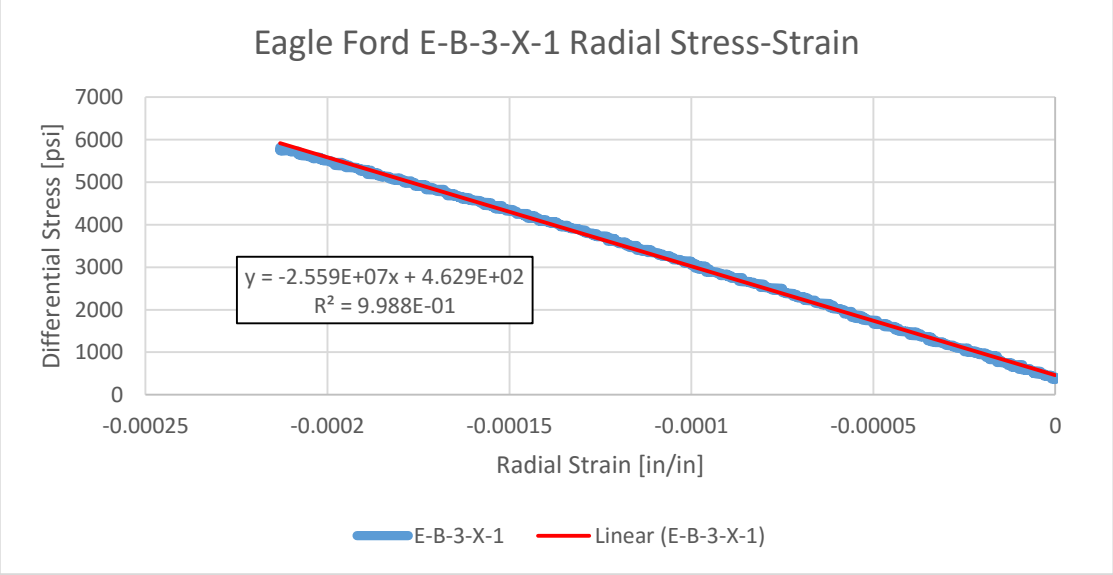

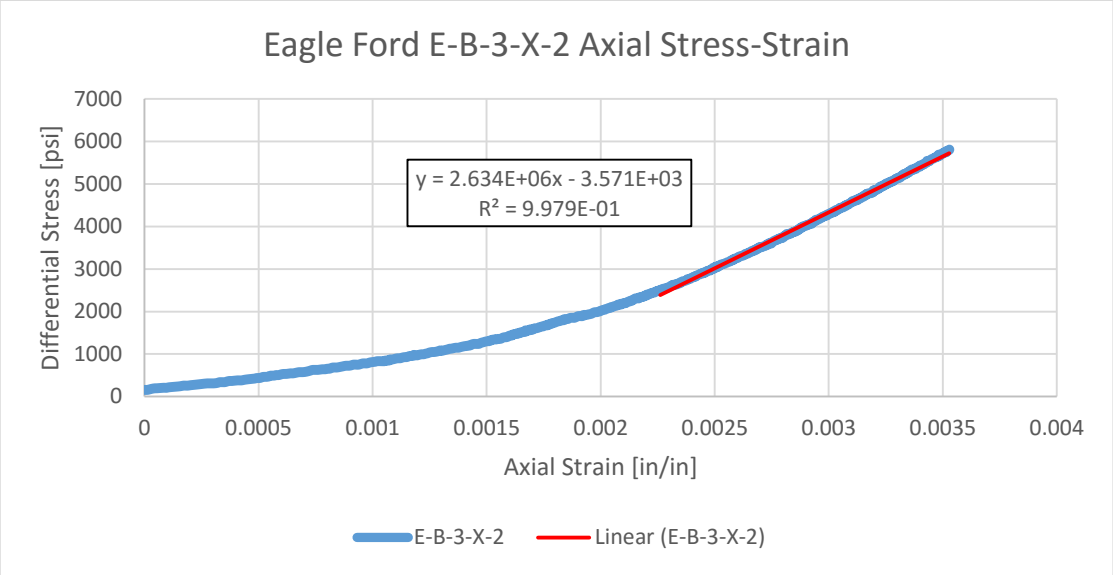
Eagle Ford E-B-3-X-2 Axial Stress-Strain
Differential Stress [psi]
7000
6000
5000
4000
3000
2000
1000
0
y = 2.634E+06x - 3.571E+03
R² = 9.979E-01
0
0.0005
0.001
0.0015
0.002
0.0025
0.003
0.0035
0.004
Axial Strain [in/in]
E-B-3-X-2
Linear (E-B-3-X-2)

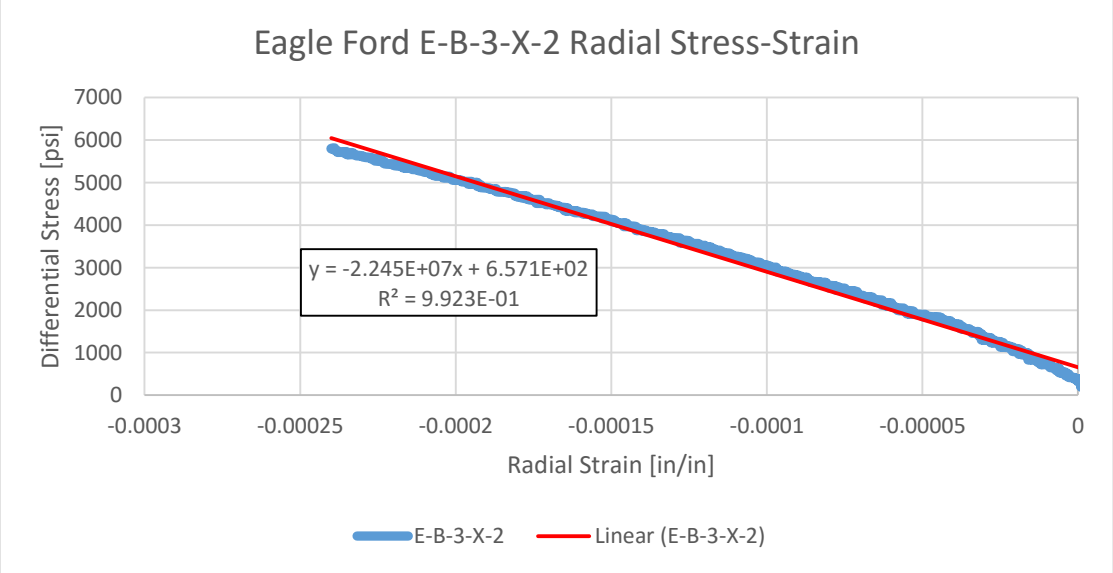
Eagle Ford E-B-3-X-2 Radial Stress-Strain
Differential Stress [psi]
7000
6000
5000
4000
3000
2000
1000
0
y = -2.245E+07x + 6.571E+02
R² = 9.923E-01
-0.0003
-0.00025
-0.0002
-0.00015
-0.0001
-0.00005
0
Radial Strain [in/in]
E-B-3-X-2
Linear (E-B-3-X-2)

Eagle Ford Facies C

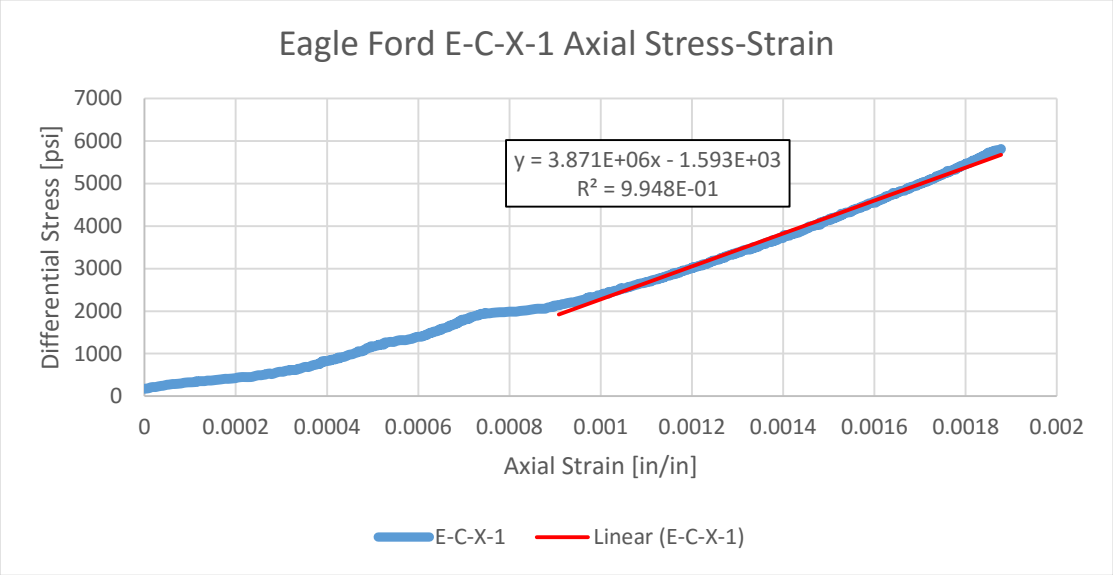

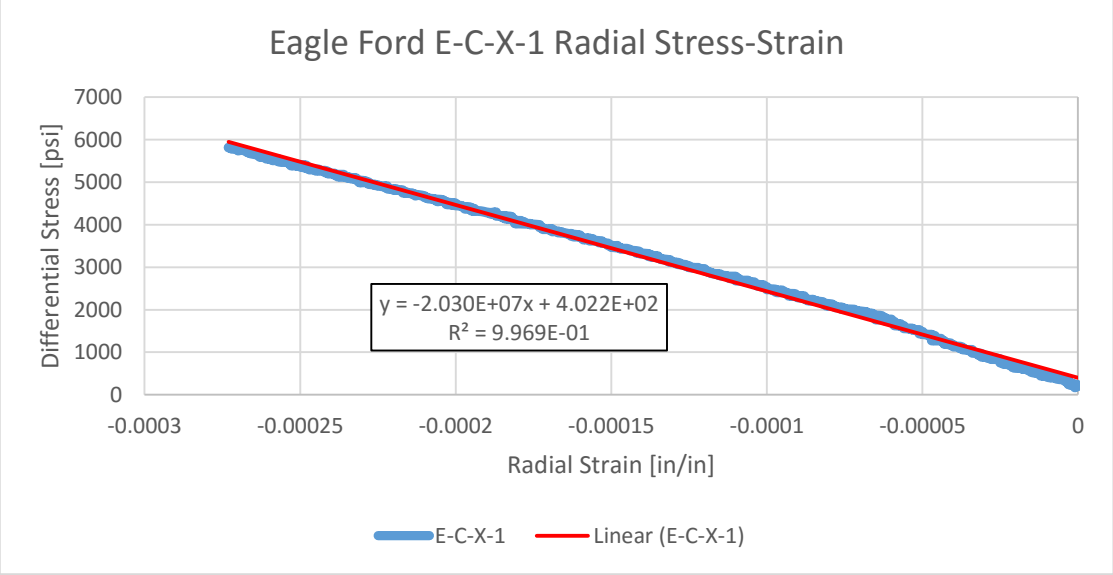

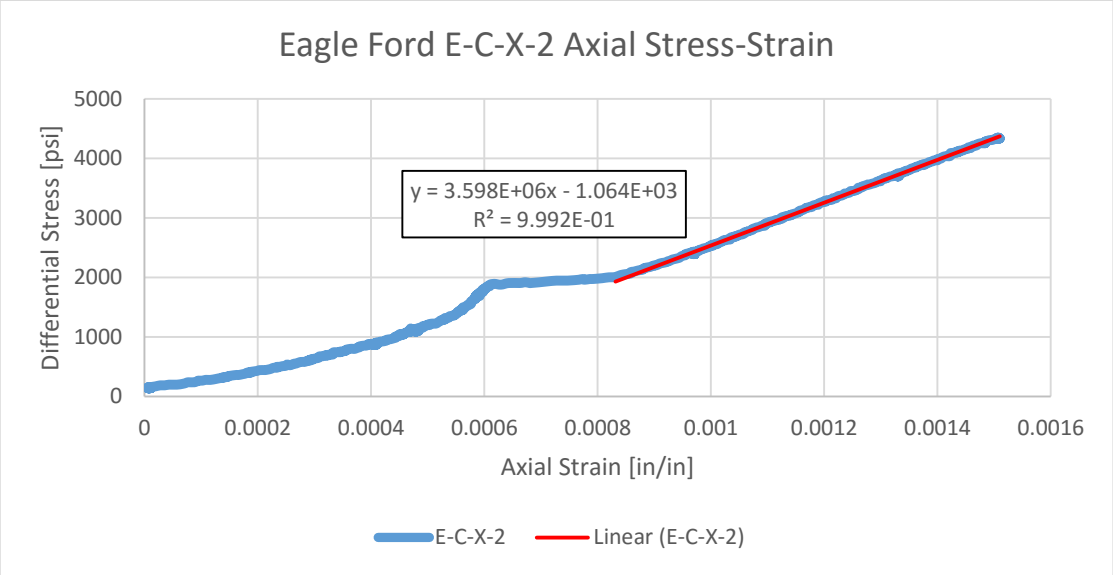
Eagle Ford E-C-X-2 Axial Stress-Strain
Differential Stress [psi]
5000
4000
3000
2000
1000
0
y = 3.598E+06x - 1.064E+03
R² = 9.992E-01
0
0.0002
0.0004
0.0006
0.0008
0.001
0.0012
0.0014
0.0016
Axial Strain [in/in]
E-C-X-2
Linear (E-C-X-2)

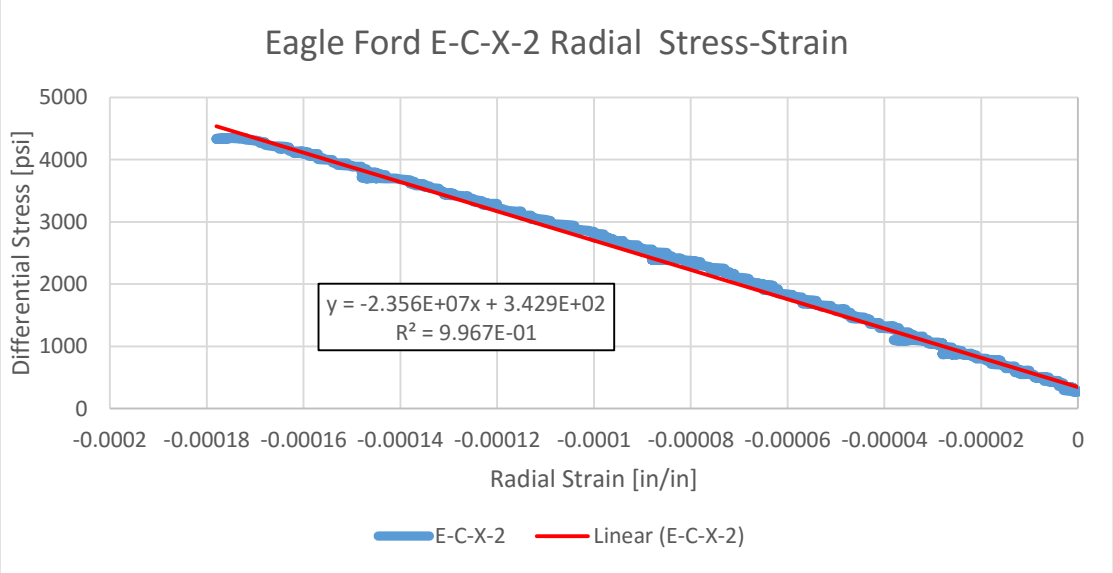
Eagle Ford E-C-X-2 Radial Stress-Strain
Differential Stress [psi]
5000
4000
3000
2000
1000
0
y = -2.356E+07x + 3.429E+02
R² = 9.967E-01
-0.0002
-0.00018
-0.00016
-0.00014
-0.00012
-0.0001
-0.00008
-0.00006
-0.00004
-0.00002
0
Radial Strain [in/in]
E-C-X-2
Linear (E-C-X-2)

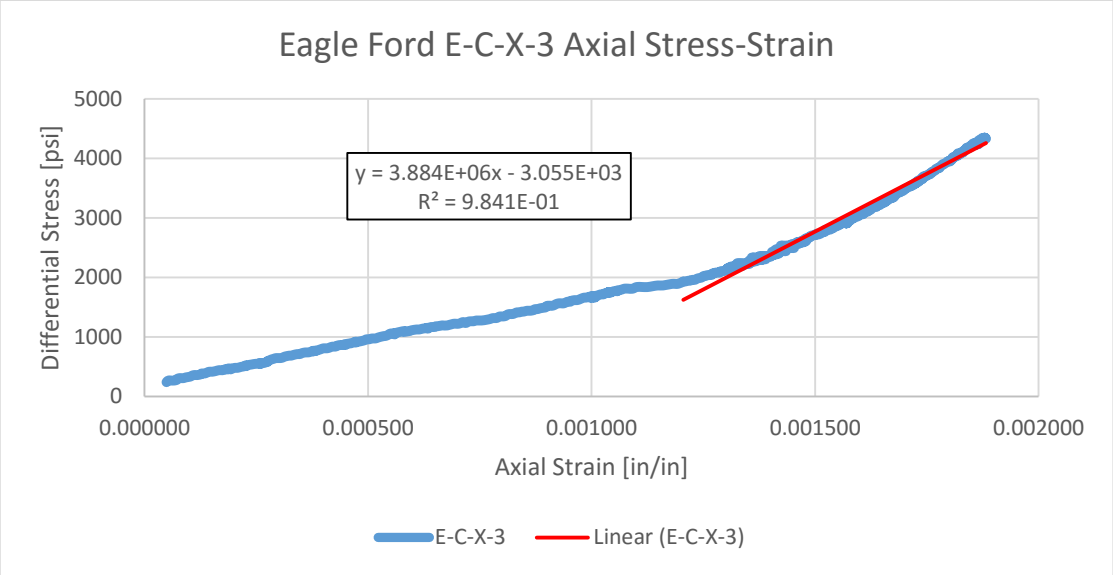
Eagle Ford E-C-X-3 Axial Stress-Strain
Differential Stress [psi]
5000
4000
3000
2000
1000
0
y = 3.884E+06x - 3.055E+03
R² = 9.841E-01
0.000000
0.000500
0.001000
0.001500
0.002000
Axial Strain [in/in]
E-C-X-3
Linear (E-C-X-3)

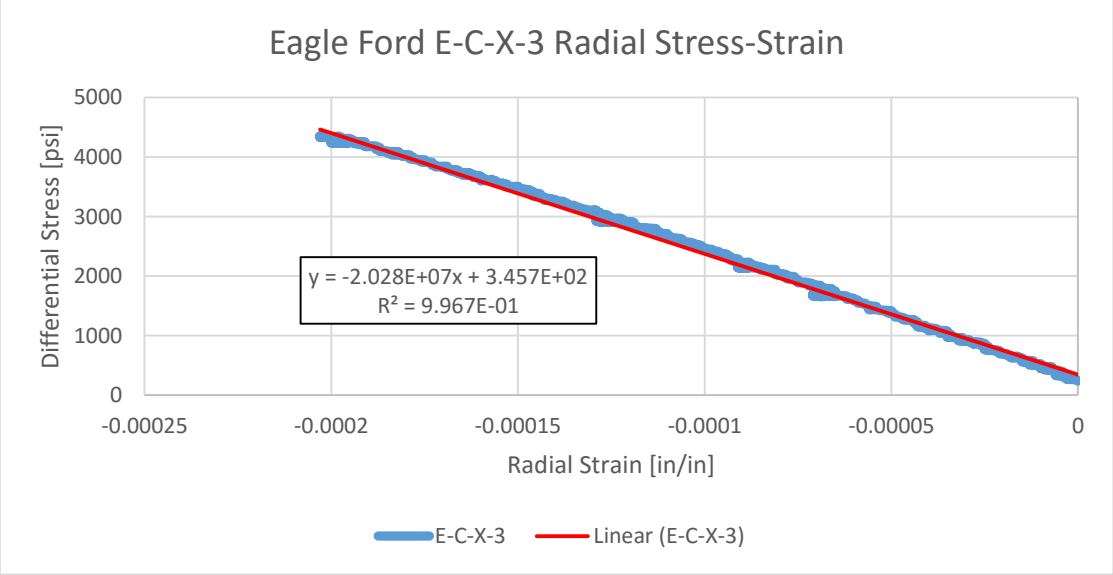
Eagle Ford E-C-X-3 Radial Stress-Strain
Differential Stress [psi]
5000
4000
3000
2000
1000
0
y = -2.028E+07x + 3.457E+02
R² = 9.967E-01
-0.00025
-0.0002
-0.00015
-0.0001
-0.00005
0
Radial Strain [in/in]
E-C-X-3
Linear (E-C-X-3)

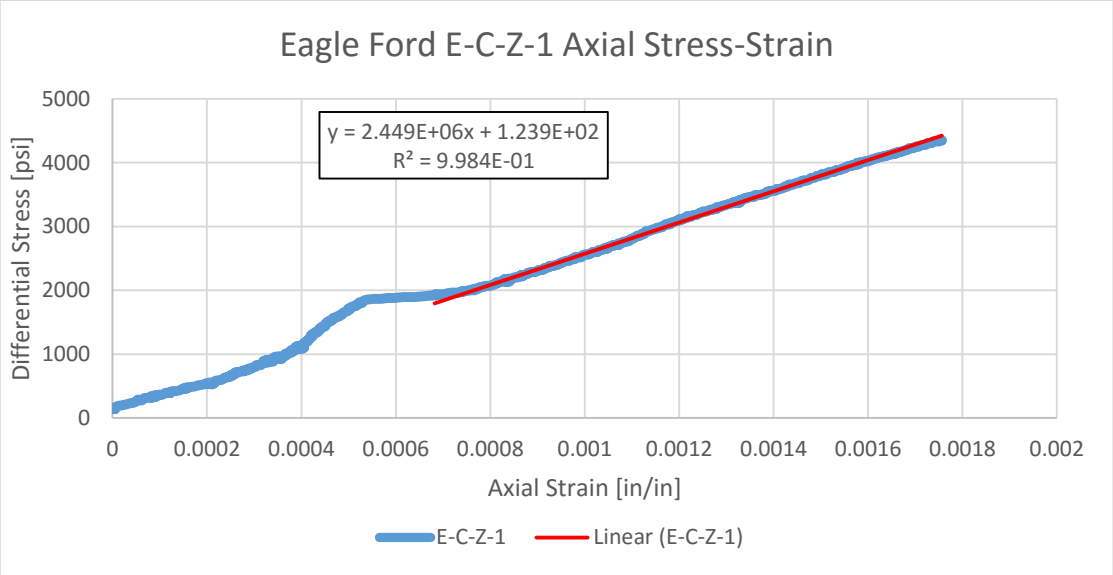
Eagle Ford E-C-Z-1 Axial Stress-Strain
y = 2.449E+06x + 1.239E+02
R² = 9.984E-01
Differential Stress [psi]
5000
4000
3000
2000
1000
0
0
0.0002
0.0004
0.0006
0.0008
0.001
0.0012
0.0014
0.0016
0.0018
0.002
Axial Strain [in/in]
E-C-Z-1
Linear (E-C-Z-1)

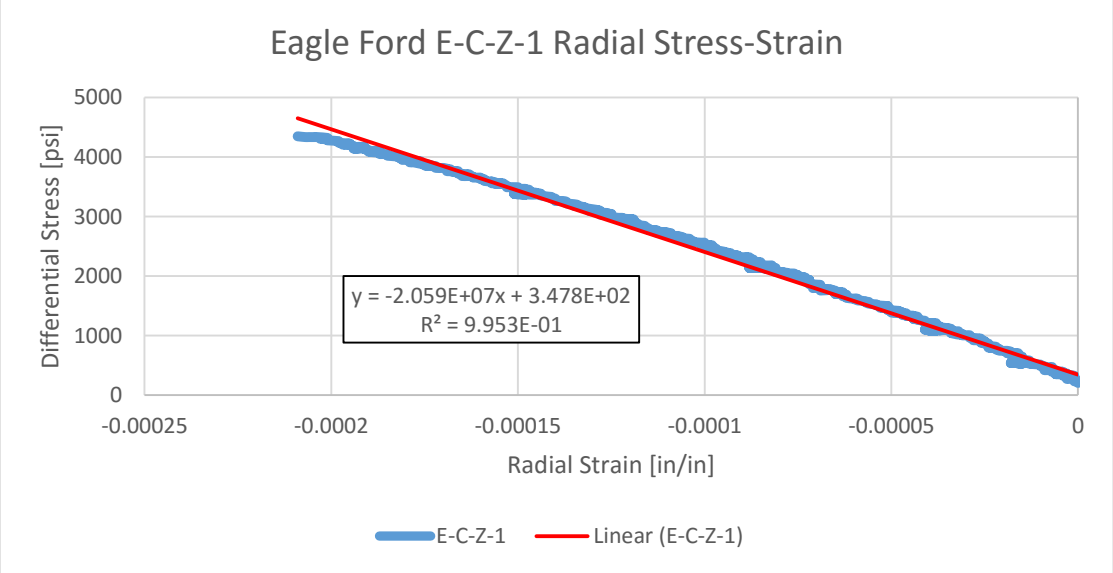
Eagle Ford E-C-Z-1 Radial Stress-Strain
y = -2.059E+07x + 3.478E+02
R² = 9.953E-01
Differential Stress [psi]
5000
4000
3000
2000
1000
0
-0.00025
-0.0002
-0.00015
-0.0001
-0.00005
0
Radial Strain [in/in]
E-C-Z-1
Linear (E-C-Z-1)

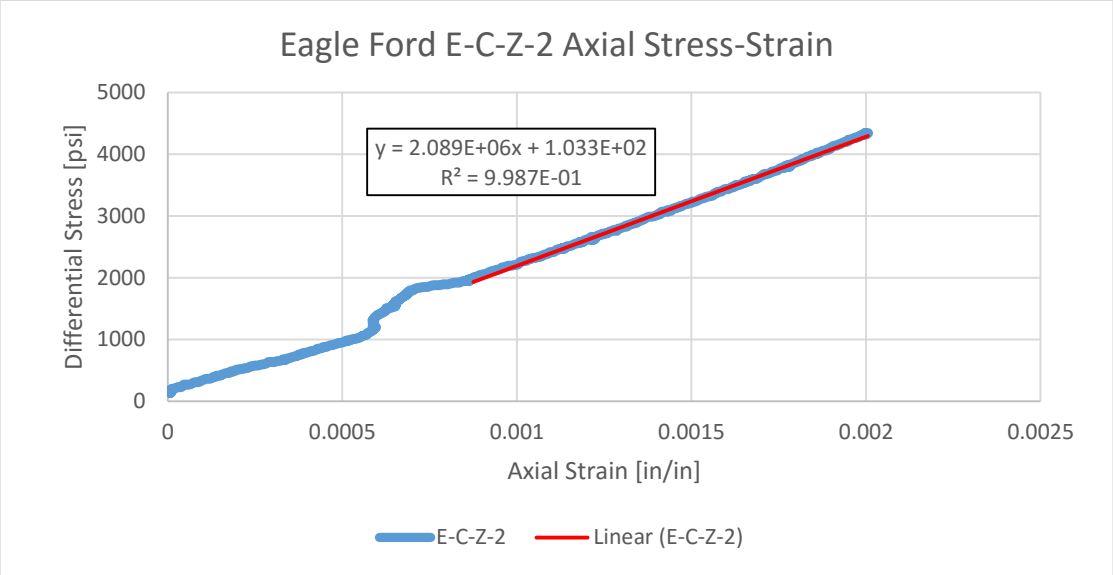
Eagle Ford E-C-Z-2 Axial Stress-Strain
y = 2.089E+06x + 1.033E+02
R² = 9.987E-01
Differential Stress [psi]
5000
4000
3000
2000
1000
0
0
0.0005
0.001
0.0015
0.002
0.0025
Axial Strain [in/in]
E-C-Z-2
Linear (E-C-Z-2)

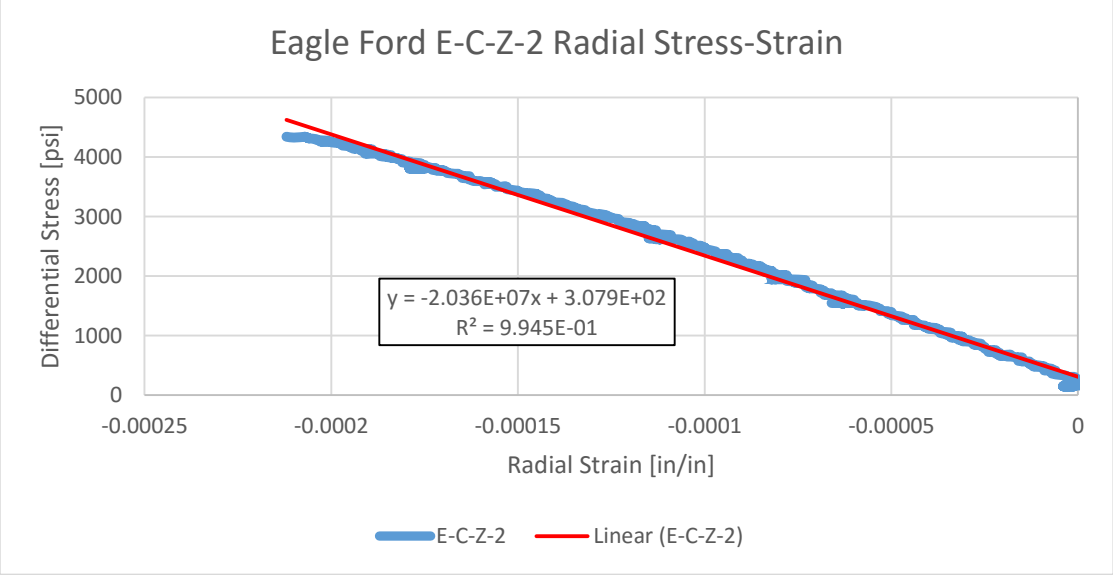
Eagle Ford E-C-Z-2 Radial Stress-Strain
y = -2.036E+07x + 3.079E+02
R² = 9.945E-01
Differential Stress [psi]
5000
4000
3000
2000
1000
0
-0.00025
-0.0002
-0.00015
-0.0001
-0.00005
0
Radial Strain [in/in]
E-C-Z-2
Linear (E-C-Z-2)

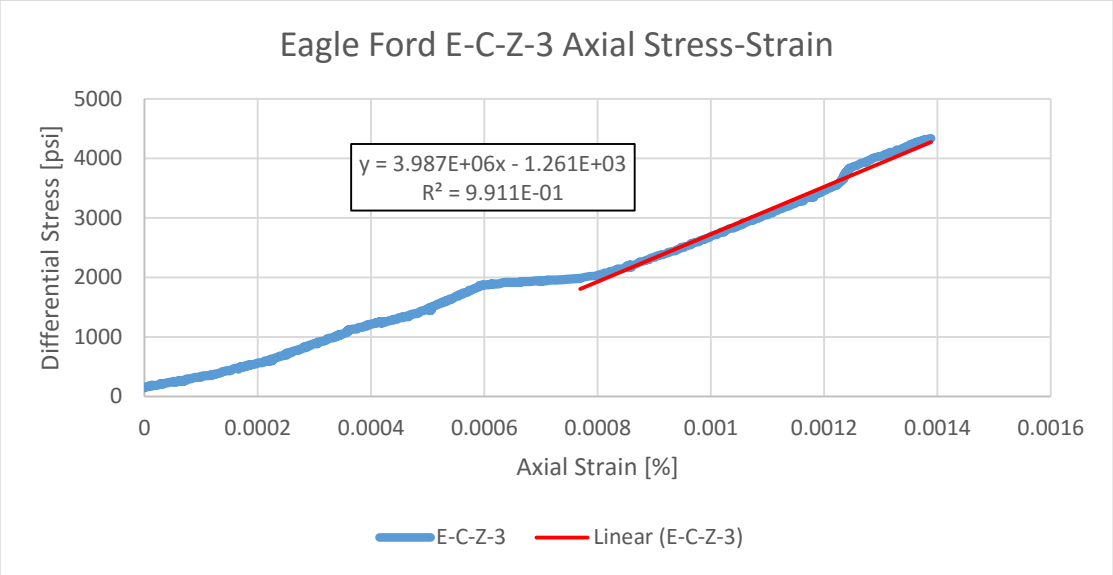
Eagle Ford E-C-Z-3 Axial Stress-Strain
y = 3.987E+06x - 1.261E+03
R² = 9.911E-01
Differential Stress [psi]
5000
4000
3000
2000
1000
0
0
0.0002
0.0004
0.0006
0.0008
0.001
0.0012
0.0014
0.0016
Axial Strain [%]
E-C-Z-3
Linear (E-C-Z-3)

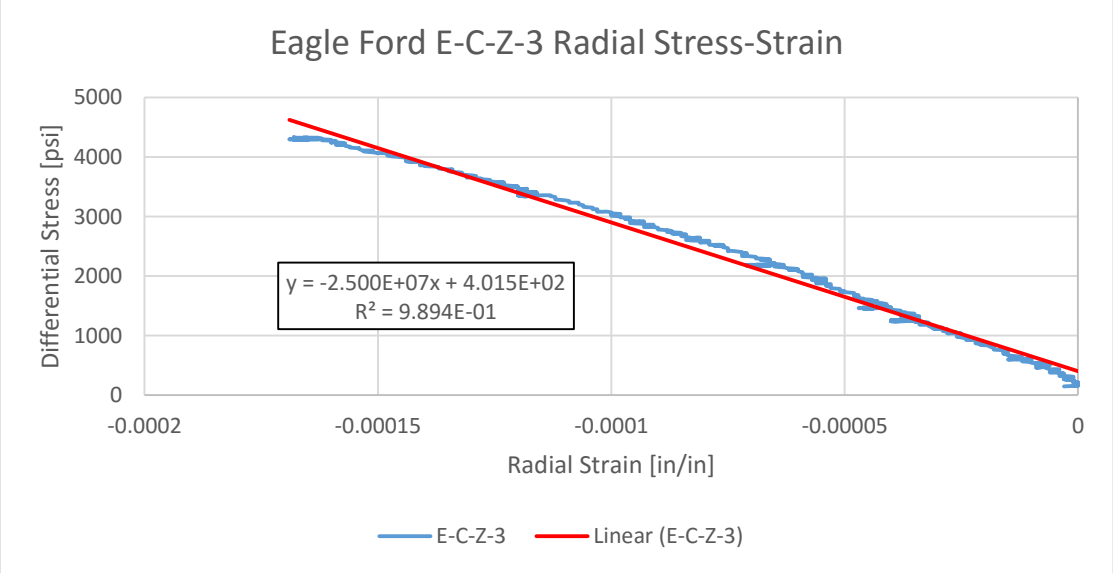
Eagle Ford E-C-Z-3 Radial Stress-Strain
y = -2.500E+07x + 4.015E+02
R² = 9.894E-01
Differential Stress [psi]
5000
4000
3000
2000
1000
0
-0.0002
-0.00015
-0.0001
-0.00005
0
Radial Strain [in/in]
E-C-Z-3
Linear (E-C-Z-3)

Eagle Ford Facies D

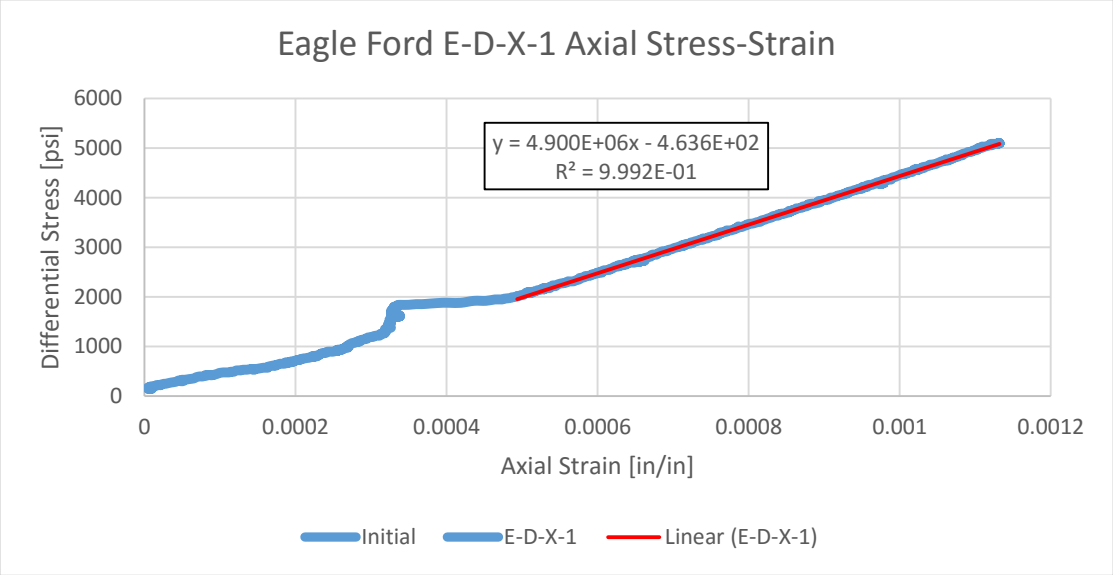

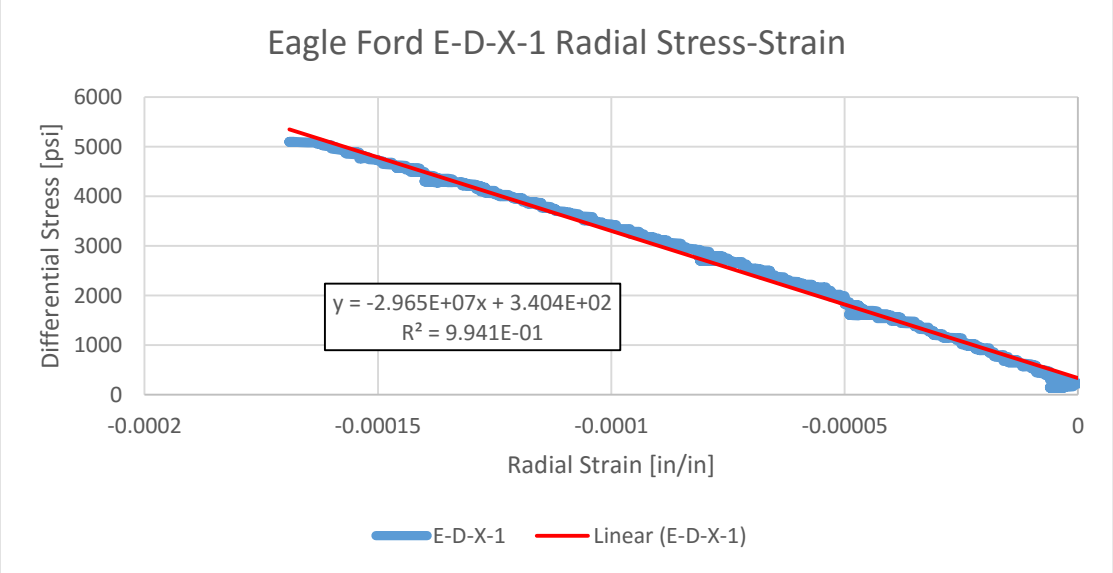

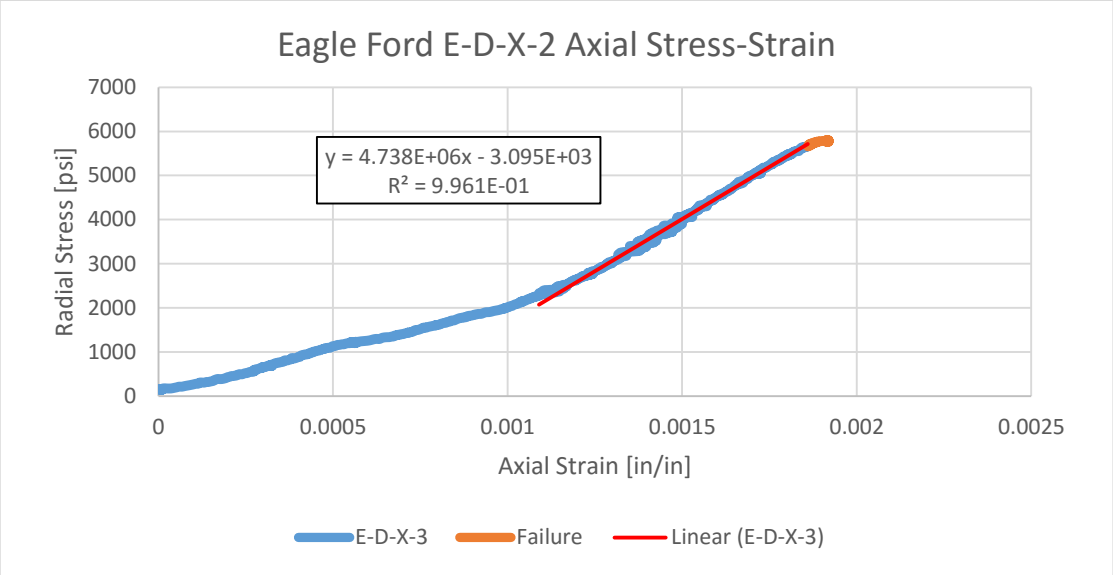
Eagle Ford E-D-X-2 Axial Stress-Strain
y = 4.738E+06x - 3.095E+03
R² = 9.961E-01
Radial Stress [psi]
7000
6000
5000
4000
3000
2000
1000
0
0
0.0005
0.001
0.0015
0.002
0.0025
Axial Strain [in/in]
E-D-X-3
Failure
Linear (E-D-X-3)

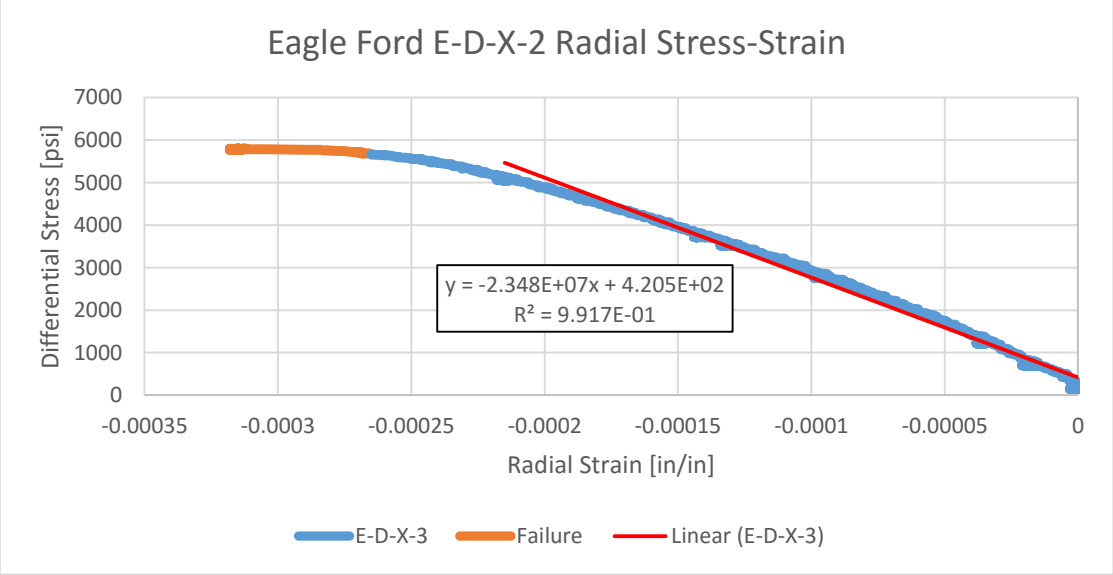
Eagle Ford E-D-X-2 Radial Stress-Strain
y = -2.348E+07x + 4.205E+02
R² = 9.917E-01
Differential Stress [psi]
7000
6000
5000
4000
3000
2000
1000
0
-0.00035
-0.0003
-0.00025
-0.0002
-0.00015
-0.0001
-0.00005
0
Radial Strain [in/in]
E-D-X-3
Failure
Linear (E-D-X-3)

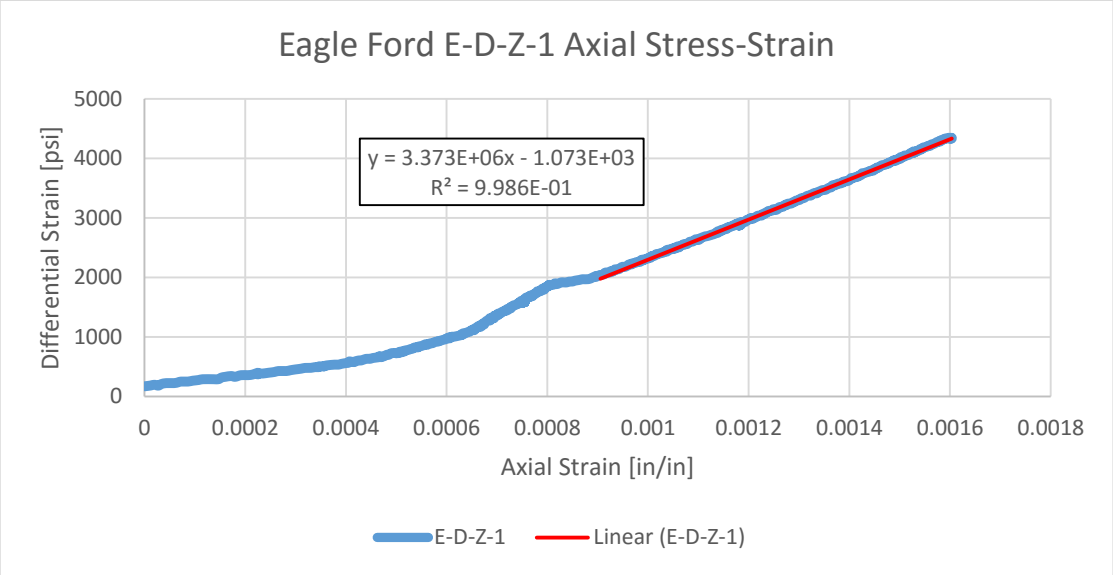
Eagle Ford E-D-Z-1 Axial Stress-Strain
y = 3.373E+06x - 1.073E+03
R² = 9.986E-01
Differential Strain [psi]
5000
4000
3000
2000
1000
0
0
0.0002
0.0004
0.0006
0.0008
0.001
0.0012
0.0014
0.0016
0.0018
Axial Strain [in/in]
E-D-Z-1
Linear (E-D-Z-1)

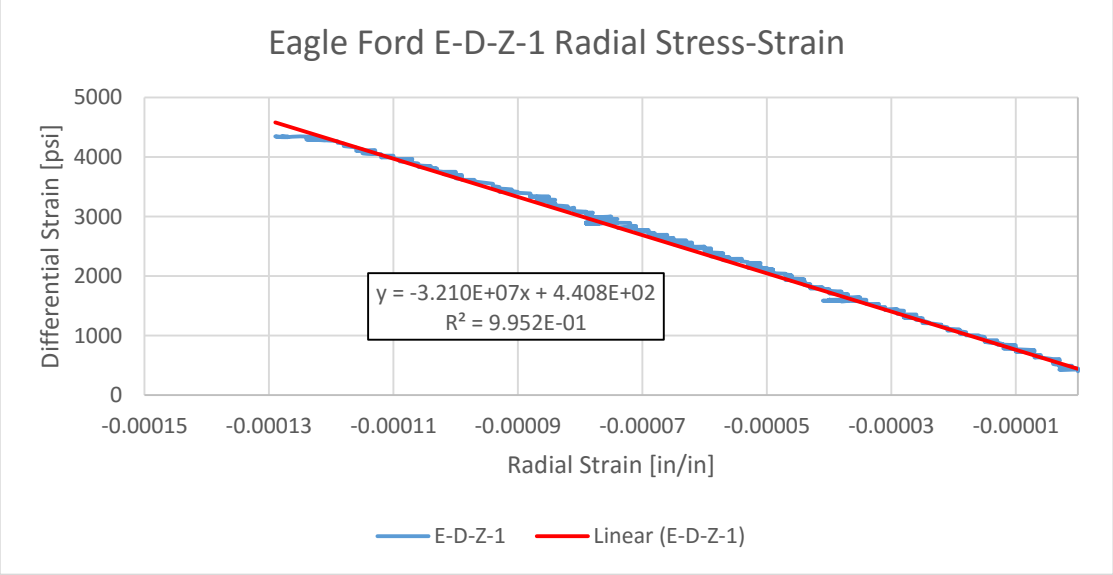
Eagle Ford E-D-Z-1 Radial Stress-Strain
y = -3.210E+07x + 4.408E+02
R² = 9.952E-01
Differential Strain [psi]
5000
4000
3000
2000
1000
0
-0.00015
-0.00013
-0.00011
-0.00009
-0.00007
-0.00005
-0.00003
-0.00001
Radial Strain [in/in]
E-D-Z-1
Linear (E-D-Z-1)

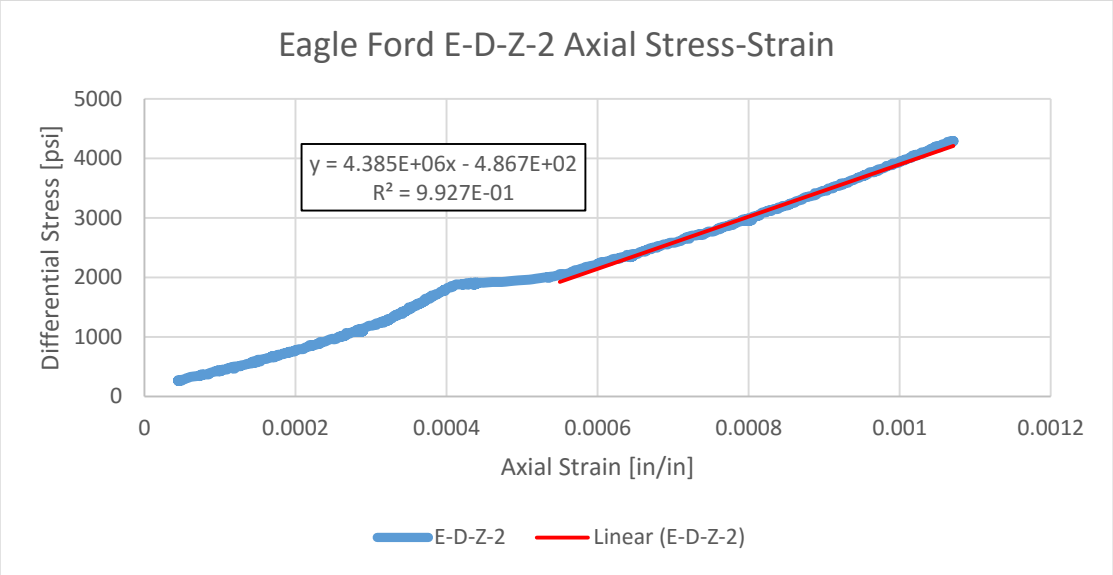
Eagle Ford E-D-Z-2 Axial Stress-Strain
Differential Stress [psi]
5000
4000
3000
2000
1000
0
y = 4.385E+06x - 4.867E+02
R² = 9.927E-01
0
0.0002
0.0004
0.0006
0.0008
0.001
0.0012
Axial Strain [in/in]
E-D-Z-2
Linear (E-D-Z-2)

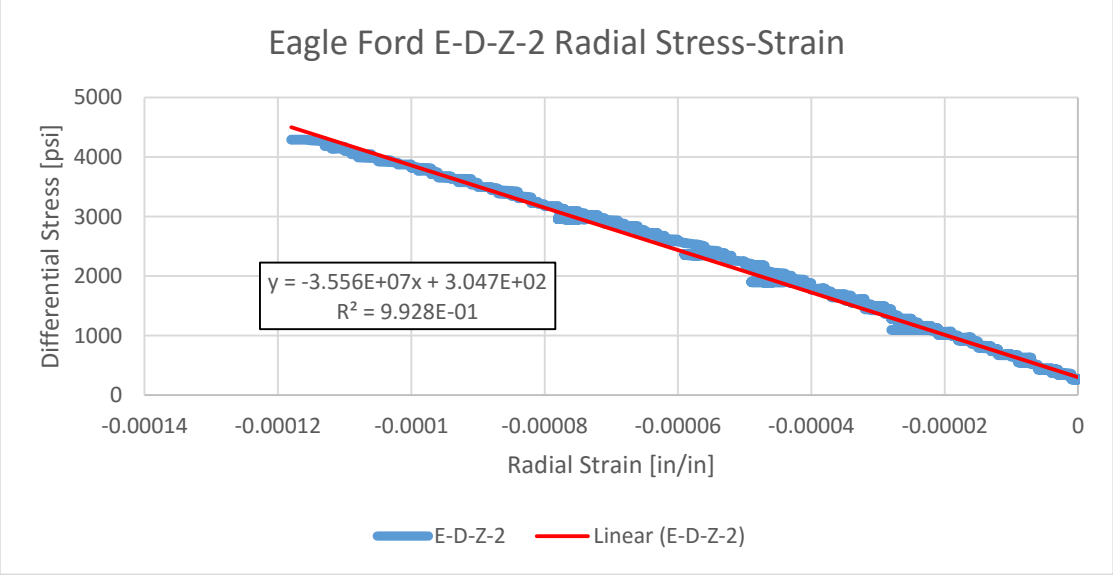
Eagle Ford E-D-Z-2 Radial Stress-Strain
Differential Stress [psi]
5000
4000
3000
2000
1000
0
y = -3.556E+07x + 3.047E+02
R² = 9.928E-01
-0.00014
-0.00012
-0.0001
-0.00008
-0.00006
-0.00004
-0.00002
0
Radial Strain [in/in]
E-D-Z-2
Linear (E-D-Z-2)

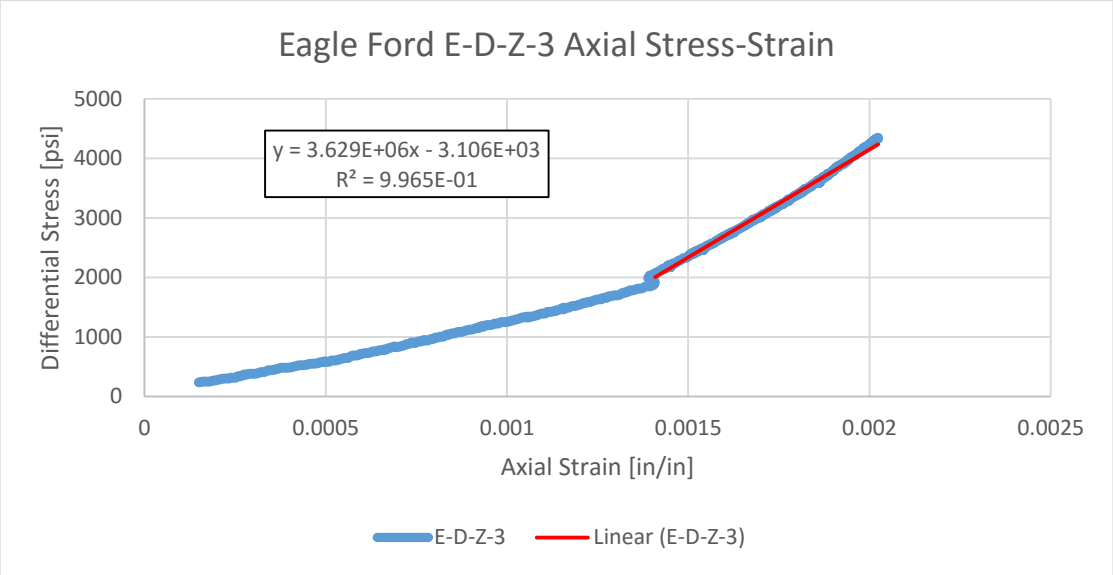
Eagle Ford E-D-Z-3 Axial Stress-Strain
y = 3.629E+06x - 3.106E+03
R² = 9.965E-01
Differential Stress [psi]
5000
4000
3000
2000
1000
0
0
0.0005
0.001
0.0015
0.002
0.0025
Axial Strain [in/in]
E-D-Z-3
Linear (E-D-Z-3)

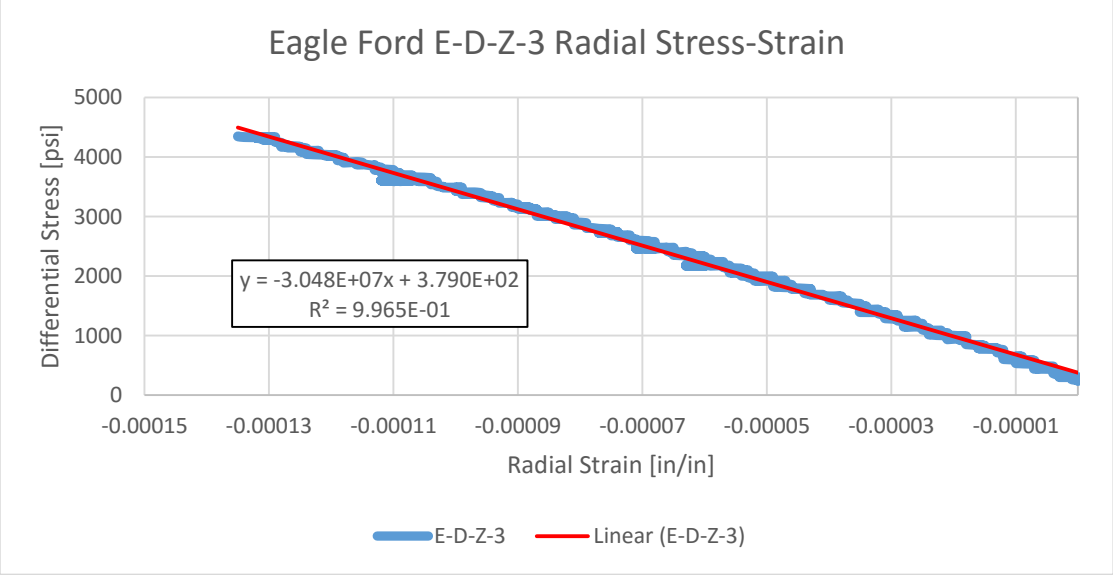
Eagle Ford E-D-Z-3 Radial Stress-Strain
y = -3.048E+07x + 3.790E+02
R² = 9.965E-01
Differential Stress [psi]
5000
4000
3000
2000
1000
0
-0.00015
-0.00013
-0.00011
-0.00009
-0.00007
-0.00005
-0.00003
-0.00001
Radial Strain [in/in]
E-D-Z-3
Linear (E-D-Z-3)

Eagle Ford Facies E

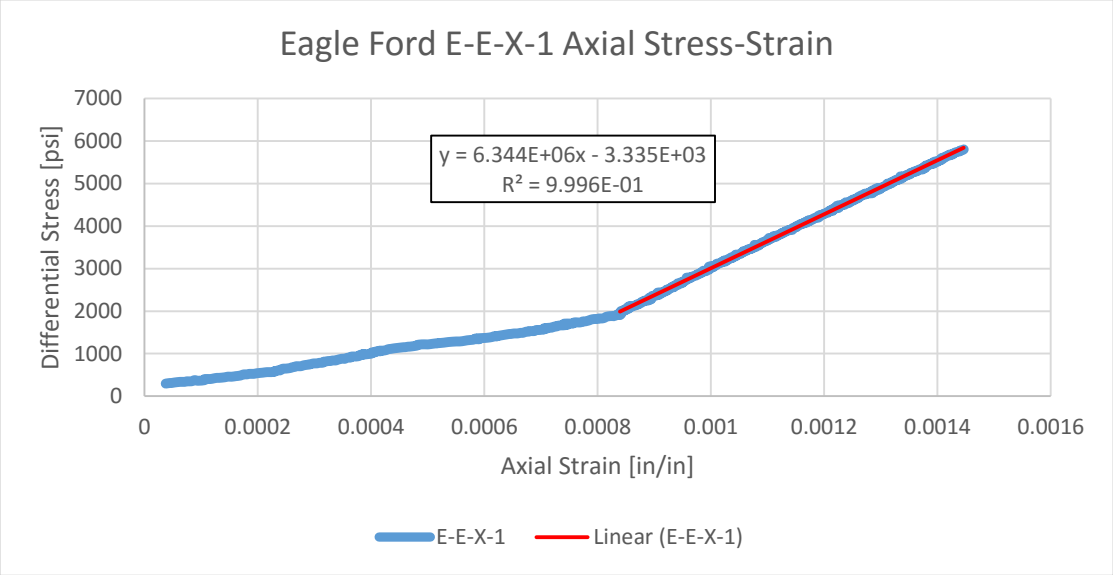

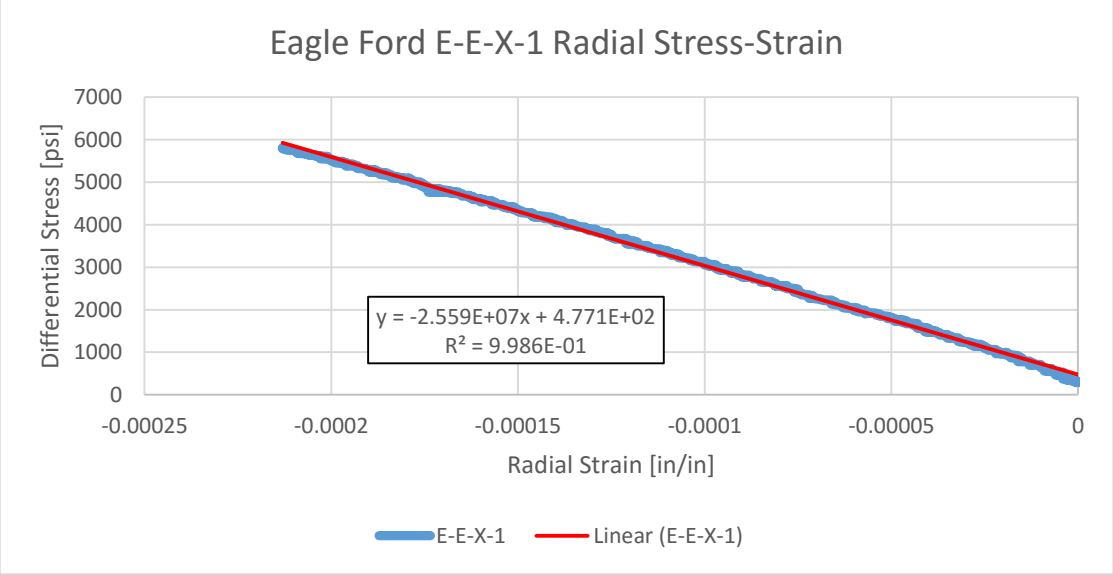

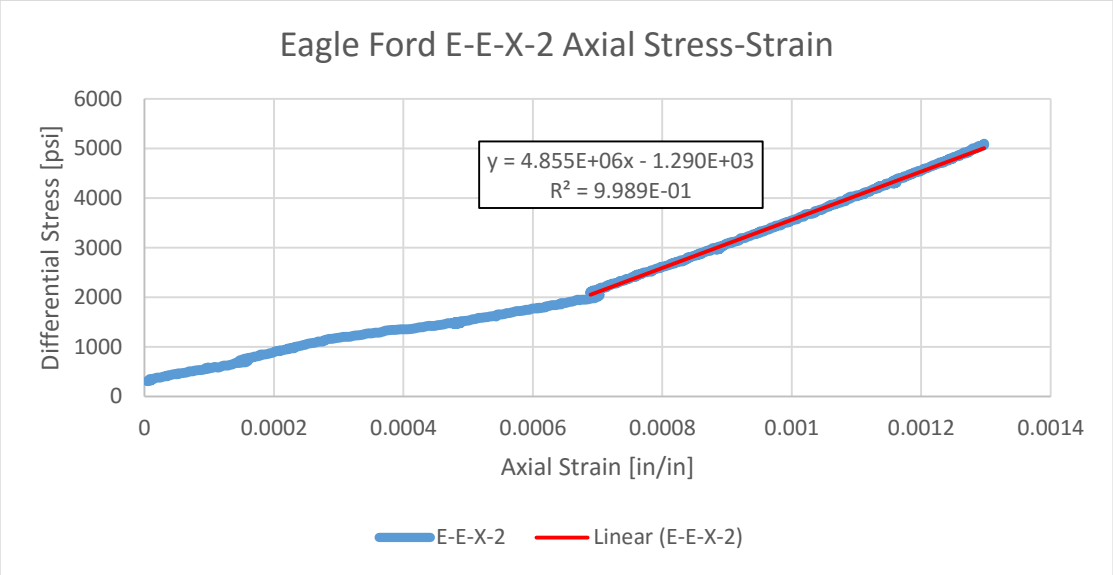
Eagle Ford E-E-X-2 Axial Stress-Strain
Differential Stress [psi]
6000
5000
4000
3000
2000
1000
0
y = 4.855E+06x - 1.290E+03
R² = 9.989E-01
0
0.0002
0.0004
0.0006
0.0008
0.001
0.0012
0.0014
Axial Strain [in/in]
E-E-X-2
Linear (E-E-X-2)

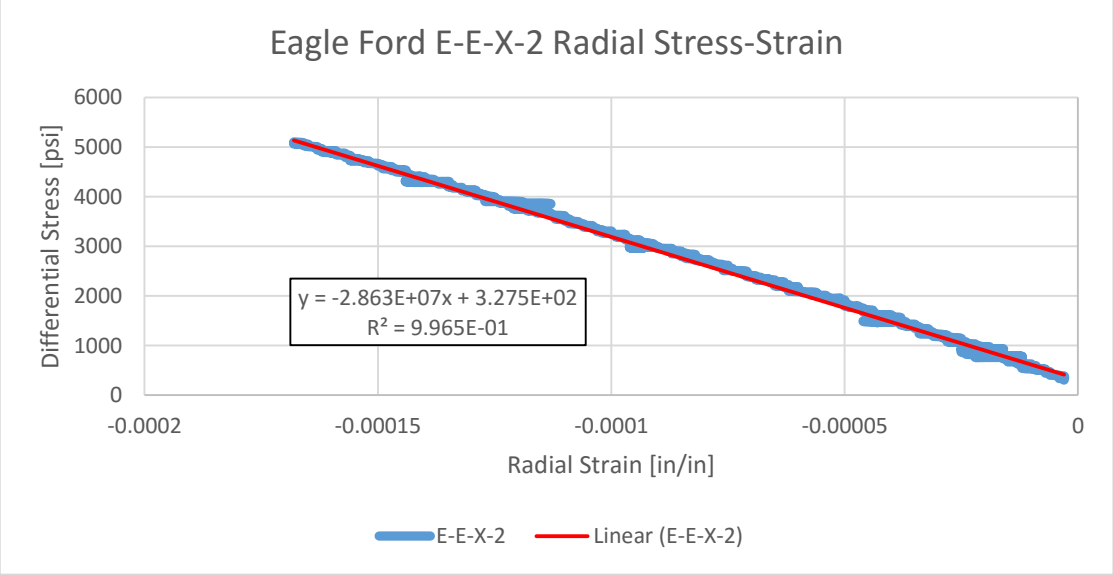
Eagle Ford E-E-X-2 Radial Stress-Strain
Differential Stress [psi]
6000
5000
4000
3000
2000
1000
0
y = -2.863E+07x + 3.275E+02
R² = 9.965E-01
-0.0002
-0.00015
-0.0001
-0.00005
0
Radial Strain [in/in]
E-E-X-2
Linear (E-E-X-2)

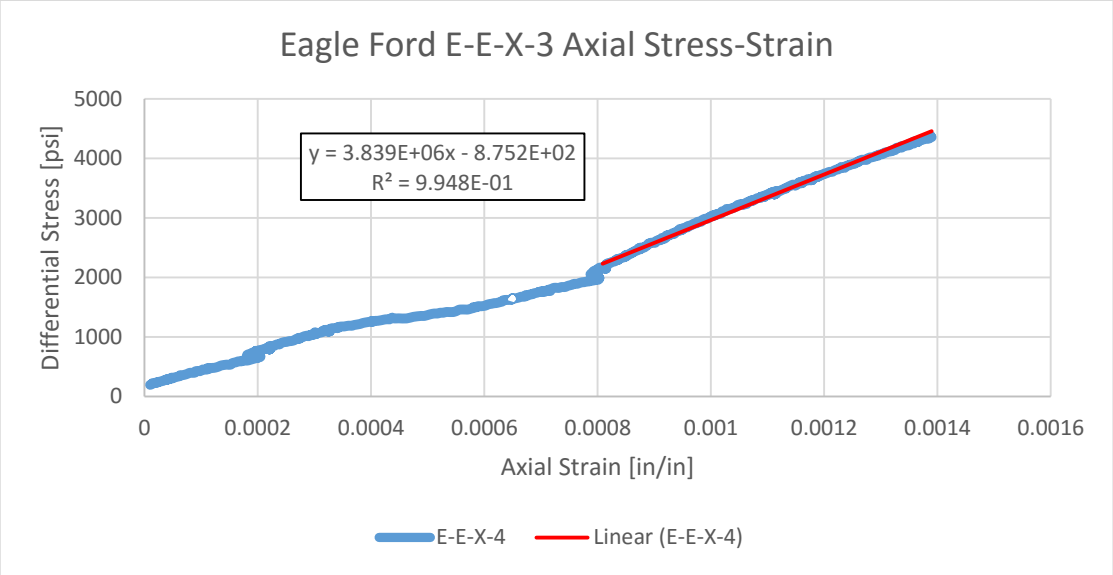
Eagle Ford E-E-X-3 Axial Stress-Strain
y = 3.839E+06x - 8.752E+02
R² = 9.948E-01
Differential Stress [psi]
5000
4000
3000
2000
1000
0
0
0.0002
0.0004
0.0006
0.0008
0.001
0.0012
0.0014
0.0016
Axial Strain [in/in]
E-E-X-4
Linear (E-E-X-4)

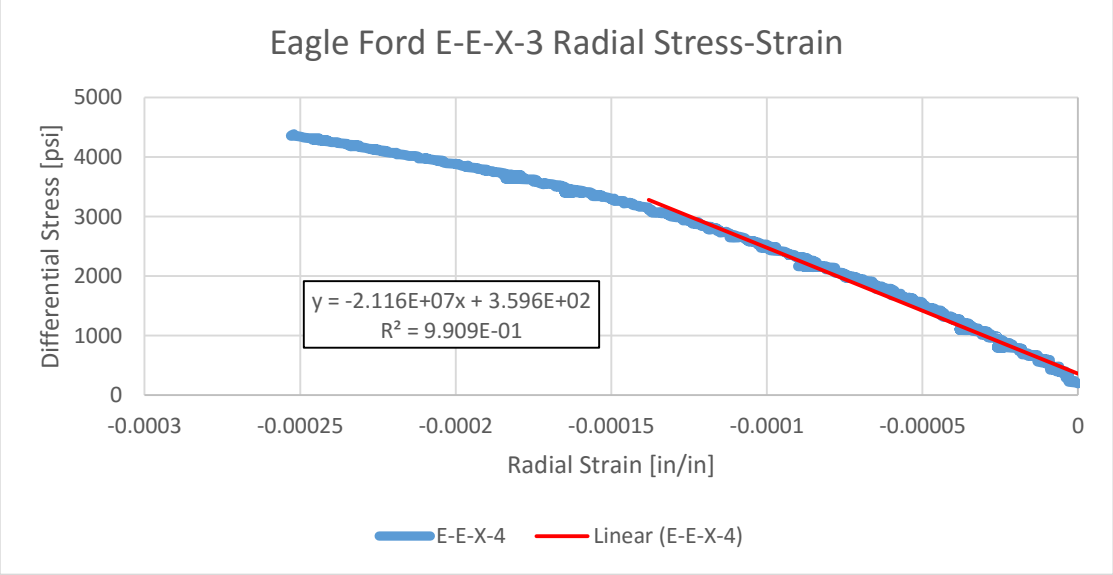
Eagle Ford E-E-X-3 Radial Stress-Strain
y = -2.116E+07x + 3.596E+02
R² = 9.909E-01
Differential Stress [psi]
5000
4000
3000
2000
1000
0
-0.0003
-0.00025
-0.0002
-0.00015
-0.0001
-0.00005
0
Radial Strain [in/in]
E-E-X-4
Linear (E-E-X-4)

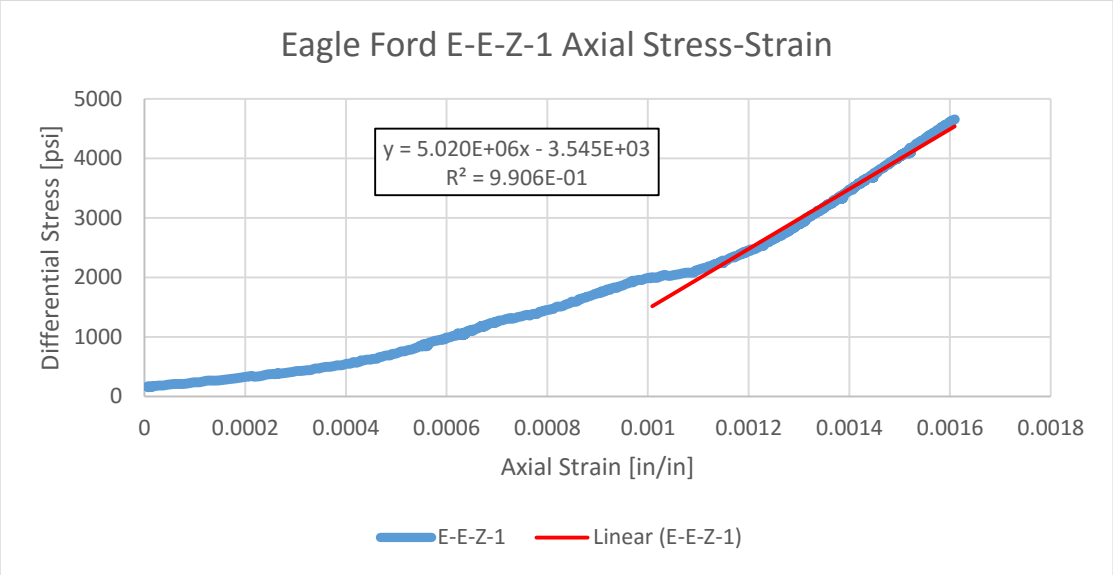
Eagle Ford E-E-Z-1 Axial Stress-Strain
y = 5.020E+06x - 3.545E+03
R² = 9.906E-01
Differential Stress [psi]
5000
4000
3000
2000
1000
0
0
0.0002
0.0004
0.0006
0.0008
0.001
0.0012
0.0014
0.0016
0.0018
Axial Strain [in/in]
E-E-Z-1
Linear (E-E-Z-1)

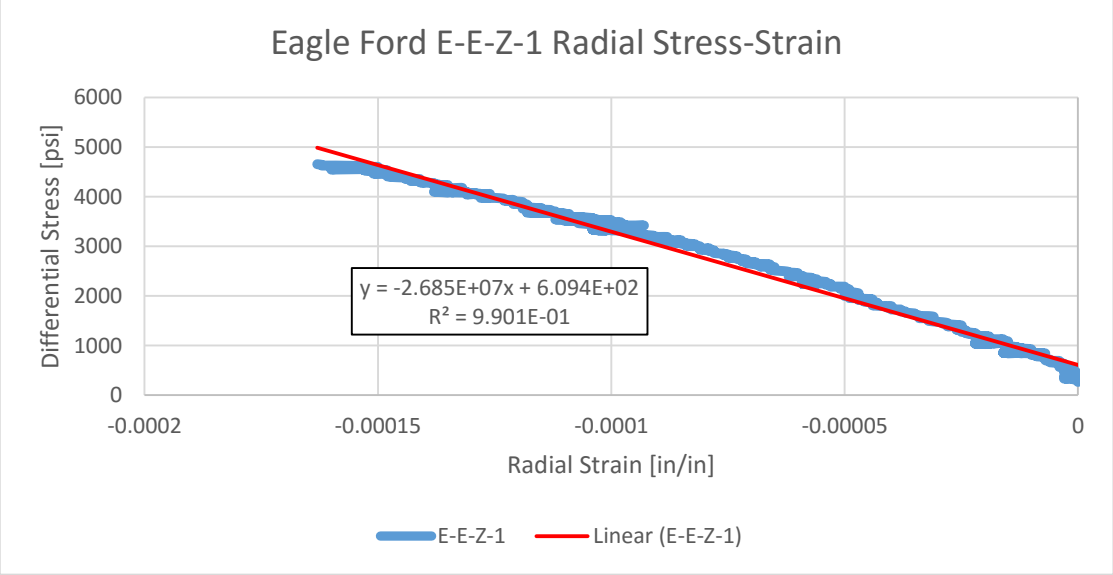
Eagle Ford E-E-Z-1 Radial Stress-Strain
y = -2.685E+07x + 6.094E+02
R² = 9.901E-01
Differential Stress [psi]
6000
5000
4000
3000
2000
1000
0
-0.0002
-0.00015
-0.0001
-0.00005
0
Radial Strain [in/in]
E-E-Z-1
Linear (E-E-Z-1)

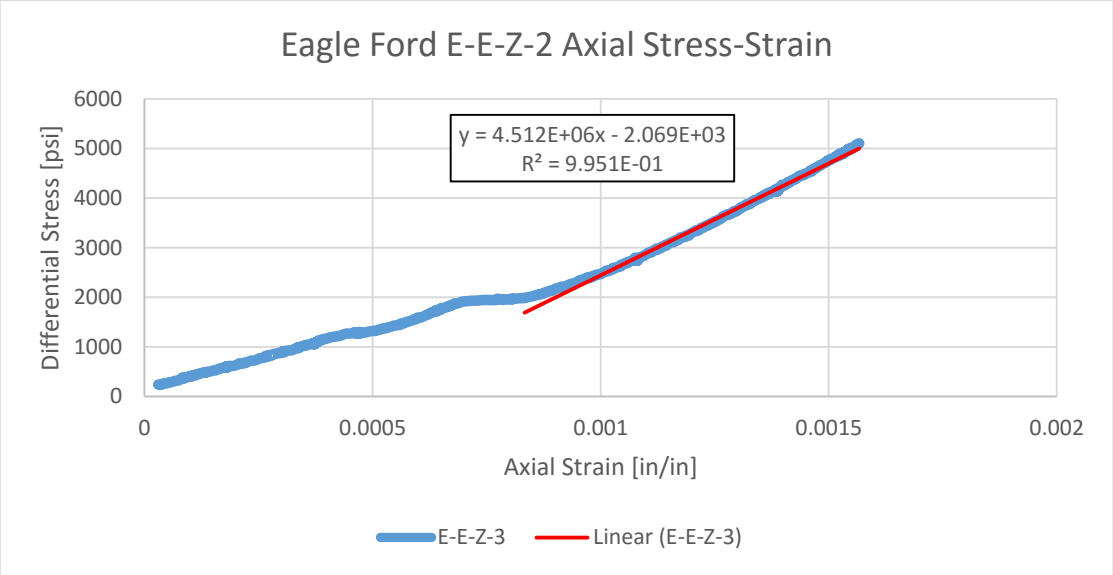
Eagle Ford E-E-Z-2 Axial Stress-Strain
y = 4.512E+06x - 2.069E+03
R² = 9.951E-01
Differential Stress [psi]
6000
5000
4000
3000
2000
1000
0
0
0.0005
0.001
0.0015
0.002
Axial Strain [in/in]
E-E-Z-3
Linear (E-E-Z-3)

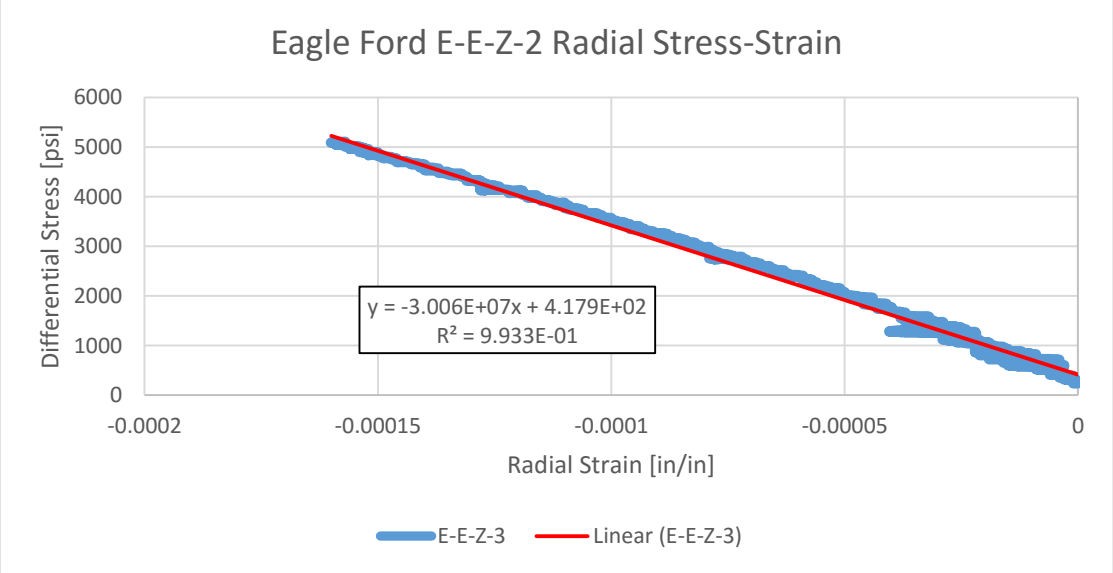
Eagle Ford E-E-Z-2 Radial Stress-Strain
y = -3.006E+07x + 4.179E+02
R² = 9.933E-01
Differential Stress [psi]
6000
5000
4000
3000
2000
1000
0
-0.0002
-0.00015
-0.0001
-0.00005
0
Radial Strain [in/in]
E-E-Z-3
Linear (E-E-Z-3)